

**Mechanical Properties of Transversely Isotropic
Fibre Network Composites**

by

Xiude Lin



Thesis submitted for the degree of Doctor of Philosophy

School of Engineering

Cardiff University

2018

DECLARATION

This work has not been submitted in substance for any other degree or award at this or any other university or place of learning, nor is being submitted concurrently in candidature for any degree or other award.

Signed..... (candidate) Date.....

STATEMENT 1

This thesis is being submitted in partial fulfillment of the requirements for the degree of(insert MCh, MD, MPhil, PhD etc, as appropriate)

Signed..... (candidate) Date.....

STATEMENT 2

This thesis is the result of my own independent work/investigation, except where otherwise stated, and the thesis has not been edited by a third party beyond what is permitted by Cardiff University's Policy on the Use of Third Party Editors by Research Degree Students. Other sources are acknowledged by explicit references. The views expressed are my own.

Signed..... (candidate) Date.....

STATEMENT 3

I hereby give consent for my thesis, if accepted, to be available online in the University's Open Access repository and for inter-library loan, and for the title and summary to be made available to outside organisations.

Signed..... (candidate) Date.....

STATEMENT 4: PREVIOUSLY APPROVED BAR ON ACCESS

I hereby give consent for my thesis, if accepted, to be available online in the University's Open Access repository and for inter-library loans **after expiry of a bar on access previously approved by the Academic Standards & Quality Committee.**

Signed..... (candidate) Date.....

STATEMENT 4: PREVIOUSLY APPROVED BAR ON ACCESS

I hereby give consent for my thesis, if accepted, to be available online in the University's Open Access repository and for inter-library loans **after expiry of a bar on access previously approved by the Academic Standards & Quality Committee.**

Signed..... (candidate) Date.....

Acknowledgements

I wish to express my earnest thanks to my supervisors, Dr Hanxing Zhu and Prof. Stephane Bordas for their devotion over the past four years. Many many thanks to Dr Zhu for guiding me throughout the research with great patience and enthusiasm. Your professionalism, persistence and passion in research have inspired me to become an independent thinker. This will have a valuable impact on my life.

I would like to thank Dr Yanhui Ma who has shared some most valuable ideas in constructing the geometric model in this research. Also, great thanks go to my colleagues in our team for their helpful discussions and continuous support in my research. I would also like to thank the staff of the Research Office and Finance Office for their assistance.

I would like to acknowledge the financial support from the China Scholarship Council and Cardiff School of Engineering which have ensured the accomplishment of the research.

Finally, the deepest love for my family for their unconditional support and belief in me in my life. I am thankful to all my friends for their company and time we have joyfully spent together. Most love to my girlfriend, Dr Lisi Liang, my beloved one, who knows me, stays with me and most importantly loves me more.

Abstract

Fibre reinforced composites have been widely applied to many fields for their extraordinary mechanical and other physical properties such as thermal and electric conduction etc. The structure of the composites can be crucial to the overall mechanical properties of the composites. The designed fibre-network composite in this research is inspired by fibrous materials with overlap, such as metal fibre sintered sheet (MFSS). With a fibre network instead of uncontacted fibres as the reinforcement, the composite is expected to produce enhanced mechanical properties. Based on the designed transversely isotropic fibre-network composite, the elastic, elastoplastic and viscoelastic properties of the composite have been investigated by the Finite Element Method (FEM) to better understand the mechanical properties of the fibre-network composite.

The in-plane stiffness has illustrated a much larger value than the out-of-plane stiffness for this designed fibre-network structure. Furthermore, the normalised in-plane stiffness has revealed a linear relationship with volume fraction, whereas the normalised out-of-plane stiffness has demonstrated a polynomial relationship with volume fraction when the volume fraction is not too large.

The in-plane and out-of-plane yield surfaces, under biaxial stress states, indicate that the yield strengths meet the Hill yield criterion. The transversely isotropic fibre network composite structure exhibits a larger out-of-plane yield strength than the in-plane yield strength, although the out-of-plane stiffness is smaller than the in-plane stiffness, which is expected to be related to the matrix properties. An analytical model has been proposed and have successfully modelled the elastoplastic stress-strain

response of the simplified RVE.

In terms of the viscoelasticity of the fibre-network structure, the collagen aerogel indicates a linear relationship with relative density for the in-plane relaxation modulus, while a cubic polynomial relation with relative density for the out-of-plane relaxation modulus. For the collagen hydrogel, it illustrates a larger in-plane strain than the out-of-plane strain under constant stress. When a constant tensile strain is applied, both the in-plane and out-of-plane relaxation moduli exhibit a nearly proportional relation with volume fraction.

Contents

Acknowledgements	I
Abstract	II
List of Figures	IX
List of Tables.....	XIV
List of Abbreviations.....	XVI
Nomenclature	XVII
Chapter 1 Introduction	1
1.1 Research Background and Objectives	1
1.2 Thesis Outline.....	3
Chapter 2 Literature Review.....	5
2.1 Fibre Reinforced Composites	5
2.1.1 Reinforcement Materials	5
2.1.2 Matrix Materials.....	9
2.1.3 General Fibre Reinforced Composites	11
2.1.3.1 Aligned Fibre Composites	11
2.1.3.2 Woven Fabric Composites.....	13
2.1.3.3 Laminates	14
2.1.3.4 Random Fibre Composites	15
2.2 Fibre Network.....	17
2.2.1 Metal Fibre Sintered Sheets	19
2.2.2 Biological Fibre Network.....	21
2.2.3 Honeycomb and Open-cell Foams	22
2.3 Characterisation of Fibre Reinforced Composites	23
2.3.1 Elasticity Analysis of Fibre Reinforced Composites	23
2.3.1.1 Stiffness and Compliance Matrix	23

2.3.1.2	Theoretical Models of Elastic Analysis.....	26
2.3.2	Elastoplastic Behaviours of Fibre Reinforced Composites.....	32
2.3.2.1	Theoretical Models for Elastoplastic Analysis of Fibre Reinforced Composites	32
2.3.2.2	Determination of Yield Strength	36
2.3.3	Viscoelasticity of Soft Tissues	39
2.3.3.1	Viscoelastic Models.....	39
2.3.3.2	Characterisation of Viscoelasticity of Soft Tissues	42
2.3.3.3	Deformation of Tissues	45
Chapter 3 Three-dimensional Geometrical Model of Transversely Isotropic Random Fibre Network Reinforced Composites		48
3.1	Introduction	49
3.2	Generation of the 3D Stochastic Fibre Network	50
3.2.1	In-plane Distribution of Fibres	51
3.2.2	Determination of Intersections in the z -direction.....	53
3.2.3	In-plane Periodicity	55
3.2.4	Out-of-plane Periodicity.....	56
3.3	Construction of Stochastic Fibre Network Reinforced Composites.....	58
3.3.1	Beam Model of Fibres.....	58
3.3.2	Assembly of Fibre Network and Matrix	60
3.3.3	Constraints between Fibre Network and Matrix	60
3.4	Mesh	62
3.5	Boundary Conditions	63
3.5.1	Periodic Boundary Conditions	63
3.5.2	Load.....	67
3.6	Key Parameters.....	69
3.6.1	Cross-linker Density.....	69

3.6.2	Overlap Coefficient	70
3.6.3	Aspect Ratio	71
3.6.4	Volume Fraction.....	72
3.7	Conclusions	74
Chapter 4 Elastic Properties of Transversely Isotropic Random Fibre Network Reinforced Composites		76
4.1	Introduction	77
4.2	Geometry and Material Properties.....	78
4.3	Discussions of RVE.....	79
4.3.1	Statistical Analysis	79
4.3.2	Mesh Sensitivity	79
4.3.3	Fibre Quantity Determination	81
4.3.4	Dependence of the RVE Thickness and Volume Fraction on the Cross-linker Density	83
4.3.5	Fibre Element Type Difference.....	84
4.3.6	Transverse Isotropy of RVE.....	86
4.4	Numerical Results	88
4.4.1	Five Independent Constants	88
4.4.2	Comparison of In-plane and Out-of-plane Elastic Properties	92
4.4.3	The Effect of Poisson's Ratio on the Elastic Properties	94
4.4.4	The Effect of Aspect Ratio on the Elastic Properties.....	99
4.4.5	The Effect of Cross-linker Density on the Elastic Properties	102
4.4.6	Discussions.....	106
4.5	Analytical Model	109
4.5.1	Geometrical and Mechanical Model	109
4.5.2	The Relationship between Young's Modulus in the x -direction and Volume Fraction	114

4.5.3	The Relationship between Young's Modulus in the z -direction and Volume Fraction	115
4.5.4	The Effect of Poisson's Ratio on the Elastic Properties	118
4.6	Conclusions	121
Chapter 5 Elastoplastic Properties of Transversely Isotropic Random Fibre Network Reinforced Composites		123
5.1	Introduction	124
5.2	Yield Criterion for Transversely Isotropic Fibre Network Reinforced Composites	125
5.3	Geometry and Material Properties.....	127
5.4	Comparison of the Models with Solid and Beam Fibre Elements	129
5.5	Numerical Results	132
5.5.1	Stress-strain Curve under Uniaxial Tensile/shearing.....	132
5.5.2	The Effect of the Stiffness of the Matrix on the Yield Strength	135
5.5.3	Yield Surface under Biaxial Stress States	136
5.5.4	Dependence of Yield Strength on the Volume Fraction	139
5.5.5	The Effect of the Combined Axial Loading and Shearing on the Yield Strength	146
5.6	Analytical Solution	148
5.7	Discussions	154
5.8	Conclusions	157
Chapter 6 Viscoelastic Properties of Aerogel and Hydrogel with Transversely Isotropic Random Fibre Network		158
6.1	Introduction	159
6.2	Viscoelastic Properties of Collagen Network Aerogel.....	160
6.2.1	Geometry and Material Properties	160
6.2.1.1	The Geometry of the RVE.....	160
6.2.1.2	Mechanical Model and Material Properties.....	161

6.2.2	Stress Relaxation under Different Strain.....	163
6.2.3	Stress Relaxation over Time	164
6.2.4	Dependence of Relaxation Modulus on Relative Density	167
6.2.4.1	Numerical Results	167
6.2.4.2	Analytical Model	173
6.3	Viscoelastic Properties of Collagen Fibre Network Hydrogel	177
6.3.1	Geometry and Material Properties	177
6.3.2	Creep	178
6.3.2.1	Creep under Constant Stress.....	178
6.3.2.2	Dependence of strain on the volume fraction.....	180
6.3.3	Stress Relaxation	182
6.3.3.1	Stress Relaxation over Time.....	182
6.3.3.2	Dependence of Relaxation Modulus on the Volume Fraction	185
6.4	Discussions	186
6.5	Conclusions	189
Chapter 7 Conclusions and Further Research		190
7.1	Conclusions	190
7.2	Further Research.....	192
References.....		194
Publications		214

List of Figures

Figure 2.1. Two-dimensional schematic of continuous (a) and discontinuous (b) aligned fibre composites [47], where the coloured bars represent fibres and the gap is supposed to be filled with matrix materials.....	12
Figure 2.2. Two-dimensional schematic of woven fabric composites [47], where the coloured bars represent fibres and the gap is supposed to be filled with matrix materials.	14
Figure 2.3. In-plane elastic modulus of plain fabric composite in terms of various off-axis angles [50].....	14
Figure 2.4. Exploded view of generic three-layered laminate with arbitrary ply orientation angles [57].....	15
Figure 2.5. Two-dimensional [62] and three-dimensional [2] schematic of random fibre composites, where the bars represent fibres and the gap is supposed to be filled with matrix materials.....	16
Figure 2.6. Microstructures of the metal fibre network by SEM and μ -CT [64].	17
Figure 2.7. An example of a bulk metal fibre sintered sheets (MFSSs) [10].....	19
Figure 2.8. Electron Microscopy of neurofilament gel in which neurofilament polymers are linked together [86].	21
Figure 2.9. (a) Open cell Al foams with a relative density of 42% by SEM [96]; (b) Voronoi honeycomb with irregular cells [100].	23
Figure 2.10. Schematic drawing of Eshelby's method in the equivalence of homogeneous inclusion (a) and inhomogeneous inclusion (b) [117].	30
Figure 2.11. Schematic plotting of several methods of yield point determination: (a) Graphic method [173]; (b) Equivalent energy method [176]; (c) Farthest Point Method [177]; (d) Apparent elastic limit.	38
Figure 2.12. Hierarchy of tendon structure according to Kastelic et al. [211].	43
Figure 2.13. A schematic of two deformation modes: short-range motion and long-range motion, in a gel consisting of a polymer network (lines) and small molecules (dots) [250].	46
Figure 3.1. The flowchart of the process of generating the representative volume element (RVE).....	51
Figure 3.2. An example of fibres randomly distributed in the square region of $L \times L$. Red dots represent the centre points of the fibres.	52

Figure 3.3. A scenario of how fibres are bonded to one another. The fibre in yellow colour drops down and intersects with other three silver fibres at the locations where they are marked with red circles, and the fibre is divided into four segments but still connected.....	55
Figure 3.4. Operations on one of the fibres that parts of it exceed the central cell. The dashed parts represent the segments cut off by the boundary of the cell and the solid parts that are inside of the cell are reserved.	56
Figure 3.5. A scenario of RVE geometry model with 50 solid fibres.....	57
Figure 3.6. Periodic RVE geometric model of the composite reinforced by a transversely isotropic random fibre network containing 200 complete fibres, where the matrix is partitioned into brick elements and the fibres are partitioned into Timoshenko beam elements.	59
Figure 3.7. A scenario of inserting beams between overlapped fibres.	59
Figure 3.8. Assembly process of fibre network and matrix.	60
Figure 3.9. A sketch for the node coupling of the ASC technique [2].....	61
Figure 3.10. The meshing of the matrix with structured 8-node linear brick solid elements (C3D8R).....	62
Figure 3.11. Two types of periodic boundary conditions: (a) Strict periodic boundary condition; (b) General periodic boundary condition.	64
Figure 3.12. A cubic representative volume element (RVE).	64
Figure 3.13. The schematic diagram of RVE undertaking shear loading τzx	69
Figure 3.14. Fibre network structure with cross-linker density (a) $N_c = 3$, (b) $N_c = 11$, (c) $N_c = 21$, and (d) $N_c = 27$, when $L/d = 100$	70
Figure 4.1. Mesh size effect on in-plane and out-of-plane Young's moduli for 10 RVEs with volume fractions of 9% and 30%, respectively.	81
Figure 4.2. Effect of cross-linker density, N_c , on RVE thickness (the curve with square symbol) and fibre volume fraction (the curve with round symbol) with aspect ratio $L/d = 100$	84
Figure 4.3. Effect of volume fraction on (a) in-plane Young's modulus E_{11} , (b) in-plane Poisson's ratio ν_{12} , (c) out-of-plane Young's modulus E_{33} , (d) out-of-plane Poisson's ratio ν_{31} and (e) out-of-plane shear modulus G_{31} with the aspect ratio $L/d = 100$ and same Poisson's ratios $\nu_f = \nu_m = 0.3$	91
Figure 4.4. Comparison of in-plane and out-of-plane elastic properties: (a) in-plane and out-of-plane Young's moduli, (b) in-plane and out-of-plane Poisson's ratios, (c) in-plane and out-of-plane shear moduli, with $E_f/E_m = 10$ and 50.	94

Figure 4.5. Dependence of elastic properties (a) E_{11} , (b) ν_{12} , (c) E_{33} , (d) ν_{31} and (e) G_{31} on the volume fraction under different Poisson's ratios.	98
Figure 4.6. The effect of aspect ratio ($L/d = 40, 80, 100, 125$) on the relationship between elastic properties (a) E_{11} , (b) ν_{12} , (c) E_{33} , (d) ν_{31} and (e) G_{31} and volume fraction.	102
Figure 4.7. The effect of cross-linker density ($N_c = 7, 15, 19, 23, 25, 27$) on the relationship between elastic properties (a) E_{11} , (b) ν_{12} , (c) E_{33} , (d) ν_{31} and (e) G_{31} and volume fraction.	105
Figure 4.8. Comparison of several results of Young's modulus E_{11} in terms of volume fraction.	107
Figure 4.9. A simplified geometrical model of the fibre network reinforced composites with aligned fibres along x and y directions.	111
Figure 4.10. Comparison of the relationships between volume fraction and cross-linker density of the fibre network reinforced composites with random fibres (the square dot curve) and the simplified regular fibre network reinforced composites (the round dot curve).	111
Figure 4.11. A representative volume element (RVE) of the simplified geometrical model of the fibre network composite.	112
Figure 4.12. The relationship between Young's modulus in the x -direction and volume fraction of the simplified analytical model.	117
Figure 4.13. The relationship between Young's modulus in the z -direction and volume fraction of the simplified analytical model.	117
Figure 4.14. Analytical results of the effect of Poisson's ratio on the elastic properties: (a) E_{11} ; (b) ν_{12} ; (c) E_{33} ; (d) ν_{31}	120
Figure 5.1. The elastoplastic response of transversely isotropic materials under uniaxial loading and pure shearing [279].	125
Figure 5.2. The stress-strain curve of stainless steel fibre (a) and matrix (PA-6: (b)-black curve, Epoxy: (b)-red curve).	128
Figure 5.3. Uniaxial tensile and shear stress ($\sigma_{11}, \sigma_{22}, \sigma_{33}, \sigma_{12}, \sigma_{23}, \sigma_{31}$)-strain curves of random fibre network reinforced composites with beam and solid fibre element types, respectively, under a strain of 5%. The volume fraction is 0.09....	131
Figure 5.4. Stress-strain curves of the steel/PA-6 composite (a) and the steel/828LVEL composite (b), with structure parameters fibre aspect ratio $L/d = 100$, number of fibres $N = 200$, cross-linker density $N_c = 21$ and overlap coefficient $c = 0.55$, under uniaxial tension or shearing. The volume fraction is 0.24.	134
Figure 5.5. The effect of stiffness of matrix on in-plane and out-of-plane yield tensile strength with structure parameters fibre aspect ratio $L/d = 100$, number of fibres $N =$	

200, cross-linker density $N_c = 21$ and overlap coefficient $c = 0.55$, under uniaxial tension. The volume fraction is 0.24.....	136
Figure 5.6. Yield surface in plane of isotropy (a) and plane of anisotropy (b) of the steel/ PA-6 composite, with structure parameters fibre aspect ratio $L/d = 100$, number of fibres $N = 200$, number of cross-linkers $N_c = 21$ and overlap coefficient $c = 0.55$, under biaxial tension/compression. The volume fraction is 0.24.....	138
Figure 5.7. Yield surface in plane of isotropy (a) and plane of anisotropy (b) of the steel/828LVEL composite, with structure parameters fibre aspect ratio $L/d = 100$, number of fibres $N = 200$, number of cross-linkers $N_c = 21$ and overlap coefficient $c = 0.55$, under biaxial tension/compression. The volume fraction is 0.24.	139
Figure 5.8. The relationship between (a) yield tensile strength and (b) yield shear strength of the steel/PA-6 composite (in-plane yield strength: Y_{12} and out-of-plane yield strength: Y_{31}) and volume fraction of fibres.....	142
Figure 5.9. In-plane (a) and out-of-plane (b) yield surfaces in terms of different volume fractions of fibres for the steel/PA-6 composite.....	143
Figure 5.10. The relationship between (a) yield tensile strength and (b) yield shear strength of the steel/828LVEL composite (in-plane yield strength: Y_{12} and out-of-plane yield strength: Y_{31}) and volume fraction of fibres.	144
Figure 5.11. In-plane (a) and out-of-plane (b) yield surfaces in terms of different volume fractions of fibres for the steel/828LVEL composite.....	145
Figure 5.12. The angle of tilt of the out-of-plane yield surface in terms of volume fraction for the steel/PA-6 composite (a) and steel/828LVEL composite (b), respectively.....	145
Figure 5.13. The effect of combined axial loading and shearing on in-plane and out-of-plane yield strength of the steel/PA-6 composite.	147
Figure 5.14. In-plane and out-of-plane yield surfaces under combined biaxial tension and shearing for the steel/PA-6 composite. Various shear stresses ($\sigma_{31}=0, 1, 2, 3$ and 3.5MPa) are applied.	148
Figure 5.15. A representative volume element (RVE) of the simplified geometry model of the fibre network composite.....	149
Figure 5.16. Comparison of the analytical and FEM stress(σ_{11})-strain relations of the simplified RVE and the FEM results of the proposed fibre network composite (steel/PA-6) with a volume fraction of 0.24.....	152
Figure 5.17. Yield tensile strengths (Y_{11}) of both the fibre network composite and the simplified RVE with respect to volume fraction. The fibres are stainless steel and the matrix is PA-6 for both models.	154
Figure 5.18. Comparisons of the proposed fibre network composite with other composites.....	156

Figure 6.1. The RVE geometric beam model of the fibre network with cross-linkers.	161
Figure 6.2. Schematic representation of Maxwell-Weichert model with two Maxwell elements.....	163
Figure 6.3. Normalised stress relaxation of collagen fibre network at various strains.	164
Figure 6.4. Normalised relaxation stress ((a) σ_{11} , (b) σ_{33} , (c) σ_{12} and (d) σ_{31}) of the collagen fibre network with the relative density of 0.15.....	166
Figure 6.5. Relaxation stress ((a) σ_{11} , (b) σ_{33} , (c) σ_{12} and (d) σ_{31}) of fibre networks with different relative densities (0.06-0.36) under constant strain $\varepsilon = 2\%$	169
Figure 6.6. Instantaneous relaxation modulus (i.e. $E(0)$ or $G(0)$) and relaxation modulus at $t = 200$ s (i.e. $E(200)$ or $G(200)$) of fibre networks with different relative densities (0.06-0.36): (a) E_{11} , (b) E_{33} , (c) G_{12} and (d) G_{31}	172
Figure 6.7. A simplified model of cross-linked fibre network with aligned fibres along x and y directions, respectively. (a) In-plane view; (b) Out-of-plane view..	173
Figure 6.8. Time-dependent in-plane (a) and out-of-plane (b) strain changes of collagen gels with different volume fractions (0.02-0.42) under the constant stress σ $= 1$ MPa. The constant stress is imposed on the collagen gels from $t = 0$ s to $t = 200$ s and then released from $t = 200$ s.	180
Figure 6.9. Dependence of in-plane strain (ε_{11}) and out-of-plane strain (ε_{33}) of collagen gels on volume fractions. Both the strains when a constant stress has been applied for 200s ($t = 200$ s) and the strains after the constant stress has been removed for 200s ($t = 400$ s) have been shown in this figure.	181
Figure 6.10. Relaxation stress ((a) σ_{11} , (b) σ_{33} , (c) σ_{12} and (d) σ_{31}) of collagen gels with different volume fractions (0.02-0.42) under constant strain $\varepsilon = 2\%$	184
Figure 6.11. Comparison of in-plane and out-of-plane relaxation moduli of collagen gels with different volume fractions (0.02-0.42) under constant tension (a) or hearing (b) strain $\varepsilon = 2\%$. $E(0)$ and $G(0)$ are the instantaneous relaxation moduli, i.e. the relaxation moduli when $t = 0$ s. $E(200)$ and $G(200)$ are the relaxation moduli at $t =$ 200 s under constant strain $\varepsilon = 2\%$	186
Figure 6.12. Comparison of the instantaneous moduli of the fibre network composites and random short fibre composites.	188

List of Tables

Table 2.1. Mechanical properties of some natural and synthetic fibres [22, 39, 41].	9
Table 2.2. Mechanical properties of selected matrix materials [43].	10
Table 3.1. The volume of the intersection with respect to the included angle and overlap coefficient.	74
Table 4.1. Materials parameters for the elasticity study in FE models.	79
Table 4.2. Mesh size effect on the in-plane and out-of-plane Young's moduli and Poisson's ratios of RVE.	80
Table 4.3. Statistic Young's modulus, E_{11} , and volume fraction of 10 RVEs for different numbers of fibres ($N = 50, 75, 100, 150, 200, 400$) with the density of cross-linker at $N_c = 11$, the overlap coefficient at $c = 0.3$, and the aspect ratio at $L/d = 100$.	82
Table 4.4. The mean ratio of paired Young's moduli.	83
Table 4.5. The independent elastic properties of RVE with beam and solid fibre element types, respectively, in which degree of cross-linkers $N_c = 15$, overlap coefficient $c = 0.4$ and aspect ratio $L/d = 30$. The values are averaged for 10 RVEs.	86
Table 4.6 Young's moduli, Poisson's ratios and shear moduli of 10 RVEs with density of cross-linkers $N_c = 11$, overlap coefficient $c = 0.3$, fibre number $N = 200$, and aspect ratio $L/d = 100$. The volume fraction is 0.09.	87
Table 4.7. Stiffness comparison between this research and others' experimental and numerical results.	106
Table 5.1. Mechanical properties of fibre and matrix materials [40].	128
Table 5.2. Yield strength values (MPa) of stochastic fibre reinforced composites with beam and solid fibre element types, respectively, under uniaxial tension and shearing simulations with structure parameters fibre aspect ratio $L/d = 30$, number of fibres $N = 50$, cross-linker density $N_c = 15$ and overlap coefficient $c = 0.4$. The volume fraction is 0.09.	131
Table 5.3. Yield strength values (MPa) of stochastic fibre reinforced composites under uniaxial tension and shearing simulations with structure parameters fibre aspect ratio $L/d = 100$, number of fibres $N = 200$, cross-linker density $N_c = 21$ and overlap coefficient $c = 0.55$. The volume fraction is 0.24.	134
Table 5.4. Mechanical properties of the simplified RVE and the proposed fibre network composite (steel/PA-6) with the volume fraction of 0.24.	153

Table 6.1. Viscoelastic parameters used in Maxwell-Weichert model for Type I collagen fibrils [205].	163
--	-----

List of Abbreviations

AFM	Atomic force microscopy
ECM	Extracellular matrix
EEM	Embedded element method
FE	Finite element
FEA	Finite element analysis
FEM	Finite element method
LAA	Laminate analogy approach
MEMS	Micro electro mechanical systems
MFSSs	Metal fibre sintered sheets
MPC	Multi-point constraint
PBC	Periodic boundary condition
QLV	Quasi-linear viscoelastic
RSA	Random sequential adsorption
RVE	Representative volume element
UC	Unit cell
UD	Uni-directional

Nomenclature

A	Area of cross section
c	Overlap coefficient
$\mathbf{C}_{ij}, \mathbf{C}$	Stiffness tensor
\mathbf{C}^f	Stiffness tensor of fibre
\mathbf{C}^m	Stiffness tensor of matrix
d, d_i	Fibre diameter
E	Young's modulus
E_C	Young's modulus of composite
E_f	Young's modulus of fibre
E_m	Young's modulus of matrix
$E_1(E_x), E_2(E_y), E_3(E_z)$	Young's modulus in the x, y, z directions
E_{\parallel}	Young's modulus parallel to fibres
E_{\perp}	Young's modulus perpendicular to fibres
E_{∞}	Time-independent elastic modulus
$E(0)$	Instantaneous relaxation modulus
$E(t)$	Relaxation modulus at time t
F_r	Reaction force of the reference node
G	Shear modulus
G_{12}, G_{23}, G_{31}	Shear modulus in the xy, yz, zx directions
$G(0)$	Instantaneous shear modulus
H	Thickness of RVE
I	Second moment of area
K	Bulk modulus
K_1	Fibre length factor
K_2	Fibre orientation factor
$K(0)$	Instantaneous volumetric modulus
L, L_i	Fibre length
l_c	Critical length of fibre
N	Fibre number
N_c	Cross-linker density

N_f	Node on fibre
N_m	matrix node
r	Radius of fibre
$\mathbf{S}_{ij}, \mathbf{S}$	Compliance tensor
\mathbf{S}^m	Compliance tensor of matrix
S_x	Area of the face perpendicular to the x -direction
S_z	Area of the face perpendicular to the z -direction
t	Time
u	Displacement of nodes
V_f	Volume fraction of fibre
V_m	Volume fraction of matrix
V_I	Volume of the intersection
W	Width of RVE
w	Load
θ	Fibre orientation
ν	Poisson's ratio
ν_{ij}	Poisson's ratios in the corresponding directions
α	Included angle between fibres
σ_e	Elastic component of stress
σ_v	Viscous component of stress
σ_y	Yield strength
σ_f	Yield strength of the fibre
σ_m	Yield strength of the matrix
σ_i	Normal stress
τ_{ij}	Shear stress
τ_1, τ_2	Relaxation time
$\varepsilon_i, \varepsilon$	Normal strain
$\varepsilon_x, \varepsilon_{11}$	Normal strain in the x -direction
$\varepsilon_z, \varepsilon_{33}$	Normal strain in the z -direction
γ_{ij}	Shear strain
η_1, η_2	Damping coefficient
$\Delta x, \Delta y, \Delta z$	Deflection in the x, y and z directions

Chapter 1 Introduction

1.1 Research Background and Objectives

Fibre reinforced composites have been increasingly used in various fields for their extraordinary mechanical and other physical properties such as thermal and electric conduction with a wide selection of constituent materials and geometry structures. Numerous different structures of fibre composites, such as uni-directional fibre composites, cross-ply fibre composites, woven fabric composites and fibre laminates etc., have been designed and applied primarily for their advantages in directional mechanical properties, specifically, axial or planar mechanical properties. However, superior properties are achieved by sacrificing the properties in the other axial or planar directions. In addition, it is inevitable in engineering that loads are applied to off-axis/plane directions. This may increase the risk of fracture and failure. For instance, delamination [1] is a common problem for laminate composites due to the weakly bonded interfaces between plies when it is subjected to loading in its inferior directions. Some three-dimensional short fibre reinforced composites are either isotropic with fibres distributed randomly in three dimensions [2] or transversely isotropic with fibres distributed stochastically in a planar direction or within a certain inclined angle [3] to the planar direction, which possess no obvious inferior directions. However, the constraints among fibres are weak because they are at most in contact but not perfectly bonded, thus rendering easy pull-out [4] of fibres and large deformation when subjected to loads.

Porous materials are another type of promising structures in engineering applications.

Porous materials, such as foam [5], honeycomb [6], and fibre network etc., indicate excellent mechanical properties as porous structures and can perfectly serve as the reinforcement to composites as well. Fibre network structure is universal in biologies such as cytoskeleton [7] and collagen gel [8, 9], and metal fibre sintered sheet (MFSS) [10-16] is one of the most common man-made fibre networks. Compared to fibrous materials like textiles which possess obvious directional mechanical properties, fibre network has demonstrated the same level of properties in the primary direction while still delivers relatively better performance in the other directions due to the introduction of cross-linkers among fibres. Zhang et al. [17] have created a numerical model of carbon-bonded carbon fibre network by inserting a beam [18] between the intersected points of the two fibres and it shows good agreement with the experimental results. A similar 3D fibre network has also been studied experimentally and numerically in [13] and the stress-strain relations indicate that the fibre-fibre connection can dramatically improve the fibre network strength.

Thus the behaviours of fibre networks imply that the introduction of fibre networks into the composites would be an advantage in improving mechanical properties of composites. Compared to conventional structures of fibre reinforced composites, the cross-linkers or intersections between fibres are supposed to enhance both the in-plane and out-of-plane mechanical properties, such as stiffness and strength. Apart from improved mechanical properties, good thermal and electrical conductivities [19, 20] can also be an advantage for fibre network composites owing to the connected network of fibres. Therefore, we aim to construct a 3D fibre network reinforced composite structure in which fibres are connected into a network. The proposed composite structure is supposed to provide more options for certain application requirements in mechanics or other properties.

The main objectives and contributions of this research can be briefly described as:

1. To generate or prepare a novel 3D transversely isotropic fibre network reinforced composite model with fibres curved and intersected to build up a network. This aims to be accomplished by altering the key parameters of the model, such as aspect ratio, cross-link density and overlap coefficient. The nature of the constructing procedure of this model tends to be extremely attractive as a composite plate structure because the through-thickness dimension is adjustable.
2. To investigate the elastic behaviours of this novel transversely isotropic fibre network composite. As cross-linkers are introduced in this composite structure, both the in-plane and out-of-plane stiffnesses are expected to be enhanced. Thus the elastic properties of this transversely isotropic structure need to be primarily explored and compared with conventional composite structures.
3. To investigate the plastic, more precisely, elastoplastic properties of this novel transversely isotropic fibre network composite. The yield behaviours of the selected material systems under different loading conditions need to be investigated.
4. To investigate the viscoelastic behaviours of this newly built transversely isotropic fibre network composite and the fibre network alone in the case of biological applications of this structure. Key characteristics such as stress relaxation and creep of the fibre network alone and the fibre network composite are focused on for the analysis.

1.2 Thesis Outline

In relation to the major objectives, the thesis is organised as follows:

Chapter 1 gives a brief introduction of the motivation of this research and outlines the framework of the thesis.

Chapter 2 reviews relevant studies with respect to fibre composite materials and fibre network materials as well as the theoretical framework of elastic, elastoplastic and viscoelastic properties.

Chapter 3 introduces the procedure of constructing a three-dimensional transversely isotropic fibre network composite model in which fibres are curved and intersected thus generating a network.

Chapter 4 explores the elastic behaviours of the transversely isotropic fibre network composite as previously developed in Chapter 3. The five independent constants in terms of volume fraction are mainly studied by finite element method (FEM). A simplified analytical model is also proposed for comparison.

Chapter 5 investigates the elastoplastic properties of the newly built transversely isotropic steel fibre network composite with a ductile matrix and brittle matrix, respectively. Based on the Hill yield criterion, the yield strength and yield surface under uniaxial and biaxial loadings are explored. An analytical model of the elastoplastic stress-strain response is explored towards the simplified RVE.

Chapter 6 focuses on the exploration of viscoelastic properties, e.g. stress relaxation and creep, of the collagen network alone and of collagen gels based on the designed fibre network structure.

Chapter 7 summarises the main conclusions of the proposed composite structure and mechanical properties it exhibits. Furthermore, limitations regarding the current work and possible further work are underlined.

Chapter 2 Literature Review

2.1 Fibre Reinforced Composites

Composites refer to materials consisting of two or more individual constituents, where they are formed with the reinforcing constituent embedded in a matrix. In composites, the properties like mechanical properties are determined by the combination of the matrix and reinforcement. By choosing the appropriate reinforcement and matrix from the variety of materials, composites with extraordinary properties over individual constituent materials can be produced. The rapidly expanding application of composites in aerospace, marine, automotive, construction, sports and other mass production industries, has encompassed an abundance of structures and materials ranging from natural to synthetic, in order to meet the requirements of producing composites with desired properties for certain applications.

2.1.1 Reinforcement Materials

Composite structures are quite common in nature, of which fibre reinforced composites is one of the most widely used structures where natural fibre and matrix are combined. Natural fibre-reinforced composites have attracted intense interest as a potential structural material [21]. Natural fibres originate from plants, animals and minerals etc. Plant or vegetable fibres are usually adopted as reinforcements for plastics and may include seed fibres, fruit fibres, bast (or stem) fibres, leaf (or hard) fibres, wood fibres, cereal stalk fibres, and other grass fibres etc [22]. Animal fibres are composed in the form of protein and may include alpha keratin fibres (hairs,

wools, quills, and other mammalian appendages), fibroin fibres (silks and spiders webs) and collagens (major components of extracellular matrix, tendons, ligaments, skin, cornea, bone and dentin etc.) [8, 23, 24], for which the mechanical properties are of primary importance to both the animal from which they originate and their ultimate applications. Mineral fibres may include basalt fibre, stone wool, slag wool, asbestos, fibrous brucite and wollastonite etc [22, 25]. The main advantages of natural fibres lie in their sustainability, renewability, recyclability, economy and environmentally friendly features. However, there are also drawbacks, such as durability, fibre strength, commercial supply and demand cycles and quality variations [26].

In order to fulfil the abundant demands of fibres with required properties, some synthetic or post-processed natural fibres have been produced to fill in the gap of properties that natural fibres fail to possess or replace natural fibres with similar properties as overall better choices. Two most common man-made fibres in the composite industry would be glass fibre and carbon fibre. Glass fibre still indicates good mechanical behaviours although not as stiff or strong as carbon fibre and it exhibits a higher elongation at break point than carbon fibre. In addition, the combining properties, i.e. high specific strength, chemical resistance, moisture resistance, heat resistance and electric insulation have made glass fibre particularly attractive in the industry [27]. Most importantly, its relatively low cost has gained glass fibre wider applications than carbon fibre, for instance, in the construction of large structures, e.g. large boats, wind turbines and so on.

To meet the demand of fibre with extremely high stiffness and strength properties, carbon fibre emerges. Carbon fibre possesses dramatically high specific stiffness and

strength due to the well aligned and bonded carbon atoms along the fibre. Together with the light weight, carbon fibre proves to be promising in applications which require extremely high strength and lightweight structures while ignoring the cost of materials preparation and manufacturing process. Furthermore, carbon fibre also possesses good impact and fatigue behaviours, thermal stability, high temperature resistant, electric conductivity and corrosion resistance etc [27]. However, carbon fibre is a very stiff and brittle material that is apt to break in a small elongation.

Another synthetic fibre that has long been used as the reinforcement for polymer composites is Kevlar fibre. Kevlar has been adapted to a variety of applications since born, such as aircraft, marine and construction. As a member of aramid fibres, Kevlar fibre has exhibited high strength, distinct tenacity, impact resistance under environmental conditions and thus it plays a crucial role in tough and damage-tolerant composites as the reinforcement [28-30]. However, the strengths of Kevlar fibre, such as high tensile strength and stiffness, have been found not to be fully utilised in composites according to predictions based on the rule of mixtures. The main reason lies in that the surfaces of Kevlar fibres are chemically inert and smooth due to high crystallinity, resulting in poor adhesion with the matrix phase to transfer stress between fibres and matrix [29]. Additionally, degradation of the fibre properties can be introduced when the fibres are exposed to thermal environments either intentionally or accidentally during the fabrication process and following usage stage [31].

Steel, which is a very common metal material to us, has been vastly adopted in various civil engineering applications, such as machines, buildings and structures. Steel fibre is also not a new synthetic fibre and has been commonly used for structural

and non-structural purposes [32, 33]. For instance, steel fibre is utilized as reinforcement of concrete in the form of fibres, wires or rebars [34, 35], and applied as reinforcement of rubber in tyres and belts in the form of continuous wires, cords and filaments [36, 37]. Steel fibres can prevent/delay crack propagation from micro-cracks to macro-cracks and decrease crack width in concrete, thus reducing the shrinkage and increasing toughness [38].

In recent years, glass and carbon fibres have drawn the major attention for their superior strengths. However, this is achieved at the expense of stiffness and the strain-of-failure is extremely low due to the low ductility of the fibres. In contrast, steel possesses the feature that its strain-of-failure can be tailored by adopting a certain heat treatment without affecting its stiffness. Thus a strain-of-failure of 22% can be achieved for ductile steel fibre reinforced composites, which is around 10 and 5 times larger than those of carbon and glass reinforced composites, respectively. Steel fibres, more specifically, annealed stainless steel fibres, with diameters ranging from 5 to 100 μm , can be conducted with combining high stiffness (193GPa) and high strain-of-failure (<20%) [39, 40]. Therefore, steel fibre reveals a promising application in structural composites which exhibit both high stiffness and good ductility.

Finally, the main mechanical properties of a variety of natural and synthetic fibres are listed and compared in Table 2.1. The selected natural and synthetic fibres have included an approximate range of 3-400GPa in Young's modulus and 130-4800MPa in tensile strength.

Table 2.1. Mechanical properties of some natural and synthetic fibres [22, 39, 41].

Fibres	Diameter(μm)	Young's modulus (GPa)	Tensile strength (MPa)	Elongation at break (%)
Flax	40-600	27.6	345-1500	2.7-3.2
Hemp	25-500	70	690	1.6
Jute	25-200	13-26.5	393-800	1.16-1.5
Kenaf	-	53	930	1.6
Ramie	-	61.4-128	400-938	1.2-3.8
Nettle	-	38	650	1.7
Sisal Henequen	50-200	9.4-22	468-700	3-7
PALF	20-80	34.5-82.5	413-1627	1.6
Abaca	-	-	430-760	-
Oil palm EFB	150-500	3.2	248	25
Cotton	12-38	5.5-12.6	287-800	7-8
Coir	100-460	4-6	131-220	15-40
E-glass	<17	73	3400	2.5
Kevlar	-	60	3000	2.5-3.7
Carbon	5-7	240-425	3400-4800	1.4-1.8
Steel	>5	193	660	17

2.1.2 Matrix Materials

Matrix is one of the constituent materials in composites and usually binds and supports the reinforcements as a base to maintain the continuity and shape of composites. Thus the mechanical and physical properties, such as force and heat, can be delivered through the interfaces between reinforcement and matrix inside the composites. The properties of the matrix can be enhanced by the imported reinforcement and, in return, the matrix also impacts the reinforcement in the way of compatibility, such as the stability of the interfaces [42].

Common matrix materials may include polymer, ceramic, metal and carbon [43]. Polymer matrices, also called resin, are most widely used for composites in commercial and high-performance aerospace applications. Based on the ingredients and structures, the polymer can be divided into several categories, of which the most widely known are polyester, vinylester, epoxy, phenolic, polyimide, polyamide, polypropylene and PEEK. Ceramic matrix and metal matrix are typically applied in extremely high-temperature environments, like engines. Carbon as a matrix is used in very high-temperature applications like carbon-carbon brakes and rocket nozzles. The main mechanical properties of selected matrix materials are listed in Table 2.2.

Table 2.2. Mechanical properties of selected matrix materials [43].

Matrix	Class	Young's modulus (GPa)	Tensile strength (MPa)	Tensile failure strain (%)
Polyester	Thermosetting	2-4.5	40-90	2
vinylester[44]	Thermosetting	3.5	80	4
Epoxy	Thermosetting	3-6	35-100	1-6
polyimide[45]	-	2.5	231	72
polyamide	Thermoplastic	1.4-2.8	60-75	40-80
polypropylene	Thermoplastic	1-4	25-38	>300
PEEK	Thermoplastic	3.6	93	50
Aluminum(6061)	Metal	69	300	10
Titanium(6Al-4V)	Metal	105	1100	10
Silicon carbide	Ceramic	520	-	<0.1
Alumina	Ceramic	380	-	<0.1
Glass(borosilicate)	Ceramic	63	-	<0.1
Carbon	Carbon	20	-	<0.1

2.1.3 General Fibre Reinforced Composites

By the combination of the abundant fibres and matrices including, but not limited to, constituent materials listed in 2.1.1 and 2.1.2, with the varying structures brought about by various fibre distributions, numerous fibre reinforced composites can be achievable to meet the growing wide demand. In general, fibre reinforced composites may include aligned fibre composites, woven fabric composites, laminates and random fibre composites [46], based on fibre orientation. For instance, all the fibres are paralleled along the designated loading direction in the case of aligned fibre reinforced composites; woven fabric composites contain fibres or fibre bundles which are typically cross-woven with fibres distributed in two perpendicular directions; laminates reinforced by fibres generally consist of several layers and each layer can be regarded as an aligned fibre reinforced plate. Thus a nearly in-plane isotropic or anisotropic structure can be obtained by laying each ply along different directions; For the case of random fibre composites, it literally means that the fibres are distributed inside the matrix randomly, either in a priority of in-plane directions or evenly in all directions.

2.1.3.1 Aligned Fibre Composites

In the case of aligned fibre composites, also known as uni-directional (UD) fibre composites, all the fibres have the same orientation, which means that fibres are all parallel to each other. Aligned fibres composites can be further categorised as two types, namely continuous and discontinuous aligned fibre composites (see Figure 2.1), according to the critical size of fibre length, which is defined as the ratio of single fibre length over the side length. Aligned fibres are occasionally grouped as

bundles to enhance the strength of fibres. Obviously, this structure is anisotropic and it is mainly designed to afford the load imposed along the fibre direction. When the load is applied to different directions, such as the directions parallel to fibres or perpendicular to fibres, the composites exhibit a dramatic difference in mechanical behaviours like stiffness and strength.

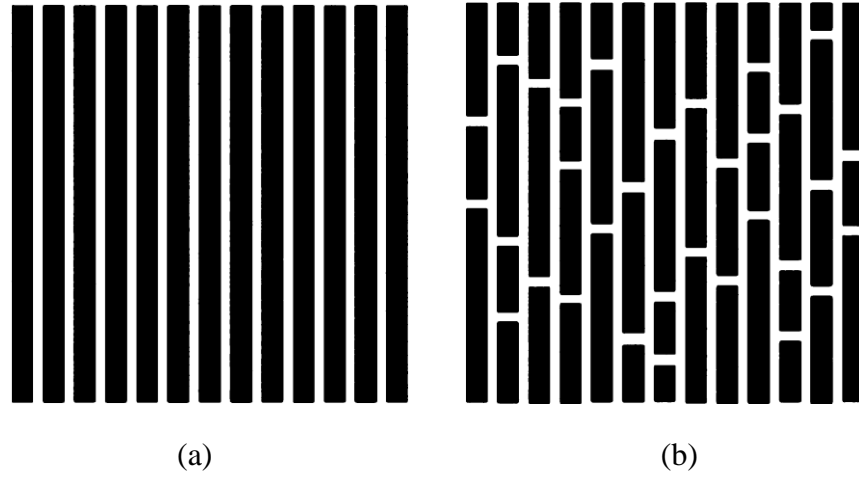


Figure 2.1. Two-dimensional schematic of continuous (a) and discontinuous (b) aligned fibre composites [47], where the coloured bars represent fibres and the gap is supposed to be filled with matrix materials.

Since all fibres are aligned in the aligned fibre composite, the effective elastic modulus of the composites can be simply presented, according to the Rule of Mixture when the composites are subjected to load parallel to or perpendicular to fibres, respectively, as

$$E_{\parallel} = E_f V_f + E_m V_m \quad (2.1)$$

$$E_{\perp} = \frac{E_f E_m}{E_f V_m + E_m V_f} \quad (2.2)$$

Where E_f and E_m are Young's moduli of fibre and matrix, respectively. V_f and V_m are the volume fractions of fibre and matrix and they obey $V_f + V_m = 1$. The

expression of E_{\parallel} is more widely known as the Voigt limit [48] and the equation of E_{\perp} is the well-known Reuss limit [49], which are often recognised as the maximum and minimum values of the modulus of a two-phase composite. It is not surprising that both the stiffness and strength of aligned fibre composites were found to decrease drastically as off-axis loading angles (i.e. angle between fibre direction and loading direction, ranging from 0 to $\pi/2$) increase [50].

One word, although aligned fibre composites can obtain a modulus close to upper limit when loaded along the fibre direction, this structure has to face the considerable weakness of the transverse modulus.

2.1.3.2 Woven Fabric Composites

Another fibre composite structure is woven fabric composites, in which fibre bundles are woven in different angles, and the plain fabric structure, as shown in Figure 2.2, is most familiar to us. The manufacturing process has long been used in textiles. The woven fabric is generally manufactured into a ply and then applied alone or stacked with several plies to create laminates. The structure is also anisotropic with largest stiffness and strength along either of the fibre direction and weaker mechanical behaviours in other directions. For example, Cai et al. [50] have measured the in-plane elastic modulus of plain fabric composite along various directions and obtained decreasing stiffness as increasing off-axis angles (see Figure 2.3). As for the out-of-plane behaviour, woven fabric composites indicate a high flexibility of deformation especially in the out-of-plane direction [51]. This may increase the risk of crack propagation and, even worse, fracture. Moreover, the constraints among intersected fibres are weak since they are at most in contact but not perfectly bonded, thus rendering easy pull-out of fibres and large deformation when just subjected to

uniaxial tension in the out-of-plane direction.

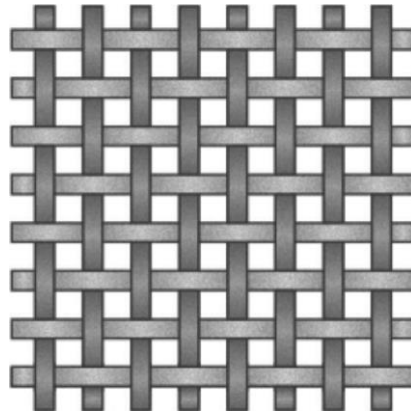


Figure 2.2. Two-dimensional schematic of woven fabric composites [47], where the coloured bars represent fibres and the gap is supposed to be filled with matrix materials.

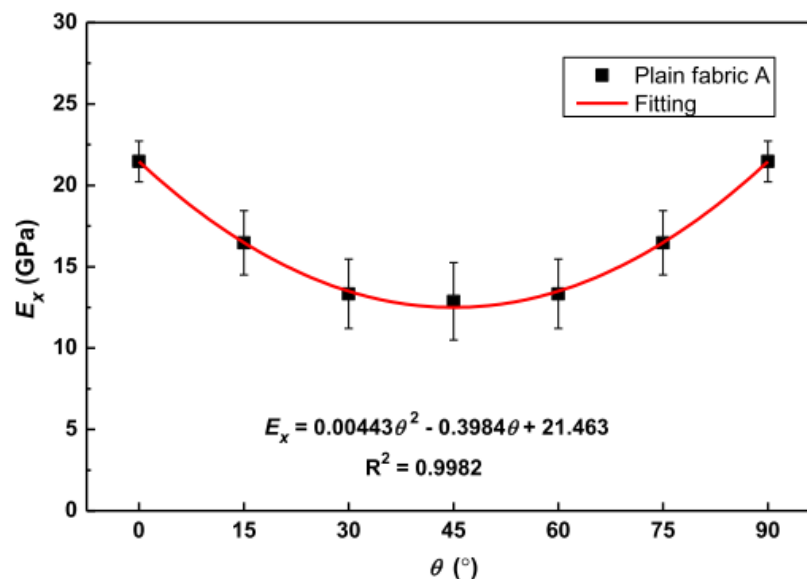


Figure 2.3. In-plane elastic modulus of plain fabric composite in terms of various off-axis angles [50].

2.1.3.3 Laminates

Laminates [52-54] are composites in which various plies are bonded together with adhesive, to give added strength, durability, or some other benefits. There is one category of laminate, in which each ply is composed of uni-directional fibres and matrix, and the laminate can be regarded as a combination of several UD composite

plies as shown in Figure 2.4. In order to ensure the in-plane isotropy or quasi-isotropy of the laminate, each stacked ply is distributed to a different orientation corresponding to the fibre directions. For example, plies distributed with orientations $0^\circ/90^\circ/+45^\circ/-45^\circ/-45^\circ/+45^\circ/90^\circ/0^\circ$ comprise a quasi-isotropic laminate. Laminates have been widely used in many fields benefitting from enhanced strength by UD fibres in all in-plane orientations rather than single direction or limited directions. However, we also have to face with the delamination [1, 55, 56] of the structure due to the weakly bonded interfaces between plies when tensile load or impact is imposed.

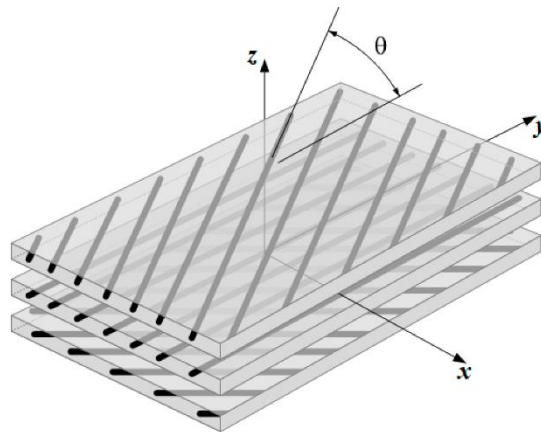


Figure 2.4. Exploded view of generic three-layered laminate with arbitrary ply orientation angles [57].

2.1.3.4 Random Fibre Composites

Random fibre composites consist of discontinuous fibres which are literally all randomly distributed inside of the composites, both in location and in orientation. Both two-dimensional and three-dimensional random fibre composite structures (see examples in Figure 2.5) have been constructed and investigated for their mechanical properties by many researchers [2, 58-61] experimentally and numerically. Since fibres are randomly distributed in a ‘unit cell’, which is a representative volume

element (RVE) of the periodic geometry, the structure exhibits in-plane isotropy or complete three-dimensional isotropy when fibre number is large enough.

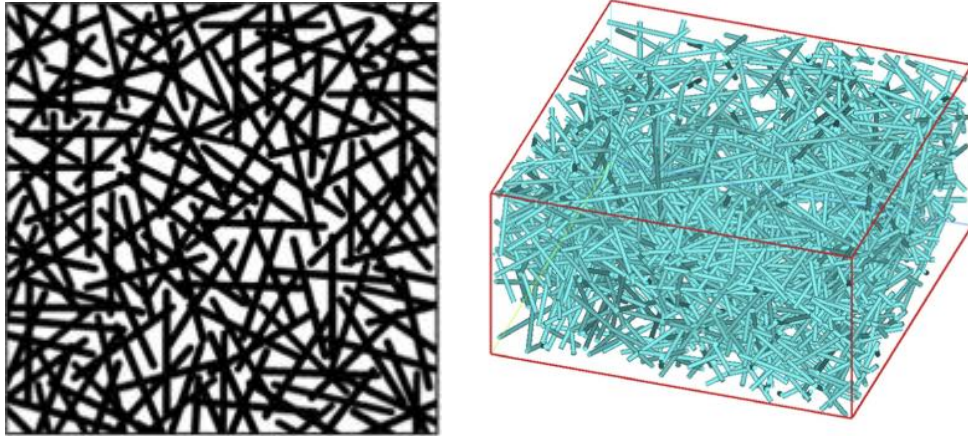


Figure 2.5. Two-dimensional [62] and three-dimensional [2] schematic of random fibre composites, where the bars represent fibres and the gap is supposed to be filled with matrix materials.

One of the most frequently used methods in generating geometries with random members, such as fibres [3], spheres [63], spherocylinders [63], ellipsoids and rods, in fibre/particle reinforced composites is the random sequential adsorption (RSA) technique. The RSA technique adds fibres sequentially in a 3D space according to the random distribution of each fibre. However, since the RSA algorithm tries to avoid any intersections among fibres and all fibres are straight, it has become essentially difficult to increase the fibre volume fraction and it is really time-consuming in constructing the models when fibre number is large enough. Different from the above fibrous structure without intersections generated by the RSA method, there is another random fibre composite, in which fibres are bonded at the intersected points thus creating a network among fibres. The appearance of this fibre network structure is of prevalence in most connective tissues of the human and animal bodies, such as cartilage, tendon and ligaments, and cornea that involve collagen fibre

networks [58], in individual cell scale like the cytoskeleton and in the artificial geometry of metal fibre sintered sheet (MFSS) [14].

2.2 Fibre Network

Fibrous materials are widely used for various purposes, owing to their variety and flexibility in structure, and high ratios of stiffness and strength to weight. Among them, fibre network is one of the specific fibrous structures in which fibres are connected as shown in Figure 2.6 thus generating a fine network instead of uncontacted and dispersed individual fibres. Fibre network can either function as a porous material alone or fundamentally serve as the reinforcement of composites in engineering applications so as to improve the overall performance.

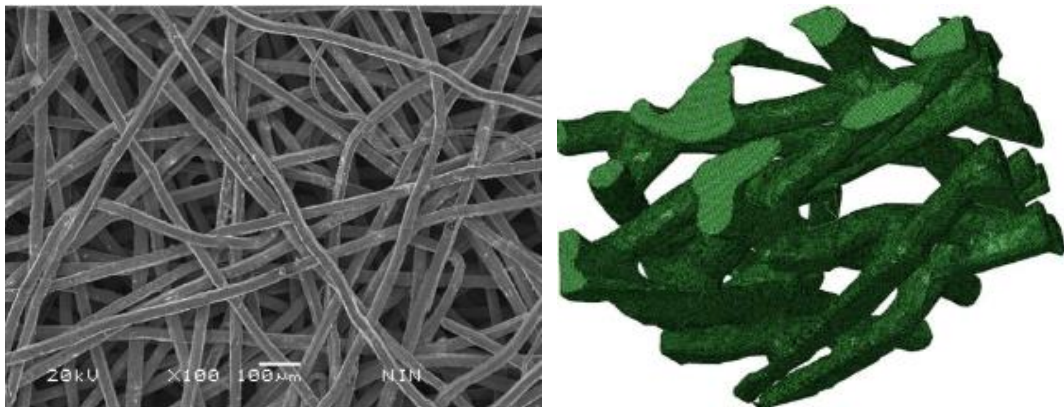


Figure 2.6. Microstructures of the metal fibre network by SEM and μ -CT [64].

Van Wyk [65] studied the mechanics of fibre network at the very early stage, in which the relation between the compression stress and volume was investigated on a 3D model with wool fibres randomly oriented and in contact with other fibres. However, it just took the bending of fibres into consideration while neglecting the effect of twisting, slippage and extension of fibres on the deformation mechanism.

Kallmes and Corte [66, 67] and other researchers have explored the statistical

geometry of paper. Both two-dimensional and three-dimensional geometries have been discussed by Kallmes and Corte and the main concept of the study was to investigate the geometry of fibre network including the effects of fibre distribution and inter-fibre spaces on the paper properties. The study also provided direct correlations between different network geometrical properties (e.g. the number of cross-linkers, average segments length between cross-linkers) and various fibre properties (e.g. fibre length, number of fibres). Different from the ‘negative exponential’ distribution of fibre to fibre distances given by Kallmes and Corte, Dent [68] has proposed a ‘general gamma’ distribution protocol which can statistically describe ‘non-random’ as well as ‘random’ structures. The more recent studies by Komori et al. [69, 70] also questioned the limitation of Van Wyk’s theory due to the lack of other compression properties and the proposed new theories for curved beams and considered fibre sliding.

After that, Toll and Manson [71] conducted theoretical analysis on the elastic compression of a fibre network with in-plane fibre orientation distribution based on beam bending and obtained a five-degree polynomial relation between pressure and volume fraction. Then a new micromechanical theory was developed by Toll [72] to demonstrate the packing mechanics of fibre reinforcement and an equation in relation to the mean number of contact points per slender fibre was derived.

Further work on fibre network was carried out by Heyden [73] who developed a finite element model of both two-dimensional and three-dimensional cellulose fibre networks for the analysis of the effect of micro-mechanical parameters on the overall mechanical behaviours. Sampson [74] modelled stochastic fibrous materials by adopting Mathematica® simply by applying different probabilities and distributions.

Zhang et al. [17] have created a numerical model of carbon-bonded carbon fibre network by inserting a beam [18] between the intersected points of the two fibres and it shows good agreement with the experimental results. A similar 3D fibre network has also been studied experimentally and numerically in [13] and the stress-strain relations indicate that the fibre-fibre connection can dramatically improve the fibre network strength.

2.2.1 Metal Fibre Sintered Sheets

Metal fibre sintered sheets (MFSSs) are a type of fibrous material with transversely isotropic nature as shown in Figure 2.7 below and attract a high interest for their light weight, high specific stiffness and strength as well as high specific surface. MFSSs have been widely used in various industrial practices benefiting from their high structural and functional performances. For example, MFSSs have been successfully applied in filtration membrane [75], structural components, sound adsorption [76], catalyst carrier [77] and heat exchanger [78].

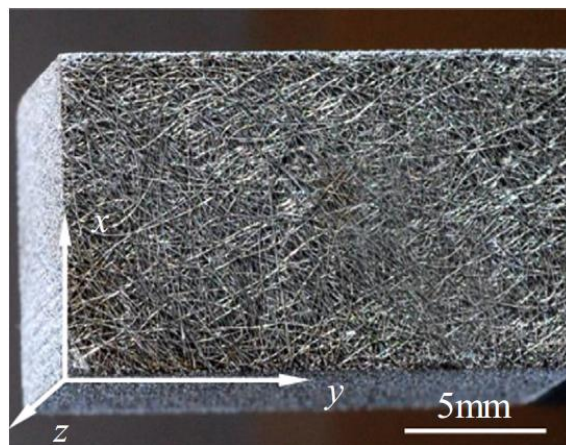


Figure 2.7. An example of a bulk metal fibre sintered sheets (MFSSs) [10].

The typical process of fabricating MFSSs includes five main stages, which are fibre chipping, mould pressing, sintering, cooling and testing [79]. By compression and

sintering, the in-plane randomly distributed individual metal fibres are merged into an in-plane transversely isotropic network with porosities in a large range. It is not surprising that the stiffness and yield strength are enhanced as the relative density increases and the relations to relative density are found to be linear [80]. More specifically, both the stiffness and yield strength in-plane are much larger than those through the thickness direction [12]. Moreover, geometry parameters such as cross-link concentration and aspect ratio etc. can also alter the mechanical behaviour of MFSS. In addition, it is noticed that the Poisson's ratio $\nu_{13} = \nu_{23} \approx 0$, which indicates that transverse loading introduces nearly no contraction or expansion to the through-thickness direction. However, the elongation can be as large as 13.5% [81] and remains relatively constant with relative density [14]. Furthermore, both the shear properties and deformation mechanisms of porous MFSSs were considered by Zhao and Chen [82] based on an experimental procedure and micromechanics models. To be specific, both of the in-plane shear modulus and strength were linearly dependent on the MFSSs relative density. In contrast, the shear modulus and strength in the through-thickness direction were found to have a quartic and cubic dependence on the relative density of MFSSs, respectively. The reason behind shear behaviour that occurred in-plane and out-of-plane lies in the different dominant deformation mechanisms. In particular, the in-plane deformation mechanism for MFSSs is fibre bending while out-of-plane is fiber stretching or compression. In addition, the in-plane shear modulus and yield strength are also much larger than the out-of-plane values. Meanwhile, yields occurred at a smaller strain when loaded in the in-plane direction than when loaded in the through-thickness direction. Uniaxial tensions in the in-plane and out-of-plane directions separately also indicate two dominated failure mode, that is, fibre fracture for the in-plane tension and fibre decohesion for

the out-of-plane tension [10].

2.2.2 Biological Fibre Network

Fibre network is also a very general structure in biologies such as tissues and cells. For example, cytoskeleton (see Figure 2.8) is a complex network of interlinking filaments and tubules and is composed of proteins. It mainly functions as the support of cell shape and mechanical resistance to deformation. It can also deform with initiatives according to the external environment change of a cell thus allowing the cell to migrate [83, 84]. Moreover, the network structure has nominated itself as a good signal transmission path inside of the cell. These biomaterials are observed to be viscoelastic, which shows that the stress response of them is dependent on strain rate, time and temperature [85], thus making the deformation extremely complicated. Therefore, the understanding of the mechanics of the cytoskeleton can be of crucial importance for the overall deformation mechanism.

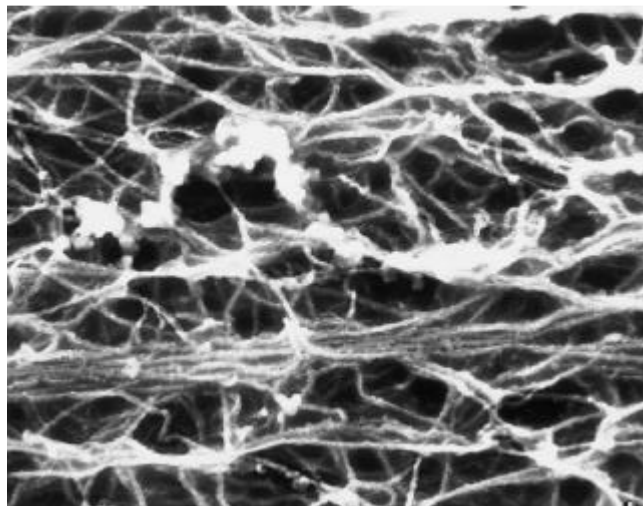


Figure 2.8. Electron Microscopy of neurofilament gel in which neurofilament polymers are linked together [86].

Another common bio-structure involving network is the extracellular matrix (ECM).

It is a complex assembly of structural proteins, of which Type I collagen is the most abundant component, that provides physical support and biochemical signalling to cells in tissues. Type I collagen self-assembles into fibrils, and these fibrils are then cross-linked to form networks in vitro [8]. Collagen networks have been found to exhibit both nonlinear elasticity and viscoelasticity, the relation of which has not been completely discovered yet [87, 88]. In tissues like ligaments and tendons, there exists the ground substance matrix surrounding the collagen fibres, mainly consisting of proteoglycan and functioning as cross-linkers among fibres and entrapment in retaining water or another solvent, thus forming a gel-like extracellular matrix [89].

2.2.3 Honeycomb and Open-cell Foams

Open-cell foams, as one category of continuous porous structures, can be equally regarded as fibre networks. Within this structure, the cells are usually in highly complex and tortuous shape, thus rendering adjustable geometrical characteristics in the specific surface, density and porosity etc. [90] for wide applications [91]. One example of the open-cell foam structure is shown in Figure 2.9 (a). Geometries with regular [92-95] and irregular cells [5, 96-98] have been intensively manufactured in industry or constructed by 3D modelling methods. Among various open-cell foams, aluminium has been the most frequently applied material due to its low density, high specific mechanical and thermal properties. The mechanical properties, such as the stress-strain response of open-cell foams, have been largely investigated and the improved specific stiffness and strength have been observed compared to bulk metal [99]. The combination of materials and cellular structure [5] has made the open-cell foam more attractive for various applications. When the 3D open-cell foam reduces to 2D structure, the structure turns into another fibre network, which is commonly

called honeycomb. As shown in Figure 2.9 (b), the honeycomb with irregular cells [100, 101] can be regarded as a 2D fibre network. Different from MFSSs, in which two fibres intersect at most cases, three or more fibres/cell walls completely emerge at the intersections for open-cell foams and honeycomb. In addition, honeycomb is size-dependent as a hierarchical structure, in which the mechanical properties are largely affected by the strain gradient effect at the microscale and influenced by the surface elasticity and initial stresses at the nanoscale [102, 103].

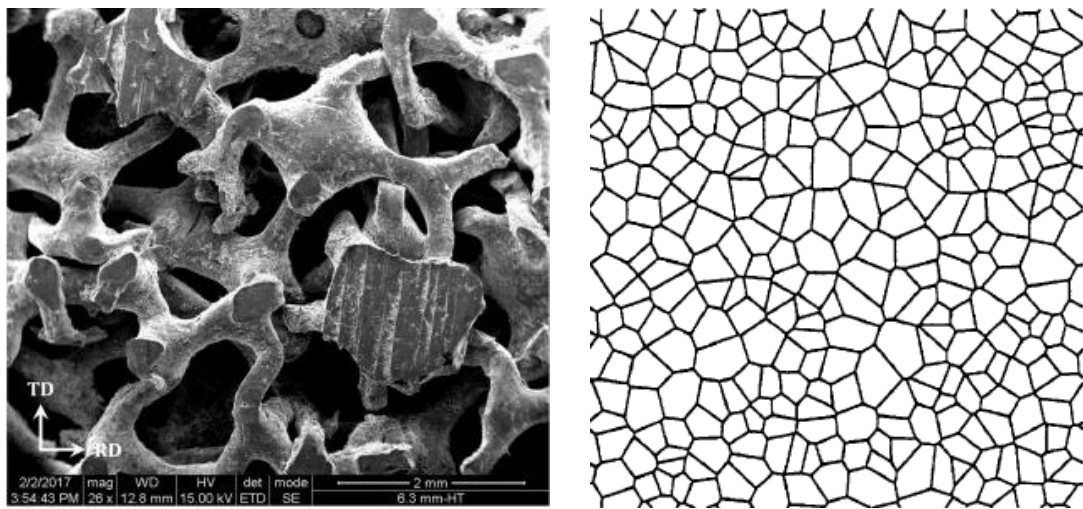


Figure 2.9. (a) Open cell Al foams with a relative density of 42% by SEM [96]; (b) Voronoi honeycomb with irregular cells [100].

2.3 Characterisation of Fibre Reinforced Composites

2.3.1 Elasticity Analysis of Fibre Reinforced Composites

2.3.1.1 Stiffness and Compliance Matrix

Fibre reinforced composites are often highly anisotropic in structure. While only two

independent elastic constants are required to describe the elasticity of isotropic materials, twenty-one constants are required for anisotropic materials with no planes of symmetry. There are normally six independent stresses and six independent strains for anisotropic materials, i.e. stresses: $\sigma_1, \sigma_2, \sigma_3, \tau_{12}, \tau_{23}, \tau_{31}$ and strains: $\varepsilon_1, \varepsilon_2, \varepsilon_3, \gamma_{12}, \gamma_{23}, \gamma_{31}$ (where 1, 2 and 3 represent x, y and z directions separately in a 3D model). Then the stress-strain relations [104] are expressed as

$$\begin{bmatrix} \sigma_1 \\ \sigma_2 \\ \sigma_3 \\ \tau_{23} \\ \tau_{31} \\ \tau_{12} \end{bmatrix} = \begin{bmatrix} C_{11} & C_{12} & C_{13} & C_{14} & C_{15} & C_{16} \\ C_{12} & C_{22} & C_{23} & C_{24} & C_{25} & C_{26} \\ C_{13} & C_{23} & C_{33} & C_{34} & C_{35} & C_{36} \\ C_{14} & C_{24} & C_{34} & C_{44} & C_{45} & C_{46} \\ C_{15} & C_{25} & C_{35} & C_{45} & C_{55} & C_{56} \\ C_{16} & C_{26} & C_{36} & C_{46} & C_{56} & C_{66} \end{bmatrix} \begin{bmatrix} \varepsilon_1 \\ \varepsilon_2 \\ \varepsilon_3 \\ \gamma_{23} \\ \gamma_{31} \\ \gamma_{12} \end{bmatrix} \quad (2.3)$$

where the $[C_{ij}]$ is the stiffness matrix and the compliance matrix $[S_{ij}]$ can be written accordingly as

$$\begin{bmatrix} \varepsilon_1 \\ \varepsilon_2 \\ \varepsilon_3 \\ \gamma_{23} \\ \gamma_{31} \\ \gamma_{12} \end{bmatrix} = \begin{bmatrix} S_{11} & S_{12} & S_{13} & S_{14} & S_{15} & S_{16} \\ S_{12} & S_{22} & S_{23} & S_{24} & S_{25} & S_{26} \\ S_{13} & S_{23} & S_{33} & S_{34} & S_{35} & S_{36} \\ S_{14} & S_{24} & S_{34} & S_{44} & S_{45} & S_{46} \\ S_{15} & S_{25} & S_{35} & S_{45} & S_{55} & S_{56} \\ S_{16} & S_{26} & S_{36} & S_{46} & S_{56} & S_{66} \end{bmatrix} \begin{bmatrix} \sigma_1 \\ \sigma_2 \\ \sigma_3 \\ \tau_{23} \\ \tau_{31} \\ \tau_{12} \end{bmatrix} \quad (2.4)$$

Laminae of fibre reinforced composites with all the fibres parallel are orthotropic materials, in which there are three mutually orthogonal planes of symmetry for mechanical properties, and there are no interactions between normal stresses and shearing strains. Therefore, the number of independent elastic constants is reduced to only nine and stress-strain relations [104] are illustrated in the compliance matrix form as

$$\begin{bmatrix} \varepsilon_1 \\ \varepsilon_2 \\ \varepsilon_3 \\ \gamma_{23} \\ \gamma_{31} \\ \gamma_{12} \end{bmatrix} = \begin{bmatrix} S_{11} & S_{12} & S_{13} & 0 & 0 & 0 \\ S_{12} & S_{22} & S_{23} & 0 & 0 & 0 \\ S_{13} & S_{23} & S_{33} & 0 & 0 & 0 \\ 0 & 0 & 0 & S_{44} & 0 & 0 \\ 0 & 0 & 0 & 0 & S_{55} & 0 \\ 0 & 0 & 0 & 0 & 0 & S_{66} \end{bmatrix} \begin{bmatrix} \sigma_1 \\ \sigma_2 \\ \sigma_3 \\ \tau_{23} \\ \tau_{31} \\ \tau_{12} \end{bmatrix} \quad (2.5)$$

By measuring Young's moduli, shear moduli and Poisson's ratios in the practical test, in addition, $v_{ij}/E_i = v_{ji}/E_j$ ($i, j=1, 2, 3$), Eq. (2.5) can be rewritten as

$$\begin{bmatrix} \varepsilon_1 \\ \varepsilon_2 \\ \varepsilon_3 \\ \gamma_{23} \\ \gamma_{31} \\ \gamma_{12} \end{bmatrix} = \begin{bmatrix} 1/E_1 & -v_{12}/E_1 & -v_{13}/E_1 & 0 & 0 & 0 \\ -v_{12}/E_1 & 1/E_2 & -v_{23}/E_2 & 0 & 0 & 0 \\ -v_{13}/E_1 & -v_{23}/E_2 & 1/E_3 & 0 & 0 & 0 \\ 0 & 0 & 0 & 1/G_{23} & 0 & 0 \\ 0 & 0 & 0 & 0 & 1/G_{31} & 0 \\ 0 & 0 & 0 & 0 & 0 & 1/G_{12} \end{bmatrix} \begin{bmatrix} \sigma_1 \\ \sigma_2 \\ \sigma_3 \\ \tau_{23} \\ \tau_{31} \\ \tau_{12} \end{bmatrix} \quad (2.6)$$

Therefore, only the nine independent elastic constants, $E_1, E_2, E_3, G_{12}, G_{23}, G_{31}, v_{12}, v_{23}$ and v_{13} are required for orthotropic materials. For the situation when the structure exhibits the same properties in x and y directions, taking cross-ply woven fabric composites for example, which means $E_1 = E_2, v_{23} = v_{13}$ and $G_{23} = G_{31}$, the number of independent elastic constants then further reduces to six (i.e. $E_1, E_3, G_{12}, G_{31}, v_{12}$ and v_{13}).

For composites such as in-plane randomly distributed fibre reinforced composites and some laminates which are transversely isotropic structure, the mechanical properties are equal in all directions in a plane, e.g. x - y plane. Then they have only five independent elastic constants, i.e. E_1, E_3, G_{31}, v_{12} and v_{13} . The stress-strain relations [104] are expressed as

$$\begin{bmatrix} \varepsilon_1 \\ \varepsilon_2 \\ \varepsilon_3 \\ \gamma_{23} \\ \gamma_{31} \\ \gamma_{12} \end{bmatrix} = \begin{bmatrix} 1/E_1 & -v_{12}/E_1 & -v_{13}/E_1 & 0 & 0 & 0 \\ -v_{12}/E_1 & 1/E_1 & -v_{13}/E_1 & 0 & 0 & 0 \\ -v_{13}/E_1 & -v_{13}/E_1 & 1/E_3 & 0 & 0 & 0 \\ 0 & 0 & 0 & 1/G_{31} & 0 & 0 \\ 0 & 0 & 0 & 0 & 1/G_{31} & 0 \\ 0 & 0 & 0 & 0 & 0 & 2(1+v_{12})/E_1 \end{bmatrix} \begin{bmatrix} \sigma_1 \\ \sigma_2 \\ \sigma_3 \\ \tau_{23} \\ \tau_{31} \\ \tau_{12} \end{bmatrix} \quad (2.7)$$

Last but not least, isotropic materials such as three-dimensional random fibre or particle reinforced composites have only two independent elastic constants (i.e. E and ν).

2.3.1.2 Theoretical Models of Elastic Analysis

Theoretical analysis has long been conducted towards the mechanical properties, like elasticity, of fibre-reinforced composites. Some preliminary attempts have been made for the prediction of mechanical behaviours and yet have exerted a fundamental influence on the further endeavour. One of the most commonly used theories for predicting the bounds of composite stiffness is the Rule of Mixture, in which the mechanical properties of a composite can be calculated simply by summing the properties of fibre and matrix with their volume fractions. For elastic modulus, Voight limit [48] is corresponding to the situation when the composite is subjected to ‘in parallel’ loading and Ruess limit [49] subjected to an ‘in serial’ loading. The overall moduli for these two situations are expressed as

$$E_{\parallel} = E_f V_f + E_m V_m \quad (2.8)$$

$$E_{\perp} = \frac{E_f E_m}{E_f V_m + E_m V_f} \quad (2.9)$$

The Voight and Ruess limits have been widely recognised as rigorous upper and lower bounds. However, these bounds are based on the isotropy of both the reinforcement and the matrix, which is not always the true situation for composites, such as aligned fibre-reinforced composites which are anisotropic. This has introduced large error and it is suggested that the Voight and Ruess limits just provide a considerably rough prediction.

Accordingly, a tighter bound estimation was proposed by Hashin and Shtrikman [105, 106] which is derived according to the variational approach and is applicable to not only isotropic materials but also heterogeneous structures. In order to further improve the bounds, more details related to the geometry of composites, e.g. fibre

length and fibre orientation, which are expected to matter dramatically to the properties of composites, are required to be taken into consideration. Bowyer and Bader [107, 108] have modified the Rule of Mixture by taking fibre length and fibre orientation into consideration and Eq. (2.8) is modified as

$$E_C = K_1 K_2 E_f V_f + E_m V_m \quad (2.10)$$

where K_1 and K_2 are the fibre length factor and fibre orientation factor, respectively.

K_1 meets [109]

$$K_1 = \begin{cases} L - l_c/2L, & L > l_c \\ L/2l_c, & L < l_c \end{cases} \quad (2.11)$$

where L is the fibre length and l_c is the critical length of the fibre [110]. In the case of misaligned fibres or off-axis loading condition, the contribution of the fibres to overall properties is then reduced. This is reflected on K_2 . For the term of fibres randomly distributed in a plane, K_2 is reduced to one third [108], and if the fibres are randomly distributed in three dimensions the factor is one sixth [111]. Thus the orientation factor K_2 may lie between 1 and 0.167 and can be adjusted according to fibre distribution.

Bert (25) has developed a simplified method in terms of the elastic properties of random fibre composites, which is based on the original model proposed by Nielsen and Chen [112] as follows

$$E_C = 3/8 E_{\parallel} + 5/8 E_{\perp} \quad (2.12)$$

Nielsen and Chen have also taken the effect of Poisson's ratio of the matrix into account in their model and gives a better fitment to experimental results [112, 113], in which,

$$E_{\perp} = \frac{E_f E_m'}{E_f V_m + E_m' V_f} \quad (2.13)$$

where $E_m' = E_m/\nu_m^2$.

Cox [111] originally developed a shear-lag model to investigate the stiffness of fibrous materials and fibre reinforced composites, in which fibres oriented either randomly or according to some definite law of statistical distribution and the effect of fibre orientation on the stiffness has been taken into consideration in his model. However, the model assumes to be only subjected to tension and the flexural stiffness and compression are negligible. Based on the shear-lag model, other researchers [114-116] found it extensively suitable for the study of aligned fibre reinforced composites, both in stiffness and in strength, in a simplified form of expressions in [111] while in a more accurate analytical model than the ideal model based on the rule of mixture. According to the shear-lag model, the elastic modulus of composites can be derived as

$$E_c = (1 - V_f)E_m + V_f E_f \left\{ \frac{1 + (E_m/E_f - 1) \tanh(\beta l/2)}{\beta l/2} \right\} \quad (2.14)$$

where E_m and E_f are the Young's modulus of the matrix and the fibre, respectively, V_f is the volume fraction of the fibres, and β is a matrix material constant [117], which is expressed as

$$\beta = \sqrt{\frac{2G_m}{r^2 E_f \ln(R/r)}} \quad (2.15)$$

where G_m is the shear modulus of the matrix and R and r are the diameters of the unit cell and a fibre separately.

A model similar to the shear-lag model is proposed by Fukuda and Kawata [118] in terms of the axial stiffness of single short fibre-reinforced composites by considering the axial stress of the fibre and interfacial shear stress. Then it is further extended to

the elasticity study of a two-dimensional random fibre-reinforced composite, which also managed to give analytical expressions of stiffness corresponding to the distribution of fibre length and fibre orientation. The expression is written [118] as

$$K_c = \frac{E_f}{E_m} R_0 C_0 V_f + 1 - V_f \quad (2.16)$$

where,

$$R_0 = -\frac{2\pi}{W_f(3 + 2\nu - \nu^2)} \int_0^\infty \left(l \int_0^l \bar{\sigma}_l(u) du \right) h(l) dl / \frac{E_f}{E_m} \quad (2.17)$$

$$C_0 = \int_0^{\pi/2} g(\theta) \cos \theta d\theta \int_0^{\theta_0} f(\theta) \cos \theta g(\theta) d\theta \quad (2.18)$$

R_0 is called the reinforcement ratio of zero dispersion, which shows the degree of the reduction of Young's modulus caused by fibre length. C_0 is defined as the coefficient of alignment which shows the degree of stiffness reduction caused by fibre misalignment. However, this model tends to under-estimate the in-plane Young's modulus for the situation of high modulus ratio and low aspect ratio [117].

Eshelby [119, 120] has explored the elasticity of a two-phase structure with an ellipsoidal inclusion embedded in an infinite matrix. The fundamental idea of this theory lies in the equivalence of the inhomogeneous inclusion and a homogeneous replacement of the inclusion with the same dimension and shape. Specifically, the inclusion with a different stiffness as the matrix is replaced by an alternative inclusion with the same stiffness as the matrix (schematic illustration see Figure 2.10), and the effective stress-strain relation is realised by equalling the two situations through the transformation strains. The average composite stiffness tensor C with respect to the fibre and matrix properties can be expressed as

$$C = C^m + v_f(C^f - C^m)[I + ES^m((C^f - C^m))]^{-1} \quad (2.19)$$

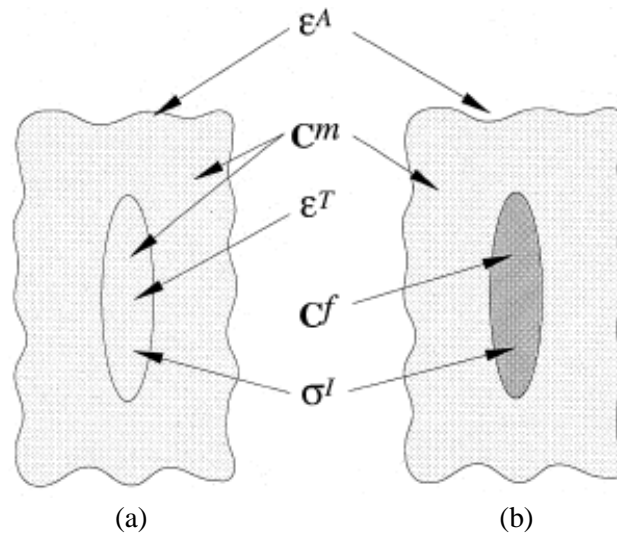


Figure 2.10. Schematic drawing of Eshelby's method in the equivalence of homogeneous inclusion (a) and inhomogeneous inclusion (b) [117].

Further work by Eshelby [121] included detailed expressions of the elastic field outside the inclusion by an improved harmonic potential. This theory has been extensively adopted as the basic theory for the further development of similar models [122, 123]. Russel [124] has predicted the moduli of aligned short-fibre composites based on Eshelby's equivalent inclusion. However, this model needs to be improved due to reason that the stiffness is predicted to be proportional to fibre volume fraction by this model and the modulus predicted is accurate only at low volume fractions (i.e. $V_f < 1\%$).

Based on Eshelby's model, a self-consistent method, also called the embedding method, has been proposed, in which a similar strain-concentration tensor $A = [I + ES((C^f - C))]^{-1}$ with Eq. (2.19) was adopted towards composites with particles and continuous, aligned fibres. Furthermore, a generalised self-consistent model was developed by Kerner [125] regarding a geometrical model with the spherical particles surrounded by a shell of matrix. Then together, they are embedded in an infinite body with average composite properties, thus also called double

embedding method. Hill [126] has adopted the self-consistent approach which took the inhomogeneity of stress and strain into account in predicting the macroscopic elastic moduli of two-phase composites.

Not limited to a single particle in an infinite matrix, Mori and Tanaka [127] have proposed a further theory regarding materials with numerous misfitting inclusions inside of the matrix. The average internal stress in the matrix is calculated under the situation that inclusions alone undergo uniform transformation strain. Based on the Mori-Tanaka model, the investigation of the stiffness of composites, which mainly focused on aligned fibre/particle reinforced composites, has been widely conducted [122, 128-130]. For instance, Abaimov et al. [129] have developed a closed form expression, which directly involved the engineering constants, of the Mori-Tanaka theory for the prediction of both longitudinal and transverse elastic constants of a unidirectional fibre-reinforced ply. Benveniste [131] has reformulated the combined equivalent inclusion idea of Eshelby [119] and the average stress concept in the matrix of Mori and Tanaka [127] in the form of a ‘direct approach’ [132] in determining the effective properties of two-phase composites with isotropic elastic constituents and an inclusion phase consisting of aligned or randomly oriented ellipsoidal particles.

The Halpin-Tsai [133] equation is also a common method in predicting the behaviours of fibre reinforced composites. It is developed based on the generalised self-consistent model of Hermans and Hill [126]. Halpin and Tsai concluded Hermans’ equations for stiffness as

$$\frac{P}{P_m} = \frac{P_f + P_m + \zeta v_f (P_f - P_m)}{P_f + P_m - v_f (P_f - P_m)} \quad (2.20)$$

where P , P_f and P_m can represent the bulk or shear moduli of composites, fibres and

matrix, respectively. ζ is a parameter which is related to the geometry of the reinforcement.

Although the Halpin-Tsai model works perfectly at low volume fractions, it tends to under-estimate the stiffness at high volume fractions. Thus some modifications [134, 135] have been conducted towards the Halpin-Tsai equation to include more precise expressions of stiffness in relation to volume fraction.

Hill [136] has managed to deduce the overall elastic moduli of fibre composites, in which both phases are homogeneous and elastically transversely isotropic about the fibre direction, independent of the detailed geometry.

2.3.2 Elastoplastic Behaviours of Fibre Reinforced Composites

2.3.2.1 Theoretical Models for Elastoplastic Analysis of Fibre Reinforced Composites

In metals, yielding occurs due to the flow of dislocations, which mainly depends on shear stress/strain. In terms of fibre reinforced composites, there are three phases: fibre, matrix and interface, and the yield and failure criteria will be dependent on all of them. Accordingly, two modes of yielding or failure, that are fibre dominated and matrix dominated, are proposed and investigated in corresponding to the regions where yielding or failure happens. Several theoretical models are developed with respect to metals and other homogeneous materials but rigorous analysis of the elastoplastic behaviour of composites is limited due to the complication in structure [137]. One relevant example is the early stage analysis conducted by Hill [138] who

has given an approximate analysis of the elastoplastic behaviour of fibre-strengthened materials under axial and transverse plane-isotropic loadings. Furthermore, Hill [139] obtained a rigorous general theory of the macro-mechanics of heterogeneous and non-linear elastoplastic systems. Approaches to the elastoplastic analysis can be categorized as micromechanical and macroscopic models.

Miwa [140] has proposed a model for the investigation of the tensile strength corresponding to composites in which short fibres are oriented random-planarly, in which the strength depends strongly on the yield shear strength at the fibre-matrix interface and can be expressed, using the critical fibre length l_c and the apparent interfacial shear strength τ , as

$$\sigma_y = \begin{cases} \frac{2\tau}{\pi} \left[2 + \ln \frac{(1 - l_c/2L)\sigma_f\sigma_m v_f + \sigma_m\sigma'_m v_m}{\tau^2} \right], & L \geq l_c \\ \frac{2\tau}{\pi} \left[2 + \ln \frac{\tau(L/d)\sigma_m v_f + \sigma_m^2 v_m}{\tau^2} \right], & L < l_c \end{cases} \quad (2.21)$$

where σ_f and σ_m are the tensile strengths of the fibre and the matrix separately, v_f and v_m are the volume fraction of the fibre and the matrix, respectively, σ'_m is the matrix stress at fracture strain of the composite, L is the fibre length and d is the fibre diameter.

The self-consistent method was originally developed by Hershey [141] and Kroner [142] for the elastic deformation study of aggregates. It involves the incremental approach [143], in which the overall incremental stress and strain are corresponding to the incremental behaviours of local individual phases. Thus the overall mechanical behaviours can be determined step by step during the deformation history [144]. Dvorak and Bahei-El-Din [145] have modified the self-consistent model for the overall instantaneous moduli calculation of fibrous composites. Then, the self-

consistent model has been improved by Budiansky & Wu [146] and intended to include plastic analysis by Kroner in [147], with elastoplastic accommodation taken into account, to solve the plastic problem of an inclusion within an infinite matrix. Hill [126] also employed the self-consistent model to estimate the global elastoplastic properties of aggregates by applying uniform tensors to local individual phases. The Hill model is also applicable in dealing with the anisotropic problem. Hutchinson has employed a self-consistent method for the exploration of the elastic-plastic behaviour of both metals and composites and also compared the models proposed by Kroner [142] and Budiansky & Wu [146], and Hill [126]. It was found that the model of Kroner and Budiansky & Wu have shown identical results with the Hill model for small-scale plastic deformation while larger plastic strain rate than the Hill model for large-scale deformation. It is also argued that Kroner's model indicates good predictions of elasticity but dissatisfactory plasticity predictions [148]. Therefore, Berveiller and Zaoui [148] have introduced the secant model, which is derived from the formulation of the self-consistent scheme, aiming to obtain a better plastic approximation of polycrystals than Kroner's model [147] by introducing a simple scalar accommodation function. In the secant model, the effective strain of individual phase is simplified as the average strain of this phase by means of strain concentration tensor. Hutchinson [149] extended the self-consistent method to the analysis of creep behaviours of polycrystalline materials together with an upper bound technique. Besides polycrystals, the self-consistent model also applies to composites. Castañeda [150] has exploited the self-consistent model to estimate the effective mechanical properties of nonlinear composites, such as a two-phase incompressible composite, in the proposed new variational model.

Extensions to the secant model have been investigated [150-154]. Suquet [155] has

developed a modified secant model, in which the effective strain of individual phase is expressed as a relation to the second-order moment of the strain field of this phase instead of the average strain of this phase described in a classical secant model. In addition, this modified model has saved the procedure of obtaining the concentration tensors [156]. Hu [153] has combined a general concept of the secant moduli method with an improved evaluating approach for the average matrix effective stress [157] to provide a more precise prediction of nonlinear effective properties of aligned fibres or void composites than the classical secant method.

Another micromechanical approach to determine the effective macroscopic mechanical behaviours of composites is the variational model [150, 158]. Hashin and Shtrikman [106] have successfully derived the upper and lower bounds for the effective magnetic permeability of multiphase materials by using the variational theory. Furthermore, they have also established various variational principles in the wide investigation of the elasticity of isotropic or anisotropic nonhomogeneous composite materials [105, 159-161]. Castañeda [150] has proposed an alternative variational structure that is capable of estimating the effective behaviours of nonlinear composites by the corresponding properties for the linear composites with the same distribution of microstructure. Lahellec and Suquet [162] have proposed an incremental variational formulation to determine the effective behaviour of nonlinear inelastic composites by describing the behaviour of constitute phases with an incremental energy function using implicit time-discretization scheme. In this way, the stress-strain relations of local phases are represented by a single potential and the effective behaviour of the whole heterogeneous composites can be solved by a homogenisation method at each time step [158].

Macroscopic models may include nonlinear elasticity [163, 164], progressive damage-elasticity [165, 166] and elastoplasticity [167-170] methods. Petit et al. [163] adopted a piecewise linear method in which the overall behaviour is obtained from the incremental stress-strain relations to study the nonlinear elastic behaviour of unidirectional laminae. However, it requires the quasi-linearity of the materials so as to neglecting the coupling among stress components. Hahn et al. [164] have derived the nonlinear stress-strain relation of laminae based on a complementary strain energy density function. As for damage-elasticity models, an anisotropic damage assessment model of lamina based on the concept of damage surface was developed by Chow et al. [165] and a nonlinear constitutive model was proposed by Lin et al. [166] for the nonlinear analysis of composite laminates by using a mixed failure criterion to detect the damage onset. Elastoplasticity models adopt an incremental plastic potential function with an associated flow rule to describe the elastic-plastic stress-strain relation [167-169]. Sun et al. [170] proposed an extensively attractive one-parameter plasticity model which is simple and still in high accuracy.

2.3.2.2 Determination of Yield Strength

The yield point is rather difficult to precisely determine due to the wide variety of stress-strain curves exhibited by various materials and structures. Possible methods can be yield point, proportional limit, elastic limit, offset yield point and upper and lower yield points etc. Offset strain method is one of the most commonly used methods in determining equivalent yield strength in non-yielding materials which are ductile or brittle. Usually, an offset strain between 0.05% and 0.3% is adopted. It is universally acknowledged that the point on the stress-strain curve, where the offset strain is equal to 0.2%, is regarded as the yield point. For example, 0.2% strain offset

is also adopted in determining the yield point of hybrid carbon fibre/self-reinforced polypropylene composites in [171]. Cahoon et al. [172] have related the yield strength to hardness in the studies of brass, steel and aluminium alloys. Apart from these methods, graphic method and equivalent energy method are also applied to the stress-strain curve to determine the yield point for certain materials. For example, in one of the graphic methods applied in the analysis of yielding and stress-strain behaviour of structured soft clay [173], the yield point is defined as a foot of a perpendicular which is through the intersection of rectilinear extrapolations of the pre-yield and post-yield portions of the stress-strain curve and perpendicular to the curve (see Figure 2.11(a)). Equivalent energy method used to be employed in the fracture mechanics analysis [174, 175]. Equivalent energy method is adopted to determine the yield point in the way that the stress-strain curve is replaced by an elastic-perfectly plastic curve with the same envelope and the strain of the elastic limit on the elastic-perfectly plastic curve is regarded as the yield strain of the original curve [176] (see Figure 2.11(b)). However, these methods are still not suitable for some newly emerged materials and structures.

In terms of composites, it becomes more complicated to determine the yield point since there is more than one material or component and the yielding of composites means the overall yielding instead of just the yielding of certain individual components. In addition, the loading conditions, such as loading directions, matter for the exhibited stress-strain behaviour due to the anisotropy of structure composites may possess. For instance, in the uniaxial tension test of aligned fibre reinforced composites exhibit only linear elastic behaviour and then break without hardening process when the load is along the fibre direction whereas indicating typical elastoplastic behaviour when the loading offset is 45° to the fibre direction. Feng et

al. [177] have proposed a method called ‘Farthest Point Method’ to determine the yield point of steel-concrete-FRP-concrete. To be specific, the point on the curve, where the tangent slope is the same as the slope of the straight line determined by the peak and origin points, is defined as the yield point (see Figure 2.11(c)). This method is practicable for traditional elastic-plastic curves and elastic-plastic curves without obvious turning [177]. Johnson has long proposed the apparent elastic limit method in view of materials without a significantly proportional stress-strain relation, in which the yield point is determined as the point at which the strain rate is 50% greater than that of the origin (see Figure 2.11 (d)). There are also various methods for determining the yield point. Yet no methods apply to all the materials. Therefore, an appropriate method should be chosen for a certain material or structure.

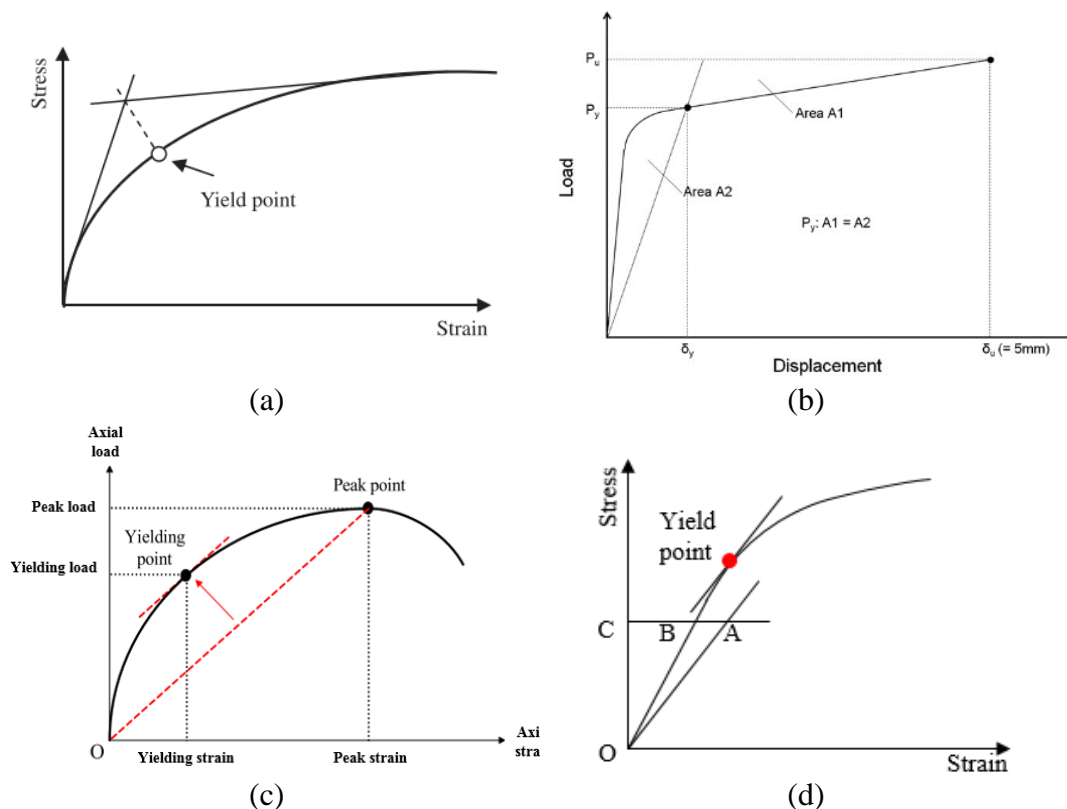


Figure 2.11. Schematic plotting of several methods of yield point determination: (a) Graphic method [173]; (b) Equivalent energy method [176]; (c) Farthest Point Method [177]; (d) Apparent elastic limit.

2.3.3 Viscoelasticity of Soft Tissues

2.3.3.1 Viscoelastic Models

Various materials, such as wood, polymers, mammal tissue and solid rocket propellants etc., exhibit viscoelastic behaviour, where the deformation is dependent on load, time and temperature [85].

In recent decades, soft biological tissue has become one of the most attractive research fields and a variety of models have been proposed for the theoretical investigation of the viscoelasticity of soft tissue, including microstructural, phenomenological/rheological, and continuum models [89, 178, 179].

Microstructural models [180-182] describe the overall mechanical behaviour of the tissue simply by combining or generalising the mechanical responses of the components, which provides a direct connection between the microscopic constituent characteristics (i.e. materials and structures) and the macroscopic response of the tissue [183-186]. Decraemer et al. [184] derived a corresponding nonlinear viscoelastic constitutive equation in the proposed model, which took the structure change, more specifically, fibre length change, into consideration. Lanir [180, 181] explored the viscoelastic behaviours of tissues under multiaxial loading. Stretching of fibres are mainly involved in the constitutive model. Egan et al. [182] also investigated the viscoelastic behaviour of soft tissues through a constitutive model. Instead of the deformation characteristics, the strain energy criteria was adopted in determining and characterising the mechanical response.

Viidik [187] proposed a rheological model, in which the viscoelasticity of soft tissues can be mathematically described by combining the basic mechanical properties, such

as elasticity, viscosity and plasticity, in the ways that simple spring (representing elasticity), dashpot (representing viscosity) and dry friction (representing plasticity) are grouped in various ways, either in series or in parallel. Further to this, Frisen et al. [188] have derived more detailed mathematical equations for the viscoelasticity and then extended the model to include the nonlinear elastic response which is manifested from the time-independent relation between force and deformation.

Sanjeevi [189] developed a mathematical model for the stress-strain characteristic that is composed of two components, i.e. elastic component and viscous component [190], and the complete viscoelastic equation is expressed as

$$\begin{aligned}\sigma &= \sigma_e + \sigma_v \\ &= E_1\varepsilon + E_2\varepsilon^2 + \eta_1\frac{d\varepsilon}{dt} + \eta_2\varepsilon\frac{d\varepsilon}{dt}\end{aligned}\quad (2.22)$$

where σ and ε are stress and strain, and E_1 , E_2 , η_1 and η_2 are constants. Further to this, Sanjeevi et al. [189] argue that the length and thickness of the chosen collagen fibre also play a crucial role in the viscoelastic response.

Since linear viscoelasticity did not completely match the nonlinear behaviours as observed in tissues [191], Fung [192] introduced the quasi-linear viscoelastic (QLV) model, which has been the most frequently used model in the study of viscoelasticity of tissues. The QLV model combines the elastic component with a time-dependent component of a tissue's mechanical response by adopting a hereditary integral formulation [178]. In the QLV model, the stress can be expressed as

$$\sigma(\varepsilon, t) = G(t)\sigma^e(\varepsilon)\quad (2.23)$$

where $G(t)$ is the reduced relaxation function and $\sigma^e(\varepsilon)$ is the time-independent elastic response. The stress at time t is then given as

$$\sigma(\varepsilon, t) = \int_{-\infty}^t G(t - \tau) \frac{\partial \sigma^e}{\partial \varepsilon} \frac{\partial \varepsilon}{\partial \tau} d\tau \quad (2.24)$$

Based on association with linear viscoelasticity, but with σ^e assuming the traditional role of strain within the linear theory, Fung [179] chose the reduced relaxation function, $G(t)$, as:

$$G(t) = \frac{1 + \int_0^{\infty} s(\tau) e^{-t/\tau} d\tau}{1 + \int_0^{\infty} s(\tau) d\tau} \quad (2.25)$$

where the relaxation spectrum

$$s(\tau) = \begin{cases} C/\tau, & \tau_1 \leq \tau \leq \tau_2 \\ 0, & \tau < \tau_1, \tau > \tau_2 \end{cases} \quad (2.26)$$

The reduced relaxation function can be rewritten in terms of exponential integrals as

$$G(t) = \frac{1 + C(E(t/\tau_2) - E(t/\tau_1))}{1 + C \ln(\tau_2/\tau_1)} \quad (2.27)$$

with exponential integral function [193]

$$E(y_1) = \int_{y_1}^{\infty} \frac{e^{-y}}{y} dy, \quad y_1 = \frac{t}{\tau_1}, \quad y = \frac{t}{\tau} \quad (2.28)$$

Based on experimental observations of the stress-strain relation of soft tissues, an exponential form is chosen for the elastic stress term:

$$\sigma^e(\varepsilon) = A(e^{B\varepsilon} - 1) \quad (2.29)$$

where A and B are material constants that relate to the magnitude and nonlinearity of the elastic stress response, respectively.

The QLV model has been intensively applied in modelling a variety of tissues [194-197], including ligaments and tendons [198-201]. Based on this model, some further work has been conducted by other researchers [183, 197, 202-204] to refine the parameters involved in the model for wider applications. Fung's model utilizes five

parameters to explain the complex viscoelastic behaviour of collagenous tissues and allows easy, direct comparisons among the studies carried out by different research groups and performed on different species and tissue types [205].

Several continuum-based approximate constitutive theories [206-209] have been proposed for characterising the nonlinear viscoelasticity of polymers and tissues. Lianis [206] developed a continuum approximation to characterise the nonlinear viscoelastic behaviours of polymeric materials according to the finite linear viscoelastic theory proposed by Coleman and Noll [210]. Then a single integral constitutive equation was derived by Bingham and Dehoff [207] based on the modification of the Lianis model [206]. Another continuum-based constitutive theory is an incompressible elastic fluid theory proposed by Bernstein, Kearsley, and Zapas (BKZ) [208]. Haut and Little [198] proposed a constitutive equation for the characterisation of the time-dependent behaviour of collagen fibre bundles and the relaxation behaviour was proven to be derived from both the Lianis theory [206] and the BKZ theory [209].

2.3.3.2 Characterisation of Viscoelasticity of Soft Tissues

Numerous studies have been conducted on the viscoelastic properties of soft tissues in recent decades, both experimentally and theoretically. Soft tissues in vitro are typically subject to uniaxial tensile or shear loading to measure mechanical behaviours, such as elastic and viscoelastic properties. Collagen is one of the most common constituents in comprising tissues in vivo and collagen is generally organised in hierarchical structures of tissues together with other constituents. For example, the tendon has five distinct substructures, including the collagen molecule, the collagen fibril, the fibril bundle, the fascicle, and the whole tendon [178]. In

tendons, the hierarchical structures can be demonstrated as shown in Figure 2.12. Accordingly, studies have been conducted towards tissue structures of different levels.

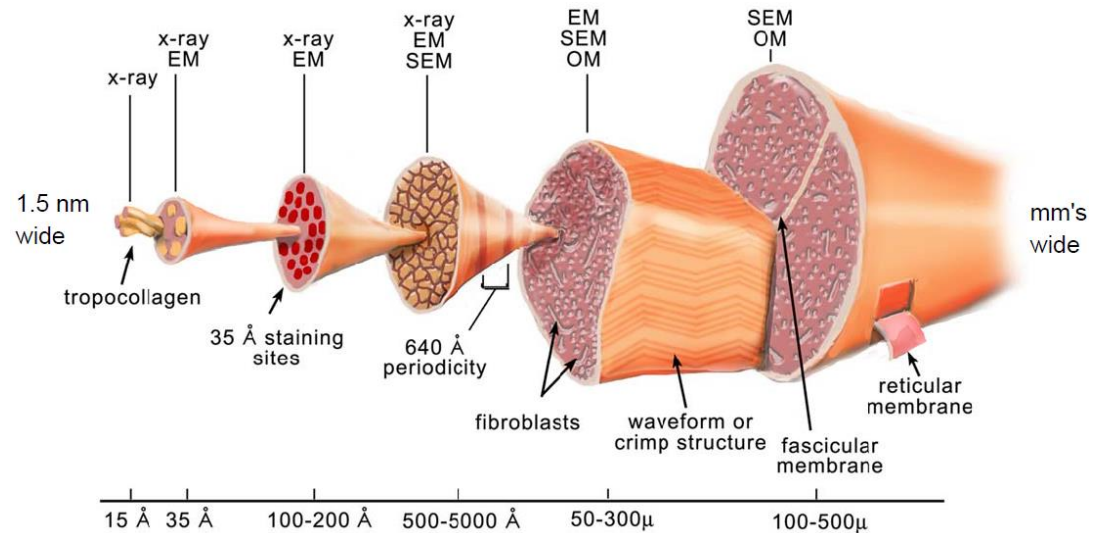


Figure 2.12. Hierarchy of tendon structure according to Kastelic et al. [211].

Generally, there are three main types of measurements towards the viscoelastic behaviours in the tissue level, that is, stress-strain relation, stress relaxation and creep. The stress-strain relation is the fundamental feature in characterising the non-linear behaviour of tissues. To measure the stress-strain relation, various magnitudes of stress are rapidly applied to the sample, respectively, and the resulting deformations (i.e. strain) can be accordingly measured after holding the load for the same short term, e.g., 30s. The stress-strain response has been investigated corresponding to cornea [212, 213], ligaments [178, 183, 214], and tendons [178, 183] etc.

In the stress relaxation measurement, the sample is subject to a constant strain for a long term and the stress will be partly released gradually over time. Then the dynamic stress over time is recorded as stress relaxation. Stress relaxation tests were carried

out on tendons [183, 204, 215-217], ligaments [183, 218, 219], heart valves [220], skin [221], bone [222], cornea [223], cartilage [224, 225] and gels [8, 226, 227] etc.

As for the creep behaviour, a constant stress is imposed on the sample and the slow deformation over time can be quantified in a plot of strain vs. time [228, 229]. Creep tests were performed on tendons [215, 230], heart valves [231], skin [232], and gels [226, 233] etc.

At the fibrillar level, direct mechanical measurements have not become feasible and reliable until the maturity of technologies like atomic force microscopy (AFM) and micro electro mechanical systems (MEMS). AFM is capable of visualizing and characterizing specimens like biopolymers on the sub-nanometer scale by contouring the surface in the way of controlling forces between a tiny and sharp probe and the specimen surface [234, 235]. The AFM nanotechnology has only recently been widely used in investigating materials [236], physics, biology [237], medicine, food and so on although it was first proposed early in 1986 [238]. The major advantage of AFM lies in its convenient operation and nearly nondetective feature to samples. Based on AFM, nanoindentation [239-241], tensile [242, 243], and bending [244, 245] tests of single collagen fibril have been possible to study the elastic modulus and the hardness of the single fibril. Svensson et al. [246] have successfully studied the strain-rate-dependent behaviour of single collagen fibrils isolated from human patellar tendon by utilising an AFM-based tensile test. However, the capability of AFM in applying only a few strains has constrained its application in strength or toughness test by axial tension. But MEMS can be complementary to this as MEMS can be used in large strain load situation. Based on MEMS method, elastic modulus, yield strength/strain, fracture strength/strain, and toughness [247-249] can all be

obtained through quasistatic tensile tests of single collagen fibrils. In addition, the further work by Shen et al. [205] has performed in vitro coupled creep and stress relaxation tests on collagen fibrils isolated from the sea cucumber dermis and managed to obtain the viscoelastic behaviour of the fibril, which can be fitted by a two-time-constant Maxwell-Weichert model. This provides solid data for the exploration of viscoelastic behaviours on larger scales like the tissue scale.

2.3.3.3 Deformation of Tissues

As parts of a body, various tissues perform multiple functions, of which mechanical properties are essential in undertaking sufficient loads/deformation and supporting the shape of the body apart from biological functions. Typically, the structures of tissues are composed of fibrous or porous structure serving as the skeleton, and solution/water surrounding the skeleton and interacting with it. Due to the high mobility of solvent, it remains a focus of research on the deformation of tissues under load, especially for the mathematical model. By means of regarding the skeleton as the basement and the solvent as the matrix, tissues can be simplified as composites possessing nonlinear elastic and viscoelastic properties. A mathematical model which is appropriate in characterising the mechanical behaviour of the matrix (i.e. solvent) in tissues, such as elasticity and viscoelasticity, has been explored. Hong et al. [250] have investigated a polymeric gel system with polymer network surrounded by molecules and have proposed two modes of deformation that may occur under stretching according to the motion of molecules, that is short-range motion and long-range motion, as sketched in Figure 2.13. In the short-range motion mode, molecules are corresponding to just the local rearrangement, resulting in only the shape change of the gel. Whereas, the long-range motion mode involves long-range migration of

the small molecules, resulting in changes of the gel not only in the shape but in the volume, thus causing swelling to the gel [250]. It is assumed that the local rearrangement is instantaneous, and the long-range migration is a time-dependent process of molecules diffusing inside the gel.

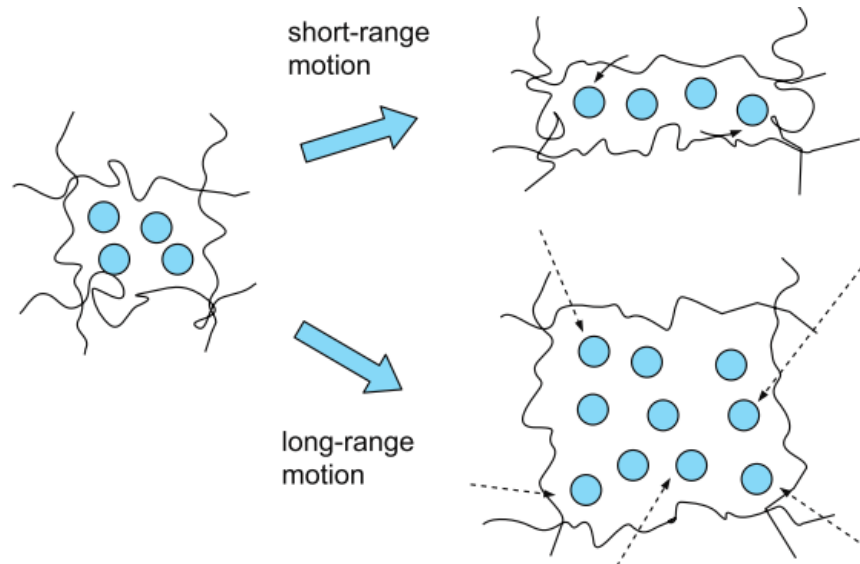


Figure 2.13. A schematic of two deformation modes: short-range motion and long-range motion, in a gel consisting of a polymer network (lines) and small molecules (dots) [250].

In tissues, like ligaments and tendons, there exists the ground substance matrix surrounding the collagen fibres, consisting of mainly proteoglycan and functioning as cross-linkers among fibres and entrapment in retaining water or another solvent, thus forming a gel-like extracellular matrix [89]. In some tissues such as skin, most of its water or another solvent can be constrained inside the tissue even under high pressure [251]. Therefore, it is usually assumed that the tissue is incompressible [252, 253] in many models during the constitutive analysis. For instance, Lanir [254] treats tissues as a bicomponent mixture of incompressible solid and fluid, and then the motions and stresses of both solid and fluid under quasistatic conditions are derived

accordingly. However, it has been proven that exudation of water from ligamentous tissue has occurred [255] and the volume of the ligament has changed during the deformation [256, 257]. This volume change in vivo may result from fluid exudation [255] or inherent compressibility of the solid phase. Because of the limited availability of experimental data describing interstitial fluid flow in ligaments and tendons, FE models have been used to gain a better understanding of the flow behaviour [258]. Chen et al. [259] have developed finite element (FE) models to investigate interstitial fluid flow behaviour and tissue permeability in terms of interfibrillar spacing and fluid properties in ligaments and tendons, and the results indicated a much higher longitudinal permeability than the transverse permeability (up to 50 times).

Chapter 3 Three-dimensional Geometrical Model of Transversely Isotropic Random Fibre Network Reinforced Composites

In this chapter, we aim to introduce the construction of the geometrical model of the fibre network composites. A novel transversely isotropic fibre network is designed and constructed, where the 3D beam elements are adopted to represent the fibres and cross-linkers among fibres are introduced to connect fibres and develop an integrated fibre network. The details about how the individual fibres are distributed and intersected with other fibres are illustrated in this chapter. Then an automatic searching & coupling (ASC) method is employed to couple the nodes of fibres and those of the solid matrix to thus generate a complete geometry of the composite. Periodic boundary condition (PBC) is applied to the representative volume element (RVE) and the way of loading for the finite element analysis (FEA) of mechanics has been explained. Last but not least, the key parameters that are dominant in the mechanical properties of the geometry, namely, cross-linker density, overlap coefficient, aspect ratio and volume fraction, are briefly described prior to the mechanical analysis of this structure.

3.1 Introduction

Fibre reinforced composites are a category of structure that has been widely used in industry. Numerous different structures of fibre composites, for instance, uni-directional fibre composites, cross-ply fibre composites and fibre laminates etc., are designed primarily for their advantages in directional mechanical properties, more precisely, axial or planar mechanical properties. However, the superior properties are achieved by sacrificing the properties in the other axes or planes. Delamination is a common problem when those structures happen to be subject to loading in their weak directions.

Porous materials are another type of promising structures in engineering applications. Porous materials, such as foam, honeycomb and fibre network etc., have indicated extraordinary mechanical properties over the adopted materials themselves benefitting from their specificity in structures. Compared to fibrous materials like textiles which possess obvious directional mechanical properties, fibre networks have demonstrated the same level of properties in the primary directions while still possessing relatively good performance in the other directions due to the introducing of cross-linkers among fibres.

Based on the aim of our structure, that is, building a transversely isotropic structure of fibre reinforced composites, the introduction of fibre network into the original fibre reinforced composites would be an advantage. The remaining directional characteristics of fibres in the fibre network reinforced composites provide the primary load bearing, in the meanwhile, cross-linkers strengthen the loading capacity of other directions.

The objective of this chapter is to construct RVEs of transversely isotropic fibre network reinforced composites where the network is formed by the cross-linking among fibres. To start with, RVEs of transversely isotropic fibre network with cross-linkers are to be constructed according to the geometrical periodicity of fibres along x , y and z directions, respectively. Then the fibre network will be combined with the solid matrix to compose the entire fibre network composites. We have tried to generate the fibre network model in a similar way of fabricating MFSS so as to make it more realistic and engineering implementable.

3.2 Generation of the 3D Stochastic Fibre Network

Before applying FEA, one common procedure is to generate a representative volume element (RVE) or a unit cell (UC) of the studied geometry. We intend to create a novel stochastic structure of fibre network reinforced composite which is transversely isotropic. In this chapter, the process of generating a three-dimensional RVE for the novel fibre network reinforced composite will be introduced. A flow chart in Figure 3.1 has demonstrated the brief procedure of how an RVE is generated, followed by the detailed description in Sections 3.2.1-3.2.4.

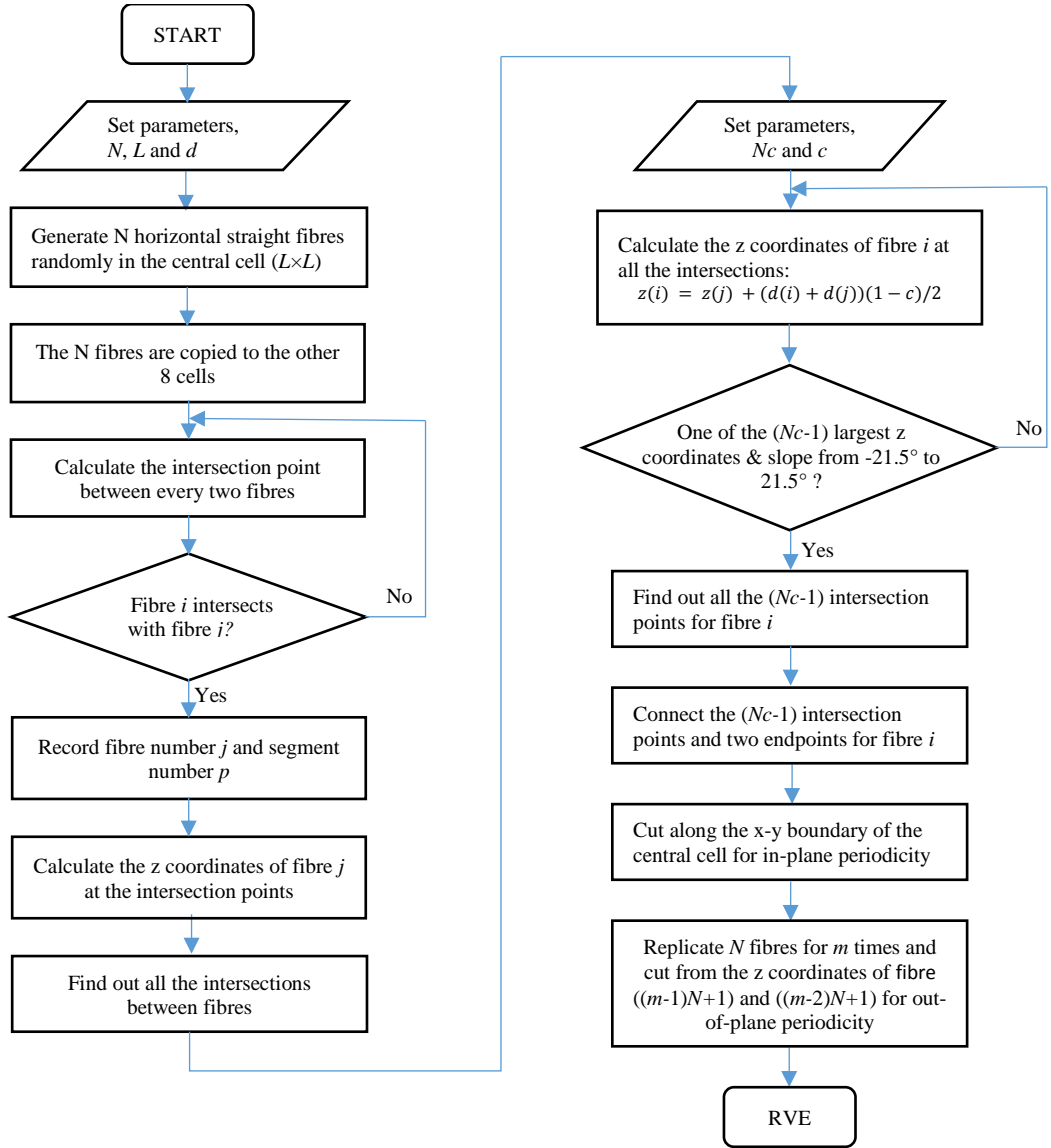


Figure 3.1. The flowchart of the process of generating the representative volume element (RVE).

3.2.1 In-plane Distribution of Fibres

The initial fibres are modelled as cylinders described by the centre point $C(x, y)$, length L , diameter d and angle θ (i.e., the angle between the cylinder and x -axis, ranging from 0 to π). For an RVE with fibre number of N , the centre point $C(x, y)$ and angle θ are generated randomly for each fibre using the function $rand()$ in Matlab. It should be noted that the function $rand()$ needs to be initialised each time

to make sure that rand seeds are from different random data. The distribution of fibre lengths is stochastic ranging from $0.8L$ to $1.2L$, thus to make the average length of the N fibres close to L . The diameters of the fibres are kept the same as d . Therefore the aspect ratio ranges from $0.8L/d$ to $1.2L/d$. The fibres will be added into a ‘unit’ cell ($L \times L$) sequentially making sure that the centre point $C(x, y)$ of any fibre is inside of the cell (see Figure 3.2). It is noted that all the fibres are originally distributed horizontally in the x - y plane during this step. In order to ensure the periodicity of geometry, the generated fibres are copied to the other 8 cells around the central cell, where ‘copy’ means that the relative position of centre points in the corresponding cell and orientation of each fibre are kept exactly the same as those in the central cell. As shown in Figure 3.2, the sketch of those fibres with dash profile in each cell are the copies of fibres lying in the central cell. Therefore, the x and y coordinates of each node on fibres are all given from this step.

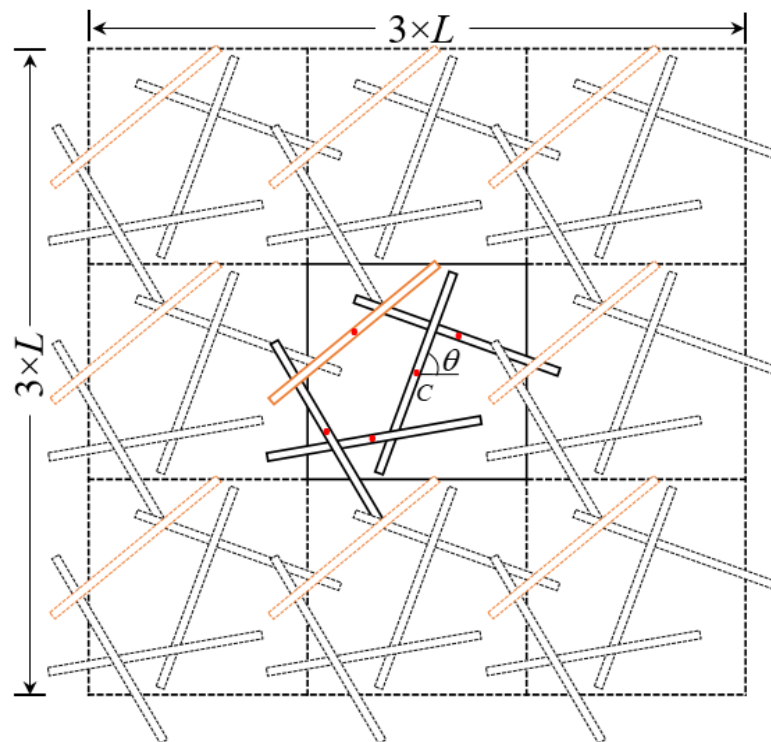


Figure 3.2. An example of fibres randomly distributed in the square region of $L \times L$. Red dots represent the centre points of the fibres.

3.2.2 Determination of Intersections in the z -direction

The previous step has just generated stochastic fibres which lie in the x - y plane and this step is to determine the z coordinates of nodes on fibres, or in other words, to determine the shape of each fibre in the z -direction, as each fibre goes up and down to intersect with other fibres and is no longer horizontally straight as generated from the last step. So each fibre will consist of several segments, where each segment is straight but is still continuous as a whole fibre. Therefore, what we need to do is to determine the coordinates of all vertexes of the segments and then the whole fibre with the segments can be formed simply by connecting the vertexes of the segments and the two vertexes of the original straight fibre. It should be noted that nodes on a fibre refer to the nodes on the axis of the fibre.

The process of determining the shape of each fibre will be conducted one by one and can be imagined as the falling down of each horizontal fibre created from $z = \infty$ to finally $z = 0$. Obviously, the first fibre is still straight since there are no other fibres to intersect with and its z coordinates are all $d/2$. For the following fibres in all the 9 cells, the x and y coordinates of the intersections between the i th ($1 < i \leq 9N$) fibre and all the former ones will be recorded. Furthermore, the fibre numbers and segment numbers are also important in figuring out which segment of fibres it intersects with. Since the shapes of fibres are determined in sequence, it means that the shapes of all the former fibres have already been obtained. Therefore, the z coordinates of the former fibres at the intersection points can be calculated from the certain segments of the former fibres that the i th fibre intersects with, according to the given x , y and z coordinates of both ends of the segment. The z coordinates of the i th fibre at the intersection points depends on the z coordinates of the former fibres at the

intersection points and the overlap coefficient c , more specifically, $z(i) = z(j) + (d(i) + d(j))(1 - c)/2$; ($1 < j < i$). Overlap coefficient c is defined as the ratio of the overlap depth over the sum of the two intersected fibres' radii, which ranges from 0 to 1. When $c = 0$, there is no intersections between fibres but they are about to intersect. When $c = 1$, the two fibres completely intersect and the z coordinates of the two fibres will be the same.

When the coordinates of the fibre at all intersections are obtained, a criterion is introduced to choose from the intersections to compose the fibre as not all intersections meet the requirement. So the first factor, cross-linker density, is introduced. Cross-linker density is defined as $N_c = L/l_c$, where l_c is the mean distance between any two neighbouring intersection points along a fibre of length L . So $(N_c - 1)$ is the maximum number of intersection points for each fibre. It is controllable and adjustable according to the manufacturing of the structure. We can imagine that when a fibre falls down, it is most likely to intersect at the intersections with large z coordinates. Another factor also needs to be considered is the slope and distance of each segment. Those segments with lengths less than d or, inclination angles larger than 21.5° [13] will be discarded. Thus, the $(N_c - 1)$ intersection points with largest z coordinates and, in the meanwhile, meeting the requirement of the second factor are eventually selected to compose the segments of a fibre in order. Apart from this, the two segments on both ends of a fibre are assumed to be horizontal.

Therefore, by controlling the maximum number of intersection points for each fibre we can successfully obtain the RVE with different volume fractions since the number of intersection points determines the extent of the fluctuation of fibres in terms of the

shapes thus influencing the compactness of fibres. In Figure 3.3, the three red circles demonstrate the bonding areas between the fibre in yellow and other fibres.

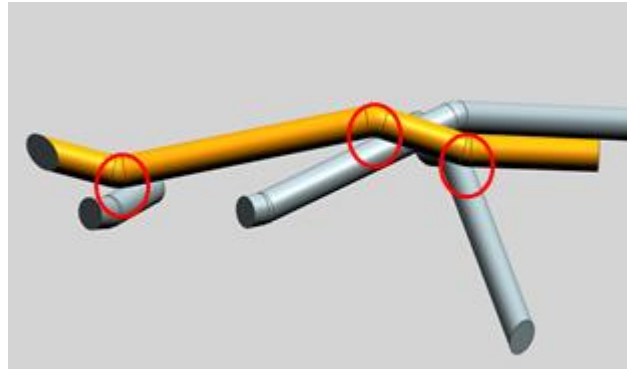


Figure 3.3. A scenario of how fibres are bonded to one another. The fibre in yellow colour drops down and intersects with other three silver fibres at the locations where they are marked with red circles, and the fibre is divided into four segments but still connected.

3.2.3 In-plane Periodicity

The whole in-plane structure of the material can be obtained by replicating the RVE itself and extending it periodically in the x and y directions, respectively. In order to keep the geometrical periodicity of the RVE, the same group of fibres is generated in the 9 cells as indicated in Figure 3.2 and the surrounding 8 cells are cut off. Then parts of fibres that exceed the edges of the central cell are cut and can be regarded as if they are translated to the opposite sides as there are copies of themselves at the corresponding position (see Figure 3.4).

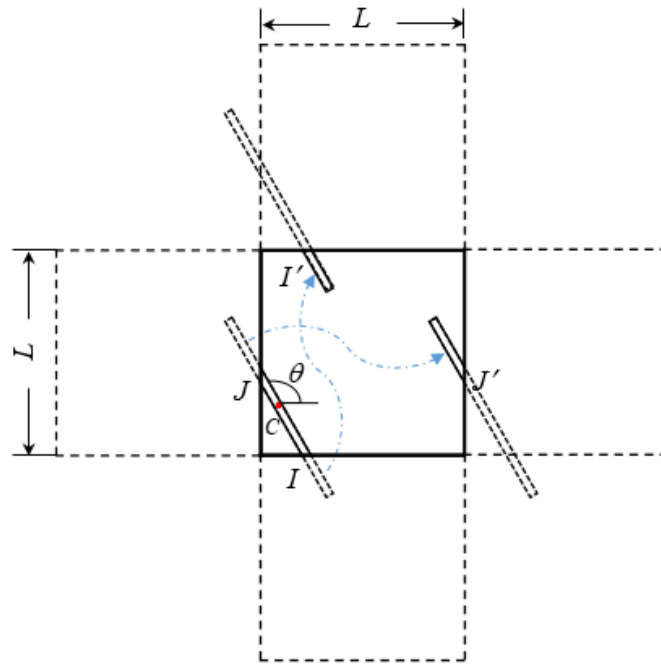


Figure 3.4. Operations on one of the fibres that parts of it exceed the central cell. The dashed parts represent the segments cut off by the boundary of the cell and the solid parts that are inside of the cell are reserved.

3.2.4 Out-of-plane Periodicity

The most complicated step is to ensure the periodicity of RVE in the z -direction as the shape of each fibre varies and is dependent on the fibres generated ahead of it. The process can also refer to the details in [260]. To fulfil the periodicity of RVE in the z -direction, we replicate the generated N fibres through the processes described in Section 3.2.1 and 3.2.2 over themselves again by assigning the same x and y coordinates for fibres $(N+i)$ and i , i.e., $x(N+i) = x(i), y(N+i) = y(i), (i = 1, 2, \dots, N)$ while the z coordinates of the fibre $(N+i)$ is determined by all the previous $(N+i-1)$ fibres. Then the process traces back to generate another N fibres sequentially again and again. Since the $(N+1)$ th fibre is generated based on the previous N fibres. Therefore, there will be a slight offset for the shapes of fibres $(N+i)$ and i . However,

the corresponding fibres will tend to be the same shape if the number of fibres N is large enough and if we repeat enough cycles. For example, if the cycle has been repeated for m times, then there will be $m \times N$ fibres generated and we assume the fibres $((m-1)N+i)$ and $((m-2)N+i)$, ($i = 1, 2, \dots, N$) share the same shape. Then the N fibres from fibre $((m-2)N+1)$ to fibre $(m-1)N$ will be the fibres we need to construct the RVE. In addition, we also have to make sure that the faces of the top and bottom boundary being flat as the constructed fibre network has to be assembled into the solid brick. Therefore, the z coordinate of one end of the fibre $((m-1)N+1)$ the z coordinate of the same end of the fibre $((m-2)N+1)$ are chosen as the upper and lower limits and the fibres are cut from these two horizontal planes. Then fibres and parts of fibres between the limits will be kept and they compose a complete RVE with full periodicity in geometry. Figure 3.5 shows a geometry model with complete periodicity in the x , y and z directions.

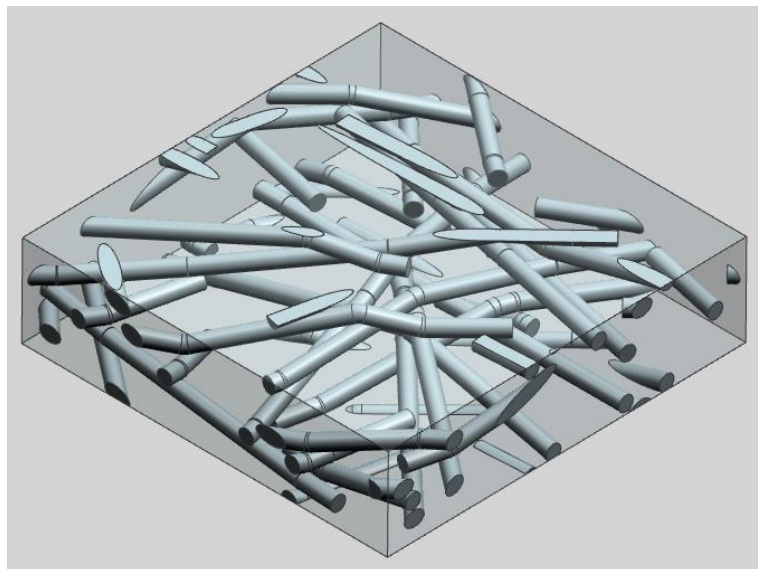


Figure 3.5. A scenario of RVE geometry model with 50 solid fibres.

3.3 Construction of Stochastic Fibre Network Reinforced Composites

3.3.1 Beam Model of Fibres

Beam elements were eventually applied to fibres instead of solid elements. The reason lies in the difficulty in meshing solid elements to both fibres and the matrix due to the complex interfaces between them, not to mention even more complicated interfaces with a large number of closed angles introduced by the overlap between fibres. Moreover, the test carried out shows that even a model with 50 fibres, which is far from enough to establish a transversely isotropic structure, generates approximately 1~2 million solid elements. Such a large number of elements dramatically increase the pre-processing time and slow down the computing speed which is relatively time-consuming. In consideration of the above two reasons, beam element is a better option in representing fibres of large aspect ratios with much less meshing elements. Moreover, beam elements indicate relatively satisfactory results in elastic and elastoplastic properties of fibres compared to solid ones in the following studies. Figure 3.6 is an example of the geometrical model of a fibre network with 200 beam fibres.

From the nature of this fibre network structure (see Figure 3.5) we can see that fibres are intersected and bonded to generate a network. However, the beams representing fibres cannot demonstrate the overlap between fibres due to their dimensional feature in diameters without thickness. Therefore, an inserted beam is applied to wherever two fibres are overlapped as indicated in Figure 3.7. Three inserted beams connect the top fibre and other three ones and fibre network are alternatively generated with

beam elements. In this model, the diameter of the inserted beam is set to be the same as that of fibres.

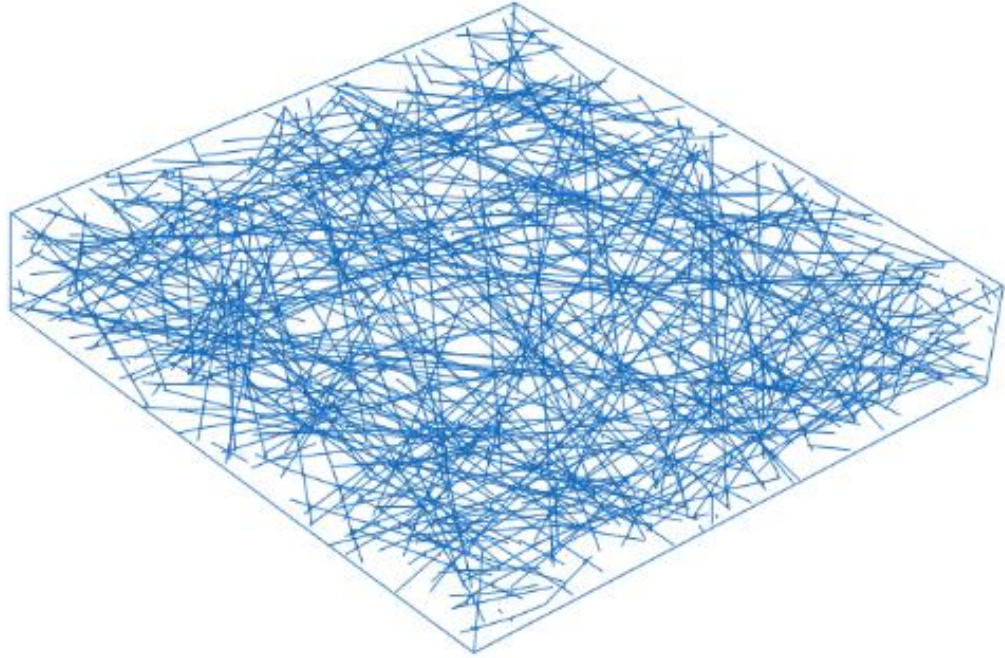


Figure 3.6. Periodic RVE geometric model of the composite reinforced by a transversely isotropic random fibre network containing 200 complete fibres, where the matrix is partitioned into brick elements and the fibres are partitioned into Timoshenko beam elements.

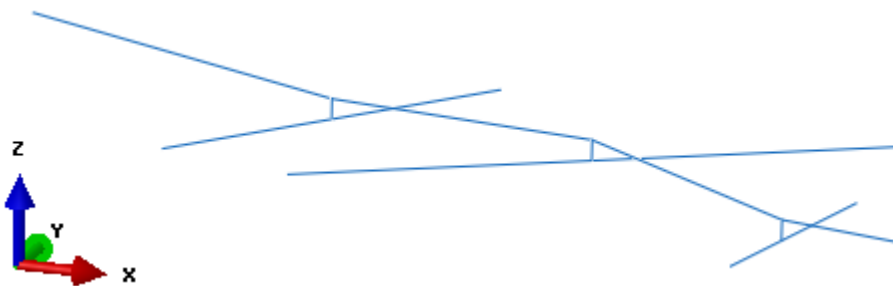


Figure 3.7. A scenario of inserting beams between overlapped fibres.

3.3.2 Assembly of Fibre Network and Matrix

After the programme of fibre network alone is obtained in Matlab, the commercial software NX from Siemens is applied for pre-processing before importing the fibre network structure into Abaqus. In Abaqus, a solid brick with exactly the same size as the fibre network in the x , y and z directions is created to represent the matrix. Then the fibre network will be translated accurately to the inside of the matrix. Furthermore, the fibre network and the matrix also share the same boundary(see Figure 3.8).

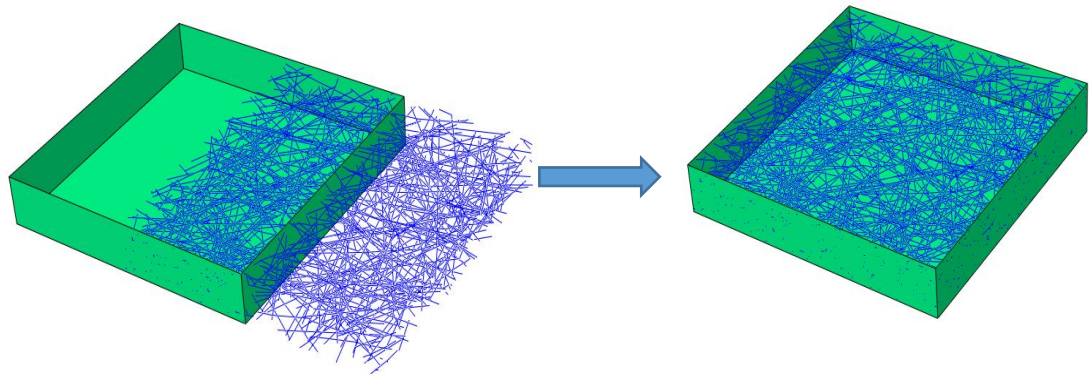


Figure 3.8. Assembly process of fibre network and matrix.

3.3.3 Constraints between Fibre Network and Matrix

Although the fibre network and matrix have been successfully assembled together, corresponding nodes in the fibre network and matrix are still independent. Therefore, constraints have to be applied to the corresponding nodes to ensure that the corresponding nodes have the same translation and rotation so as to transfer the load between fibres and matrix. One common method is the Embedded Element Method (EEM), in which method each node of the fibre network will be coupled with the

nodes of the coinciding element. However, one reason that this method cannot be applied to this model is that over-constraint occurs when both periodic boundary condition and embedded element method are applied to the matrix nodes on the surface simultaneously. Therefore, another method, ASC [2] technique, has been adopted in this model because the conflict can be avoided in this method.

There are two steps for application of ASC technique: node searching and coupling. Firstly, for each node, N_f (see Figure 3.9), in the fibre network, a searching algorithm will be carried out to search through matrix nodes around the node of the fibre network. The closest matrix node, N_m , is then found out eventually for the coupling with the corresponding node of the fibre network. Secondly, the translational freedom degrees of N_m and N_f will be coupled. Since there are six degrees of freedom in beam fibres while only three degrees of freedom in the solid matrix, the rotational degrees of freedom of fibres will be dismissed after the coupling. In this way, all the corresponding nodes will be coupled and constrained for mechanical analysis.

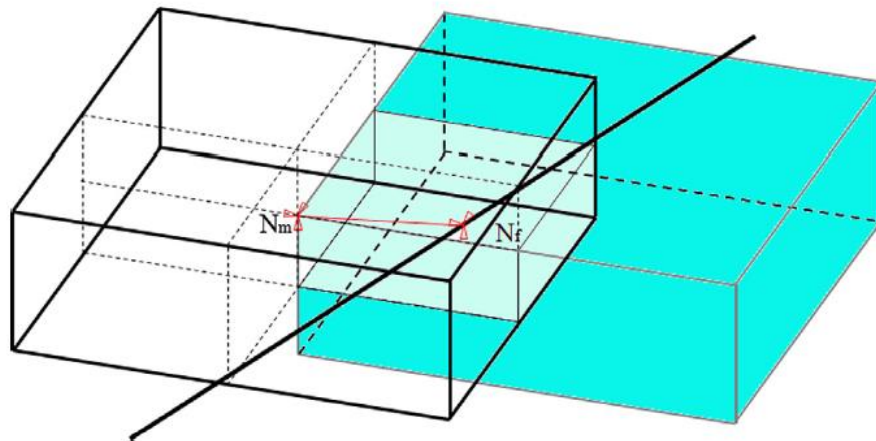


Figure 3.9. A sketch for the node coupling of the ASC technique [2].

3.4 Mesh

One of the advantages of applying ASC technique is that no complex meshing is needed for matrix thus saving times in mesh generation and computing. Since the matrix is structural, the structured technique can be conveniently applied by generating meshes with 8-node linear brick solid elements (C3D8R) for the matrix (see Figure 3.10). There are two beam models that are often used for fibres, which are Timoshenko beam model and Euler-Bernouli beam model, both showing good predictions of mechanical properties of long and slender beams. However, the Timoshenko model can predict the mechanics more accurately for short beams [58] and shear deformation effects are considered in this model. Furthermore, due to the random length of each segment of a fibre, it is anticipated that there exist a large number of short segments which cannot be precisely modelled with the Euler-Bernoulli formulation. Therefore, 2-node linear beam elements (B31) are applied to fibres. Moreover, the cross sections are assumed to be circular throughout the beams.

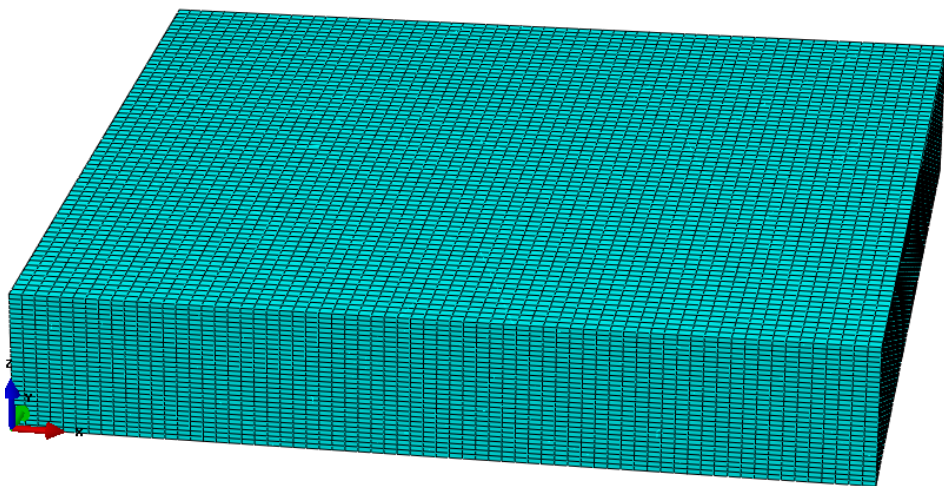


Figure 3.10. The meshing of the matrix with structured 8-node linear brick solid elements (C3D8R).

3.5 Boundary Conditions

3.5.1 Periodic Boundary Conditions

Composite materials can be envisaged as a periodic replication of the RVEs. Therefore, the periodic boundary conditions also must be applied to the RVE models. This implies that each RVE in the composite has the same deformation mode and there is no separation or overlap between the neighbouring RVEs.

There are two types of periodic boundary conditions which are briefly described in Figure 3.11 for the 2D case. In Figure 3.11 (a), the left edge is fixed and no displacement will happen along the x -direction when loaded in the x -direction. Thus, take two arbitrary nodes on the corresponding edges perpendicular to the x -axis for example,

$$u_I = 0; u_J = 0 \quad (3.1)$$

$$u_{I'} - u_I = \Delta x \quad (3.2)$$

$$u_{J'} - u_J = \Delta x \quad (3.3)$$

It is obvious that $u_{J'} = u_{I'} = \Delta x$, which indicates that the right edge keeps straight after loading. However, this constraint seems too strong since the shape of the RVE does not necessarily have to be straight in all the edges due to the stress concentration of fibre reinforced composites. Therefore, a general periodic boundary condition is applied as shown in Figure 3.11 (b), where

$$u_{I'} - u_I = \Delta x \quad (3.4)$$

$$u_{J'} - u_J = \Delta x \quad (3.5)$$

While $u_I \neq u_J$ and $u_{J'} \neq u_{I'}$, which means that only the displacement differences of the corresponding nodes are constrained to be the same. In addition, the RVE also meets the requirement of replicating itself to form the whole composites under this deformation mechanism since the corresponding edges in the x -direction and in the y -direction remain the same shape. Therefore, the general periodic boundary condition is more appropriate for the RVE of fibre network reinforced composites.

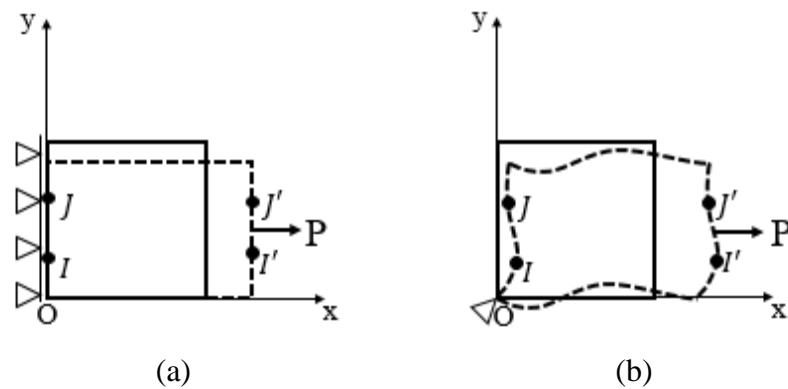


Figure 3.11. Two types of periodic boundary conditions: (a) Strict periodic boundary condition; (b) General periodic boundary condition.

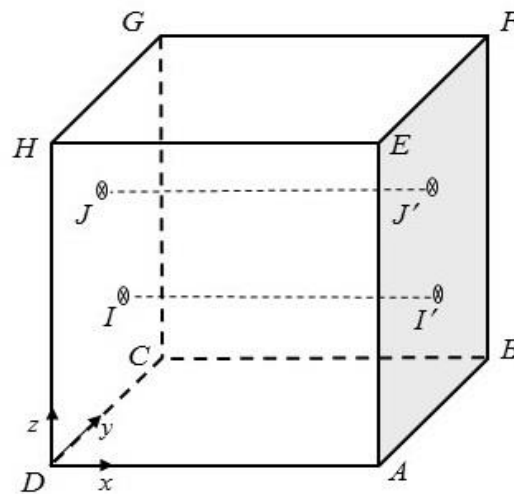


Figure 3.12. A cubic representative volume element (RVE).

For the case of 3D geometries in this research, the general boundary conditions have

to be applied to the nodes on the corresponding faces, edges and joints separately in finite element analysis. Otherwise, over-constraints will occur. Furthermore, only three degrees of freedom, i.e., translation (x , y and z), need to be constrained for solid elements. Therefore, for a unit cell ($L \times W \times H$) (In the specific case of a transversely isotropic structure in this research, $L=W$) as shown in Figure 3.12, the linear constraint equations of boundary conditions can be categorised as follows under the strain load situations ($\varepsilon_x, \varepsilon_y, \varepsilon_z, \gamma_{xy}, \gamma_{yz}, \gamma_{xz}$) [261]:

1) Constraint equations for the corresponding faces;

- a) For the relative nodes on the corresponding faces that are perpendicular to the x -axis (i.e., faces ABFE and DCGH), the constraint equations can be expressed as

$$\begin{cases} u|_{x=L} - u|_{x=0} = L\varepsilon_x \\ v|_{x=L} - v|_{x=0} = 0 \\ w|_{x=L} - w|_{x=0} = 0 \end{cases} \quad (3.6)$$

- b) As for the relative nodes on the corresponding faces that are perpendicular to the y -axis (i.e., faces ADHE and BCGF), the constraint equations can be described as

$$\begin{cases} u|_{y=W} - u|_{y=0} = W\gamma_{xy} \\ v|_{y=W} - v|_{y=0} = W\varepsilon_y \\ w|_{y=W} - w|_{y=0} = 0 \end{cases} \quad (3.7)$$

- c) In terms of the relative nodes on the corresponding faces that are perpendicular to the z -axis (i.e., faces ABCD and EFGH), the constraint equations can be expressed as

$$\begin{cases} u|_{z=H} - u|_{z=0} = H\gamma_{xz} \\ v|_{z=H} - v|_{z=0} = H\gamma_{yz} \\ w|_{z=H} - w|_{z=0} = H\epsilon_z \end{cases} \quad (3.8)$$

Where the three faces on $x=L$, $y=W$ and $z=H$ are called master planes while those faces opposite to the master planes are slave planes. Constraint equations listed above are applied to each pair of nodes (one on the master plane and the other on the slave plane) which are relative in coordinates.

2) Constraint equations for the corresponding edges;

Take the corresponding nodes among the four edges parallel to the z -axis (i.e., edges EA, FB, GC and HD) for example, constraint equations are given below:

$$\begin{cases} u_{EA} - u_{HD} = L\epsilon_x \\ v_{EA} - v_{HD} = 0 \\ w_{EA} - w_{HD} = 0 \end{cases} \quad (3.9)$$

$$\begin{cases} u_{FB} - u_{HD} = L\epsilon_x + W\gamma_{xy} \\ v_{FB} - v_{HD} = W\epsilon_y \\ w_{FB} - w_{HD} = 0 \end{cases} \quad (3.10)$$

$$\begin{cases} u_{GC} - u_{HD} = W\gamma_{xy} \\ v_{GC} - v_{HD} = W\epsilon_y \\ w_{GC} - w_{HD} = 0 \end{cases} \quad (3.11)$$

Similarly, constraint equations to the corresponding nodes among the four edges parallel to the x -axis (i.e., edges DA, CB, HE and GF) and the y -axis (i.e., edges AB, DC, EF and HG), respectively, can be obtained.

3) Constraint equations for the corresponding joints.

Take point D as the datum point, examples of constraint equations between points

E/F/G and D are

$$\begin{cases} u_E - u_D = L\varepsilon_x + H\gamma_{xz} \\ v_E - v_D = H\gamma_{yz} \\ w_E - w_D = H\varepsilon_z \end{cases} \quad (3.12)$$

$$\begin{cases} u_F - u_D = L\varepsilon_x + W\gamma_{xy} + H\gamma_{xz} \\ v_F - v_D = W\varepsilon_y + H\gamma_{yz} \\ w_F - w_D = H\varepsilon_z \end{cases} \quad (3.13)$$

$$\begin{cases} u_G - u_D = W\gamma_{xy} + H\gamma_{xz} \\ v_G - v_D = W\varepsilon_y + H\gamma_{yz} \\ w_G - w_D = H\varepsilon_z \end{cases} \quad (3.14)$$

Then the constraint equations between A/B/C/H and D can also be obtained according to the relative positions.

Eventually, the complete constraints can be achieved from all the 57 constraint equations. In the application of MPC equations in Abaqus, several reference nodes are set to represent the relative faces and get involved in the constraint equations. In this way, all the nodes are integrated to the reference nodes so as to simplify the process of loading and obtaining results which will be demonstrated in the next part (3.5.2).

3.5.2 Load

Since reference nodes are created to represent the relative faces, they will undertake the applied load. For example, when the RVE is applied a uniaxial loading in the x -direction, the three translation freedoms of the origin of coordinates which is marked as D in Figure 3.12 are restrained, in the meanwhile, a normal strain ε_x along the x -

direction is applied to the reference node for the face ABFE (see Figure 3.12). By this way, the reaction force of the reference node F_r , which is the concentrated force of the whole face ABFE, can be obtained and the displacements of faces BCGF and EFGH (u_y and u_z) separately can be achieved from the corresponding reference nodes for these faces. Thus, the Young's modulus in the x -direction can be acquired from

$$E_x = \frac{F_r}{S_x \varepsilon_x} \quad (3.15)$$

where S_x is the initial area of the face ABFE. It should be noted that the stress and strain calculated are all engineering values.

The Poisson's ratios ν_{xy} and ν_{xz} can simply be obtained from

$$\nu_{xy} = -\frac{u_y}{W \varepsilon_x} \quad (3.16)$$

$$\nu_{xz} = -\frac{u_z}{H \varepsilon_x} \quad (3.17)$$

where W and H are the dimensions of RVE in the y -direction and z -direction, respectively.

In terms of shear modulus, taking G_{zx} for example, the shear strain γ_{zx} is applied to the reference node to the top face as indicated in Figure 3.13 and the node at O is fixed in all three degrees of freedom. With periodic boundary conditions applied to RVE, the cubic RVE shows a deformation and the schematic profile of RVE is similar as indicated dash lines which are actually not necessary to be straight as discussed in 3.5.1. Therefore, with the reaction force obtained from the reference node, the shear modulus of G_{zx} can be calculated by

$$G_{zx} = \frac{F_r}{S_z \gamma_{zx}} \quad (3.18)$$

where S_z is the initial area of the top face.

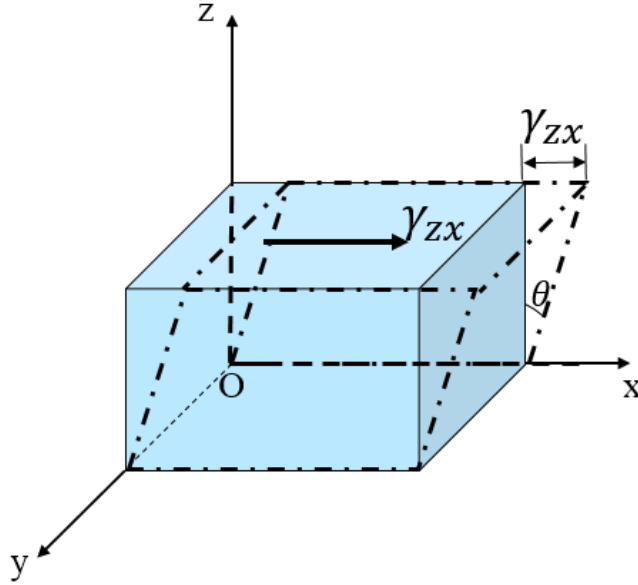


Figure 3.13. The schematic diagram of RVE undertaking shear loading τ_{zx} .

3.6 Key Parameters

3.6.1 Cross-linker Density

The cross-linker density N_c is defined by the ratio of L/l_c , where l_c is the mean distance between the intersections along a fibre of length L . In the numerical model, an innovative way to deal with the intersections is introduced in the three-dimensional random beam model. As shown in Figure 3.2, each fibre is represented by a line of length L , and the lengths are not uniform, ranging from 80 to 120 dimensionless. All the lines are deposited with random position and orientation with a range of $0 \sim 2\pi$. An additional beam is inserted at the intersection point of two lines in the thickness direction (z direction). The inserted beams represent the cross-linkers.

It is not hard to imagine that, as the cross-linker density getting larger, which means more intersections between fibres, each fibre will fluctuate more frequently to a larger extent thus making fibres condenser. Therefore, thickness decreases (see Figure 3.14) and volume fraction increases as we increase the cross-linker density.

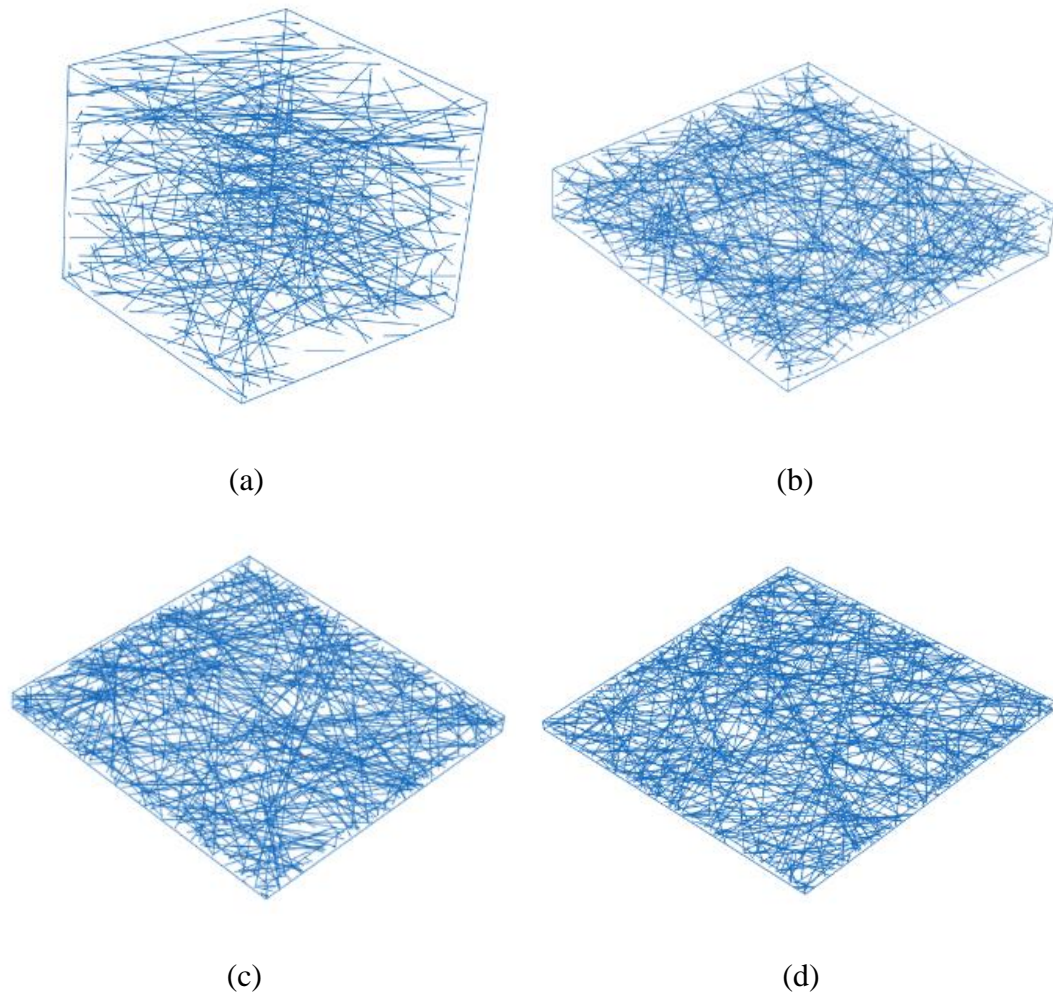


Figure 3.14. Fibre network structure with cross-linker density (a) $N_c = 3$, (b) $N_c = 11$, (c) $N_c = 21$, and (d) $N_c = 27$, when $L/d = 100$.

3.6.2 Overlap Coefficient

Overlap coefficient defines the extent that one fibre is capable of intersecting to the neighbour fibres. It ranges from 0 to 1, where 0 means no overlap and 1 means totally intersected. Taking the processing procedure of this structure into consideration, the

intersecting process is similar to the heat treatment process of randomly piled fibres in which there is no any overlap yet. When the temperature is increased gradually, fibres tend to be softened and drop down to contact other fibres. When the temperature is high enough, fibres will start to intersect with the contacting fibres instead of just contacting with each other. The heat treatment temperature and time determine the overlap coefficient and cross-linker density at the same time. Therefore we can conclude that the two factors, i.e., cross-linker density and overlap coefficient, are dependent on each other. It is noted that in reference [260], only two fixed values of the fibre overlap coefficients, i.e. $c = 0.05$ and $c = 0.6$, are considered; while in this paper, the value of fibre overlap coefficient is not a constant, but always increases with the volume fraction of the fibre-network or the density of cross-linkers. Since there is a positive correlation between these two factors, a linear relation is assumed to be reasonable and applied to them for simplification of computing as given by $c = 0.025(N_c + 1)$. For an RVE model containing N complete fibres, its thickness H depends on the density of crosslinkers and can be determined during the construction process of the fibre-network model.

3.6.3 Aspect Ratio

Aspect ratio is defined as the ratio of the length over the diameter of a fibre. It plays a crucial role in changing the volume fraction of fibres in fibre reinforced composites since it is obvious that the volume fraction is closely dependent on both L and d , as obtained in Eq. (3.20). Composites with fibres of different aspect ratios have been studied and proven to show variant elastic and plastic properties. Therefore, fibre network composites with different aspect ratios in this model will be investigated to compare the mechanical properties of different conditions.

3.6.4 Volume Fraction

The volume fraction is the key parameter to elucidate the mechanical behaviours of composites. In this model, it depends on the above mentioned cross-linker density, overlap coefficient and aspect ratio. By calculating the distance between the corresponding nodes in the z -direction, the thickness H is obtained. The scale of the RVE in the x and y directions are both set as 100 with the same unit as other parameters like L , d and H . Thus the volume of RVE can be obtained as $100 \times 100 \times H$. As for the volume of the fibre network, it cannot be calculated simply by summing the volumes of individual fibres due to the overlap of fibres, especially when the cross-linker density and overlap coefficient are large enough and the volume fraction difference caused by the intersections can be dramatic. Therefore, the volume of the intersected parts should be deducted from the total volume of individual fibres. In experiments, the cross-section area of the intersection depends on the way the overlap is formed and on the compliance of the fibre material [262]. Chen and Silberstein [263] have calculated the bond/overlap area A as $\pi D \sqrt{R_1 R_2}$ (where R_1, R_2 are the fibre radii and D is the indentation distance) according to the non-adhesive elastic contact solution [264]. Deogekar and Picu [262] assumed the bond cross-section to be square which is actually not exactly the real case. Moreover, since the fibres are curved into segments and the orientations of individual fibres vary from 0 to π in the current designed fibre network, the shape of the intersections can also be dependent on the included angle of the two intersected fibres and overlap coefficient. To this end, we aim to obtain the analytical relation of the volume of intersections with the included angle and overlap coefficient.

A schematic model with two intersected fibre segments is illustrated in Table 3.1.

The diameters of both segments are set as 1. The geometry of intersected fibres with various included angles (see Table 3.1) are constructed in the Siemens NX software and the volumes of the intersections with combined included angle and overlap coefficient are also tabulated in Table 3.1. An approximate calculation of the intersection is also approached in terms of combined included angle α and overlap coefficient as

$$\begin{aligned}
 V_{ij} &= 4 \times \left\{ \frac{1}{2} \left(\frac{d}{2} \right)^2 \arctan \left(\frac{\sqrt{c(2-c)}}{1-c} \right) - \frac{1}{2} \left(\frac{d}{2} - \frac{cd}{2} \right) \frac{d\sqrt{c(2-c)}}{2} \right\} \\
 &\quad \times \frac{d(\sqrt{c(2-c)} + 2\sqrt{c(1-c)})}{2 \sin \alpha} \\
 &= \frac{d^3(\sqrt{c(2-c)} + 2\sqrt{c(1-c)})}{4 \sin \alpha_{ij}} \\
 &\quad \times \left\{ \arctan \left(\frac{\sqrt{c(2-c)}}{1-c} \right) - (1-c)\sqrt{c(2-c)} \right\} \quad (3.19)
 \end{aligned}$$

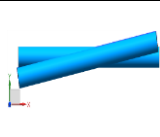
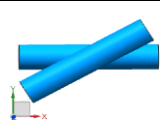
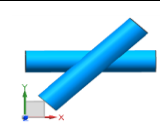
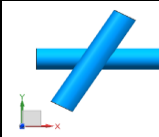
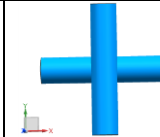

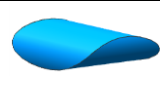
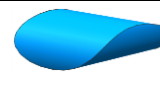
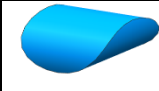
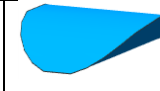
where α_{ij} and V_{ij} are respectively the angle and the overlap volume between the two connected fibres at the j th crosslinker of fibre i . The calculated values of overlap volume according to Eq. (3.19) are also tabulated in Table 3.1 and they indicate a good agreement with the accurate volume of the intersection obtained from the measurement in Siemens NX. Therefore, V_{ij} will be subtracted from the total volume of individual fibres when calculating the volume fraction of the fibre network.

Then, combined with Eq. (3.19), the volume fraction of the fibre network composite can be specified as

$$V_f = \frac{\sum_{i=1}^N \left(L_i \times \left(\frac{1}{4} \pi d^2 \right) - \sum_{j=1}^{N_c} V_{ij} \right)}{100 \times 100 \times H} \quad (3.20)$$

where L_i is the fibre length, N is the number of fibres and d is the diameter of the circular cross section. The diameters of fibres in this model are assumed to possess the same value.

Table 3.1. The volume of the intersection with respect to the included angle and overlap coefficient.

Fibres						
Intersection						
θ		10	30	45	60	90
c	V_{ij}					
0.1	Meas.	0.0871	0.0297	0.0208	0.0173	0.015
	Calc.	0.0875	0.0304	0.0215	0.0175	0.0152
0.2	Meas.	0.3229	0.1132	0.0789	0.0653	0.0565
	Calc.	0.3295	0.1144	0.0809	0.0660	0.0572
0.3	Meas.	0.6913	0.2388	0.168	0.1384	0.1197
	Calc.	0.6937	0.2409	0.1703	0.1391	0.1204
0.4	Meas.	1.145	0.3968	0.2807	0.2306	0.1994
	Calc.	1.1461	0.3980	0.2814	0.2298	0.1990
0.5	Meas.	1.6594	0.5809	0.4096	0.3357	0.2903
	Calc.	1.6500	0.5730	0.4052	0.3308	0.2865
0.6	Meas.	2.181	0.7733	0.5467	0.4468	0.3864
	Calc.	2.164	0.7516	0.5314	0.4339	0.3757

3.7 Conclusions

A transversely isotropic fibre network with beam elements has been successfully constructed and it is designed to function as the reinforcement of the composite structure. Compared to laminates or cross-ply composites, the fibre network based

composites proposed in this research is supposed to possess an advantage in the enhanced out-of-plane mechanical properties, attributed to the vertical cross-linkers that are introduced among fibres to connect fibres and develop an integrated fibre network instead of dispersed fibres. Based on this motivation, the transversely isotropic fibre network reinforced composite is developed for the following mechanical studies in Chapters 4-6.

In order for the coupling of the nodes of fibres and those of the solid matrix, an automatic searching & coupling (ASC) method is employed and this has avoided the over constraints that the application of both embedded element method (EEM) and periodic boundary conditions (PBC) would have brought about. Furthermore, the ASC method has dramatically reduced the complexity of meshing as a structural mesh with hexagonal solid elements. Periodic boundary condition (PBC) is essential to the representative volume element (RVE) in terms of replicating itself to represent the entire geometry and transferring force and displacement through the boundaries. and the way of loading for the finite element analysis (FEA) of mechanics has been explained. Last but not least, the key parameters that are dominant to the mechanical properties of the geometry, namely, cross-linker density, overlap coefficient, aspect ratio and volume fraction, are briefly described. The volume fraction of the fibre network is the key parameter corresponding to the mechanical properties of fibre reinforced composites. It is dominated by the cross-linker density and overlap coefficient collectively. As the cross-linker density and overlap coefficient increase, the fibre network is getting denser, thus decreasing the thickness and increasing the volume fraction of RVE.

Chapter 4 Elastic Properties of Transversely Isotropic Random Fibre Network Reinforced Composites

A transversely isotropic composite geometry with beam fibre network serving as the reinforcement has been successfully constructed in Chapter 3 and, in this chapter, the FEA of elastic properties is performed on this novel structure where vertical cross-linkers are introduced among fibres to develop an integrated fibre network. As a transversely isotropic structure, the five independent constants for the transversely isotropic geometry are obtained to fully characterise the elasticity, especially the diverse in-plane and out-of-plane elastic properties of it. The influence of Poisson's ratios of the fibres and matrix on the stiffness of the geometry is also investigated. Moreover, aspect ratio and cross-linker density are key factors in affecting the elastic properties by varying the volume fraction. Therefore, the dependence of elasticity on aspect ratio and cross-linker density, respectively, is explored. Furthermore, a simplified model, which is similar to the structure of the novel fibre network reinforced composites, is developed for the analytical investigation of the elastic properties of the geometrical model and comparison with the numerical results.

4.1 Introduction

As the RVE of the 3D transversely isotropic fibre network composites has been successfully generated, the relative mechanical properties aimed to be discovered towards this new structure, in which elasticity is certainly the fundamental yet most important properties of the composites. The elastic properties of composites are not invariable, and they are mainly dependent on the constituent materials and phase structures. In addition, the interface between phases is also very important for the elasticity of the composites although it contributes a major effect on the plasticity of the composites. The overall composite structure can be either isotropic or anisotropic and there are wide choices for the selection of reinforcement and matrix materials as shown in Chapter 2. All these factors have made composites considerably complicated and characteristic in terms of the mechanical and other properties, in the meanwhile, opening more possibilities for various promising applications of composite structures.

Due to the complicated structure of 3D fibre network composites, it is extremely challenging in obtaining the relation between mechanical properties and internal structure. Finite element analysis (FEA) provides an efficient method in the investigation of the mechanical properties of the complex fibre network composites [17, 265]. FEM reduces the cost in experimental test and material and structural exploration and provides a more direct approach for in-depth investigation of mechanical properties regarding structures in different scales compared to the theoretical methods [266]. Thus, the elastic properties can be determined through the stress-strain response by applying FEM to the RVE.

The objective of this chapter is to investigate the elastic behaviours of transversely isotropic fibre network composites. To begin with, the FEA results of both the in-plane and out-of-plane elastic behaviours of the composites have been predicted. The influences of Poisson's ratio, aspect ratio and cross-linker density, respectively, on the stiffness of composites have also been considered. Secondly, a simplified analytical model has been proposed for comparison with the numerical results. Finally, the stiffness of this fibre network composite has been compared with other composite structures.

4.2 Geometry and Material Properties

Transversely isotropic RVEs with different volume fractions have been generated according to the procedure of developing an RVE as introduced in Chapter 3. The RVE size is set as $100\text{ mm}\times 100\text{ mm}\times H$ in this research where H is the thickness of the RVE and the value of H differs in different models depending on the cross-linker density and overlap coefficient. The fibres are meshed using linear beam elements (B31) and the matrix is meshed using 8-node linear brick solid elements (C3D8R). The material parameters that are applied to the fibres and matrix for the elasticity study are listed in Table 4.1. Instead of applying certain values of Young's moduli for the fibres and matrix, different ratios of Young's moduli of the fibres and matrix are applied in order to study the elastic properties of a wide variety of composites with combinations of different fibres (listed in Table 2.1) and matrices (listed in Table 2.2), such as Glass/polymer, carbon/ceramic and metal matrix (carbon/Titanium) composites.

Table 4.1. Materials parameters for the elasticity study in FE models.

The ratio of Young's moduli of fibre and matrix, E_f/E_m	Fibre's Poisson's ratio, ν_f	Matrix's Poisson's ratio, ν_m
100		
50		
10	0.3	0.3
5		
100	0.05	0.495
100	0.495	0.05
100	0.495	-0.8

4.3 Discussions of RVE

4.3.1 Statistical Analysis

In this study, periodic random structures have been constructed with a range of fibre lengths and orientations taken into consideration. These random data is obtained from the function in Matlab, which generates uniformly distributed pseudorandom numbers between 0 and 1 with $rand()$. Therefore, all the fibre network models are randomly generated and the mechanical behaviour has a significant specimen to specimen variation [100, 267]. So, in order to get the mechanical parameters, massive calculations and statistical analysis are needed. Mean results and standard deviations are obtained from a number of independent, but similar structural models with the same set/combination of parameters.

4.3.2 Mesh Sensitivity

As we know, the FE model is considerably sensitive to the mesh size. Therefore, it is

necessary to study the effective stiffness difference caused by mesh densities. Different mesh configurations have been applied to models in 9% V_f and 30% V_f cases and the in-plane and out-of-plane Young's moduli and Poisson's ratios have been obtained and listed in Table 4.2. The convergence of both in-plane and out-of-plane moduli in Figure 4.1 gives us a more transparent vision of mesh sensitivity of the results. Taking the computing precise and efficient into consideration, matrix mesh size of 1.5 mm×1.5 mm×0.6 mm through the x , y and z directions has been chosen for the following analysis. With this element mesh size and RVE size of 100mm × 100mm × H , the number of solid C3D8R elements in matrix varies from 20000 to 230000 depending on the thickness of RVE and the number of Timoshenko beam elements (B31) in fibres is around 60000 with the fibre mesh size of 1 mm.

Table 4.2. Mesh size effect on the in-plane and out-of-plane Young's moduli and Poisson's ratios of RVE.

Elastic properties	Mesh 1	Mesh 2	Mesh 3	Mesh 4	Mesh 5	Mesh 6	
Size of elements (mm× mm×mm)	4×4×1	1.5×1.5×0.8	1.5×1.5×0.6	1.25×1.2×0.6	1×1×0.5	0.8×0.8×0.4	
9%(V_f)	E_{11}	4.37	3.99	3.86	3.8	3.74	3.7
	E_{33}	1.89	1.71	1.565	1.54	1.5	1.48
	ν_{12}	0.339	0.337	0.336	0.335	0.335	0.334
	ν_{31}	0.094	0.096	0.097	0.098	0.1	0.101
30%(V_f)	E_{11}	12.4	12.01	11.9	11.88	11.86	11.87
	E_{33}	4.15	3.81	3.55	3.46	3.45	3.4
	ν_{12}	0.291	0.288	0.332	0.331	0.329	0.328
	ν_{31}	0.039	0.041	0.041	0.041	0.042	0.042

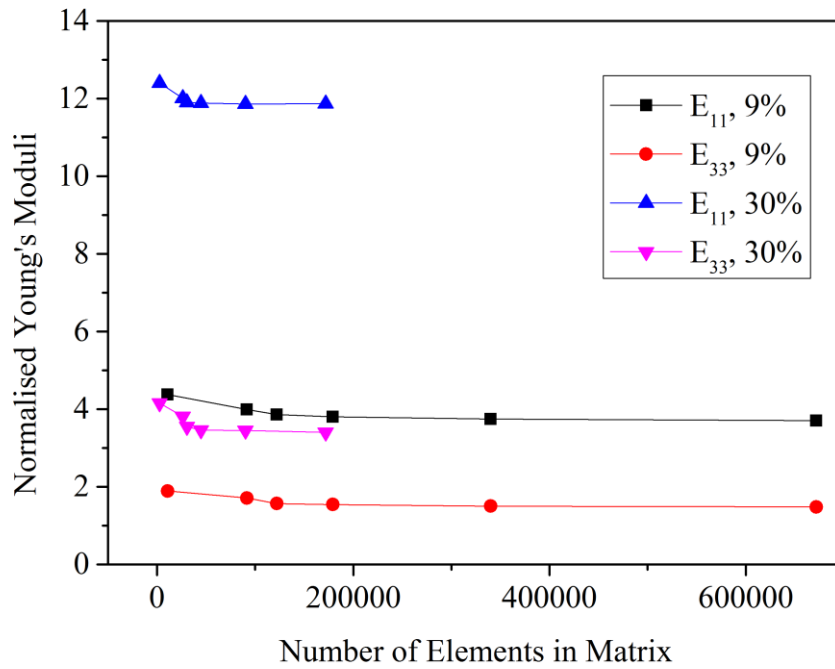


Figure 4.1. Mesh size effect on in-plane and out-of-plane Young's moduli for 10 RVEs with volume fractions of 9% and 30%, respectively.

4.3.3 Fibre Quantity Determination

In order to ensure that the RVE generated can best represent the properties of the materials, it is necessary to determine the number of fibres required. Therefore, RVE models with different numbers of fibres, $N = 50, 75, 100, 150, 200, 400$, have been investigated while remaining the same density of cross-linker, $N_c = 11$, the same aspect ratio, $L/d = 100$, and the same overlap coefficient, $c = 0.3$. Since the fibres are distributed according to the stochastic number of fibres orientations in Matlab, there exists instability in geometries. Thus, to eliminate the error, ten samples of RVE models which only differ in random numbers of fibres orientations were generated for each fibre quantity and statistical mechanical results were explored for discussion. With the materials properties $E_f/E_m = 100$ and $v_f = v_m = 0.3$, the mean in-plane

Young's modulus E_{11} and volume fraction V_f of ten RVEs with fibre number $N = 50, 75, 100, 150, 200$ and 400 have been obtained and listed in Table 4.3 to study the difference caused by the number of fibres.

It can be seen from Table 4.3 that the volume fractions of RVE are almost identical in all cases while Young's moduli are approaching the exact value and the standard deviations for both tend to be smaller as the number of fibres increases. That means that the more fibres there are, the smaller the error will be. Furthermore, the ratio of Young's moduli of each double layers and single layer (i.e., $N = 100$ vs. $N = 50$, $N = 200$ vs. $N = 100$) has been compared and shown in Table 4.4. When the number of fibres is large enough, Young's moduli of double layers and a single layer should be the same and the ratio is expected to be 1. Table 4.4 indicates that, when the number of fibres increases to 200, the ratio is very close to 1 which means that $N = 200$ is already sufficient for the computation. Taking the above conclusion and computational efficiency into consideration, the number of fibres in each RVE is fixed at $N = 200$ in all the following models.

Table 4.3. Statistic Young's modulus, E_{11} , and volume fraction of 10 RVEs for different numbers of fibres ($N = 50, 75, 100, 150, 200, 400$) with the density of cross-linker at $N_c = 11$, the overlap coefficient at $c = 0.3$, and the aspect ratio at $L/d = 100$.

	Volume Fraction, V_f				Normalised Young's Modulus, E_{11}			
	Mean	STDEV	MAX	MIN	Mean	STDEV	MAX	MIN
$N=50$	0.0983	0.0095	0.1149	0.0842	3.9127	0.4063	4.4528	3.1564
$N=75$	0.0896	0.0052	0.0956	0.0809	3.6167	0.3770	4.0178	2.7895
$N=100$	0.0905	0.0031	0.0955	0.0853	3.8132	0.2019	4.2661	3.6298
$N=150$	0.0908	0.0039	0.0988	0.0869	3.7868	0.2717	4.3925	3.4796
$N=200$	0.0924	0.0026	0.0972	0.0880	3.8653	0.1973	4.2450	3.5497
$N=400$	0.0923	0.0016	0.0937	0.0896	3.8604	0.1790	4.1071	3.6346

Table 4.4. The mean ratio of paired Young's moduli.

	$N100/N50$	$N150/N75$	$N200/N100$	$N400/N200$
Mean Ratio	1.055485	1.051586	1.031098	0.983844
Abs. Error	0.055485	0.051586	0.031098	0.016156

4.3.4 Dependence of the RVE Thickness and Volume Fraction on the Cross-linker Density

The volume fraction of fibres is the crucial parameter for the properties of this 3D structure. From the regulation of how the RVE is generated, it is not difficult to figure out that there are two factors, i.e., cross-linker density and overlap coefficient, in determining the volume fraction of fibres on condition that the aspect ratios of fibres remain constants. According to the definition of cross-linker density, it is no doubt that the larger the cross-linker density is, the more intersections there will be for each fibre, which means that each fibre needs to drop down deeper to connect to other fibres below, thus decreasing the thickness of the RVE and, in the meanwhile, increasing the volume fraction. Then the volume fraction of fibres is only determined by the single factor cross-linker density and, as shown in Figure 4.2, the relationship of the thickness and volume fraction against cross-linker density is obtained. From the figure, we can see that there is an exponential decay in the thickness of the RVE while an exponential rise in volume fraction as the cross-linker density N_c increases. These trends agree with how this structure is constructed. This has also inspired us of a method of manufacturing the fibre composite plate that a plate with only a single layer and the required thickness can be produced simply by controlling the geometry parameters such as cross-linker coefficient. In addition, this reduces the possibility of delamination compared to laminates. Therefore, this advantage highlights a

promising application of fibre network composite in industry. In addition, a structure with a considerably large volume fraction of 0.42 can be achieved by this geometrical model. By curve fitting, volume fraction as a function of cross-linker density can be approximately fitted as

$$V_f = 1.1816 \times 10^{-5} N_c^3 - 2.2327 \times 10^{-5} N_c^2 + 0.00715 N_c - 0.00286 \quad (4.1)$$

It indicates that V_f is a cubic polynomial of N_c .

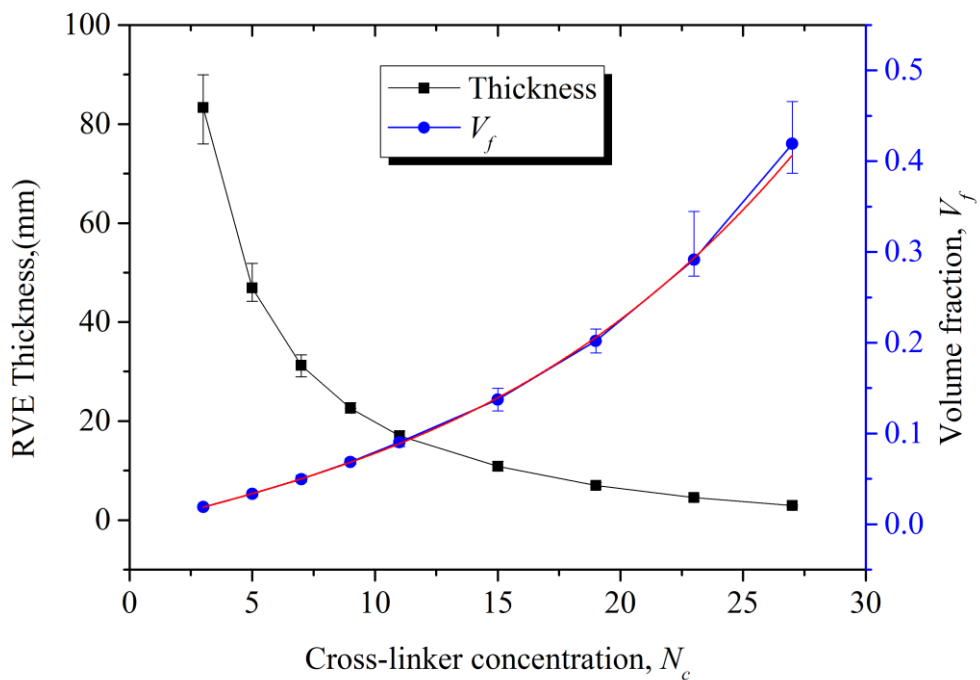


Figure 4.2. Effect of cross-linker density, N_c , on RVE thickness (the curve with square symbol) and fibre volume fraction (the curve with round symbol) with aspect ratio $L/d = 100$.

4.3.5 Fibre Element Type Difference

The above results are based on the analysis of RVE with beam elements applied to the fibres and solid elements to the matrix. As mentioned before, the ASC Technique has been adopted to constrain every single node of the beam elements within the corresponding solid elements in the matrix. This method greatly reduces the

complexity of pairing the coincident nodes on fibres to that in the matrix. However, it has to be aware that there are limitations to this technique. The biggest concern lies in that additional stiffness might be added to RVE. Therefore, it is necessary to investigate the difference introduced by the application of beam elements to fibres compared to solid elements.

Ten RVEs which consist of 50 fibres each were generated with a degree of cross-linkers $N_c = 15$, overlap coefficient $c = 0.4$ and aspect ratio $L/d = 30$. Beam and solid elements were ensured to be applied to the same model, respectively, while keeping the other conditions the same. The value of E_f/E_m is assumed as 100 and Poisson's ratios of fibres and matrix are kept the same as 0.3. A uniaxial tensile/shearing strain of 0.001 was applied to the models and the corresponding reaction force was recorded. Table 4.5 lists the mean results of the five independent elastic constants with two different element types. E_{11} and G_{31} of the RVEs with beam elements show smaller values than those of the RVEs with solid elements whereas E_{33} of the RVEs with beam elements is larger than that of the RVEs with solid elements. It can be calculated that the largest difference between the stiffnesses of the RVEs with the two different element types is around 15%. It is also noticed that the model with beam fibre elements tends to underestimate the in-plane stiffness and overestimate the out-of-plane stiffness compared to the model with solid fibre elements. One unavoidable problem is computing efficiency. When solid elements is adopted, the quantity of the RVE elements reaches 1-2 million or even larger depending on the dimensions of fibres, which is really time-consuming and unaffordable for a research involving several hundreds of such RVEs. Therefore, it can be a good choice to use beam elements considering feasibility, efficiency and accuracy in computation. This is also how most other researchers deal with complex

fibre reinforced composites and fibre network.

Table 4.5. The independent elastic properties of RVE with beam and solid fibre element types, respectively, in which degree of cross-linkers $N_c=15$, overlap coefficient $c = 0.4$ and aspect ratio $L/d = 30$. The values are averaged for 10 RVEs.

Fibre element type	E_{11}	ν_{12}	E_{33}	ν_{31}	G_{31}
Beam	2.496059	0.225184	1.383805	0.207891	0.466779
Solid	2.862772	0.190082	1.142895	0.227317	0.526806

4.3.6 Transverse Isotropy of RVE

In order to testify the transverse isotropy of the generated RVEs, Young's moduli, shear moduli and Poisson's ratios of 10 models with the density of cross-linkers $N_c = 11$, the overlap coefficient $c = 0.3$ and the aspect ratio $L/d = 100$ are tabulated in Table 4.6 and the mean values are calculated. It is shown that the mean values of Young's modulus and Poisson's ratio for the 10 models are almost identical in the x and y directions. In addition, the observed values of Young's modulus and Poisson's ratio satisfy

$$\frac{E_{11}}{E_{22}} * \frac{\nu_{21}}{\nu_{12}} = 0.998364 \quad (4.2)$$

$$\frac{E_{11}}{E_{33}} * \frac{\nu_{31}}{\nu_{13}} = 1.002852 \quad (4.3)$$

$$\frac{E_{22}}{E_{33}} * \frac{\nu_{32}}{\nu_{23}} = 1.002748 \quad (4.4)$$

The above equations imply that the relationship between Young's modulus and Poisson's ratio meets

$$\frac{E_i}{E_j} = \frac{\nu_{ij}}{\nu_{ji}} \quad (4.5)$$

The results also show that the shear modulus, Young's modulus and Poisson's ratio in the x and y directions meet that

$$G_{12} = \frac{E_{11}}{2(1 + \nu_{12})} \quad (4.6)$$

where E_{11} can be replaced by E_{22} , and ν_{12} can be replaced by ν_{21} . In addition, $G_{13} = G_{31}$, $\nu_{13} = \nu_{23}$ and $\nu_{31} = \nu_{32}$ with the largest error less than 5%. These all suggest that the stochastic fibre network composite structure is transversely isotropic and only five independent constants, E_{11} , ν_{12} , E_{33} , ν_{31} and G_{31} are needed for full elastic analysis.

Table 4.6 Young's moduli, Poisson's ratios and shear moduli of 10 RVEs with density of cross-linkers $N_c = 11$, overlap coefficient $c = 0.3$, fibre number $N = 200$, and aspect ratio $L/d = 100$. The volume fraction is 0.09.

	E_{11}	ν_{12}	ν_{13}	E_{22}	ν_{21}	ν_{23}	...
01	3.874956	0.313329	0.245138	3.833344	0.309964	0.248317	
02	3.972831	0.338440	0.235412	3.702278	0.315392	0.242851	
03	3.960358	0.373321	0.226916	3.374779	0.318121	0.243142	
04	3.777534	0.361487	0.227803	3.546943	0.339420	0.233979	
05	3.624164	0.329107	0.239986	3.838568	0.348577	0.234099	
06	4.245049	0.354521	0.233621	3.498124	0.292142	0.249743	...
07	3.549718	0.298000	0.254791	3.896780	0.327136	0.245870	
08	3.797864	0.310732	0.245548	3.941230	0.322462	0.240366	
09	3.989732	0.324433	0.241150	3.779278	0.307320	0.246934	
10	3.861258	0.360456	0.231369	3.452893	0.322335	0.240102	
Mean	3.865346	0.336383	0.238173	3.686422	0.320287	0.242540	
Std.	0.197312	0.025311	0.008820	0.202581	0.016048	0.005491	...

	E_{33}	ν_{31}	ν_{32}	G_{12}	G_{23}	G_{31}
01	1.562067	0.098820	0.101188	1.392429	0.454912	0.452931
02	1.579220	0.093577	0.103589	1.439120	0.453450	0.456408

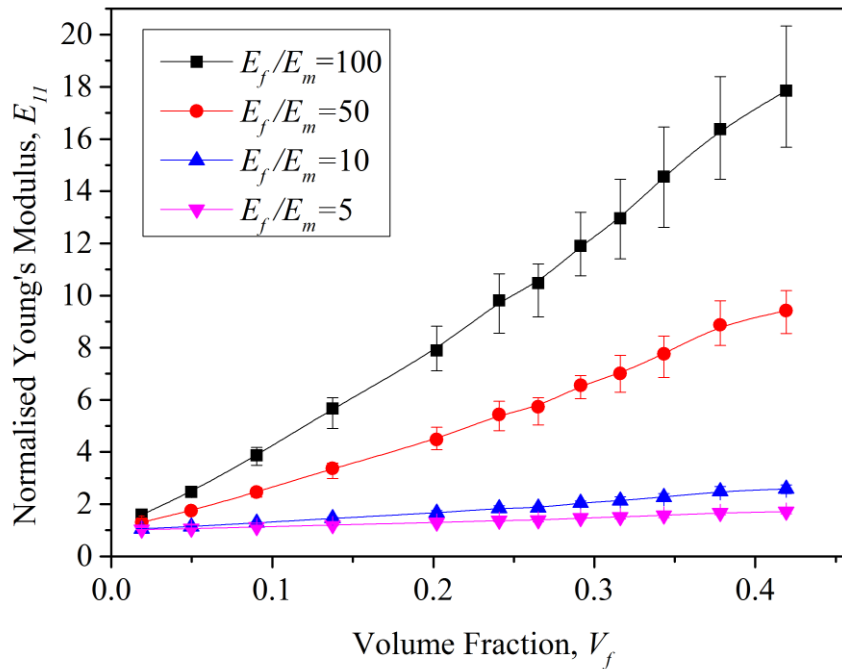
03	1.560705	0.089424	0.112444	1.484580	0.448540	0.457150
04	1.575962	0.095038	0.103961	1.525346	0.452607	0.456802
05	1.565345	0.103655	0.095464	1.468601	0.455882	0.452770
06	1.570637	0.086438	0.112133	1.433872	0.449030	0.460255
07	1.531894	0.109956	0.096656	1.344693	0.452540	0.447162
08	1.576973	0.101958	0.096176	1.410652	0.455451	0.453879
09	1.567528	0.094746	0.102420	1.406203	0.451545	0.453021
10	1.560764	0.093522	0.108530	1.459255	0.448647	0.456727
Mean	1.565110	0.096713	0.103256	1.436475	0.452260	0.454711
Std.	0.013519	0.006999	0.006245	0.051342	0.002785	0.003582

4.4 Numerical Results

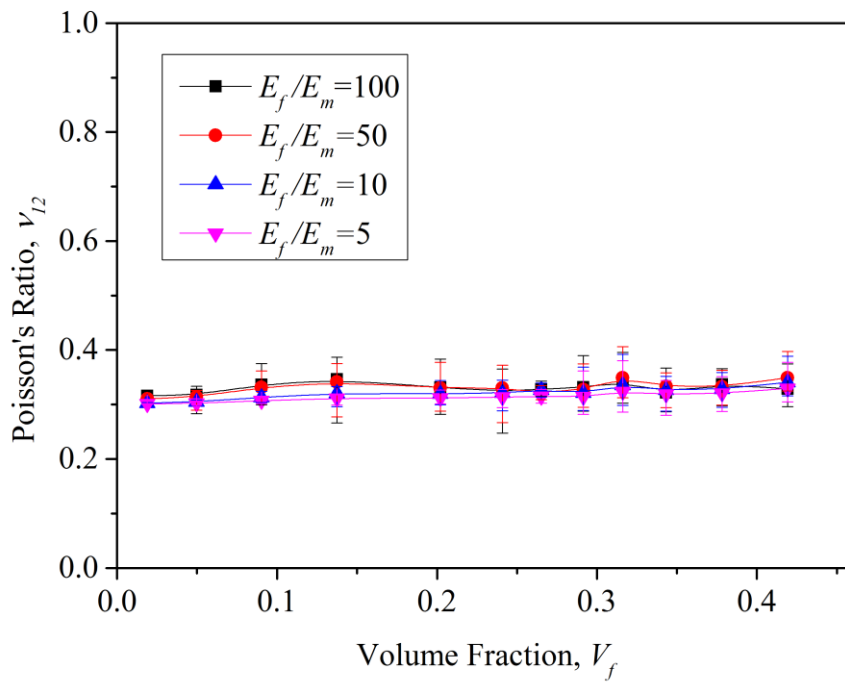
4.4.1 Five Independent Constants

As mentioned in 4.3.6, only five independent constants, namely E_{11} , ν_{12} , E_{33} , ν_{31} and G_{31} , are needed to study the elastic properties. By imposing a tensile or shear strain of 0.001 to the RVEs with the aspect ratio $L/d=100$, the same Poisson's ratios $\nu_f = \nu_m = 0.3$ and various values of $E_f/E_m (=100, 50, 10, 5)$, the results of the five independent constants in terms of volume fraction, respectively, have been obtained and shown in Figure 4.3, where E_{11} , E_{33} and G_{31} are normalised by E_m . From the figure, we can see that the in-plane Young's modulus E_{11} , out-of-plane Young's modulus E_{33} and shear modulus G_{31} all increase as the volume fraction increases, which indicates that both tensile and shear properties can be improved by raising the volume fraction of the fibre network. Specifically, E_{11} shows a linear relationship with the volume fraction while E_{33} possesses a nonlinear relation, where E_{33} grows faster and faster as the volume fraction arises when the volume fraction is still less

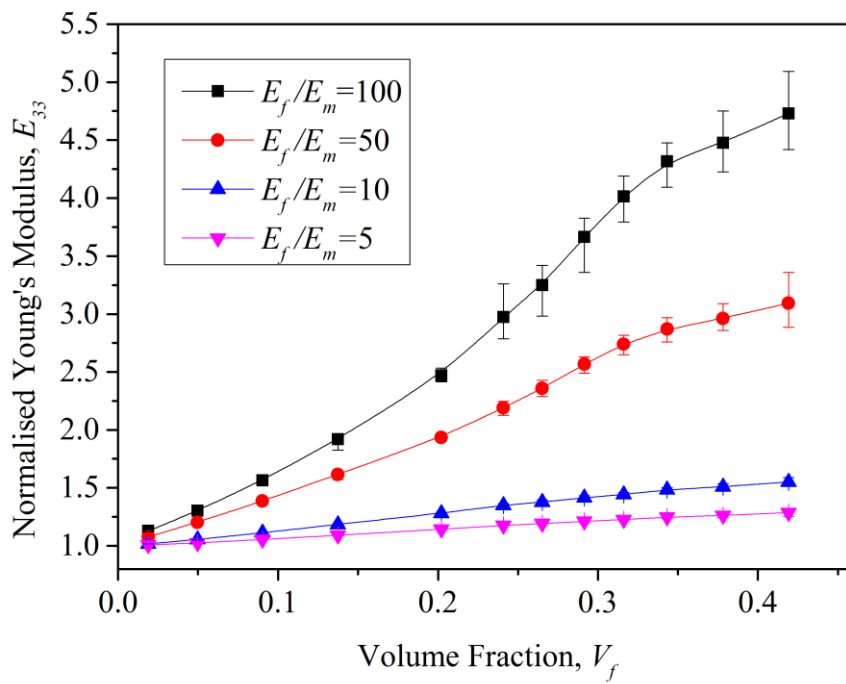
than 0.4 approximately and then tends to slow down as the volume fraction continues to increase. G_{13} indicates a similar relationship with the volume fraction as E_{33} . In terms of Poisson's ratio, it can be seen from Figure 4.3 (b) and (d) that ν_{12} slightly fluctuates around 0.32, which is consistent with the results by Markaki and Clyne [268, 269] and this is not affected by the matrix, for different volume fractions while ν_{31} decreases as the volume fraction increases. In addition, there is no doubt that E_{11} , E_{33} and G_{31} will be strengthened with larger value of E_f/E_m . However, ν_{12} seems not to be affected by the changing of the value of E_f/E_m whereas ν_{31} decrease as E_f/E_m increases. Interestingly, Poisson's ratio ν_{31} tends to be very small enough when the ratio of E_f/E_m is as large as 100 and the volume fraction is large as well. In the case of both the value of E_f/E_m and volume fraction approaching large enough, ν_{31} tends to reach 0 which indicates that out-of-plane tension/compression introduces almost no effect on in-plane expansion under this condition.



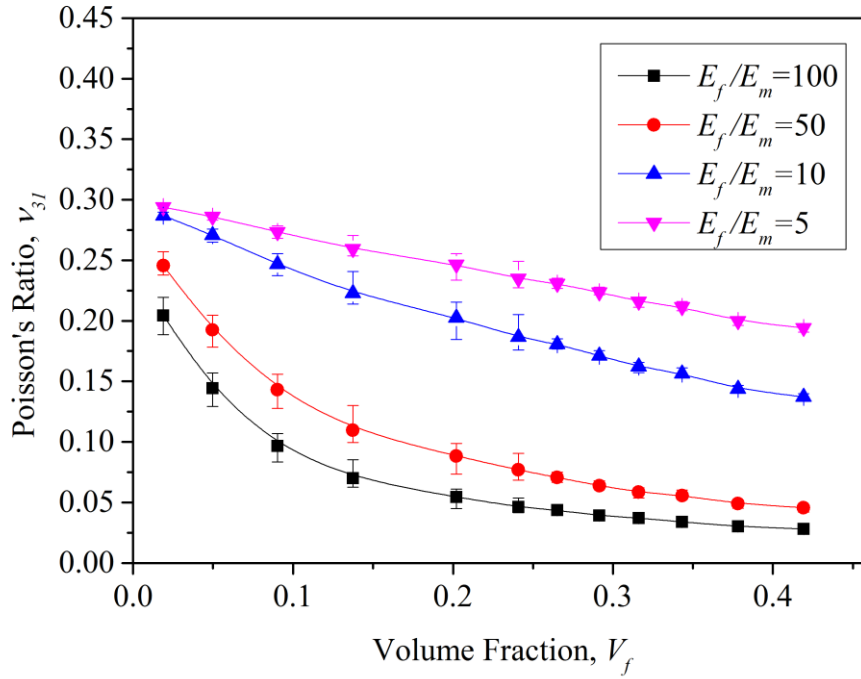
(a)



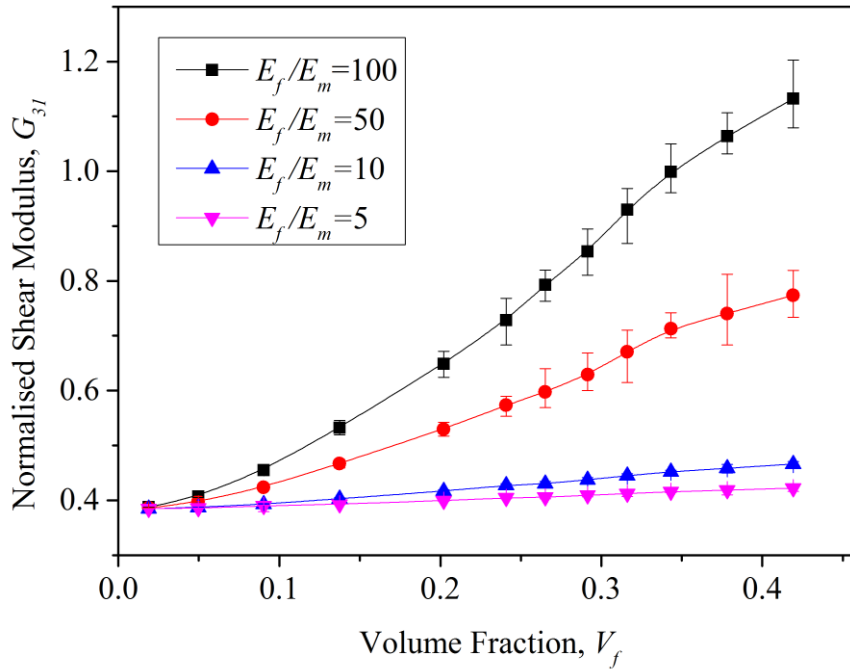
(b)



(c)



(d)



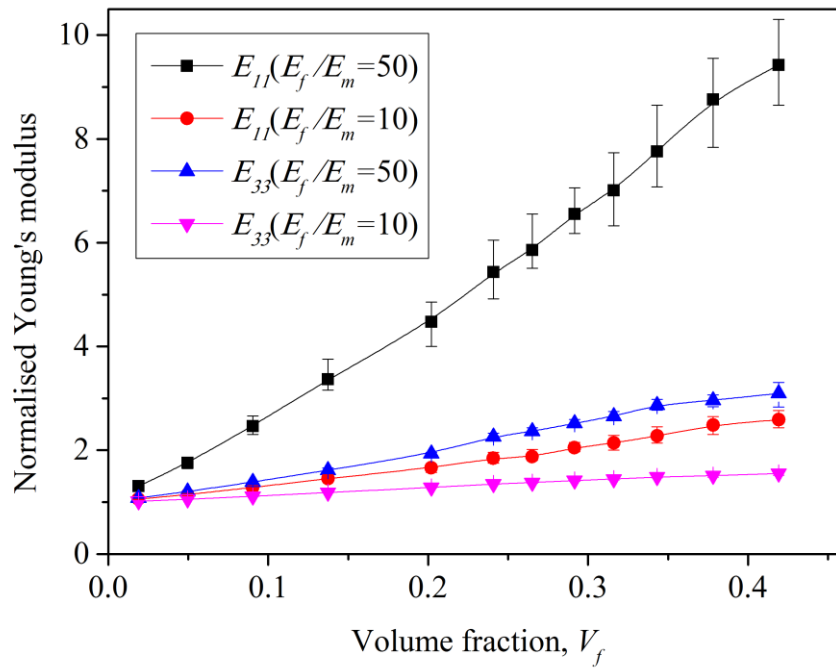
(e)

Figure 4.3. Effect of volume fraction on (a) in-plane Young's modulus E_{11} , (b) in-plane Poisson's ratio ν_{12} , (c) out-of-plane Young's modulus E_{33} , (d) out-of-plane Poisson's ratio ν_{31} and (e) out-of-plane shear modulus G_{31} with the aspect ratio $L/d = 100$ and same Poisson's ratios $\nu_f = \nu_m = 0.3$.

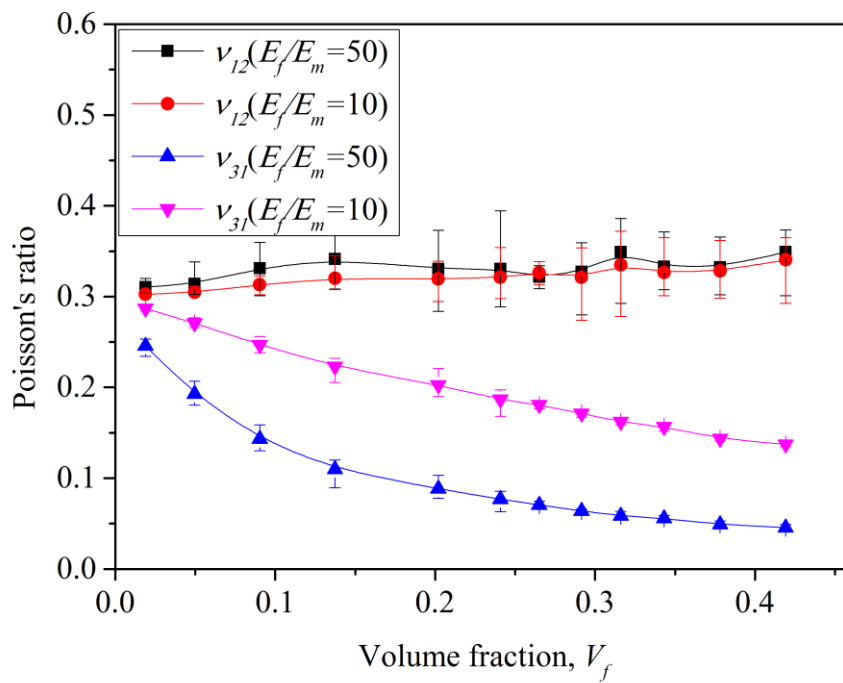
4.4.2 Comparison of In-plane and Out-of-plane Elastic Properties

In consideration of the transverse isotropy characteristic of this geometry, it obviously possesses different elastic properties transversely (i.e. in-plane direction) and longitudinally (i.e. out-of-plane direction) (see Figure 4.3). Therefore, this section aims to compare the in-plane and out-of-plane elastic properties so as to better understand the directional properties of the geometry. Figure 4.4 is simply the re-organised data from Figure 4.3 with Poisson's ratios $\nu_f = \nu_m = 0.3$ and the ratio of $E_f/E_m = 50$ and 10 , respectively. Also, E_{11} , E_{33} and G_{31} are normalised by E_m . The results in Figure 4.4 indicate that the in-plane Young's modulus E_{11} shows a higher value than the out-of-plane Young's modulus E_{33} . Moreover, the larger the volume fraction is, the bigger the difference between the in-plane Young's modulus and out-of-plane Young's modulus is. The in-plane Young's modulus can be three times of the out-of-plane Young's modulus when the volume fraction of fibres reaches approximately 50% and the ratio of $E_f/E_m = 50$ (see Figure 4.4(a)). Figure 4.4(b) shows that the out-of-plane Poisson's ratio ν_{31} is always smaller than the in-plane Poisson's ratio ν_{12} and the difference between them is getting larger. This is because the volume fraction increases since in-plane Poisson's ratio remains constants whereas the out-of-plane Poisson's ratio decreases with the volume fraction increasing. Furthermore, the in-plane shear modulus G_{12} and out-of-plane shear modulus G_{31} are also compared in Figure 4.4(c). We can see that the in-plane shear modulus is also always larger than the out-of-plane shear modulus. For instance, the in-plane shear modulus is almost five times of the out-of-plane shear modulus when the volume fraction of fibres reaches approximately 50% and the ratio of

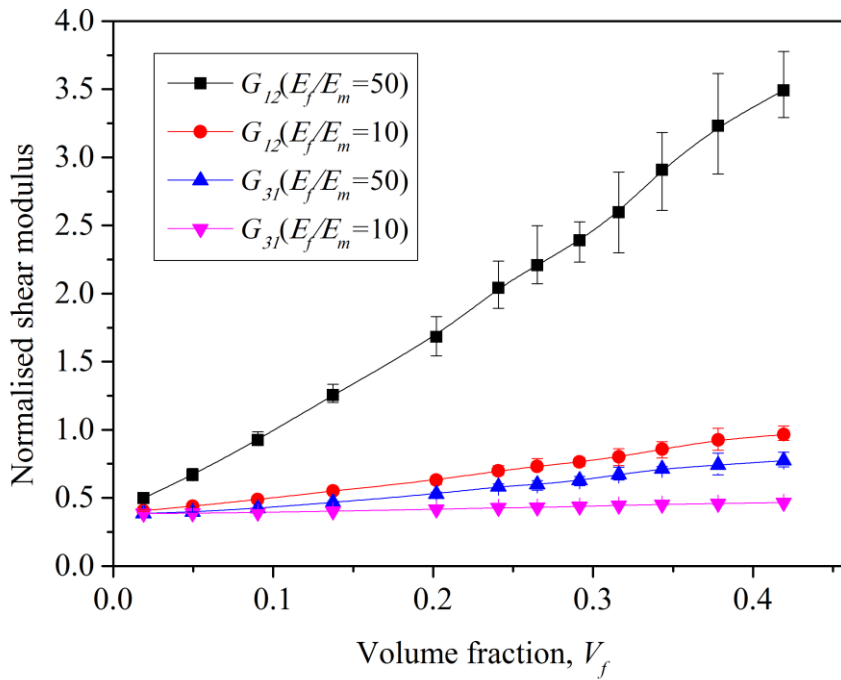
$$E_f/E_m = 50.$$



(a)



(b)



(c)

Figure 4.4. Comparison of in-plane and out-of-plane elastic properties: (a) in-plane and out-of-plane Young's moduli, (b) in-plane and out-of-plane Poisson's ratios, (c) in-plane and out-of-plane shear moduli, with $E_f/E_m = 10$ and 50.

4.4.3 The Effect of Poisson's Ratio on the Elastic Properties

Poisson's ratio is a crucial parameter for the mechanical properties of materials. The effective elastic properties of fibre-reinforced composites are significantly related to the Poisson's ratios of fibres and matrix. It is well known that Poisson's ratios of most solid materials range from 0.1 to 0.4 and this range has been widely extended to $(-1, 0.5)$ by some materials or designed structures. For instance, auxetic materials have a Poisson's ratio close to -1 ; open cell foams constructed with re-entrant cells show negative Poisson's ratios; cork has a Poisson's ratio close to 0 and polymer or rubber possesses a Poisson's ratio close to 0.5 [270, 271].

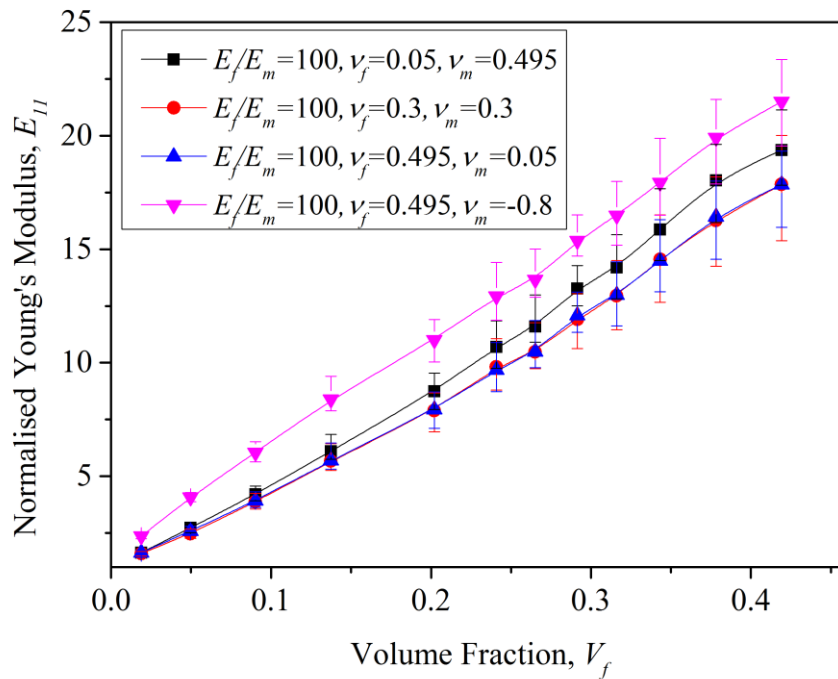
In order to explore the influence of Poisson's ratio alone on the elastic properties of the composites, the ratio of E_f and E_m is kept constant (e.g. the value of 100 is applied to E_f/E_m here) while a combination of different Poisson's ratios, either positive or negative, is adopted (i.e. $v_f = 0.05$ & $v_m = 0.495$, $v_f = 0.3$ & $v_m = 0.3$, $v_f = 0.495$ & $v_m = 0.05$ and $v_f = 0.495$ & $v_m = -0.8$). The effect of Poisson's ratio on the relationships between E_{11} , v_{12} , E_{33} , v_{31} and G_{31} , respectively, and volume fraction are shown in Figure 4.5(a)-(e), where E_{11} , E_{33} and G_{31} are normalised by E_m .

For the in-plane Young's modulus E_{11} , the proportional increasing tendency seems not to be affected by the selection of different Poisson's ratios. Specifically, there is no difference for the situations $v_f = 0.3$ & $v_m = 0.3$ and $v_f = 0.495$ & $v_m = 0.05$ whereas the situation when $v_f = 0.05$ & $v_m = 0.495$ shows a slightly higher value than the former two situations. However, we have also noticed that a selection of negative Poisson's ratio (down triangle dot curve) can remarkably increase the in-plane Young's modulus compared to those with positive Poisson's ratios. This inspires us of a method to enhance the elastic modulus during the material design. As for the out-of-plane Young's modulus E_{33} , positive Poisson's ratios can also dramatically affect it, let alone negative Poisson's ratios. We can see from Figure 4.5(c) that E_{33} with the case of $v_f = 0.05$ & $v_m = 0.495$ indicates a smaller value than that of $v_f = 0.495$ & $v_m = -0.8$ when the volume fraction is less than around 10% and then surpasses and increases faster than it as the volume fraction keeps arising. Still, the situations when $v_f = 0.3$ & $v_m = 0.3$ and $v_f = 0.495$ & $v_m = 0.05$ demonstrate almost identical results in E_{33} .

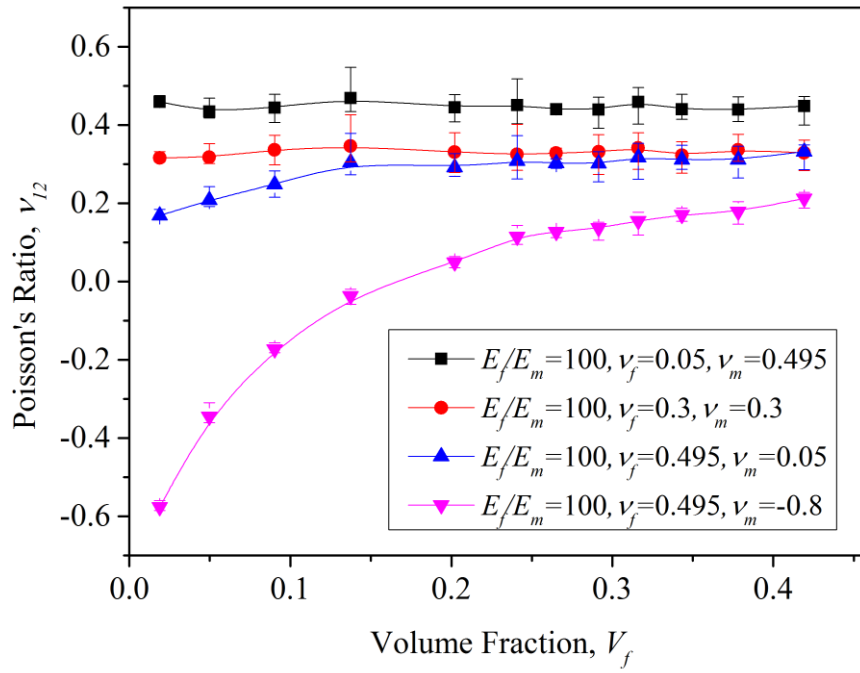
When the in-plane and out-of-plane Poisson's ratios (v_{12} and v_{31}) of the composites

are compared, we can see that both are affected by different combinations of fibres and matrix Poisson's ratios. However, ν_{12} shows a smaller variety (0.2-0.5) than ν_{31} (0-0.5) for the cases of positive fibres and matrix Poisson's ratios. For the scenario of composites with negative matrix Poisson's ratio, ν_{12} varies from -0.6 to 0.2 while ν_{31} ranges from -0.6 to 0 . Therefore, we can design the geometry with the expected effective in-plane and out-of-plane Poisson's ratios varying from negative to positive. It is also noticed that the out-of-plane shear modulus G_{31} does not change significantly as the Poisson's ratio varies in positive ranges whereas negative Poisson's ratios drastically improve G_{31} .

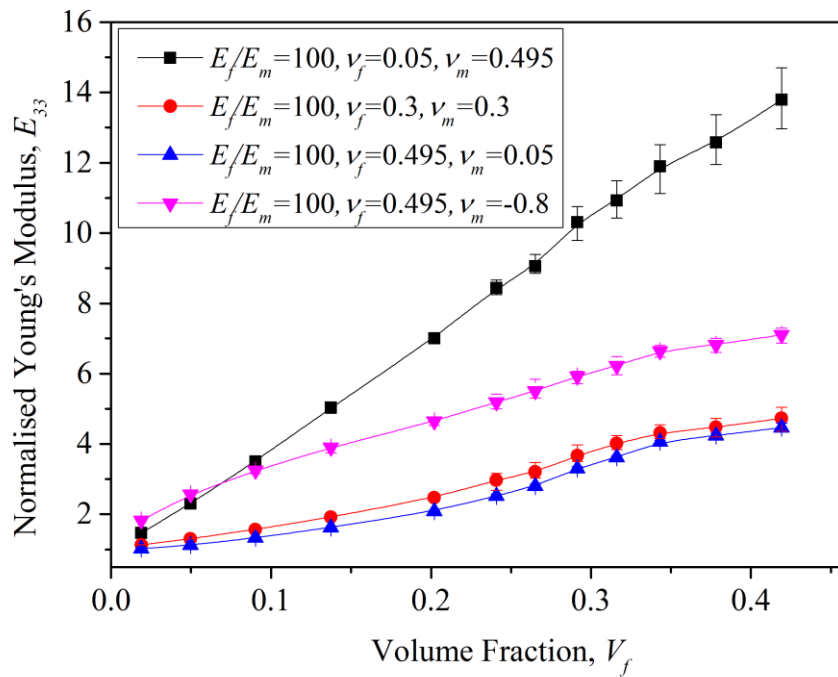
In conclusion, we can either select the certain materials for their inherent properties or adopt the hierarchical foams to obtain the designated Young's moduli and certain Poisson's ratios of fibres and matrix ranging from -1 to 0.5 . Thus a two-phase composite with desired elastic properties can be achieved on demand.



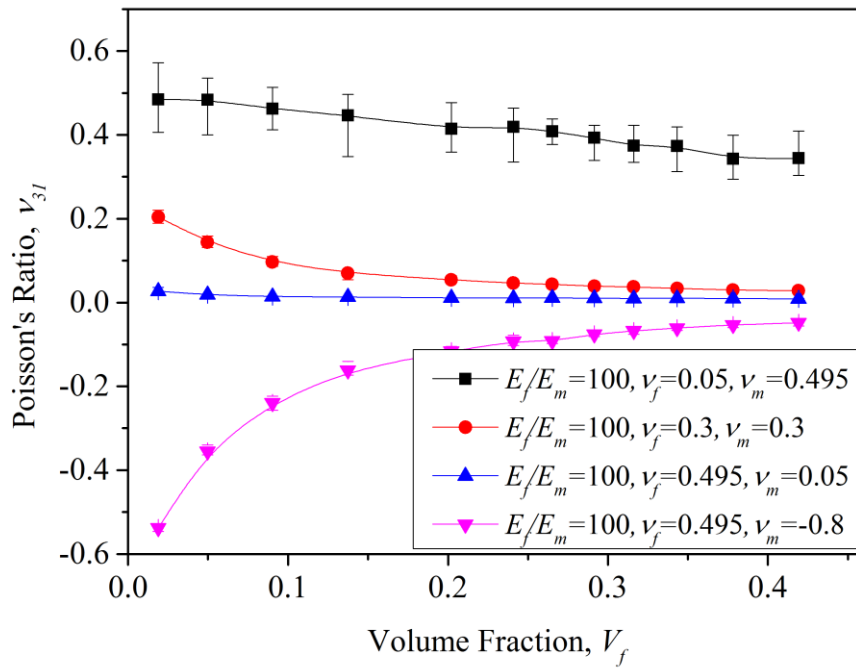
(a)



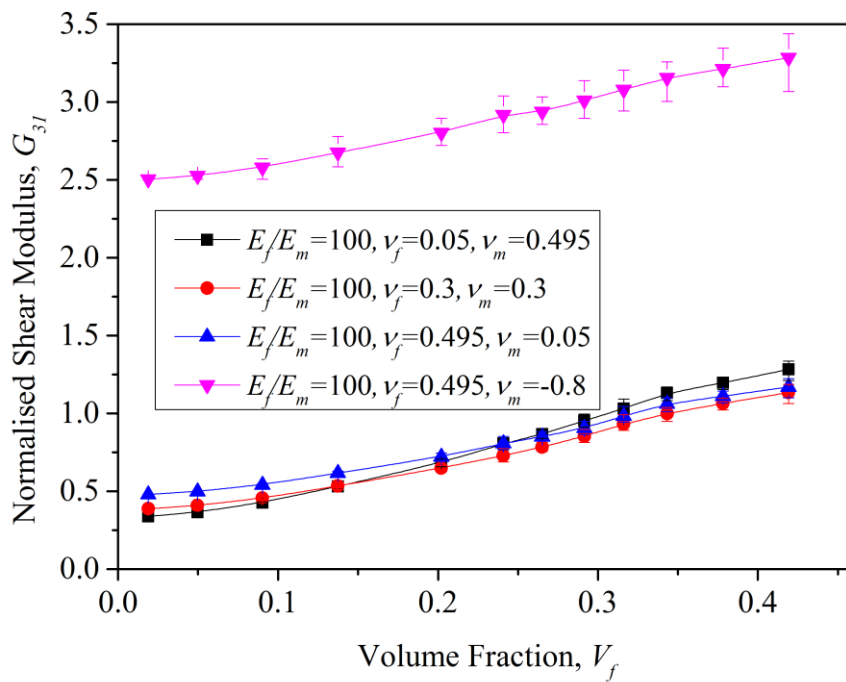
(b)



(c)



(d)



(e)

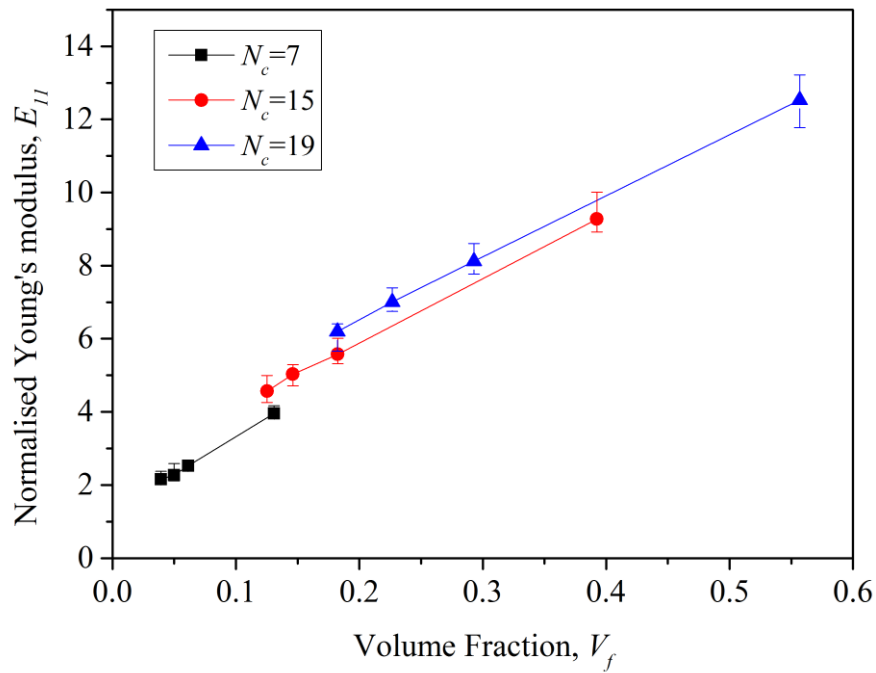
Figure 4.5. Dependence of elastic properties (a) E_{11} , (b) ν_{12} , (c) E_{33} , (d) ν_{31} and (e) G_{31} on the volume fraction under different Poisson's ratios.

4.4.4 The Effect of Aspect Ratio on the Elastic Properties

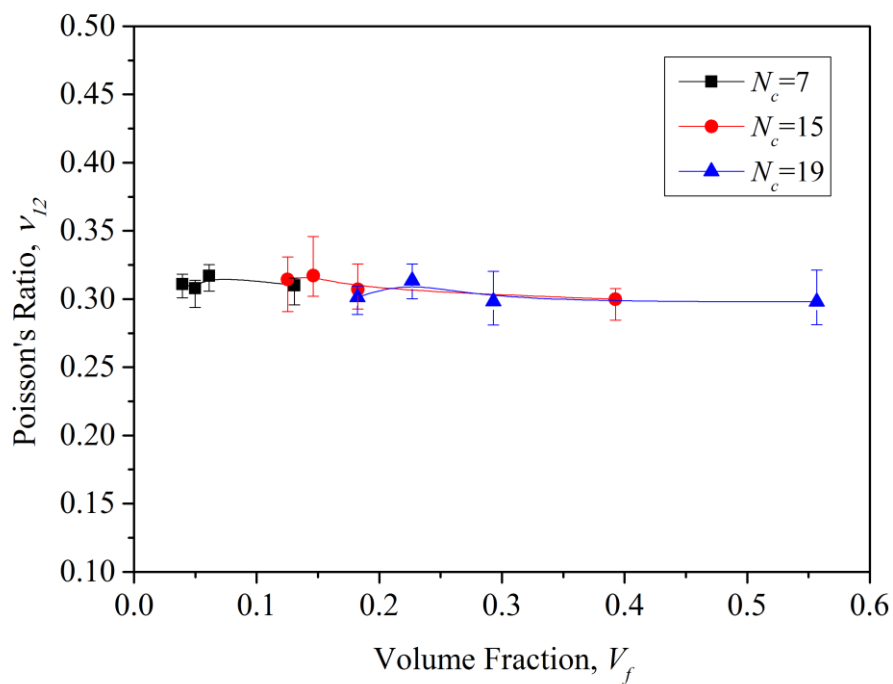
Aspect ratio is one of the key parameters for RVE models. It is dependent on dimensions (length L and diameter d) of fibres which can alter the volume fraction, thus influencing the elastic properties of the RVE models. Therefore, it is necessary to study the effect of aspect ratio on elastic properties. Elastic results of the RVEs with different aspect ratios ($L/d = 40, 80, 100, 125$) will be compared to figure out the effect of aspect ratio on elastic properties of the structure.

To obtain geometries with fibre aspect ratios of 40, 80, 100 and 125, the average length of fibres is set as constant 100 which is the same size as the width of an RVE here. Therefore, the fibres' aspect ratio is changed to be 40, 80, 100 and 125, respectively by adjusting the diameter of the fibres. In Figure 4.6, the curves for the dependence of the five independent constants on fibre aspect ratios under three different cross-linker densities ($N_c = 7, 15, 19$) are obtained for comparison. In addition, the value of E_f/E_m is fixed as 100 and the Poisson's ratios of the fibre and the matrix are set the same as 0.3. All the elastic and shear moduli are normalised by E_m . From Figure 4.6 (a) and (b), we can see that both E_{11} and E_{33} increase as the volume fraction increases. According to the relationship between volume fraction and aspect ratio, which is specifically, volume fraction decreases as aspect ratio increases, we can therefore relate elastic/shear moduli with volume fraction as that elastic/shear moduli decrease as aspect ratio increases. This result is consistent with the trend of in-plane Young's modulus from FEA and laminate analogy approach (LAA) in [2]. Furthermore, E_{11} and E_{33} show the same tendency, specifically, growing linearly as aspect ratio decreasing independent of cross-linker density. This linear growth indicates that the aspect ratio does not affect the change of stiffness.

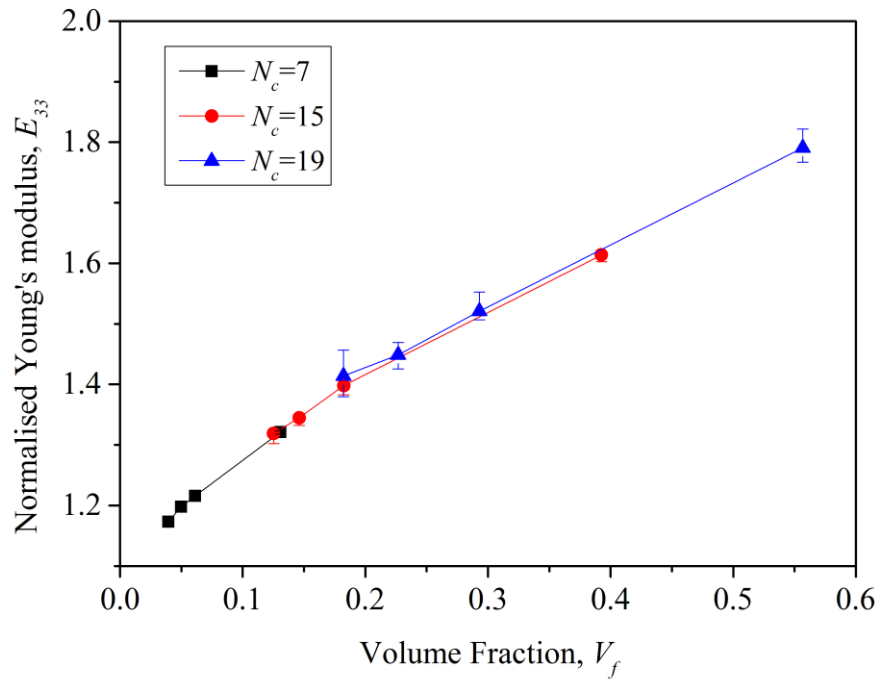
The similar situation also happens to G_{31} yet it decreases as the aspect ratio decreases. ν_{12} fluctuates around 0.32 which is consistent with the results by Markaki and Clyne [268, 269]. In addition, the rise of aspect ratio can cause the increase of ν_{31} .



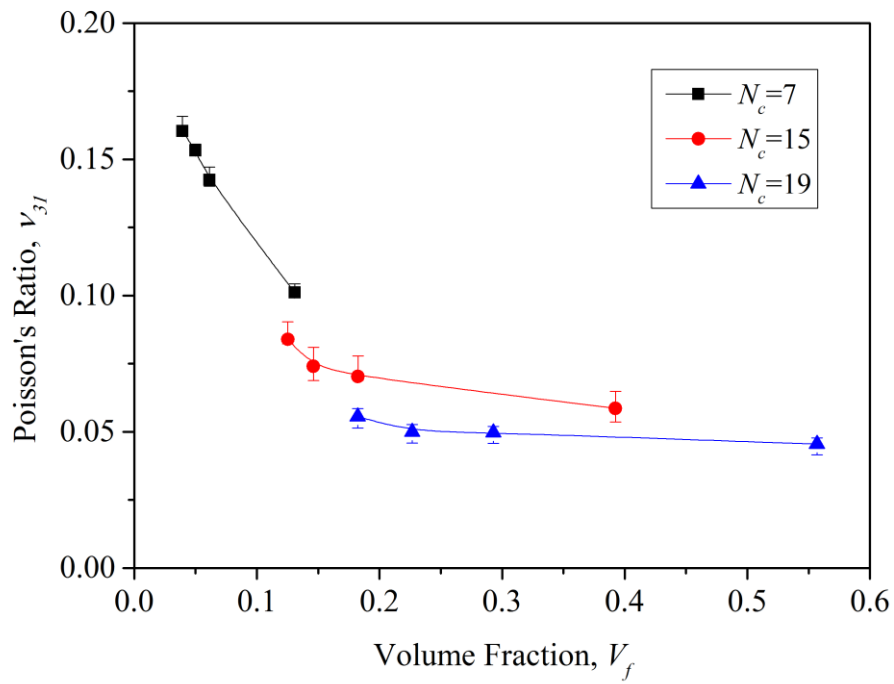
(a)



(b)



(c)



(d)

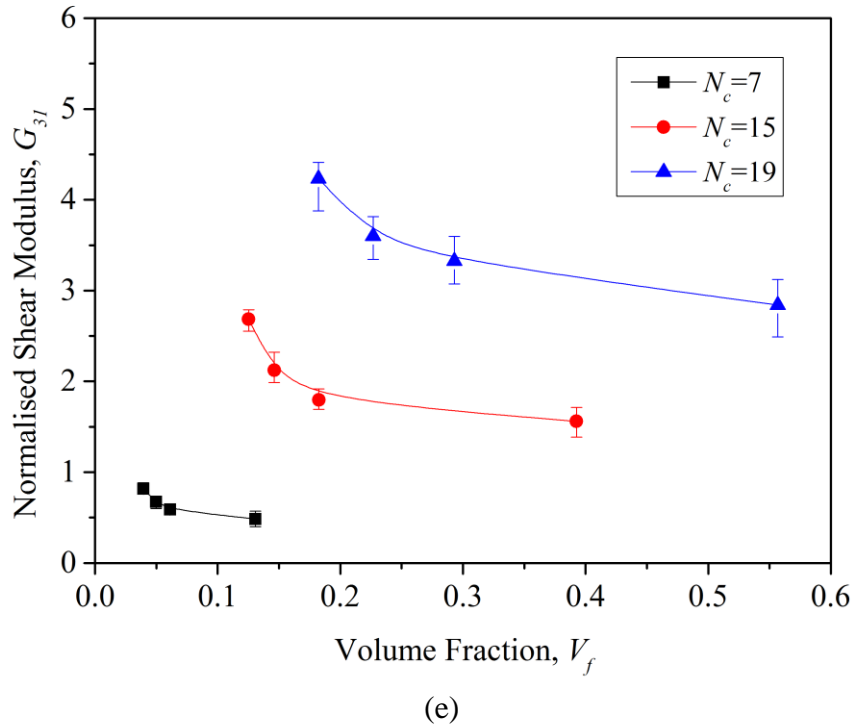
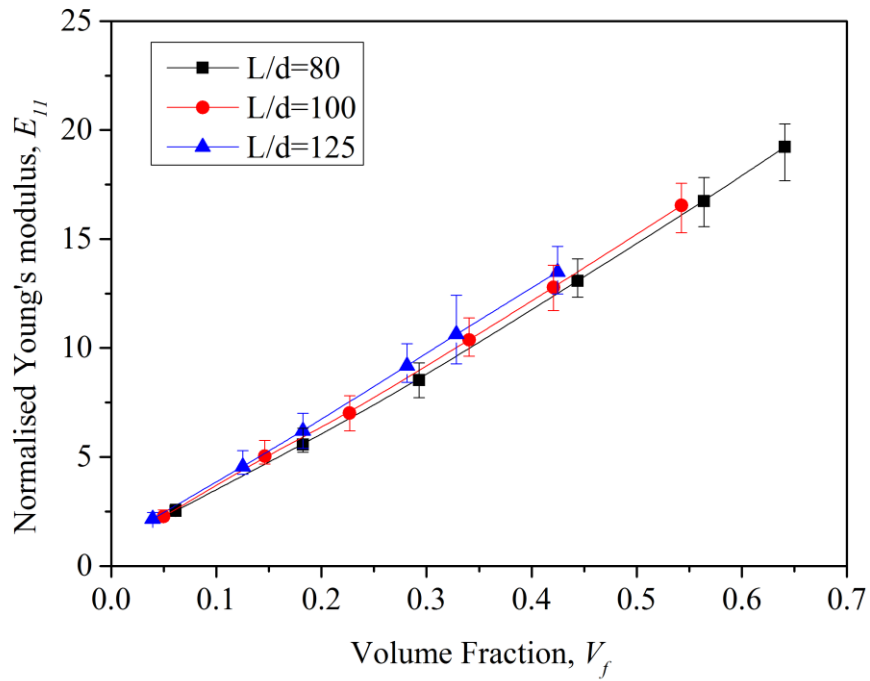


Figure 4.6. The effect of aspect ratio ($L/d = 40, 80, 100, 125$) on the relationship between elastic properties (a) E_{11} , (b) ν_{12} , (c) E_{33} , (d) ν_{31} and (e) G_{31} and volume fraction.

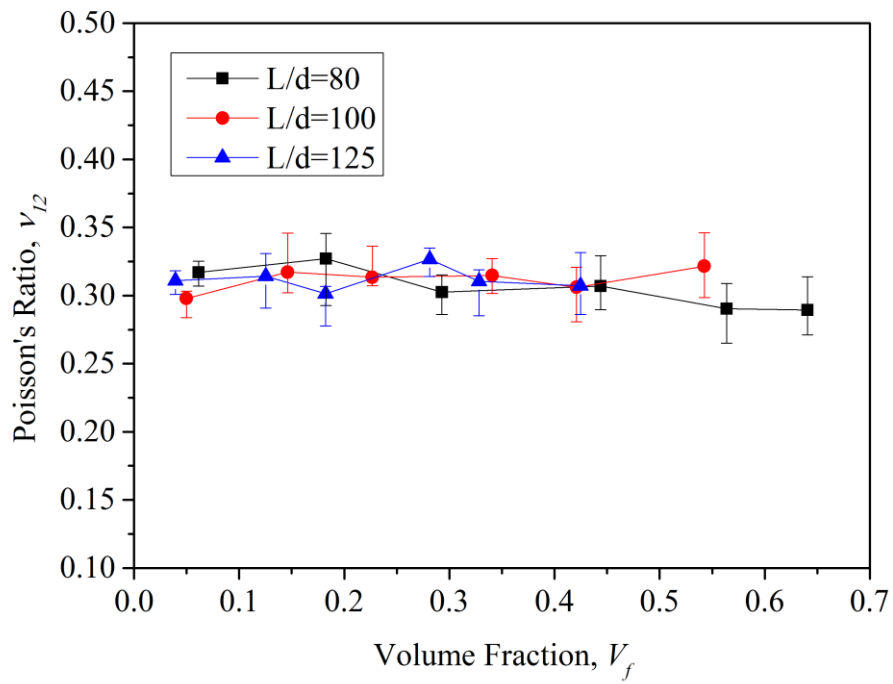
4.4.5 The Effect of Cross-linker Density on the Elastic Properties

Cross-linker density is the dominant parameter in determining the fibre volume fraction of the composites. As described in the section of construction of the geometry, volume fractions within a wide range can be obtained by changing the cross-linker density. In order to study the effect of cross-linker density on the elastic properties, RVEs with different volume fractions have been generated by changing the cross-linker density ($N_c = 7, 15, 19, 23, 25, 27$) while fixing the aspect ratio as 80, 100 or 125. The results of the five constants against the volume fraction have been

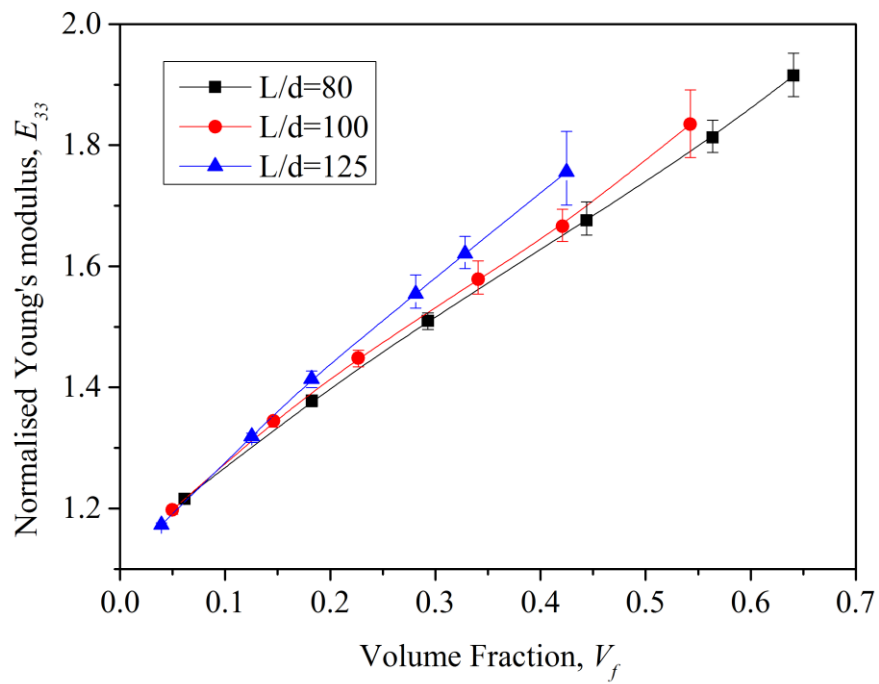
presented in Figure 4.7 where the value of E_f/E_m is fixed as 100 and the Poisson's ratios of fibres and matrix are set the same as 0.3. We can see that E_{11} indicates a linear relationship with volume fraction as we increase the cross-linker density. Furthermore, the curves of E_{11} under different aspect ratios nearly coincide, demonstrating that aspect ratio does not affect the trend of E_{11} . This result is also consistent with that in section 4.4.4. E_{33} grows faster when the volume fraction is small and then slows down to show a linear relationship with volume fraction as we increase the cross-linker density. G_{31} shows an exponential increase as volume fraction increases. Still, ν_{12} fluctuates around 0.3 without being influenced by the change of cross-linker density. In addition, ν_{31} drops dramatically to close to 0.



(a)



(b)



(c)

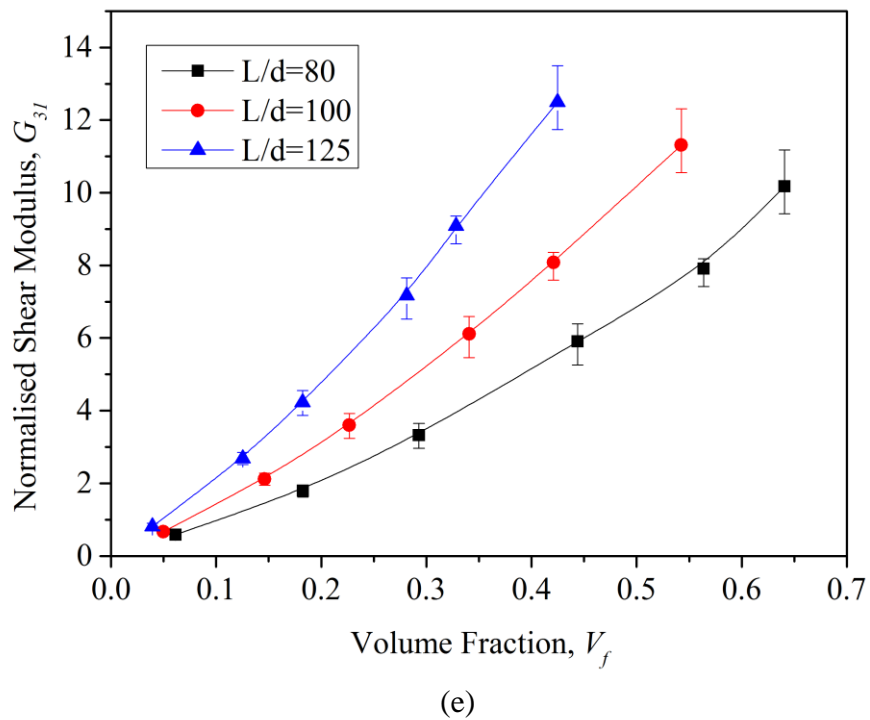
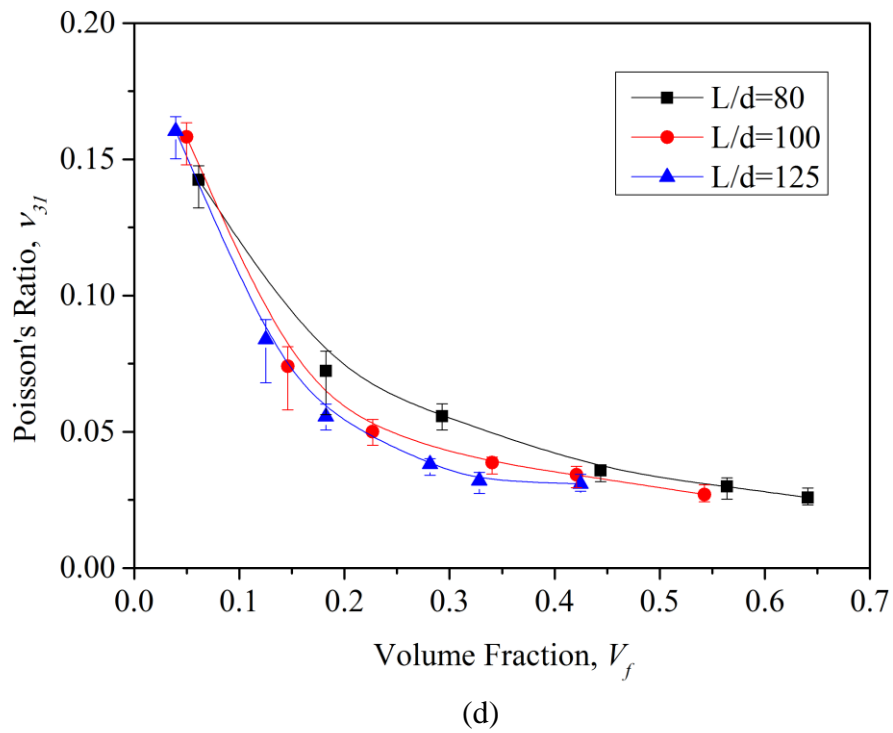


Figure 4.7. The effect of cross-linker density ($N_c = 7, 15, 19, 23, 25, 27$) on the relationship between elastic properties (a) E_{11} , (b) ν_{12} , (c) E_{33} , (d) ν_{31} and (e) G_{31} and volume fraction.

4.4.6 Discussions

In order to demonstrate the superior elastic properties of this new type of 3D transversely isotropic fibre-network reinforced composite, we compared their in-plane and out-of-plane Young's moduli with the experimental [16, 40, 272-274] and numerical [2, 3, 275-277] results of other conventional fibre or particle composites (see Table 4.7 and Figure 4.8). When compared to the simulation results of two transversely isotropic fibre composites without any intersections among the fibres, one with inclined randomly distributed short straight fibres [3] and the other with curved planar randomly distributed short fibres [275], both the in-plane and out-of-plane stiffnesses of our proposed composites indicate significantly greater values. Further comparison with the cross-ply composites [40] has been conducted and our proposed composite still demonstrates superior in-plane stiffness to the later. In addition, the new type of fibre-network composite demonstrates much larger in-plane stiffness than particle composites (Glass/epoxy [273] and Particle/matrix [276]). These results verified the expectation of the elastic properties of this novel structure, that is, with the intersections among fibres, the network can greatly enhance the stiffness of the composite.

Table 4.7. Stiffness comparison between this research and others' experimental and numerical results.

Composites	$V_f(\%)$	E_f (GPa)	E_m (GPa)	ν_f	ν_m	Stiffness E_{11} (GPa)	Stiffness E_{33} (GPa)
Cross-ply [40]	43	193	0.7	0.3	0.3	29	-
This research	41.9	193	0.7	0.3	0.3	33.36	-
Short fibre [3]	13.5	70	3	0.2	0.35	6.8656	5.7658

This research	13.7	70	3	0.2	0.35	10.2261	7.1698
Short curved fibre [275]	35.1	70	3	0.2	0.35	14.47	9.49
This research	34.3	70	3	0.2	0.35	17.15	12.31
Glass/epoxy [273]	31	69	3	0.15	0.35	5.3	-
This research	32	69	3	0.15	0.35	10.3765	-
Particle/matrix [276]	20	450	70	0.17	0.3	96	-
This research	20.2	450	70	0.17	0.3	105.4307	-

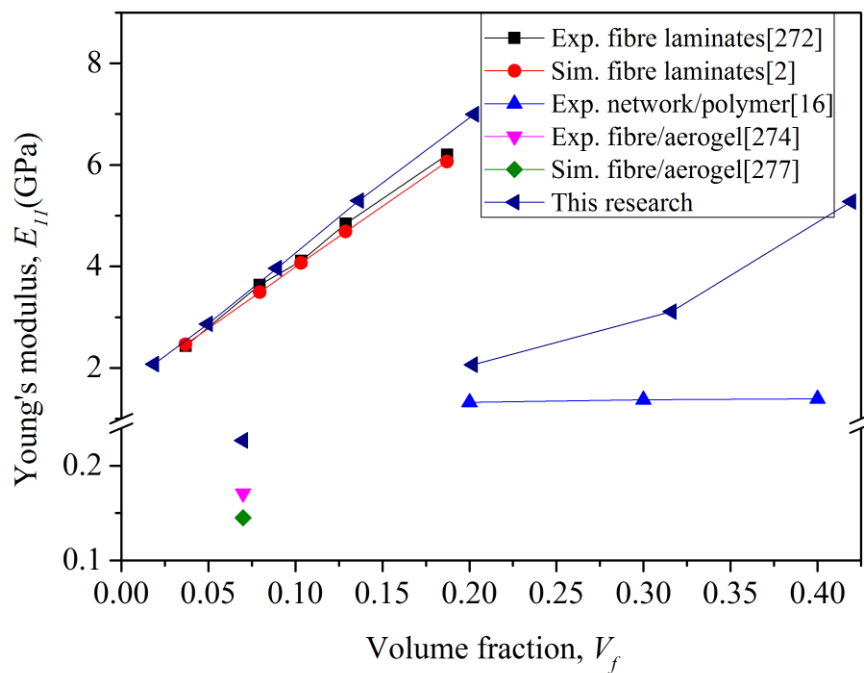


Figure 4.8. Comparison of several results of Young's modulus E_{11} in terms of volume fraction.

The in-plane Young's modulus of our proposed composite is also compared with both the experimental results [272] and the FEA results [2] where all the fibres in the composites are randomly distributed in parallel to the transverse plane (i.e. the x - y

plane). By applying the same materials properties ($E_f=75\text{GPa}$, $E_m=1.6\text{GPa}$, $\nu_f=0.25$ and $\nu_m=0.35$) as given in [2], the relationship between E_{11} and the fibre volume fraction of our proposed composite has been obtained and demonstrated in Figure 4.8 together with the experimental results [272] and the FEA results [2] for comparison. All the results have demonstrated an approximately proportional tendency, which is consistent with the numerical results of E_{11} as shown in Figure 4.3(a). As can be seen in Figure 4.8, the values of the in-plane Young's modulus of the novel composite are larger than the experimental results [272] and the FEA results [2] under the same volume fraction. It should be noted that all fibres are straight and planar randomly distributed in the composites in [2] and [272] whereas the fibres are curved and the fibre segments are inclined out of the transverse plane in the proposed fibre network composites. Similarly, the transversely isotropic composite architecture studied in [274] (experimental study) and [277] (numerical analysis) is composed of fibres which are physically overlaid on each other [277] and intersections among fibres are ignored. The in-plane stiffness of our proposed composite also exhibits a larger value than both experimental and numerical results. In addition, the proposed composite has also been compared with the similar composite reinforced by a fibre network mat [16]. As shown in Figure 4.8, the proposed fibre network composite still illustrates larger stiffnesses. This is possibly due to the difference in in-plane curvatures of fibres, which are straight in the proposed model and curved in [16]. This is consistent with a conclusion drawn in [277] that the Young's modulus decreases as the fibre curvature increases. Besides, it should be noted that the in-plane stiffness tends to be under-estimated when the fibres are modelled as beam elements compared to the model with solid elements as discussed in the Section 4.3.5. Therefore, the actual in-plane stiffness of the proposed model can be even larger than other composites

compared here.

To conclude, the reason why our composite structure has a larger stiffness can be attributed to the introduction of cross-linkers between the fibres in the composites. Furthermore, there is no doubt that the cross-linkers along the out-of-plane direction in the fibre network composites also render a superior out-of-plane stiffness to planar random fibre composites. Therefore, it is conjectured that both the in-plane and the out-of-plane stiffnesses of our new type of composite are superior to those of planar random fibre composites.

4.5 Analytical Model

4.5.1 Geometrical and Mechanical Model

Based on the simulation results of elastic properties we have obtained on this fibre network reinforced composites, we also aim to investigate the theoretical results for comparison. Since the fibres are randomly distributed, it increases the complexity and difficulty of deducing the theoretical expressions, not to mention the structures with two phases. Therefore, for simplification and similarity, a simplified scaffold alike model has been proposed for analysis as shown in Figure 4.9. The fibre network consists of several layers in the x - y plane, in which a certain number of parallel fibres are distributed in the x -direction and y direction alternately. Furthermore, the fibres in the adjacent layers will intersect to some extent which is determined by the overlap coefficient c . Also, the cross-section of each fibre is set as a square shape with an edge length of d for the sake of predigesting analysis and the error caused by the cross section difference is assumed to be neglectable when the fibres are slender (i.e.

the aspect ratio of a fibre is large enough). Therefore, the overlapping thickness between two fibres will be cd . For a geometry model with a fibre length of L and cross-linking density of N_c , the length of each fibre segment will be $N_c = L/l_c$. In this way, a regular fibre network with cross-linking has been generated and the volume fraction of fibres can be dominated by adjusting N_c and c changing accordingly ($c = 0.025(N_c + 1)$). Then the matrix fills in the gap of the fibre network in three dimensions to make it a complete composite structure. Although the simplified geometry model is not strictly transversely isotropic as fibres are along either the x direction or the y direction, the deformation mechanism under axial loading is still similar and can be referential to this type of fibre network reinforced composites, including the geometry model we proposed with stochastic fibres.

In order to illustrate the similarity of the regular fibre network reinforced composites (Figure 4.9) and the fibre network reinforced composites with stochastic fibres (Figure 3.6) in structures, the relationships between volume fraction and cross-linker density of both geometries have been compared in Figure 4.10. As already obtained in Section 4.3.4, the volume fraction of the fibre network reinforced composites with random fibres has indicated a three-degree polynomial relationship with the cross-linker density. We can also see from Figure 4.10 that the volume fraction of the simplified regular fibre network reinforced composites also demonstrates a similar trend as that of the fibre network reinforced composites with random fibres with cross-linker density increasing although there exists a big difference in the value of the volume fraction under the same cross-linker density which has been brought about due to the simplification of the model. This has provided a solid ground that the trend of the elastic properties under axial tension of the simplified geometry model can be worthy of reference for the novel geometry model we have proposed.

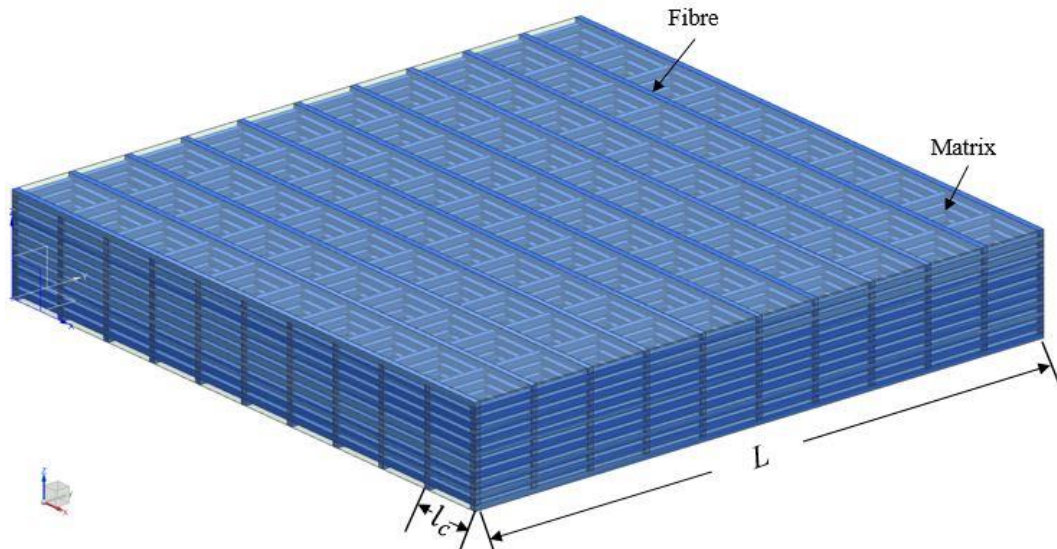


Figure 4.9. A simplified geometrical model of the fibre network reinforced composites with aligned fibres along x and y directions.

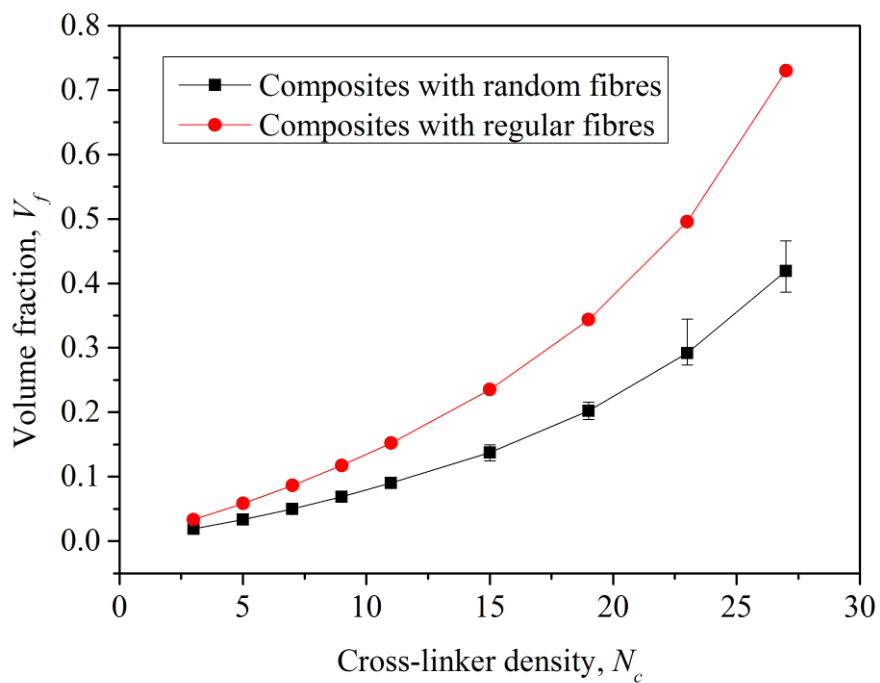


Figure 4.10. Comparison of the relationships between volume fraction and cross-linker density of the fibre network reinforced composites with random fibres (the square dot curve) and the simplified regular fibre network reinforced composites (the round dot curve).

Now that the simplified geometry model can represent the novel geometry model we

proposed, theoretical analysis based on the simplified model will be carried out in this part. Considering the periodicity of the simplified structure, a representative volume element (RVE) of it can be selected to simplify the analysis as shown in Figure 4.11. The dark blue blocks with square cross-section represent fibres and the rest light green blocks represent the matrix. Besides, due to the existing of overlap between adjacent fibres, which renders the cross-section of fibres more complex at the joints, the whole RVE has to be divided into a number of sub-cells (exactly, 20 sub-cells in total) as indicated with dash lines in Figure 4.11.

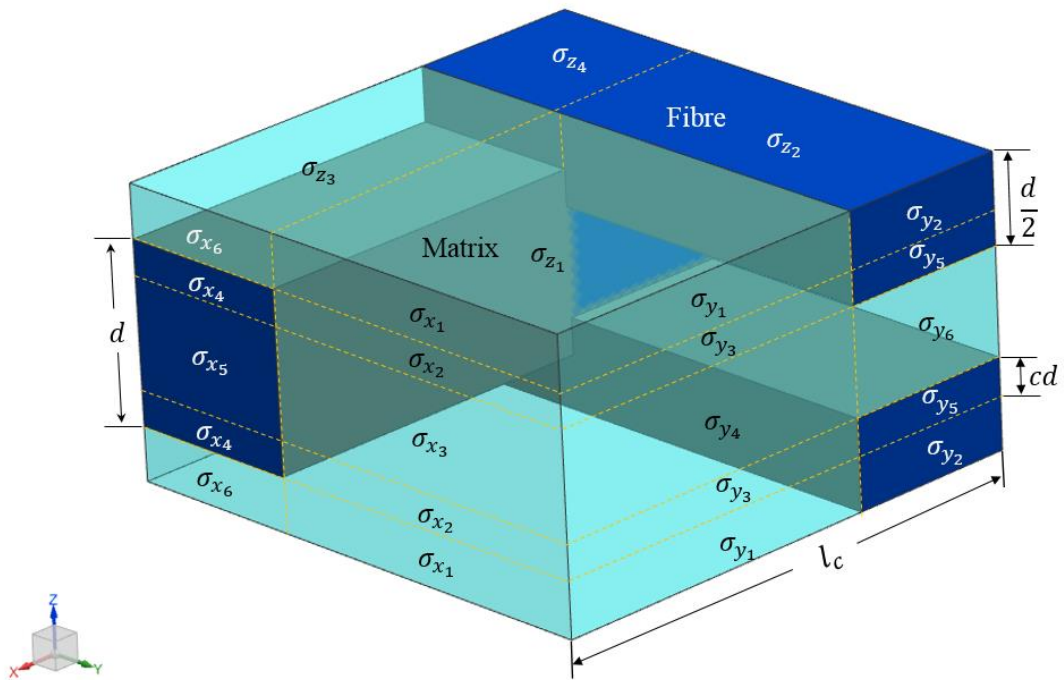


Figure 4.11. A representative volume element (RVE) of the simplified geometrical model of the fibre network composite.

The interfaces between fibres and matrix are assumed to be perfectly bonded and we only consider the normal stresses within the 20 sub-cells and the compatibility conditions on the outer surfaces while ignoring the shear stresses and the compatibility conditions on the interfaces of the cuboids [270]. Thus when an axial

load is applied, only the three normal stresses on the surface of each cuboid will be taken into account and the three normal stresses inside of each cuboid are assumed to be constants. In addition, the RVE is also symmetrical in the z -direction. Therefore there will be 6 different normal stresses (i.e. σ_{x_1} , σ_{x_2} , σ_{x_3} , σ_{x_4} , σ_{x_5} and σ_{x_6}) in the x -direction, 6 different normal stresses (i.e. σ_{y_1} , σ_{y_2} , σ_{y_3} , σ_{y_4} , σ_{y_5} and σ_{y_6}) in the y -direction and 4 different normal stresses (i.e. σ_{z_1} , σ_{z_2} , σ_{z_3} and σ_{z_4}) in the z -direction as labelled in Figure 4.11 when an axial force/displacement is loaded, either in the x -direction or in the z -direction. Furthermore, periodic boundary conditions are applied to the RVE. In the elastic study, the normal stress-strain relations for the cuboids in series can be expressed as follows (Eq. (4.7)~(4.22)) according to Hook's law:

1) Normal stress-strain relations in the x -direction:

$$\frac{(l_c - d)}{l_c E_m} (\sigma_{x_1} - \nu_m \sigma_{y_1} - \nu_m \sigma_{z_1}) + \frac{d}{l_c E_f} (\sigma_{x_1} - \nu_f \sigma_{y_2} - \nu_f \sigma_{z_2}) = \varepsilon_x \quad (4.7)$$

$$\frac{(l_c - d)}{l_c E_m} (\sigma_{x_2} - \nu_m \sigma_{y_3} - \nu_m \sigma_{z_1}) + \frac{d}{l_c E_f} (\sigma_{x_2} - \nu_f \sigma_{y_5} - \nu_f \sigma_{z_2}) = \varepsilon_x \quad (4.8)$$

$$\frac{(l_c - d)}{l_c E_m} (\sigma_{x_3} - \nu_m \sigma_{y_4} - \nu_m \sigma_{z_1}) + \frac{d}{l_c E_m} (\sigma_{x_3} - \nu_m \sigma_{y_6} - \nu_m \sigma_{z_2}) = \varepsilon_x \quad (4.9)$$

$$\frac{(l_c - d)}{l_c E_f} (\sigma_{x_4} - \nu_f \sigma_{y_3} - \nu_f \sigma_{z_3}) + \frac{d}{l_c E_f} (\sigma_{x_4} - \nu_f \sigma_{y_5} - \nu_f \sigma_{z_4}) = \varepsilon_x \quad (4.10)$$

$$\frac{(l_c - d)}{l_c E_f} (\sigma_{x_5} - \nu_f \sigma_{y_4} - \nu_f \sigma_{z_3}) + \frac{d}{l_c E_f} (\sigma_{x_5} - \nu_f \sigma_{y_6} - \nu_f \sigma_{z_4}) = \varepsilon_x \quad (4.11)$$

$$\frac{(l_c - d)}{l_c E_m} (\sigma_{x_6} - \nu_m \sigma_{y_1} - \nu_m \sigma_{z_3}) + \frac{d}{l_c E_f} (\sigma_{x_6} - \nu_f \sigma_{y_2} - \nu_f \sigma_{z_4}) = \varepsilon_x \quad (4.12)$$

2) Normal stress-strain relations in the y -direction:

$$\frac{(l_c - d)}{l_c E_m} (\sigma_{y_1} - \nu_m \sigma_{x_1} - \nu_m \sigma_{z_1}) + \frac{d}{l_c E_m} (\sigma_{y_1} - \nu_m \sigma_{x_6} - \nu_m \sigma_{z_3}) = \varepsilon_y \quad (4.13)$$

$$\frac{(l_c - d)}{l_c E_f} (\sigma_{y_2} - \nu_f \sigma_{x_1} - \nu_f \sigma_{z_2}) + \frac{d}{l_c E_f} (\sigma_{y_2} - \nu_f \sigma_{x_6} - \nu_f \sigma_{z_4}) = \varepsilon_y \quad (4.14)$$

$$\frac{(l_c - d)}{l_c E_m} (\sigma_{y_3} - v_m \sigma_{x_1} - v_m \sigma_{z_1}) + \frac{d}{l_c E_f} (\sigma_{y_3} - v_f \sigma_{x_4} - v_f \sigma_{z_3}) = \varepsilon_y \quad (4.15)$$

$$\frac{(l_c - d)}{l_c E_m} (\sigma_{y_4} - v_m \sigma_{x_3} - v_m \sigma_{z_1}) + \frac{d}{l_c E_f} (\sigma_{y_4} - v_f \sigma_{x_5} - v_f \sigma_{z_3}) = \varepsilon_y \quad (4.16)$$

$$\frac{(l_c - d)}{l_c E_f} (\sigma_{y_5} - v_f \sigma_{x_2} - v_f \sigma_{z_2}) + \frac{d}{l_c E_f} (\sigma_{y_5} - v_f \sigma_{x_4} - v_f \sigma_{z_4}) = \varepsilon_y \quad (4.17)$$

$$\frac{(l_c - d)}{l_c E_m} (\sigma_{y_6} - v_m \sigma_{x_3} - v_m \sigma_{z_2}) + \frac{d}{l_c E_f} (\sigma_{y_6} - v_f \sigma_{x_5} - v_f \sigma_{z_4}) = \varepsilon_y \quad (4.18)$$

3) Normal stress-strain relations in the z -direction:

$$\begin{aligned} & \frac{1}{E_m} \{ 2d(1-c)\sigma_{z_1} - (d-2cd)v_m\sigma_{x_1} - 2cdv_m\sigma_{x_2} - (d-2cd)v_m\sigma_{x_3} \\ & - (d-2cd)v_m\sigma_{y_1} - 2cdv_m\sigma_{y_3} - (d-2cd)v_m\sigma_{y_4} \} = 2d(1-c)\varepsilon_z \end{aligned} \quad (4.19)$$

$$\begin{aligned} & \left(\frac{d}{E_f} + \frac{d-2cd}{E_m} \right) \sigma_{z_2} - (d-2cd) \frac{v_f \sigma_{x_1}}{E_f} - 2cd \frac{v_f \sigma_{x_2}}{E_f} - (d-2cd) \frac{v_m \sigma_{x_3}}{E_m} \\ & - (d-2cd) \frac{v_f \sigma_{y_2}}{E_f} - 2cd \frac{v_f \sigma_{y_5}}{E_f} - (d-2cd) \frac{v_m \sigma_{y_6}}{E_m} = 2d(1-c)\varepsilon_z \end{aligned} \quad (4.20)$$

$$\begin{aligned} & \left(\frac{d}{E_f} + \frac{d-2cd}{E_m} \right) \sigma_{z_3} - 2cd \frac{v_f \sigma_{x_4}}{E_f} - (d-2cd) \frac{v_f \sigma_{x_5}}{E_f} - (d-2cd) \frac{v_m \sigma_{x_6}}{E_m} \\ & - (d-2cd) \frac{v_m \sigma_{y_1}}{E_m} - 2cd \frac{v_f \sigma_{y_3}}{E_f} - (d-2cd) \frac{v_f \sigma_{y_4}}{E_f} = 2d(1-c)\varepsilon_z \end{aligned} \quad (4.21)$$

$$\begin{aligned} & \frac{1}{2d(1-c)E_f} \{ 2d(1-c)\sigma_{z_4} - 2cdv_f\sigma_{x_4} - (d-2cd)v_f\sigma_{x_5} - (d-2cd) \\ & v_f\sigma_{x_6} - (d-2cd)v_f\sigma_{y_2} - 2cdv_f\sigma_{y_5} - (d-2cd)v_f\sigma_{y_6} \} = \varepsilon_z \end{aligned} \quad (4.22)$$

4.5.2 The Relationship between Young's Modulus in the x -direction and Volume Fraction

In the case of strain loading in the x -direction, which means ε_x is given, the rest 18 unknown normal stresses and strains need to be solved according to Eq. (4.7)-(4.22)

In addition, since periodic boundary conditions are applied to the RVE, there will be

zero total force in the y and z directions. Thus, the normal stresses in the y and z directions, respectively, meets

$$(l_c - d)(d - 2cd)\sigma_{y_1} + d(d - 2cd)\sigma_{y_2} + 2cd(l_c - d)\sigma_{y_3} \\ + (l_c - d)(d - 2cd)\sigma_{y_4} + 2cd^2\sigma_{y_5} + d(d - 2cd)\sigma_{y_6} = 0 \quad (4.23)$$

$$(l_c - d)^2\sigma_{z_1} + d(l_c - d)\sigma_{z_2} + d(l_c - d)\sigma_{z_3} + d^2\sigma_{z_4} = 0 \quad (4.24)$$

Thereby, the 18 unknown normal stresses and strains can be determined by combining Eq. (4.7)-(4.22), (4.23) and (4.24). Accordingly, Young's modulus in the x -direction can be worked out through

$$E_x = \frac{\sigma_x}{\varepsilon_x} \\ = \frac{(l_c - d)(d - 2cd)\sigma_{x_1} + 2cd(l_c - d)\sigma_{x_2} + (l_c - d)(d - 2cd)\sigma_{x_3}}{2dl_c(1 - c)\varepsilon_x} \\ + \frac{2cd^2\sigma_{x_4} + d(d - 2cd)\sigma_{x_5} + d(d - 2cd)\sigma_{x_6}}{2dl_c(1 - c)\varepsilon_x} \quad (4.25)$$

With the same group of parameters as Section 4.4.1, where $d = 1$, $E_f/E_m = 100$ and $\nu_f = \nu_m = 0.3$, applied to the simplified geometry model, the Young's modulus in the x direction in terms of volume fraction (ranging from 0 to 0.35) can be obtained as shown in Figure 4.12, where the effective Young's modulus is normalised by E_m . The Young's modulus has indicated a linear relation with the volume fraction. The trend is identical to the numerical results obtained from our designed geometric model with random fibres, which is the round dotted curve illustrated in Figure 4.12.

4.5.3 The Relationship between Young's Modulus in the z -direction and Volume Fraction

Similar to the case of loading in the x -direction, ε_z will be given when a strain load

is applied in the z direction. Then the rest 18 unknown normal stresses and strains need to be solved according to Eq. (4.7)-(4.22). In addition, there will be zero total force in the x and y directions, which respectively requires

$$(l_c - d)(d - 2cd)\sigma_{x_1} + 2cd(l_c - d)\sigma_{x_2} + (l_c - d)(d - 2cd)\sigma_{x_3} + 2cd^2\sigma_{x_4} + d(d - 2cd)\sigma_{x_5} + d(d - 2cd)\sigma_{x_6} = 0 \quad (4.26)$$

$$(l_c - d)(d - 2cd)\sigma_{y_1} + d(d - 2cd)\sigma_{y_2} + 2cd(l_c - d)\sigma_{y_3} + (l_c - d)(d - 2cd)\sigma_{y_4} + 2cd^2\sigma_{y_5} + d(d - 2cd)\sigma_{y_6} = 0 \quad (4.27)$$

Thereby, the 18 unknown normal stresses and strains can be determined by combining Eq. (4.7)-(4.22), (4.26) and (4.27). Accordingly, Young's modulus in the z -direction can be worked out through

$$E_z = \frac{\sigma_z}{\varepsilon_z} = \frac{(l_c - d)^2\sigma_{z_1} + d(l_c - d)\sigma_{z_2} + d(l_c - d)\sigma_{z_3} + d^2\sigma_{z_4}}{l_c^2\varepsilon_z} \quad (4.28)$$

The same group of parameters as Section 4.4.1, where $d = 1$, $E_f/E_m = 100$ and $\nu_f = \nu_m = 0.3$, have been applied to the simplified geometry model and the Young's modulus in the z direction in terms of volume fraction (ranging from 0 to 0.3) has been obtained as shown in Figure 4.13, where the effective Young's modulus is normalised by E_m . The Young's modulus has indicated a polynomial relation with the volume fraction. Comparing the analytical results (round dotted curve) with the numerical results of E_{33} in terms of the volume fraction in Figure 4.13 when the volume fraction is less than 0.3, both results demonstrate a similar tendency.

In conclusion, the dependence of Young's moduli in the x and z directions separately on volume fraction has highlighted the preponderance of this designed geometry. Specifically, the in-plane stiffness can be improved proportionally, in the meanwhile, the out-of-plane stiffness can be dramatically strengthened by increasing the volume fraction in the way of increasing the cross-linker density N_c and overlap coefficient

c accordingly.

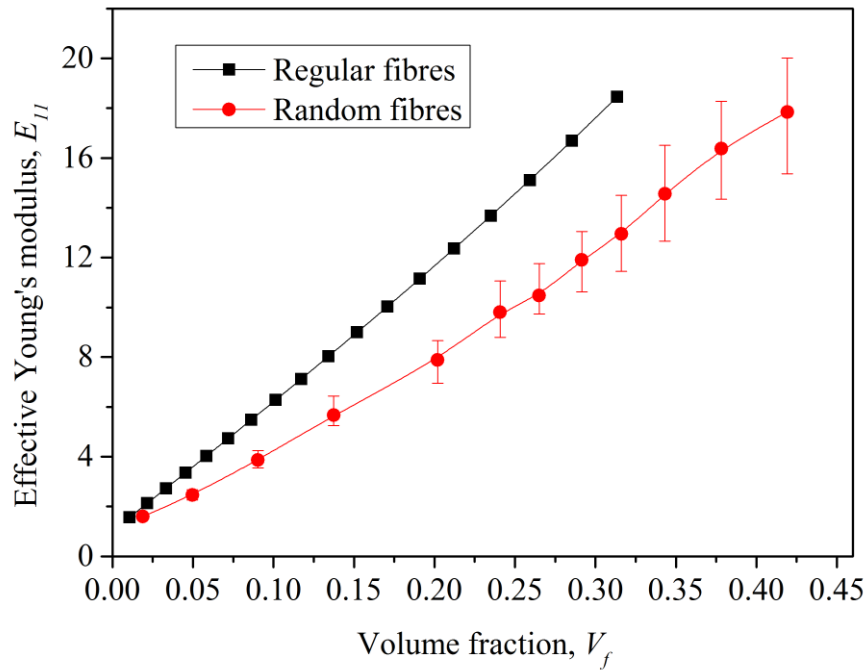


Figure 4.12. The relationship between Young's modulus in the x -direction and volume fraction of the simplified analytical model.

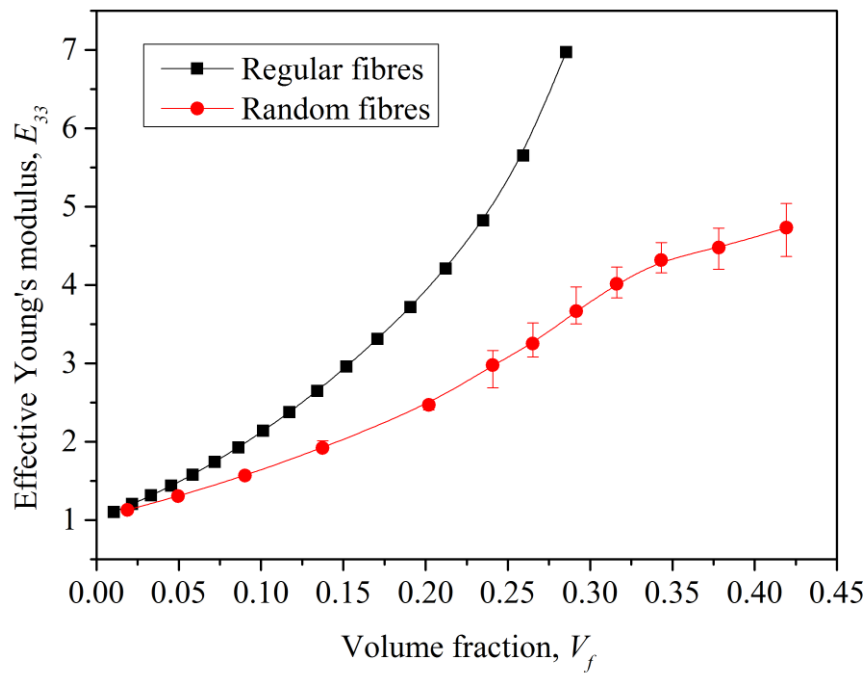
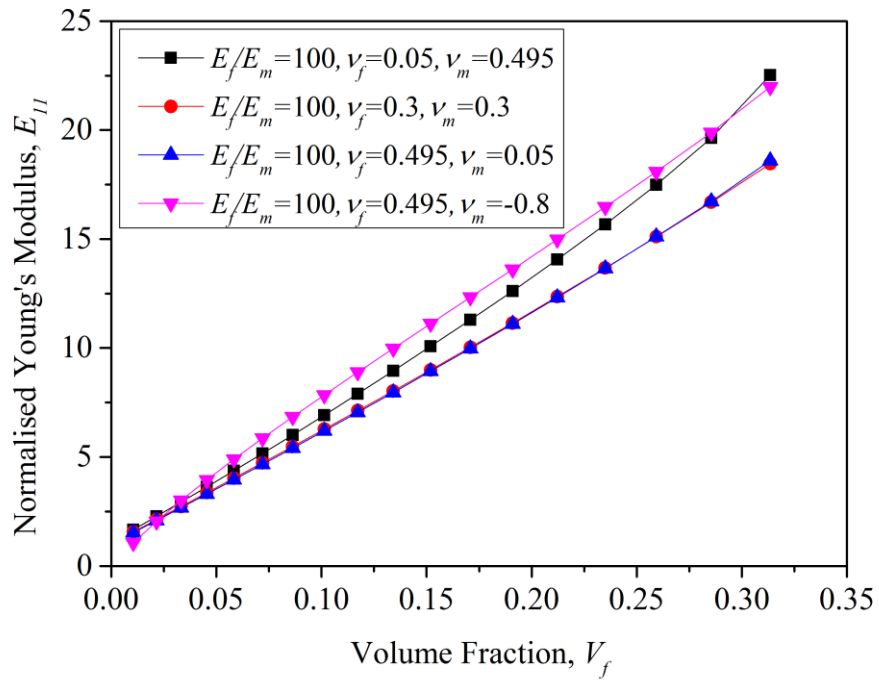


Figure 4.13. The relationship between Young's modulus in the z -direction and volume fraction of the simplified analytical model.

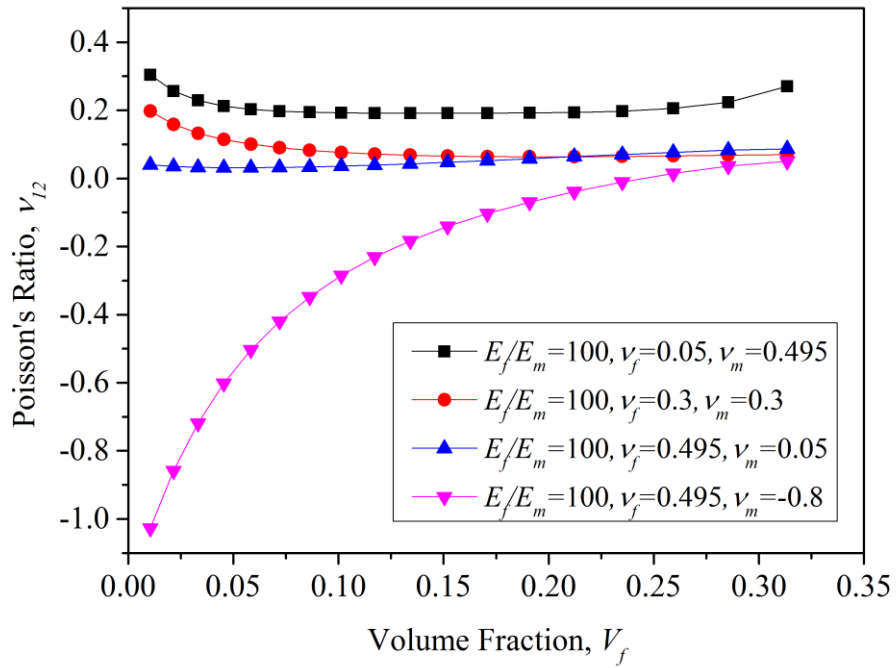
4.5.4 The Effect of Poisson's Ratio on the Elastic Properties

In this section, we also aim to take advantage of the simplified geometrical model to obtain the analytical results of the effect of Poisson's ratio on the elastic properties so as to verify the numerical results in section 4.4.3. By applying the same combinations of Poisson's ratios (i.e. $\nu_f = 0.05$ & $\nu_m = 0.495$, $\nu_f = 0.3$ & $\nu_m = 0.3$, $\nu_f = 0.495$ & $\nu_m = 0.05$ and $\nu_f = 0.495$ & $\nu_m = -0.8$) and the same value of $E_f/E_m = 100$ to the model, we have obtained the relationships of E_{11} , ν_{12} , E_{33} and ν_{31} , respectively, with volume fraction in Figure 4.14(a)-(d).

On the whole, the numerical results in Figure 4.5 agree well with the analytical results in Figure 4.14 in respect of the trend of each curve and the relative relation among curves under different combinations of Poisson's ratios. For example, both E_{11} and E_{33} , when $\nu_f = 0.3$ & $\nu_m = 0.3$ and $\nu_f = 0.495$ & $\nu_m = 0.05$ are applied separately, have shown almost identical values; both increase dramatically from negative values to nearly 0 or even positive values; E_{33} under the case of $\nu_f = 0.05$ & $\nu_m = 0.495$ indicates a smaller value than that of $\nu_f = 0.495$ & $\nu_m = -0.8$ when the volume fraction is less than around 10% and then surpasses it as the volume fraction arises. However, we also have to point out that the numerical and analytical results do have some aspects of disagreement, especially for the relative relations when the volume fraction is very large (i.e. larger than around 25%) or very small (i.e. less than around 5%). Additionally, the analytical results in Figure 4.14(c) have revealed that E_{33} increases drastically as the volume fraction increases when the volume fraction is large enough whereas E_{33} in Figure 4.5(c) grows fast first and then tend to slow down when the volume fraction is large enough.



(a)



(b)

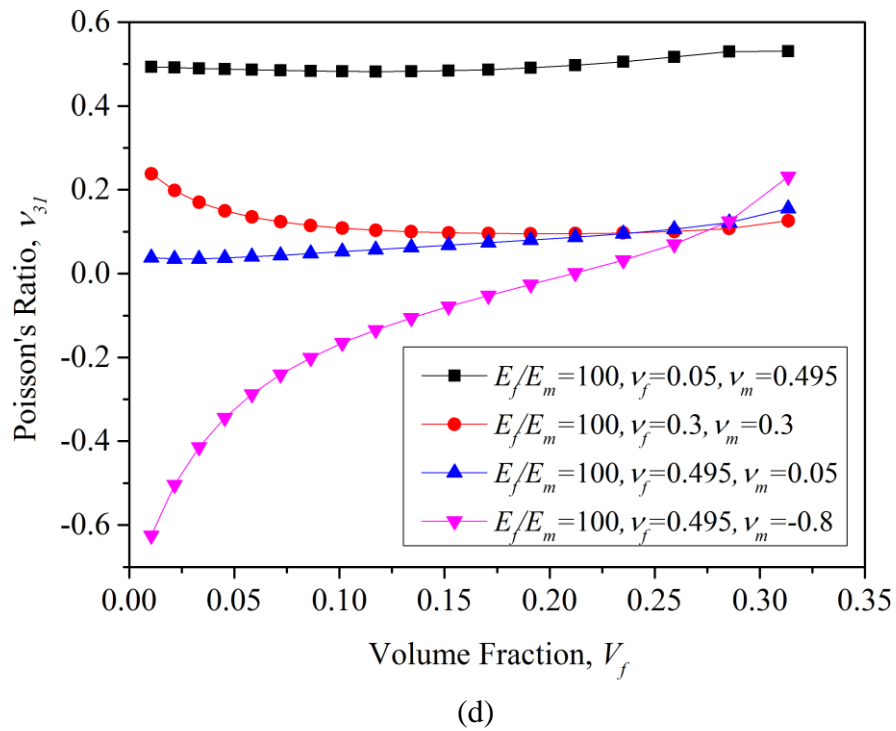
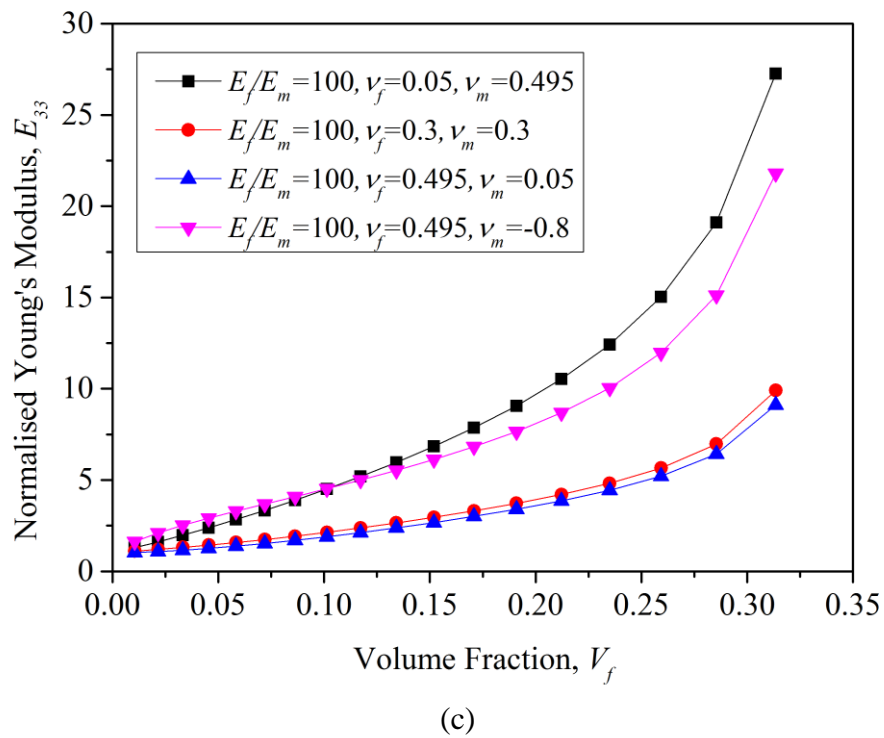


Figure 4.14. Analytical results of the effect of Poisson's ratio on the elastic properties: (a) E_{11} ; (b) ν_{12} ; (c) E_{33} ; (d) ν_{31} .

Generally speaking, the numerical results agree with the analytical results on condition that the volume fraction is neither too large nor too small and the numerical results can be reliable in predicting the trend and relation between the elastic properties and volume fraction under the influence of Poisson's ratio.

4.6 Conclusions

The generated composite structure reinforced by beam fibre network with vertical cross-linkers are proven to be transversely isotropic according to the numerical results and only the five independent constants E_{11} , ν_{12} , E_{33} , ν_{31} and G_{31} are needed for full elastic analysis for the transversely isotropic fibre network composite. To ensure the transverse isotropy of the generated RVEs, the quantity of fibres should be large enough. In addition, statistical treatment of the varying data by obtaining the mean values of the data is also essential for the transverse isotropy of RVEs. The comparison of the independent constants of the same geometry models with solid fibre elements and beam fibre elements, respectively, indicates that the simplification of solid fibres with beam elements is acceptable.

The in-plane stiffness has illustrated a much larger value than the out-of-plane stiffness which reflects the in-plane priority in stiffness of the designed fibre network. Moreover, the normalised in-plane stiffness has revealed a linear relation with volume fraction whereas the normalised out-of-plane stiffness has demonstrated a polynomial relation with volume fraction when the volume fraction is not too large, which indicates that the out-of-plane stiffness grows faster than the in-plane stiffness as the volume fraction increases. This is due to the increasing quantity of cross-linkers in the out-of-plane direction as we raise the volume fraction, thus enhancing

the out-of-plane stiffness dramatically. Poisson's ratio, especially negative Poisson's ratio of the matrix, plays a crucial role in affecting the overall elastic modulus and Poisson's ratio of the composite. The analytical exploration of the simplified model which is similar to the structure of the novel fibre network reinforced composites has also shown a good agreement with the numerical results under moderate volume fractions.

Chapter 5 Elastoplastic Properties of Transversely Isotropic Random Fibre Network Reinforced Composites

The elastoplasticity of the proposed fibre network composites constructed in Chapter 3 is explored in this chapter. The yield criterion corresponding to the transversely isotropic fibre network composite structure is discussed. Both the composite with ductile fibres and ductile matrix and the composite with ductile fibres and brittle matrix are employed in the fibre network composite structure to investigate the elastoplasticity response of the structure, more specifically, the yield strength of it. Uniaxial normal strain and biaxial normal strains, respectively, are applied to both of the composite systems so as to obtain the stress-strain curves, the yield surfaces and some yield points separately under uniaxial or biaxial loading conditions. Furthermore, the relationships between the yield strength and volume fraction under uniaxial tension or pure shearing are investigated to show the trends of the yield strengths as the volume fraction changes. The in-plane and out-of-plane yield strengths and yield shear strengths are compared to illustrate the directional yield strength difference of this structure. Moreover, an incremental method based analytical solution is raised in solving the elastoplastic response specific to a simplified geometry model and utilised to compare with the numerical results of the proposed transversely isotropic fibre network composite structure.

5.1 Introduction

Due to the introduction of overlap among fibres, the newly constructed transversely isotropic geometry has been proven to exhibit an enhanced in-plane and out-of-plane stiffness of the fibre network composite in Chapter 4. It can also be predicted that the fibre network composite may possess extraordinary plastic properties compared to dispersed fibre reinforced composites. Therefore, it is necessary to investigate the plastic behaviour of the fibre network composite so as to obtain a better understanding of this structure. Apart from experimental methods, finite element method (FEM) also provides a convenient way in analysing the continuous mechanics of the fibre-network composite by easily altering the geometry parameters such as cross-linker density and volume fraction, especially when the fibre-network composite is relatively complex in structure due to the introduction of overlap among fibres.

In this chapter, the fibre network is assumed to be composed of stainless steel fibres. The reason why we adopt steel fibres lies in that ductile materials exhibit the strain hardening stage thus making it possible to determine the yield strength, which will be the main objective in the elastoplastic analysis in this chapter. More specifically, the in-plane and out-of-plane yield strengths and yield surfaces under uniaxial and biaxial stress states will be investigated, respectively. Furthermore, both ductile and brittle matrix materials are adopted in the fibre network composites in order to also study the difference matrix materials may have caused to the composite. Moreover, an analytical solution specific to a simplified geometry model is proposed to simply model the elastoplastic stress-strain response.

5.2 Yield Criterion for Transversely Isotropic Fibre Network Reinforced Composites

Hill [278] proposed a yield condition for anisotropic material which is a natural generalisation of the Mises condition:

$$f(\sigma_{ij}) = F(\sigma_{22} - \sigma_{33})^2 + G(\sigma_{33} - \sigma_{11})^2 + H(\sigma_{11} - \sigma_{22})^2 + 2L\sigma_{23}^2 + 2M\sigma_{31}^2 + 2N\sigma_{12}^2 = 1 \quad (5.1)$$

where σ_{ij} are the stresses and F, G, H, L, M, N are constants that have to be determined experimentally. The Hill yield criterion depends only on the deviatoric stresses and predicts the same yield tensile/compression (hydrostatic pressure independent). When $F = G = H = 1$ and $L = M = N = 3$, the yield criterion reduces to the von Mises yield criterion.

For transversely isotropic solids, $F = G$ and $L = M$. The uniaxial response of a transversely isotropic material ($E_1 = E_2$) can be schematically represented by the stress-strain graphs in Figure 5.1.

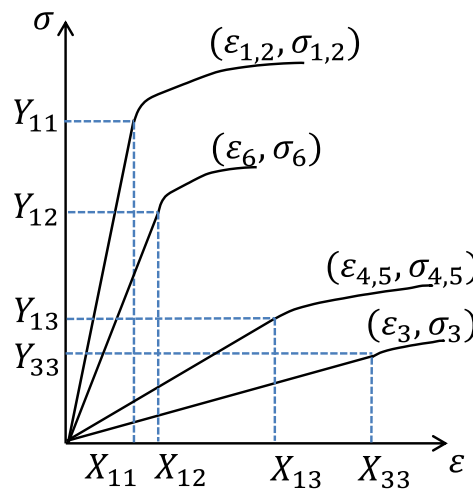


Figure 5.1. The elastoplastic response of transversely isotropic materials under uniaxial loading and pure shearing [279].

In addition, under the uniaxial loading in the three directions, respectively, we can write

$$\begin{aligned}
 (G + H)Y_{11}^2 &= 1 \\
 (F + H)Y_{22}^2 &= 1 \\
 (F + G)Y_{33}^2 &= 1 \\
 2LY_{23}^2 &= 1 \\
 2MY_{31}^2 &= 1 \\
 2NY_{12}^2 &= 1
 \end{aligned} \tag{5.2}$$

where Y_{ij} are the normal yield stresses and shear yield stresses with respect to the axes of anisotropy and can be obtained from the uniaxial loading or pure shearing test. Consequently we have

$$\begin{aligned}
 F &= G = \frac{1}{2Y_{33}^2} \\
 H &= \frac{1}{Y_{11}^2} - \frac{1}{2Y_{33}^2} \\
 L &= M = \frac{1}{2Y_{31}^2} \\
 N &= \frac{1}{2Y_{12}^2}
 \end{aligned} \tag{5.3}$$

Thus the yield criterion can be rewritten as

$$\begin{aligned}
 f(\sigma_{ij}) &= \frac{1}{2Y_{33}^2} (\sigma_{22} - \sigma_{33})^2 + \frac{1}{2Y_{33}^2} (\sigma_{33} - \sigma_{11})^2 \\
 &+ \left(\frac{1}{Y_{11}^2} - \frac{1}{2Y_{33}^2} \right) (\sigma_{11} - \sigma_{22})^2 + \frac{1}{Y_{31}^2} (\sigma_{23}^2 + \sigma_{31}^2) + \frac{1}{Y_{12}^2} \sigma_{12}^2 = 1
 \end{aligned} \tag{5.4}$$

By conducting uniaxial loadings in the three principal directions and pure shearings, respectively, tensile and shear yield strengths (Y_{11}, Y_{33}, Y_{31} and Y_{12}) can be determined from the stress-strain responses, thus the exact expression for the yield

criterion of transversely isotropic materials can be obtained. More specifically, Hooke's law for transversely isotropic materials [103] can be expressed as

$$\begin{bmatrix} \varepsilon_{11} \\ \varepsilon_{22} \\ \varepsilon_{33} \\ \varepsilon_{23} \\ \varepsilon_{31} \\ \varepsilon_{12} \end{bmatrix} = S\sigma$$

$$= \begin{bmatrix} 1/E_1 & -\nu_{12}/E_1 & -\nu_{13}/E_1 & 0 & 0 & 0 \\ -\nu_{12}/E_1 & 1/E_1 & -\nu_{13}/E_1 & 0 & 0 & 0 \\ -\nu_{13}/E_1 & -\nu_{13}/E_1 & 1/E_3 & 0 & 0 & 0 \\ 0 & 0 & 0 & 1/2G_{31} & 0 & 0 \\ 0 & 0 & 0 & 0 & 1/2G_{31} & 0 \\ 0 & 0 & 0 & 0 & 0 & (1 + \nu_{12})/E_1 \end{bmatrix} \begin{bmatrix} \sigma_{11} \\ \sigma_{22} \\ \sigma_{33} \\ \sigma_{23} \\ \sigma_{31} \\ \sigma_{12} \end{bmatrix} \quad (5.5)$$

where the elastic properties of a transversely isotropic material ($E_1 = E_2$) can be written in terms of the five independent elastic constants i.e. E_1 , E_3 , G_{31} , ν_{12} and ν_{13} .

Thus,

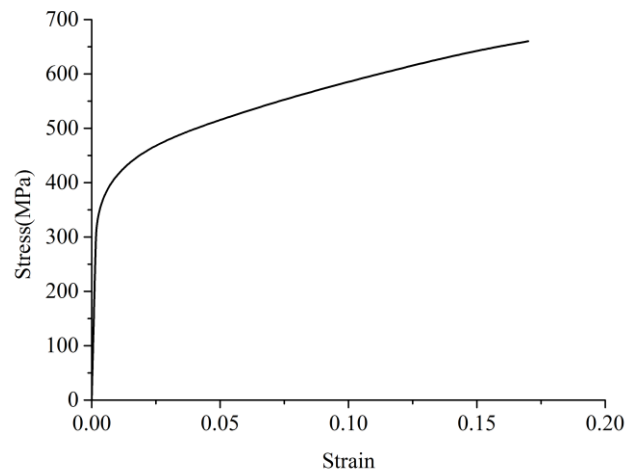
$$S = \begin{bmatrix} 1/E_1 & -\nu_{12}/E_1 & -\nu_{13}/E_1 & 0 & 0 & 0 \\ -\nu_{12}/E_1 & 1/E_1 & -\nu_{13}/E_1 & 0 & 0 & 0 \\ -\nu_{13}/E_1 & -\nu_{13}/E_1 & 1/E_3 & 0 & 0 & 0 \\ 0 & 0 & 0 & 1/2G_{31} & 0 & 0 \\ 0 & 0 & 0 & 0 & 1/2G_{31} & 0 \\ 0 & 0 & 0 & 0 & 0 & (1 + \nu_{12})/E_1 \end{bmatrix} \quad (5.6)$$

5.3 Geometry and Material Properties

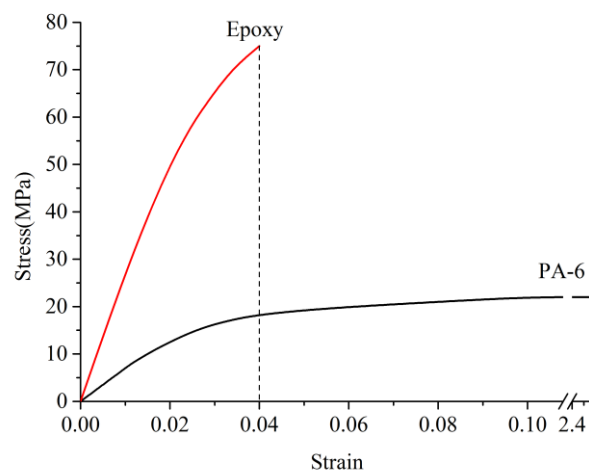
In the study of the yield behaviours of the fibre network composites, both brittle material (Epikote 828LVEL) and ductile material (Polyamide 6 (PA-6)) are employed as the matrix to see the difference that matrix can cause to the yield behaviours. Stainless steel which possesses both high stiffness and good ductility as introduced in Section 2.1.1 and exhibits a certain yield point is adopted as the fibre materials. Details of the properties of fibre and matrix materials are listed in Table 5.1 and the stress-strain curves are shown in Figure 5.2.

Table 5.1. Mechanical properties of fibre and matrix materials [40].

	Fibre	Matrix	
	Stainless steel	Polyamide 6 (PA-6)	Epikote 828LVEL
Young's modulus, E (GPa)	193	0.7	2.9
Poisson's ratio, ν	0.3	0.39	0.35
Tensile strength, σ (MPa)	660	22	75
Tensile strain, ε	17%	250%	4%
Yield strength (0.2%), σ_y (MPa)	365	-	-



(a)



(b)

Figure 5.2. The stress-strain curve of stainless steel fibre (a) and matrix (PA-6: (b)-black curve, Epoxy: (b)-red curve).

5.4 Comparison of the Models with Solid and Beam

Fibre Elements

Similar to the method of dealing with fibre element types, fibres will also be treated as beam elements (B31) instead of solid elements for the elastoplastic analysis of the geometry. Then, one necessary step that requires to be conducted before continuing with the in-depth analysis is to figure out the difference this simplification can give rise to for the elastoplastic results. The same geometry models that have already been generated for elasticity comparison in section 4.3.5 will be transplanted into this part for the continuing process of elastoplastic simulation.

Those ten generated RVEs consist of 50 fibres each with cross-linker density $N_c = 15$, overlap coefficient $c = 0.4$ and aspect ratio $L/d = 30$. Beam and solid elements were applied to the same model, respectively, while the other conditions remain the same. As for material properties, the plastic properties of stainless steel and PA-6 were applied to fibres and matrix, respectively. A uniaxial tensile/shearing strain of 5% which is supposed to be enough to obtain a complete elastic-plastic curve was applied to the models.

Figure 5.3 demonstrates the curves of uniaxial tensile and shear stresses (σ_{11} , σ_{22} , σ_{33} , σ_{12} , σ_{23} , σ_{31}) in terms of strain for the models with either beam elements or solid elements types. Firstly, it should be pointed out that the in-plane and out-of-plane tensile/shear stress curves (σ_{11} vs σ_{22} and σ_{23} vs σ_{31}) are not identical to each other which indicates that the average of these models is not completely transversely isotropic. This is principally caused by the generated models which only include far from enough number of fibres (i.e. 50 fibres) due to the

limitation of the solid element quantity of the models. This problem can be disregarded since the aim of this section is to compare the elastoplastic properties of the same models with solid and beam elements and the comparison of all the six stress states will be taken into consideration. When comparing the corresponding stress curves of models with beam and solid elements, we can see that σ_{11} and σ_{22} of the models with solid elements are dramatically larger than that of the models with beam elements while σ_{33} is nearly identical in the models with either fibre element type. In terms of shear stress, σ_{12} is consistent when either fibre element type is adopted meanwhile both σ_{23} and σ_{31} of the models with beam elements are much larger than that with solid elements. Therefore, we can conclude that there is a large difference in in-plane stresses (σ_{11} , σ_{22} , σ_{23} and σ_{31}), whereas no big difference exists in out-of-plane stresses (σ_{33} and σ_{12}). Further to the large difference in in-plane stresses (σ_{11} , σ_{22} , σ_{23} and σ_{31}), Table 5.2 has listed the in-plane and out-of-plane yield strains and strengths of the models with beam and solid fibre element types, respectively, according to the curves in Figure 5.3. Since there are no obvious yield points on those curves, the method described in 5.5.1 has been employed for the determination of yield points. From the results in Table 5.2, we can see that there is no significant difference (the largest error is within 5%) in yield strengths, no matter in tension or shearing, of the models with different fibre element types although there seems to be a large difference in yield strains. This indicates that the method of representing fibres with beams is dependable in the following study in yield behaviours.

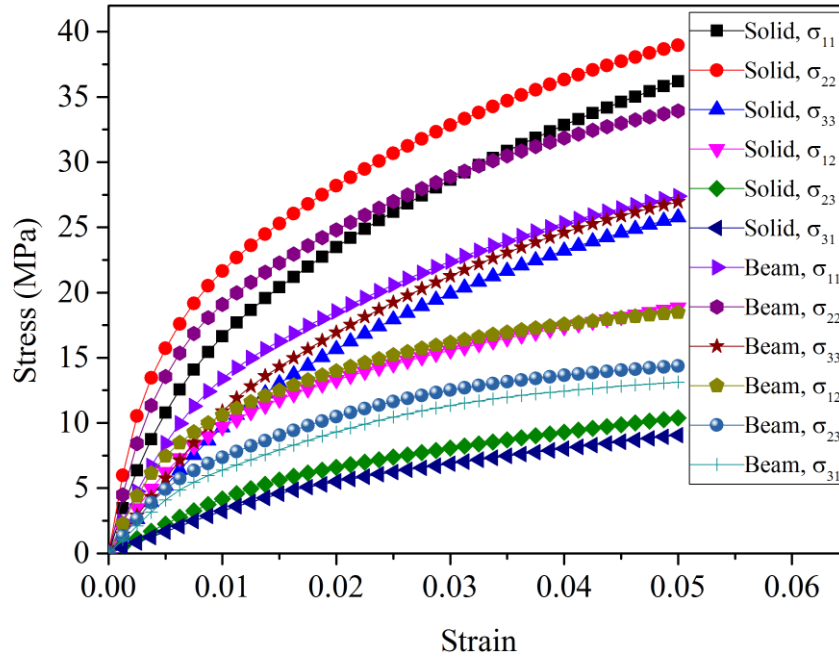


Figure 5.3. Uniaxial tensile and shear stress (σ_{11} , σ_{22} , σ_{33} , σ_{12} , σ_{23} , σ_{31})-strain curves of random fibre network reinforced composites with beam and solid fibre element types, respectively, under a strain of 5%. The volume fraction is 0.09.

Table 5.2. Yield strength values (MPa) of stochastic fibre reinforced composites with beam and solid fibre element types, respectively, under uniaxial tension and shearing simulations with structure parameters fibre aspect ratio $L/d = 30$, number of fibres $N = 50$, cross-linker density $N_c = 15$ and overlap coefficient $c = 0.4$. The volume fraction is 0.09.

Fibre Element Type	Y_{11}	X_{11}	Y_{22}	X_{22}	Y_{33}	...
Solid	11.0712	0.00519	11.7283	0.00297	14.452	...
Beam	11.3109	0.00753	12.2741	0.00425	13.847	

X_{33}	Y_{12}	X_{12}	Y_{23}	X_{23}	Y_{31}	X_{31}
0.0176	7.5794	0.006625	5.7777	0.01569	5.2655	0.01838
0.0142	7.5204	0.005063	5.8624	0.0065	5.5435	0.007688

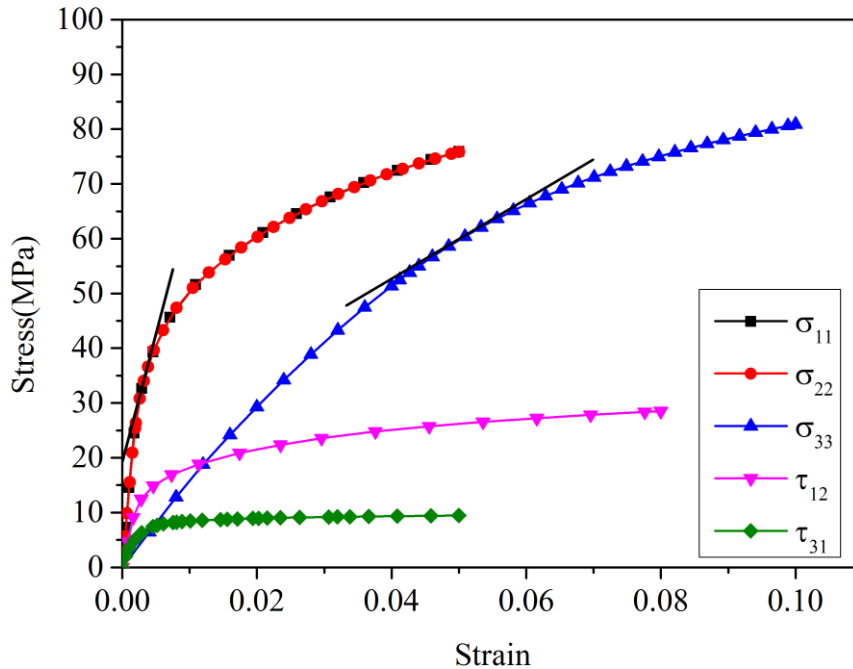
5.5 Numerical Results

5.5.1 Stress-strain Curve under Uniaxial Tensile/shearing

To obtain the yield strength of the composites, a tensile/shear strain which is large enough for the structure to yield is applied to the RVE with cross-linker density $N_c = 21$ and aspect ratio $L/d = 100$. Figure 5.4 is the stress-strain curves of the steel/PA-6 composite and the steel/828LVEL composite under uniaxial tension/shearing, which can be used to determine the yield points for materials. It is universally acknowledged that an offset yield strain of 0.2% is most frequently used when determining the yield points of materials without precise yield point, like aluminium and high strength steel. However, this definition does not work for this study since the stress-strain curves show very gentle gradient changes. To determine the yield strength of stochastic fibre network composites, several definitions have been testified and the apparent elastic limit proposed by Johnson [280] has been chosen as the yield point, in which the yield point is determined when the rate of deformation is 50 percent larger than that at the origin. In other words, the tangent modulus of the yield point on the stress-strain curve decreases to $2/3$ of the initial value. For instance, in order to determine the yield point (X_{11}, Y_{11}) under uniaxial tension in the x direction, curve fitting and interpolation techniques are utilized so that the tangent gradient of the curve can be approximately represented by the gradient of the nearby two data points. Young's modulus E_{11} is obtained first from the initial gradient which can be calculated according to the first several data points on the curve. Therefore, the yield point (X_{11}, Y_{11}) is determined when the gradient of the nearby two data points starts to be smaller than $2/3$ of E_{11} . That is

$$\frac{\sigma_{i+1} - \sigma_i}{\varepsilon_{i+1} - \varepsilon_i} < \frac{2}{3} E_{11} \quad (5.7)$$

Then $(\varepsilon_{i+1}, \sigma_{i+1})$ can be regarded as the approximate (X_{11}, Y_{11}) . The yield points have been roughly pointed out in Figure 5.4 by drawing a line according to the slope. Table 5.3 is the tensile and shear yield stresses and strains obtained by this method for the steel/PA-6 composite and the steel/828LVEL composite. When comparing both in-plane and out-of-plane uniaxial tensile and shear yield strengths, i.e., Y_{11} , Y_{33} , Y_{12} and Y_{31} , of the two composites, we can conclude that all those values of the steel/828LVEL composite are larger than those of the steel/PA-6 composite. This is attributed to the difference of matrix materials [40], due to the fact that the brittle 828LVEL matrix can carry higher load than the ductile PA-6 matrix due to the higher stiffness and strength.



(a)

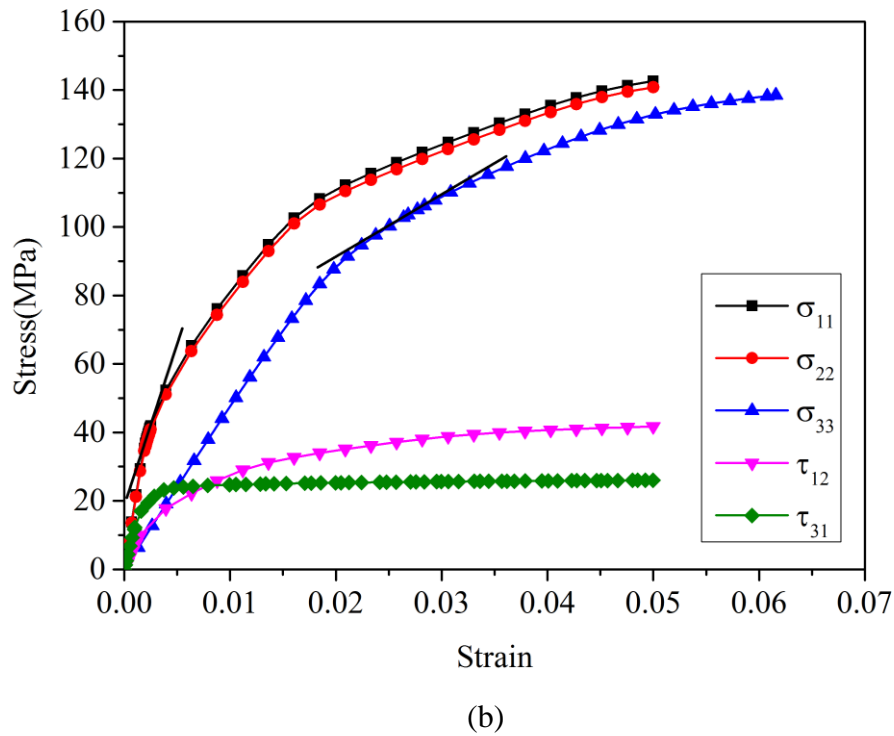


Figure 5.4. Stress-strain curves of the steel/PA-6 composite (a) and the steel/828LVEL composite (b), with structure parameters fibre aspect ratio $L/d = 100$, number of fibres $N = 200$, cross-linker density $N_c = 21$ and overlap coefficient $c = 0.55$, under uniaxial tension or shearing. The volume fraction is 0.24.

Table 5.3. Yield strength values (MPa) of stochastic fibre reinforced composites under uniaxial tension and shearing simulations with structure parameters fibre aspect ratio $L/d = 100$, number of fibres $N = 200$, cross-linker density $N_c = 21$ and overlap coefficient $c = 0.55$. The volume fraction is 0.24.

Composites	Y_{11}	X_{11}	Y_{33}	X_{33}	Y_{12}	X_{12}
steel/PA-6	31.94	0.0022	57.358	0.0469	10.241	0.0021 ...
steel/828LVEL	40.481	0.0024	100.28	0.0251	13.708	0.0024

Y_{31}	X_{31}	E_{11}	E_{33}
3.944	0.0012	16492.46	1608.76
15.947	0.0014	19792.94	4830.13

5.5.2 The Effect of the Stiffness of the Matrix on the Yield Strength

There is an interesting point from the results of Table 5.3: the out-of-plane yield tensile strength (Y_{33}) is even larger than the in-plane yield tensile strength (Y_{11}) for both composites as explored, although the out-of-plane stiffness (E_{33}) is smaller than the in-plane stiffness (E_{11}). According to the outcomes achieved by other researchers [93, 94] on solid foams, both the stiffness and yield strength exhibit higher values in in-plane directions than in out-of-plane directions for geometries in which fibres are normally distributed along in-plane directions. Compared to the fibre network without matrix [260], the in-plane yield strength of which shows much larger value than the out-of-plane yield strength, the fibre network combined with matrix demonstrates larger out-of-plane yield strength than the in-plane yield strength instead. So we tend to assume that the import of matrix affects in-plane and out-of-plane yield strength. In order to verify this hypothesis, the steel/PA-6 composite is applied with the stiffness of matrix varying from nearly zero to large enough (i.e. 35, 175, 350, 700 and 7000MPa) while keeping the other parameters as they are. From the results in Figure 5.5, we can see that the geometry shows a smaller out-of-plane yield strength than the in-plane yield strength when the stiffness of the matrix is small enough, e.g. 35 MPa. Following this, the out-of-plane yield strength starts to surpass the in-plane yield strength at some point and then the stiffness of matrix continues increasing. This result verifies the hypothesis and we can conclude that the introduction of the matrix has tremendously improved the load bearing capacity, especially the out-of-plane yield strength. This finding showcases the complication of composites but also provides us with a choice to design composites with certain

in-plane and out-of-plane yield strength.

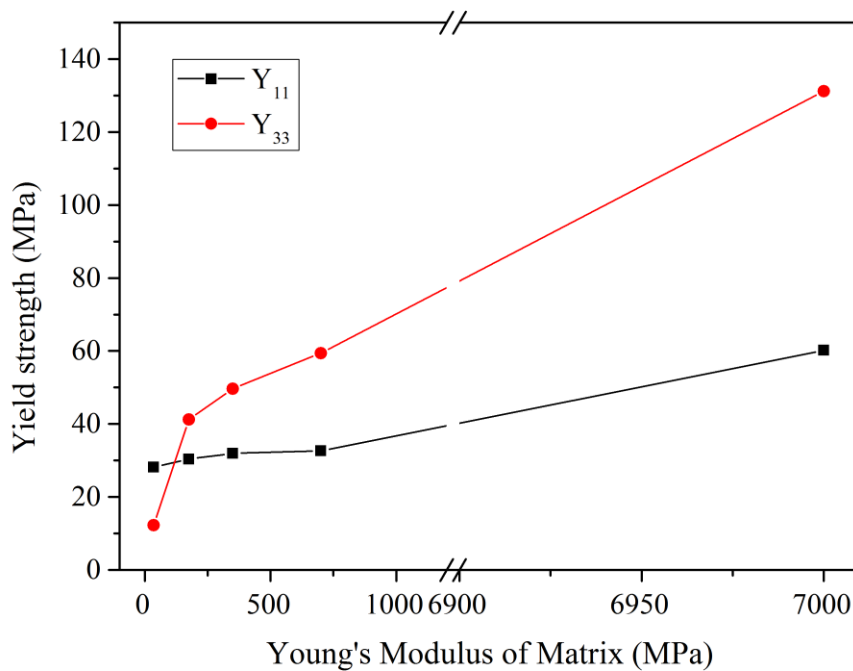
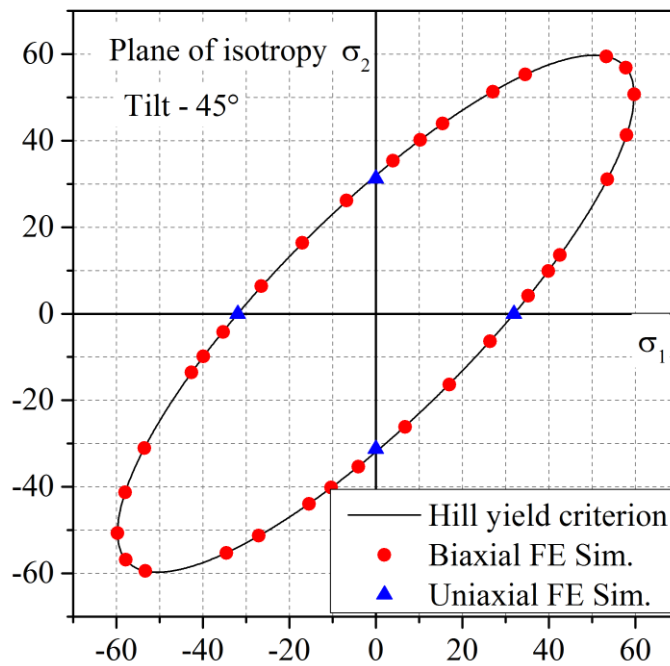


Figure 5.5. The effect of stiffness of matrix on in-plane and out-of-plane yield tensile strength with structure parameters fibre aspect ratio $L/d = 100$, number of fibres $N = 200$, cross-linker density $N_c = 21$ and overlap coefficient $c = 0.55$, under uniaxial tension. The volume fraction is 0.24.

5.5.3 Yield Surface under Biaxial Stress States

By applying combined biaxial tension/compression to the two composite systems with structure parameters fibre aspect ratio $L/d = 100$, number of fibres $N = 200$, cross-linker density $N_c = 21$ and overlap coefficient $c = 0.55$, the yield surfaces of the plane of isotropy (i.e. in-plane) and the plane of anisotropy (i.e. out-of-plane) have been obtained and shown in Figure 5.6 and Figure 5.7. The volume fraction is 0.24. From the in-plane yield surface (Figure 5.6(a) and Figure 5.7(a)), we can see that the tilt is approximately 45 degrees which again indicates the transverse isotropy of the geometry. As a comparison, tilts larger than 45 degrees were observed for the

plane of anisotropy (Figure 5.6(b) and Figure 5.7(b)), which indicate larger out-of-plane yield strengths than in-plane yield strengths. This is consistent with the results in 5.5.1 and discussions in 5.5.2. Extending the comparison within uniaxial tension (Figure 5.4) to biaxial tension (Figure 5.6 and Figure 5.7), likewise, both the in-plane and out-of-plane yield surfaces of the steel/828LVEL composite invariably overpass those of the steel/PA-6 composite. In addition, the out-of-plane yield surface of the steel/828LVEL composite illustrates a larger tilt than that of the steel/PA-6 composite.



(a)

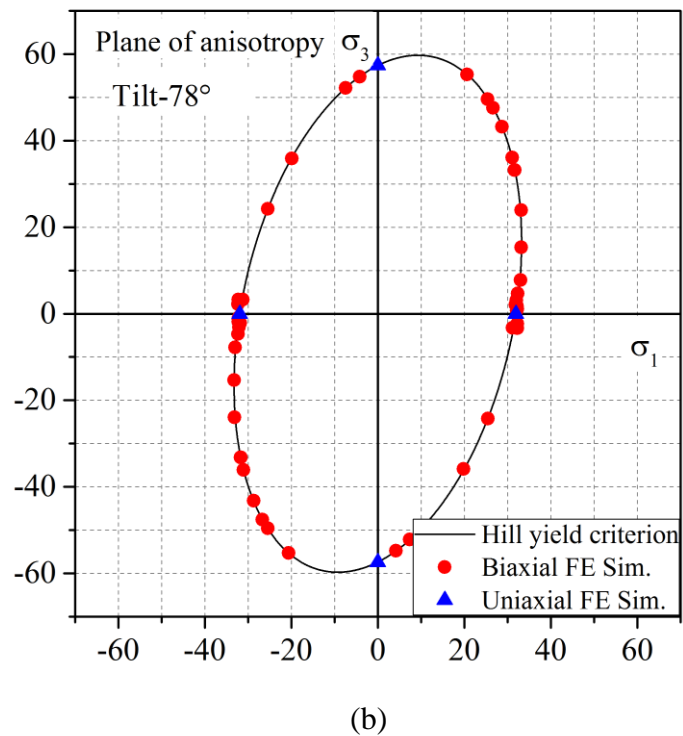
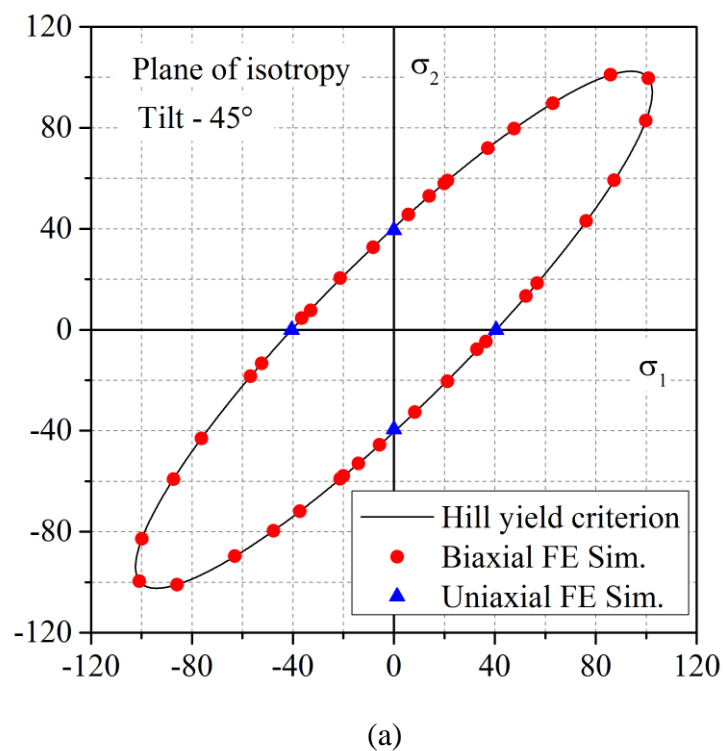


Figure 5.6. Yield surface in plane of isotropy (a) and plane of anisotropy (b) of the steel/ PA-6 composite, with structure parameters fibre aspect ratio $L/d = 100$, number of fibres $N = 200$, number of cross-linkers $N_c = 21$ and overlap coefficient $c = 0.55$, under biaxial tension/compression. The volume fraction is 0.24.



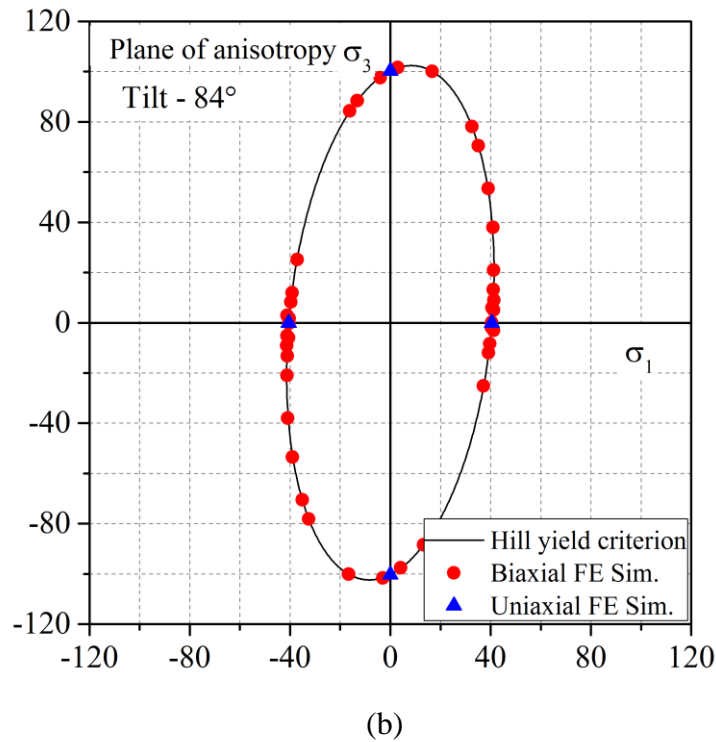


Figure 5.7. Yield surface in plane of isotropy (a) and plane of anisotropy (b) of the steel/828LVEL composite, with structure parameters fibre aspect ratio $L/d = 100$, number of fibres $N = 200$, number of cross-linkers $N_c = 21$ and overlap coefficient $c = 0.55$, under biaxial tension/compression. The volume fraction is 0.24.

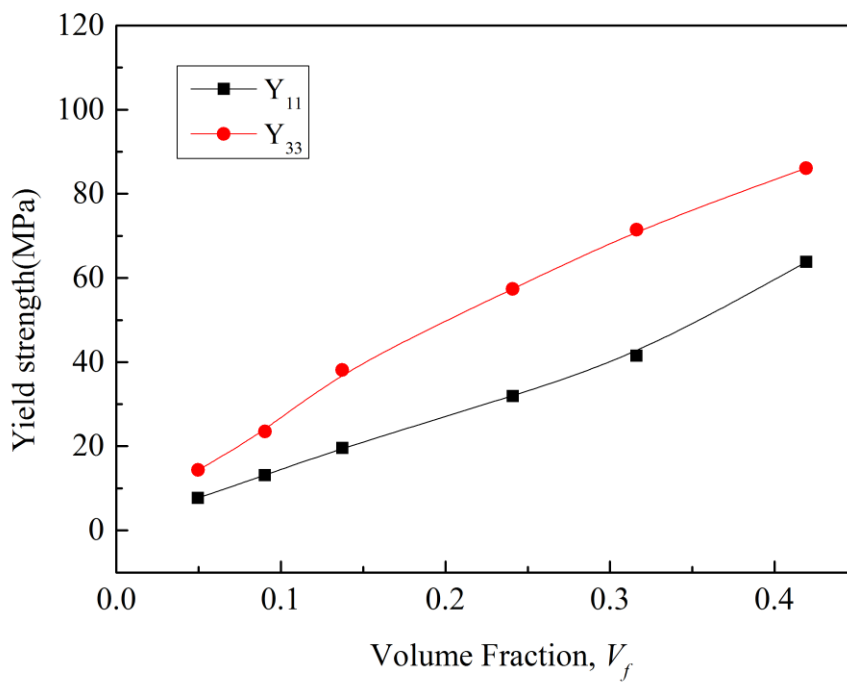
5.5.4 Dependence of Yield Strength on the Volume Fraction

In this section, we aim to investigate the relation of yield strength with volume fraction. Figure 5.8 and Figure 5.10 are the results of the yield tensile/shearing strengths of the two composites, respectively, with respect to volume fraction. For the steel/PA-6 composite with the ductile matrix in Figure 5.8, both in-plane tensile and shearing strengths show a nearly linear relationship with volume fraction. The larger the volume fraction is, the larger the yield tensile/shearing strength is. The out-of-plane tensile and shearing strengths also increase with volume fraction. However, they indicate nonlinear relationships with volume fraction. For example, the growth

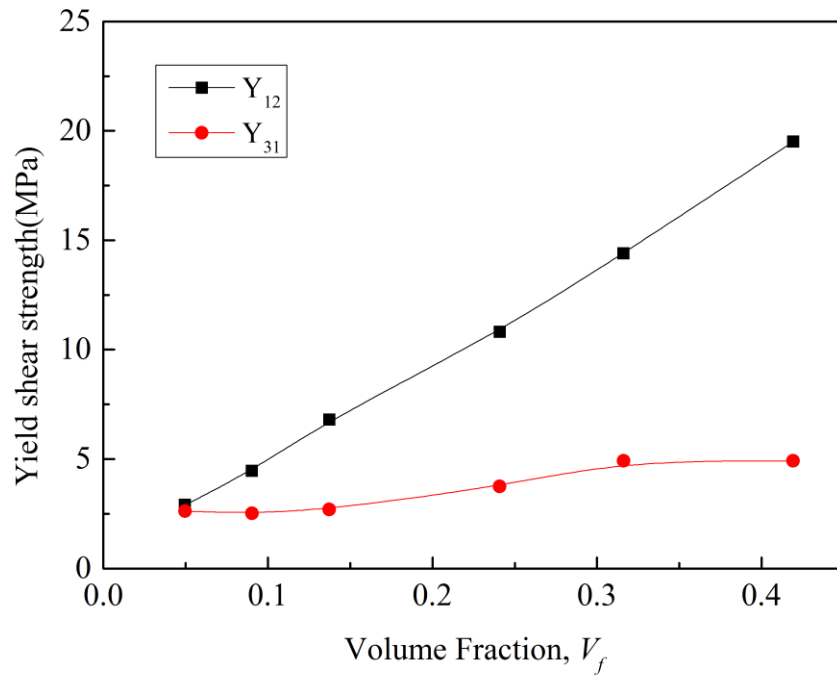
rate of the out-of-plane tensile strength decreases as the out-of-plane tensile strength increases with volume fraction. The difference between in-plane and out-of-plane is even getting larger as volume fraction increases. One interesting result that commands our attention is that the out-of-plane yield strength is always larger than the in-plane yield strength for both composites under any volume fraction that we have researched. This is consistent with the discussion that we presented about Figure 5.5 in section 5.5.2. For PA-6 and 828LVEL with Young's moduli of 700 MPa and 2.9 GPa, respectively, the values are both sufficient to give rise to a larger out-of-plane yield tensile strength than the in-plane one. Besides, both in-plane and out-of-plane tensile and shearing strengths exhibit a nearly linear relation with volume fraction and the steel/828LVEL composite possess a larger difference in in-plane and out-of-plane yield tensile strengths than the steel/PA-6 composite. In contrast, for the yield shear strength, the two composites show different tendencies. The in-plane shear strength is always larger than the out-of-plane shear strength for the steel/PA-6 composite with the ductile matrix. For the steel/828LVEL composite with the brittle matrix, the out-of-plane shear strength arises slowly while the in-plane shear strength increases dramatically and exceeds the out-of-plane shear strength when volume fraction is getting larger.

In order to demonstrate the yield surface evolution with volume fraction, the in-plane and out-of-plane yield surfaces under biaxial stress states in terms of volume fraction for both composites are shown in Figure 5.9 and Figure 5.11. There is no doubt that the sizes of both in-plane and out-of-plane yield surfaces increase, since the corresponding in-plane and out-of-plane yield strengths rise as the volume fraction increases. The angle of tilt for the in-plane yield surface is 45° due to the transversely isotropic nature of the structure. As for the out-of-plane yield surface, the angle of

tilt for the yield surface of the steel/PA-6 composite indicates no large difference (the angle of tilt θ_1 is around 80°) for different volume fractions except when the volume fraction is as large as 0.42 (the angle of tilt θ_2 is around 65°). As a comparison, the angle of tilt for the out-of-plane yield surface of the steel/828LVEL composite decreases as volume fraction increases which indicates that the extent of anisotropy of the composite is weakened by the increasing of the volume fraction. The angle of tilt of the out-of-plane yield surface in terms of volume fraction for the steel/PA-6 composite and steel/828LVEL composite, respectively, can also be compared in Figure 5.12.

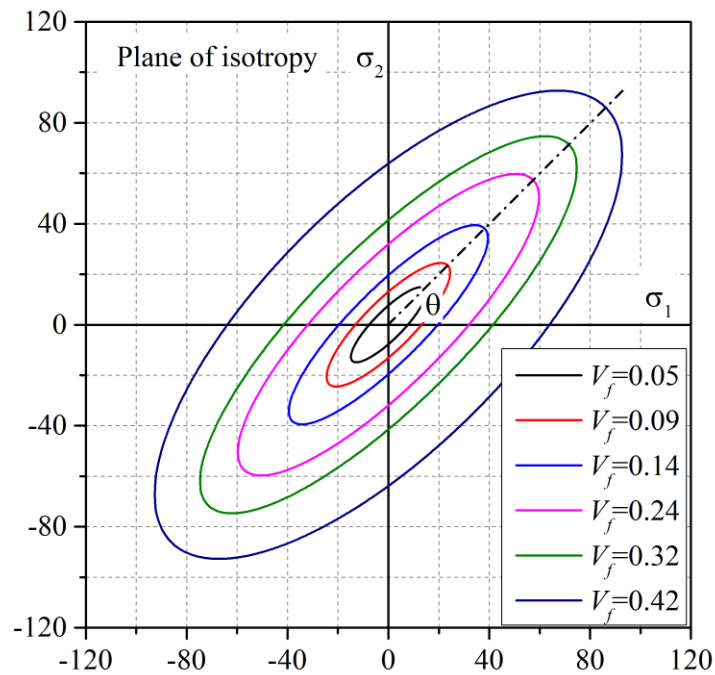


(a)



(b)

Figure 5.8. The relationship between (a) yield tensile strength and (b) yield shear strength of the steel/PA-6 composite (in-plane yield strength: Y_{12} and out-of-plane yield strength: Y_{31}) and volume fraction of fibres.



(a)

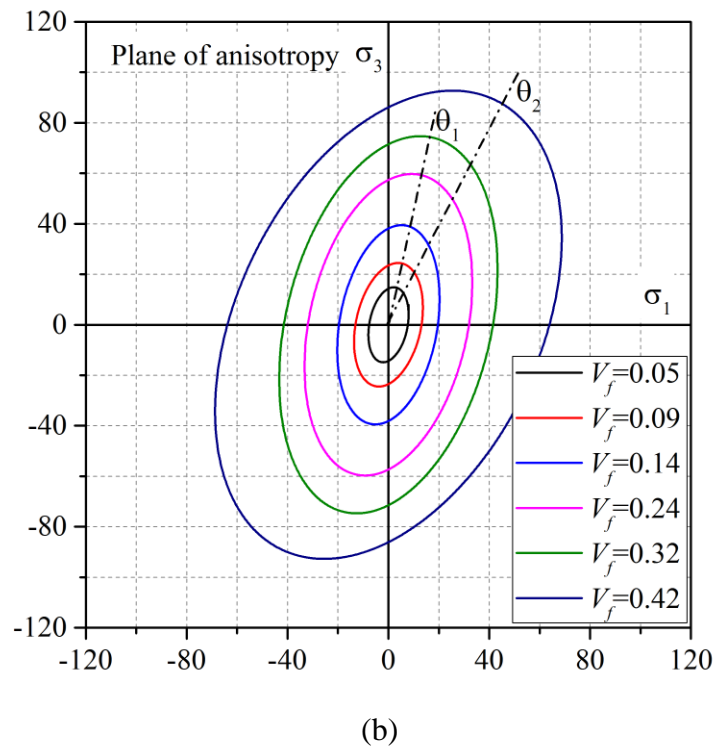
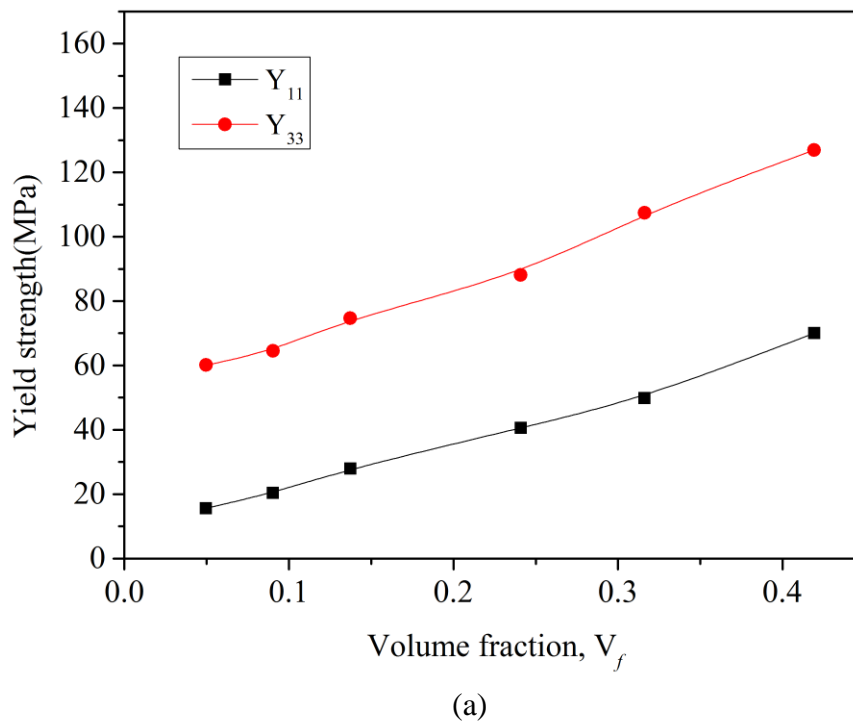


Figure 5.9. In-plane (a) and out-of-plane (b) yield surfaces in terms of different volume fractions of fibres for the steel/PA-6 composite.



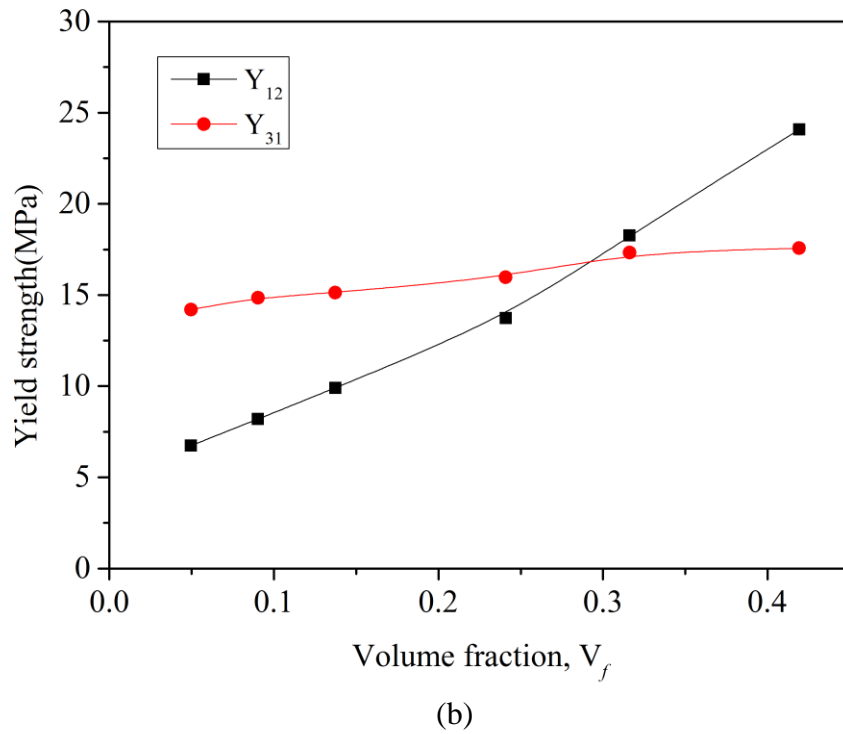
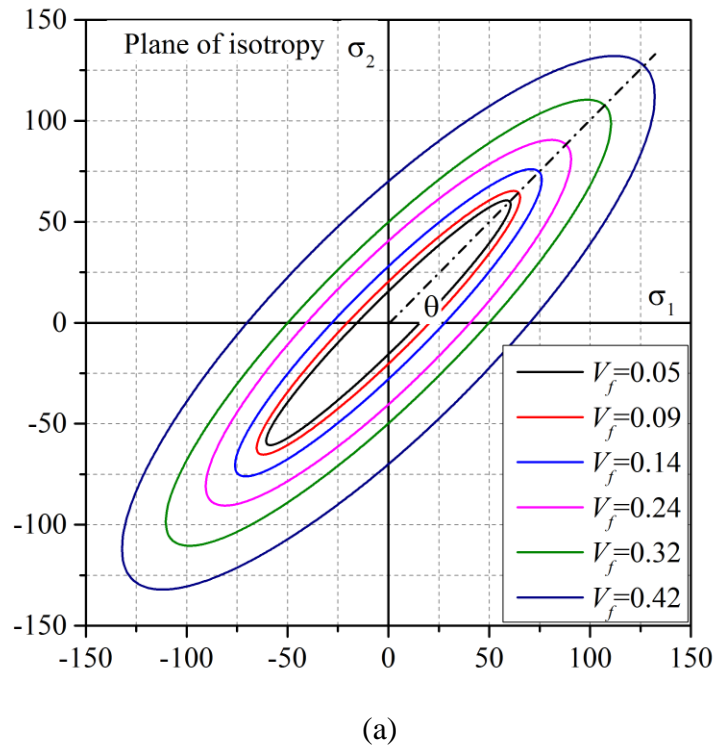


Figure 5.10. The relationship between (a) yield tensile strength and (b) yield shear strength of the steel/828LVEL composite (in-plane yield strength: Y_{12} and out-of-plane yield strength: Y_{31}) and volume fraction of fibres.



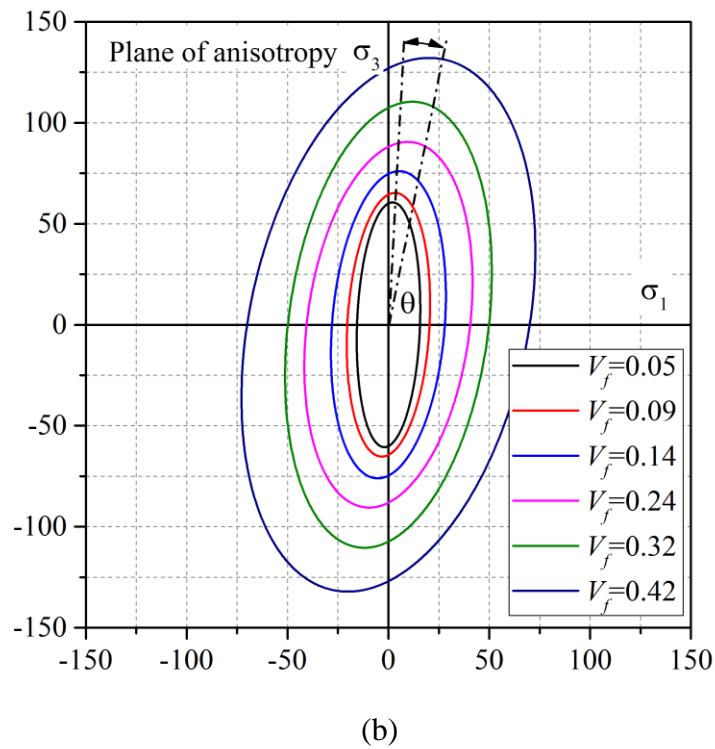


Figure 5.11. In-plane (a) and out-of-plane (b) yield surfaces in terms of different volume fractions of fibres for the steel/828LVEL composite.

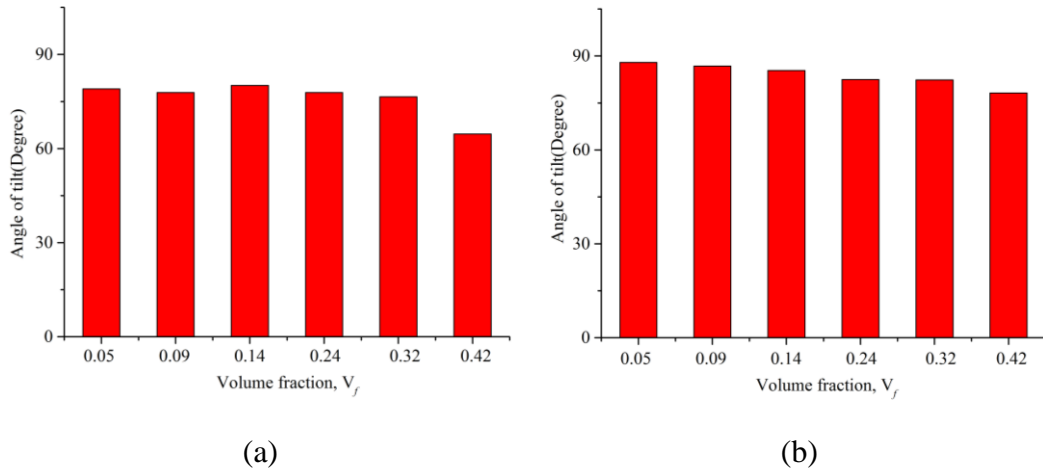


Figure 5.12. The angle of tilt of the out-of-plane yield surface in terms of volume fraction for the steel/PA-6 composite (a) and steel/828LVEL composite (b), respectively.

5.5.5 The Effect of the Combined Axial Loading and Shearing on the Yield Strength

In the previous sections, yield strengths under uniaxial and biaxial tension or shearing have been investigated. However, real engineering conditions are extremely complex and may involve the combination of tension/compression and shearing. Therefore, taking the steel/PA-6 composite for investigation, the combined axial tension and shearing are applied to the steel/PA-6 composite. With uniaxial tension and various pure shearing (with shear strain ε_{31} of 0.001, 0.002, 0.003 and 0.004) applied, the relationships between in-plane and out-of-plane yield strength and shearing have been obtained in Figure 5.13. The results indicate that both in-plane and out-of-plane yield strengths decrease as shear loading increases, which means that the imposition of shearing will reduce the in-plane and out-of-plane yield strengths. Further to this, when combined biaxial tension and shearing are applied to the steel/PA-6 composite, in-plane and out-of-plane yield surfaces can be derived from Eq.(5.4) which is based on the Hill criterion. The in-plane and out-of-plane yield surfaces under various certain shearing stresses, i.e. 0, 1MPa, 2MPa, 3MPa and 3.5MPa, are shown in Figure 5.14 (a) and (b). The results also illustrate that the addition of shear can dramatically weaken the in-plane and out-of-plane yield surfaces while retaining the angle of tilt unaffected for different shearing stresses. Therefore, the composite is more likely to fail under multi stress states.

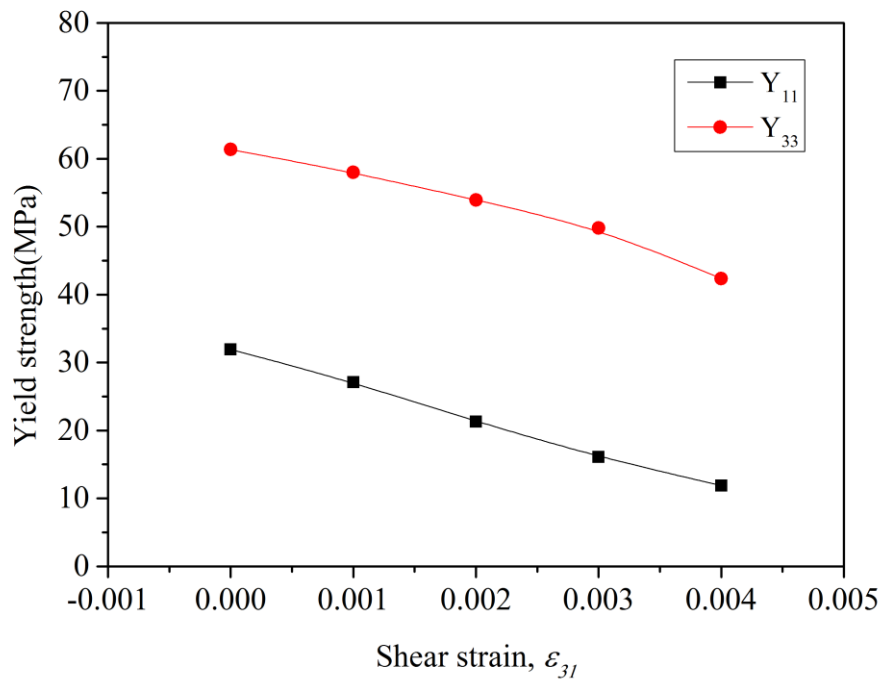
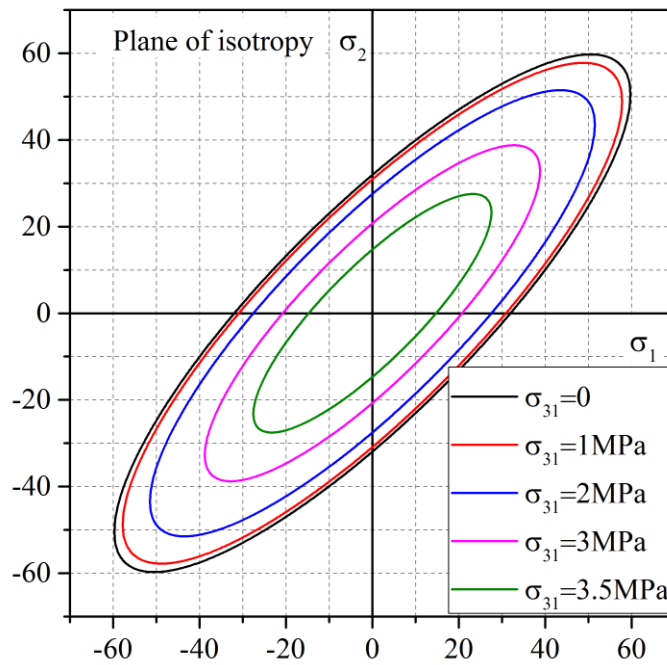
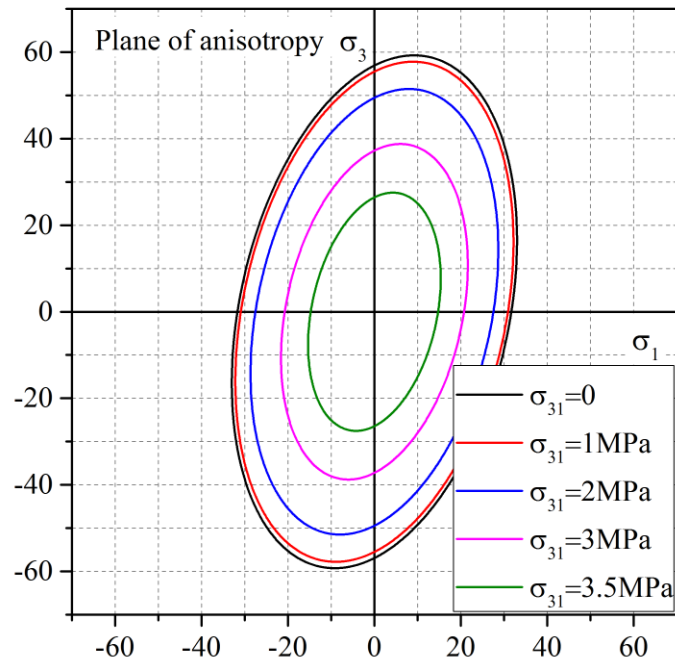


Figure 5.13. The effect of combined axial loading and shearing on in-plane and out-of-plane yield strength of the steel/PA-6 composite.



(a)



(b)

Figure 5.14. In-plane and out-of-plane yield surfaces under combined biaxial tension and shearing for the steel/PA-6 composite. Various shear stresses ($\sigma_{31}=0, 1, 2, 3$ and 3.5MPa) are applied.

5.6 Analytical Solution

As FE analysis provides a direct method for obtaining the elastoplastic stress-strain relations of the materials in the macroscale, some theoretical methods, such as the self-consistent method [141, 142], secant method [148, 150-155] and variational method [150, 158, 162] etc., have also been of great interest in the elastoplastic investigations. In this section, we aim to conduct the theoretical investigation of the elastoplastic response specific to the proposed fibre network composite so as to give a prediction of the elastoplasticity to the specific microstructure and provide comparisons with the numerical results.

Due to the random distribution of fibres and connections among fibres, the microstructure of the fibre network composite is considerably complicated and variational. To ensure the feasibility of theoretical analysis, the microstructure needs to be simplified by re-employing the RVE with cross-aligned fibres as shown in Figure 4.11 of Section 4.5.1 and as reproduced here in Figure 5.15 for convenient reference. The homogenisation method of the microstructure treatment is inherited to the elastoplastic deformation stage by dividing the RVE into 20 homogenised sub-cells and the incremental approach is applied for the non-linear stress-strain response by calculating the stress-strain relations of each sub-cells step-by-step. Feng et al. [281] also adopt these similar methods to conduct the theoretical calculation of the elastoplastic response of the interpenetrating composites, which shows good agreement with experimental results.

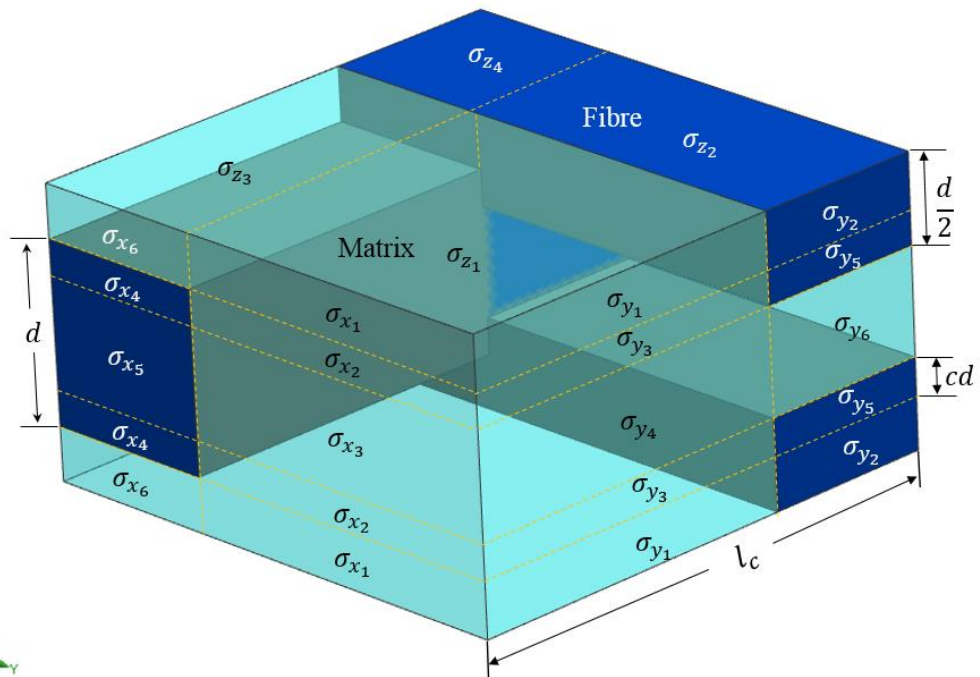


Figure 5.15. A representative volume element (RVE) of the simplified geometry model of the fibre network composite.

The procedure of calculating the stress-strain response can be introduced by the following steps:

- 1) The linear elastic stress-strain response of each sub-cell is calculated with the same equations as Eq. (4.7-22) adopted in Section 4.5.1 at the early small-deformation stage for each time-step;
- 2) The obtained stress of each sub-cell is compared to the stress-strain relation of the constituent to check whether the sub-cell reaches the strain-hardening stage. If it reaches the strain-hardening stage, the original linear elastic relation will be replaced by the nonlinear stress-strain relation of the constituent and the corresponding equations are updated for the further calculations; If does not, that sub-cell waits for the next step of calculation without any changes;
- 3) The stress-strain relations of all the sub-cells are updated to Eq. (4.7-22) and adopted for the next-step calculation. Then it goes back to Step 2. Thus, Step 2 and Step 3 are repeated until all the sub-cells shows the plastic deformation.

As for the updating procedure of equations mentioned in Step 2, more descriptions are provided hereby. Taking the steel/PA-6 composite as an example, the stress-strain relations of the steel fibre and PA-6 matrix are shown in Figure 5.2 (a) and (b), respectively. By curve fitting, the approximate expressions of stress in terms of strain for the strain-hardening stage can be given as $\sigma_f = 855.3621\varepsilon_f^{0.1587}$ and $\sigma_m = 21.7194 - 23.9e^{-48.0583\varepsilon_m}$. Thus, the stress-strain relations of the fibre and matrix follows:

$$\sigma_f = \begin{cases} E_f \varepsilon_f & \text{if } \sigma_f < \sigma_f^s \\ 855.3621 \varepsilon_f^{0.1587} & \text{if } \sigma_f \geq \sigma_f^s \end{cases}$$

$$\sigma_m = \begin{cases} E_m \varepsilon_m & \text{if } \sigma_m < \sigma_m^s \\ 21.7194 - 23.9e^{-48.0583\varepsilon_m} & \text{if } \sigma_m \geq \sigma_m^s \end{cases} \quad (5.8)$$

where E_f and E_m are Young's moduli of the stainless steel fibre and PA-6 matrix, respectively, and σ_r^S and σ_m^S are the yield strengths of the fibre and matrix. Thus, the stress states of all the sub-cells can be updated as the strain loading increases. It is noted that the fibres and matrix are assumed to be perfectly bonded and there is no element failure even when the composite undergoes the plastic deformation.

By applying a uniaxial loading in the x -direction, the incremental stress-strain relation calculated by the combination of Eq. (4.7-24) and Eq. (5.8) can be given as

$$\sigma_{11} = \frac{(l_c - d)(d - 2cd)\sigma_{x_1} + 2cd(l_c - d)\sigma_{x_2} + (l_c - d)(d - 2cd)\sigma_{x_3}}{2dl_c(1 - c)} + \frac{2cd^2\sigma_{x_4} + d(d - 2cd)\sigma_{x_5} + d(d - 2cd)\sigma_{x_6}}{2dl_c(1 - c)} \quad (5.9)$$

where σ_{x_1} - σ_{x_6} are all dependent on the incremental strains according to Eq. (5.8).

Similarly, the incremental stress-strain relation in the z -direction can be calculated by the combination of Eq. (4.7-24) and Eq. (5.8) as

$$\sigma_{33} = \frac{(l_c - d)^2\sigma_{z_1} + d(l_c - d)\sigma_{z_2} + d(l_c - d)\sigma_{z_3} + d^2\sigma_{z_4}}{l_c^2} \quad (5.10)$$

where σ_{z_1} - σ_{z_4} are all dependent on the incremental strains according to Eq. (5.8).

Figure 5.16 has illustrated the elastoplastic stress-strain response of the analytical solution (the dash-dot curve) of the simplified RVE (Figure 5.15) with a volume fraction of 0.24 when a uniaxial tension strain of 0.05 is applied. In order to verify the reliability of the analytical results, the FE analysis of the simplified RVE has also been carried out in Abaqus/standard. The interface is assumed to be perfectly bonded. We can see from Figure 5.16 that the analytical and FEM stress-strain responses demonstrate a good agreement in the linear elastic stage and the early strain-hardening stage and tend to expand the errors as the strain-hardening stage

progresses. This indicates that our analytical results are reliable in predicting the stiffness and yield strength of the simplified RVE although the analytical solution tends to underestimate the tensile strength, which may be due to the reason that the shear stresses are ignored in the calculation of the stress-strain responses of the sub-cells. However, this imperfect analytical model can still meet our requirement, since we only consider the yielding behaviours for relatively small strains in this section.

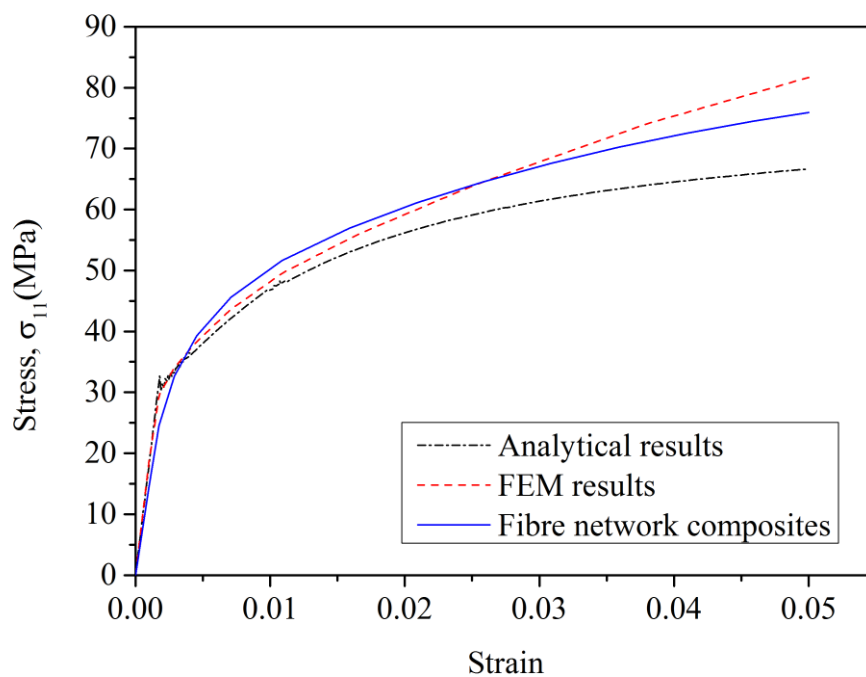


Figure 5.16. Comparison of the analytical and FEM stress(σ_{11})-strain relations of the simplified RVE and the FEM results of the proposed fibre network composite (steel/PA-6) with a volume fraction of 0.24.

With the stress-strain curve (the solid curve) of the fibre network composite of volume fraction 0.24 also presented in Figure 5.16, the elastoplastic behaviours of the fibre network composite and the simplified RVE are compared. We can see from the curves that the random fibre network composite exhibits a slightly smaller elastic modulus and requires a larger strength to yield than the simplified RVE. This can be

related to the microstructure difference between the two models. Since all the fibres are distributed aligned in the x and y directions in the simplified RVE, the stiffness is enhanced compared to the randomly distributed fibre network composite. However, the aligned fibres only undergo tension while the random fibres withstand both tension and bending. Thus, the simplified RVE is easier to yield than the random fibre network composite. The main mechanical properties of the analytical results of the simplified RVE and the FEM results of the fibre network composite obtained from Figure 5.16 are tabulated in Table 5.4. The yield strength and strain are determined by Johnson's apparent elastic limit [280]. Consistent with the above discussions about the yield strength of the two models, the proposed fibre network composite exhibits a larger yield strength than the simplified RVE.

Moreover, further yield strength data of the fibre network composite and simplified RVE under the uniaxial tension in the x -direction is shown in Figure 5.17 for comparison. Generally speaking, the yield strengths of both models demonstrate a consistent trend as the volume fraction increases and the fibre network composite possesses a relatively larger value than the simplified RVE from the analytical solution. This proves the advantage of the composite reinforced by a random fibre network in the aspect of strength improvement compared to the simplified RVE which can be regarded as an interpenetrating two-phase composite.

Table 5.4. Mechanical properties of the simplified RVE and the proposed fibre network composite (steel/PA-6) with the volume fraction of 0.24.

	Young's modulus E_{11} (MPa)	Yield strain X_{11}	Yield strength, Y_{11} (MPa)
Analytical results	18709.1	0.0018	29.73
Fibre network composites	14592.4	0.0022	31.94

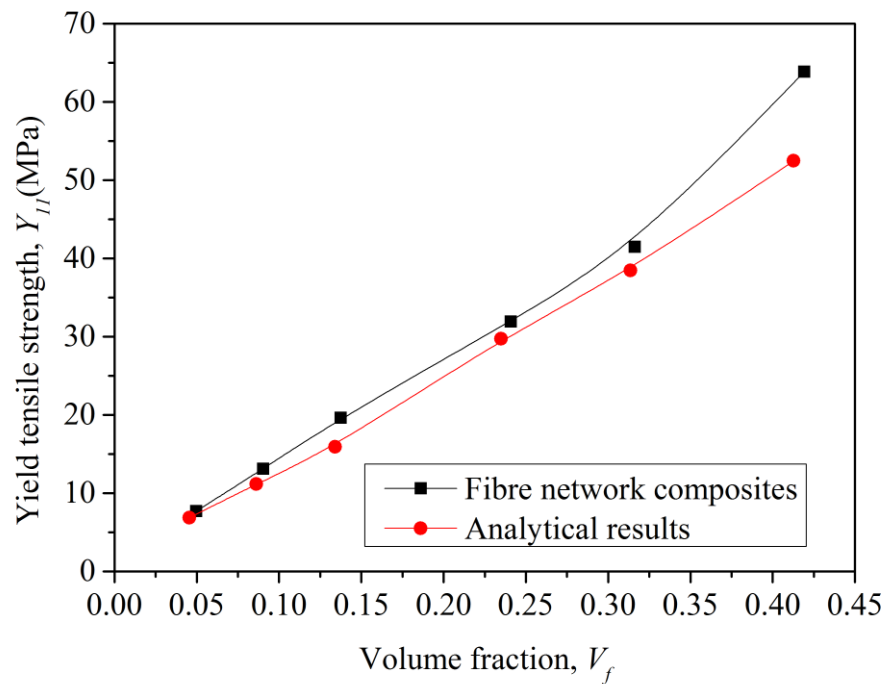


Figure 5.17. Yield tensile strengths (Y_{11}) of both the fibre network composite and the simplified RVE with respect to volume fraction. The fibres are stainless steel and the matrix is PA-6 for both models.

5.7 Discussions

As discussed in Section 5.6, the proposed fibre network composite has shown a superior yield strength than the composite reinforced by the cross-aligned fibre network, which has demonstrated the advantage of the fibre network structure with a random distribution of curved fibres in the proposed composite. In order to investigate further the elastoplastic behaviours – more specifically, the yield strength of the proposed fibre network composite – more comparisons will be carried out with other composites reinforced by either continuous or interpenetrating inclusions. In this respect, some relevant experimental data regarding yield strength has been presented in Figure 5.18. It is noted that each comparison between the proposed fibre

network composite and other composite structures corresponds to a certain volume fraction and the yield strengths under different volume fractions are actually not relevant in this figure, since the constituents in each comparison are different with different material properties.

When compared to the Al/In601 fibre network composite [282], marked in square symbol in Figure 5.18, which is in a very close microstructure to the proposed fibre network composite, the proposed fibre network composite exhibits a comparative yet slightly larger yield strength (the volume fraction is 0.2). This has proved the reliability of the numerical results in this research and shown the improvement of the fibre network in this research.

Furthermore, the proposed composite has also been compared to the cross-ply composite [40] with a volume fraction of around 0.4. It is apparent that there are two numerical data (down-triangle symbol when the volume fraction is about 0.4) corresponding to only one data (Red dot) of the cross-ply composite. The two numerical data are actually the in-plane and out-of-plane yield strengths, respectively, with the data lower than that of the cross-ply composite representing the in-plane data and the larger data representing the out-of-plane data. Thus, the yield strength of the cross-ply composite is larger than the in-plane yield strength and smaller than the out-of-plane yield strength of the proposed fibre network composite.

In addition, we have also compared the proposed composite structure with the interpenetrating phase composites [281, 283, 284]. Both experimental [283] and analytical [281] results have been obtained towards the interpenetrating steel/bronze composite with volume fractions of 0.6 and 0.8. Due to the limitation of the geometry construction algorithm, it is not easy to generate a fibre network composite with a

volume fraction as large as 0.6. Thus we have used the simplified RVE as instructed in Section 5.6 instead to compare with the interpenetrating steel/bronze composite. The yield strengths of the simplified RVE with both volume fractions have indicated larger yield strengths than the interpenetrating steel/bronze composite (marked in up-triangle symbol). Since the actual fibre network composite possesses much larger yield strengths than the simplified RVE. Therefore, we can imagine that the proposed fibre network composite structure exhibits higher yield strengths than the interpenetrating phase composite.

In conclusion, the proposed fibre network possesses a relatively high yield strength with the in-plane random distribution of fibres, inclined fibre segments along the out-of-plane directions and network generated by the intersections fibres.

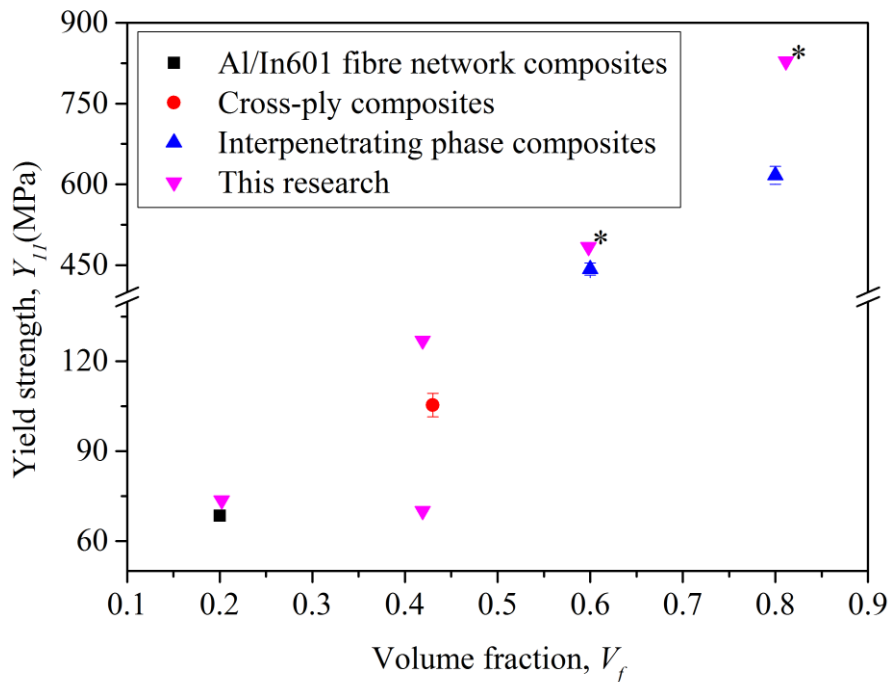


Figure 5.18. Comparisons of the proposed fibre network composite with other composites.

*: The simplified RVE is adopted to replace the proposed fibre network composite for comparison.

5.8 Conclusions

The in-plane and out-of-plane yield surfaces under biaxial stress states indicate that the yield strengths meet the Hill yield criterion. The transversely isotropic fibre network composite structure exhibits larger out-of-plane yield strength than in-plane yield strength, although the out-of-plane stiffness is smaller than the in-plane stiffness. This is related to the matrix properties. The introduction of the matrix into the fibre network has increased the out-of-plane yield strength more drastically compared to the in-plane yield strength. Furthermore, the rise of volume fraction can enhance both in-plane and out-of-plane tensile and shearing yield strengths. As volume fraction increases, both in-plane and out-of-plane yield surfaces are expanded. However, the out-of-plane angle of tilt of the steel/PA-6 composite shows no major difference, excluding when the volume fraction is as large as 0.42. As a comparison, the out-of-plane angle of tilt of the steel/828LVEL composite keeps decreasing as volume fraction increases. Moreover, the addition of shear loading reduces the yield strength or yield surface, both in-plane and out-of-plane. The proposed transversely isotropic fibre network composite possesses comparative yield strength compared to other composites with similar microstructure.

Chapter 6 Viscoelastic Properties of Aerogel and Hydrogel with Transversely Isotropic Random Fibre Network

In this chapter, the research is focused on the viscoelastic properties of tissues based on the transversely isotropic fibre network. Both collagen aerogel and hydrogel with transversely isotropic collagen fibre networks are investigated in terms of the viscoelastic behaviours that they possess in biological tissues. Thus the common viscoelastic behaviours, such as stress relaxation and creep, are explored with respect to component mechanical properties as well as network structures. A Maxwell-Weichert model consisting of two Maxwell elements are adopted to characterise the viscoelastic behaviours of collagen fibres. For collagen aerogel, the fibre network is composed of collagen fibres while the pore is left a void. Thus, the in-plane and out-of-plane stress relaxation behaviours of the porous alike transversely isotropic collagen aerogel in terms of relative density are explored. Furthermore, a simplified geometrical model is proposed, and the analytical results have been deduced and compared with the numerical results. As for collagen hydrogel, the fibre network is composed of collagen fibres while the pore is filled with water and other nonfibrillar proteins etc., which is also recognised as the ground substance. Then, both the stress relaxation and creep behaviours of collagen hydrogel in terms of volume fraction are investigated.

6.1 Introduction

Various materials, such as wood, polymers, mammal tissue and solid rocket propellants etc., exhibit viscoelastic behaviour, where the deformation is dependent on load, time and temperature [85]. In the past several decades, soft biological tissue has become one of the most attractive research fields. Collagen fibre network, such as the cytoskeleton and extracellular matrix, which acts as the skeleton in cells or tissues is a common structure in biological tissues. The structure of the network can be isotropic, transversely isotropic, orthotropic or anisotropic. The novel 3D transversely isotropic fibre network shows a relatively similar structure as observed in some cytoskeletons, e.g. the neurofilament gel in Figure 2.8, and cornea. Thus the investigation of the viscoelastic behaviours of our designated fibre network is meaningful and helpful in understanding the behaviours of soft tissues with similar structures. Two categories of structures can be studied based on the generated geometric model, that is the aerogel which is composed of the porous collagen fibre network alone and the hydrogel which is also composed of the porous collagen fibre network but surrounded with fluid ground substance. Due to the viscoelastic behaviours of collagen fibres, the aerogel and hydrogel are also supposed to exhibit viscoelastic properties in response to external loads. A variety of analytical models, such as microstructural, phenomenological/rheological, and continuum models [89, 178, 179], have been proposed for the theoretical investigation of the viscoelasticity of soft tissue. A Maxwell-Weichert model based on the rheological model is widely used in exploring the viscoelastic properties of soft tissues in the FE analysis. Therefore, both aerogel and hydrogel with the collagen fibre network will be investigated based on the Maxwell-Weichert model. More specifically, the stress

relaxation and creep behaviours in terms of volume fraction will be the focus of the analysis.

6.2 Viscoelastic Properties of Collagen Network

Aerogel

Rubber and most tissues possess viscoelastic properties and undergo stress relaxation when applied to a constant strain. We aim to study the viscoelastic properties of the fibre network first, which can also be regarded as an aerogel, in order to investigate the viscoelastic effect that brought about by the designated structure of the fibre network alone. Therefore the generated fibre network without matrix will be employed in section 6.2 for its viscoelastic response study of aerogel, of which stress relaxation behaviours will be focused on in this investigation.

6.2.1 Geometry and Material Properties

6.2.1.1 The Geometry of the RVE

Since only the fibre network will be studied in this section, the 3D transversely isotropic beam fibre networks, but without matrix, are constructed in the same procedure as shown in Chapter 3. Still, curved beam fibres are cross-linked by the added fibres at the intersection points so as to generate a network among fibres. An example of a similar RVE beam model is illustrated in Figure 6.1. Eventually, several groups of fibre networks with relative densities ranging from 0.06 to 0.36 are prepared for the following analysis. It should be noted that all the data shown in the figures from now on are the mean value of 10 RVEs for each corresponding relative density/volume fraction.

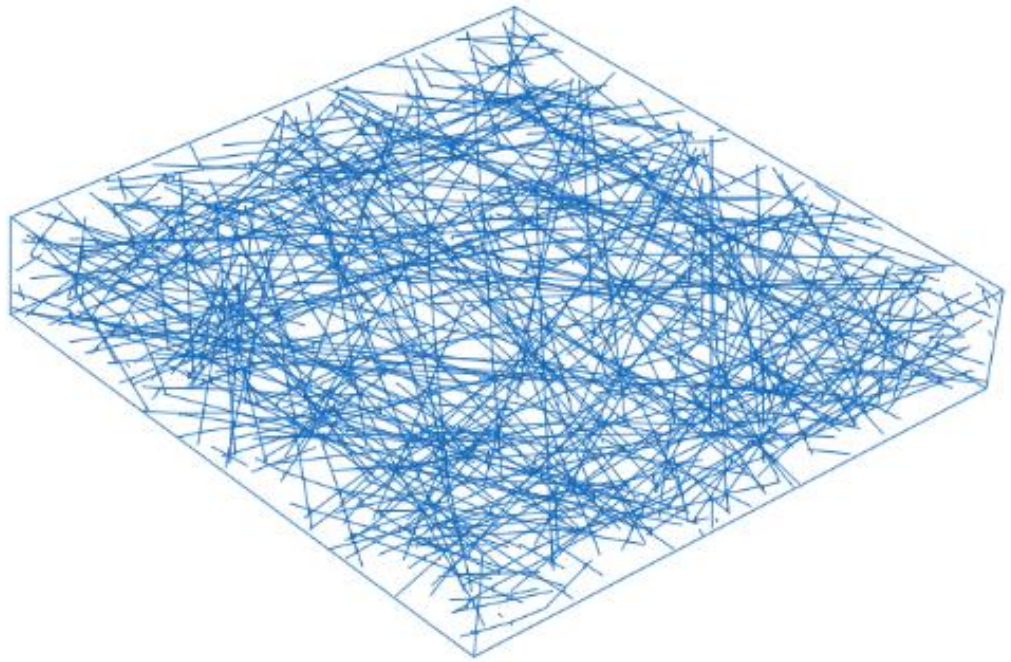


Figure 6.1. The RVE geometric beam model of the fibre network with cross-linkers.

6.2.1.2 Mechanical Model and Material Properties

For simplification, the viscoelastic behaviour of the fibre network is characterised by a Maxwell-Weichert model consisting of two Maxwell elements (one nonlinear spring (with constant modulus E_1) in series with a dashpot (with damping coefficient η_1) and another nonlinear spring (with constant modulus E_2) in series with a dashpot (with damping coefficient η_2), parallel to a linear spring (with constant modulus E_∞) as shown in Figure 6.2. The reason why the Maxwell model with two elements is adopted lies in that a single relaxation time is not sufficient to accurately fit the experimental results [205]. According to the Maxwell-Weichert model, the equation of relaxation modulus as a function of time can be expressed as:

$$E(t) = E_\infty + E_1 e^{-\frac{t}{\tau_1}} + E_2 e^{-\frac{t}{\tau_2}} \quad (6.1)$$

where E_∞ is the time-independent elastic modulus and $\tau_i = \eta_i/E_i$. Under the

condition of $t = 0$ s, $E(0)$ is the instantaneous elastic modulus. Thus, the relaxation response can be characterised by the three linear springs with elastic moduli (E_∞ , E_1 and E_2) and two dashpots with relaxation times (τ_1 and τ_2).

In Abaqus, viscoelasticity is implemented by employing Prony series. Both shear and volumetric responses have been considered separately. For homogenous elastic materials, the relationships between shear modulus G and bulk modulus K are well known as:

$$G = \frac{E}{2(1 + \nu)} \quad (6.2)$$

$$K = \frac{E}{3(1 - 2\nu)} \quad (6.3)$$

where E is the elastic modulus and ν is the Poisson's ratio of elastic materials.

Similarly, in viscoelasticity, $G(t)$ and $K(t)$ are expressed as:

$$G(t) = G_0 \left(\alpha_\infty^G + \alpha_1^G e^{-\frac{t}{\tau_1}} + \alpha_2^G e^{-\frac{t}{\tau_2}} \right) \quad (6.4)$$

$$K(t) = K_0 \left(\alpha_\infty^K + \alpha_1^K e^{-\frac{t}{\tau_1}} + \alpha_2^K e^{-\frac{t}{\tau_2}} \right) \quad (6.5)$$

When $t = 0$ s with the full stiffness,

$$G(0) = G_0(\alpha_\infty^G + \alpha_1^G + \alpha_2^G) \quad (6.6)$$

$$K(0) = K_0(\alpha_\infty^K + \alpha_1^K + \alpha_2^K) \quad (6.7)$$

where $G(0)$ and $K(0)$ are the instantaneous shear modulus and volumetric modulus.

Type I collagen, which is the most abundant protein in animal tissues such as tendon, skin, bone and cornea etc., has been adopted as the material of the fibre network. Viscoelastic parameters used in Maxwell-Weichert model for the collagen fibre network have been listed in Table 6.1. It is noted that the stress relaxation parameters are obtained from a MEMS-based technique [205] towards the Type I collagen fibrils

isolated from the dermis of sea cucumber.

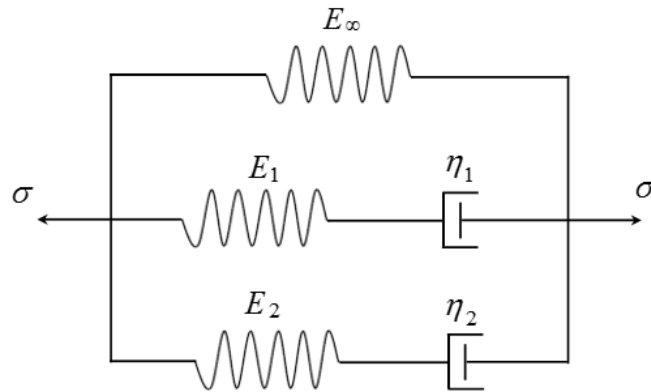


Figure 6.2. Schematic representation of Maxwell-Weichert model with two Maxwell elements.

Table 6.1. Viscoelastic parameters used in Maxwell-Weichert model for Type I collagen fibrils [205].

Parameters	E_∞ (MPa)	E_1 (MPa)	E_2 (MPa)	τ_1 (s)	τ_2 (s)
Mean Value	123±46	13±6	16±7	7±2	102±5

6.2.2 Stress Relaxation under Different Strain

In this section, the influence of applied constant strain to stress relaxation has been investigated by stretching the fibre network along the x -direction to different extents with strains $\varepsilon = 0.02, 0.04, 0.06, 0.1, 0.2, 0.5$ and 1 . To simplify the comparison among different relaxation results, all relaxation stresses are normalised by the initial elastic stress. For a time period of over 100s, all relaxation stresses completely coincide (see Figure 6.3), which indicates that the amount of strain value that applied shows no effect in the relaxation process by adopting this stress relaxation model. Besides, the following analysis will only be focused on a quasi-static state. Therefore, the strain-enhanced stress relaxation effect is not considered in this research and an

arbitrary strain of 0.02 is selected for the following stress relaxation analysis.

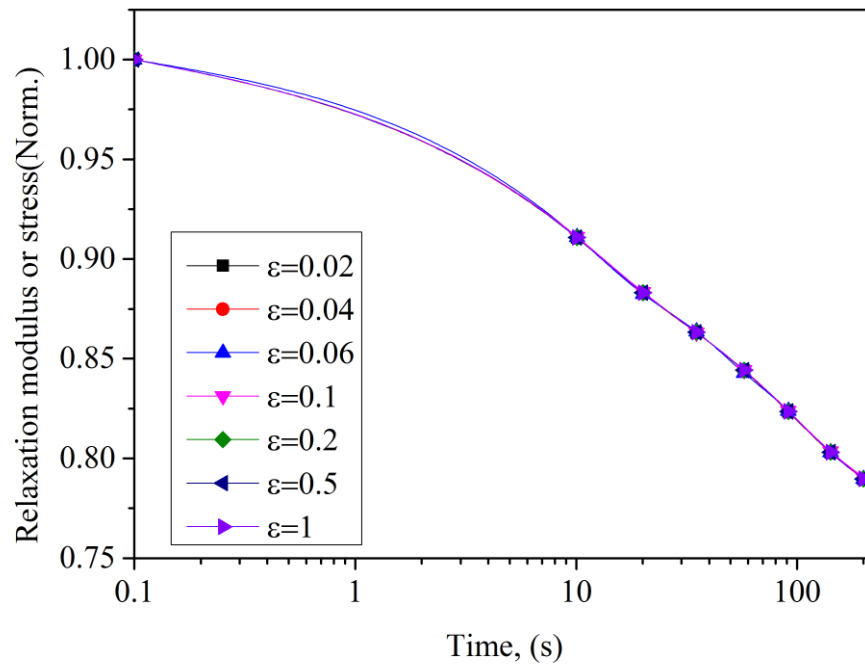
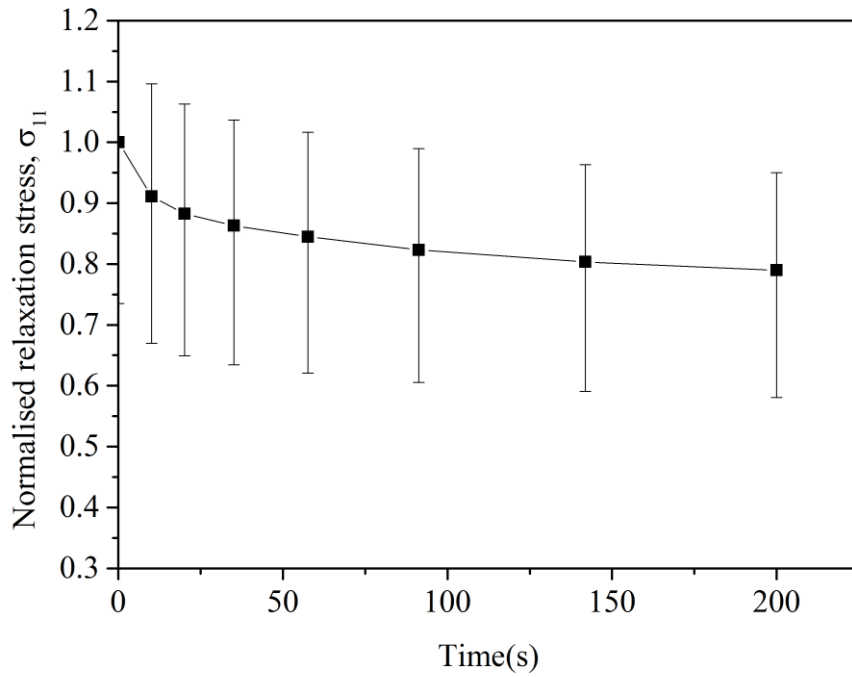


Figure 6.3. Normalised stress relaxation of collagen fibre network at various strains.

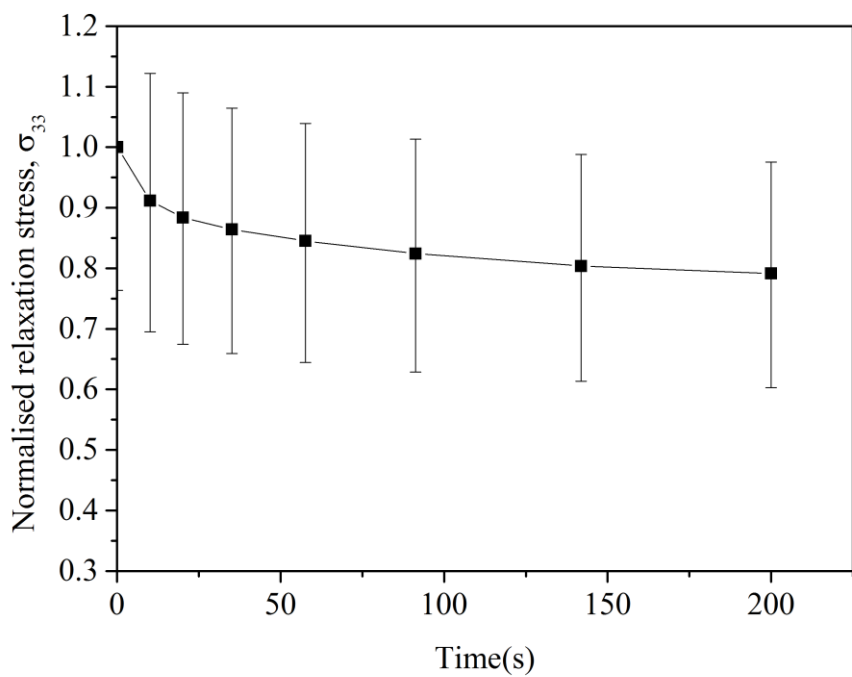
6.2.3 Stress Relaxation over Time

In order to fulfil the process of stress relaxation with time, the tensile/shearing test was imposed on the RVEs by stretching them with a strain of 0.02 at a constant speed. Then the strain was held for a period of 200s. The restoring reaction force with time ($F(t)$) was recorded. The restoring stress (i.e. engineering stress) can be solved by $\sigma(t) = F(t)/A$, where A is the initial cross sectional area. In this way, the relaxation stresses (normalised by $\sigma(0)$), σ_{11} , σ_{33} , σ_{12} and σ_{31} , as a function of time has been demonstrated in Figure 6.4 for the fibre network with a relative density of 0.15. All the data of the stresses in Figure 6.4 are normalised by the instantaneous stresses, which are the stresses when $t = 0$ s. We can see from Figure 6.4 that the decay of the stresses from initial stresses down to the long-term stresses depending on the two

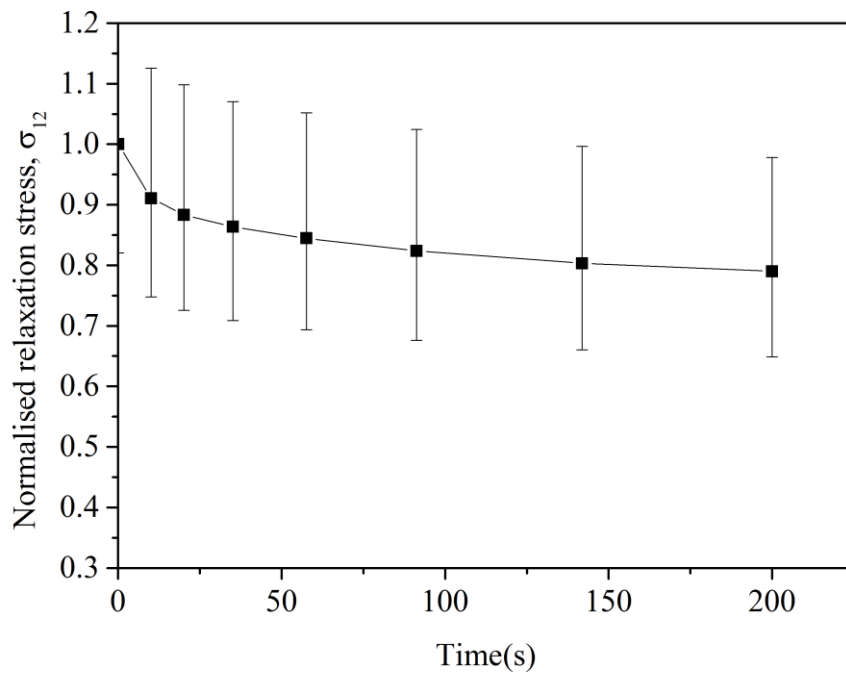
relaxation times τ_1 and τ_2 of two dashpots employed as above. Thus, the further characterisation of the stress relaxation behaviours in terms of the network structure will be conducted according to the same method.



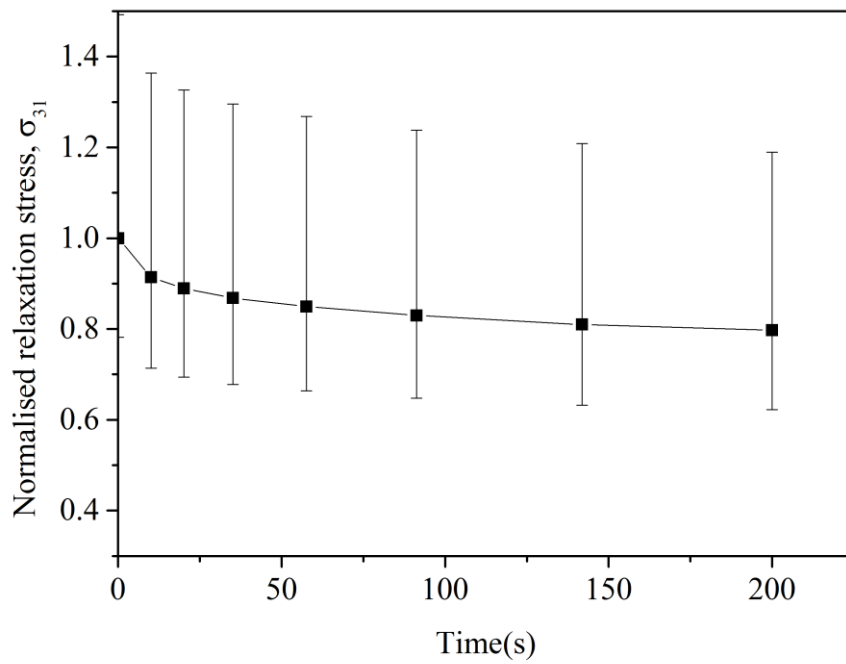
(a)



(b)



(c)



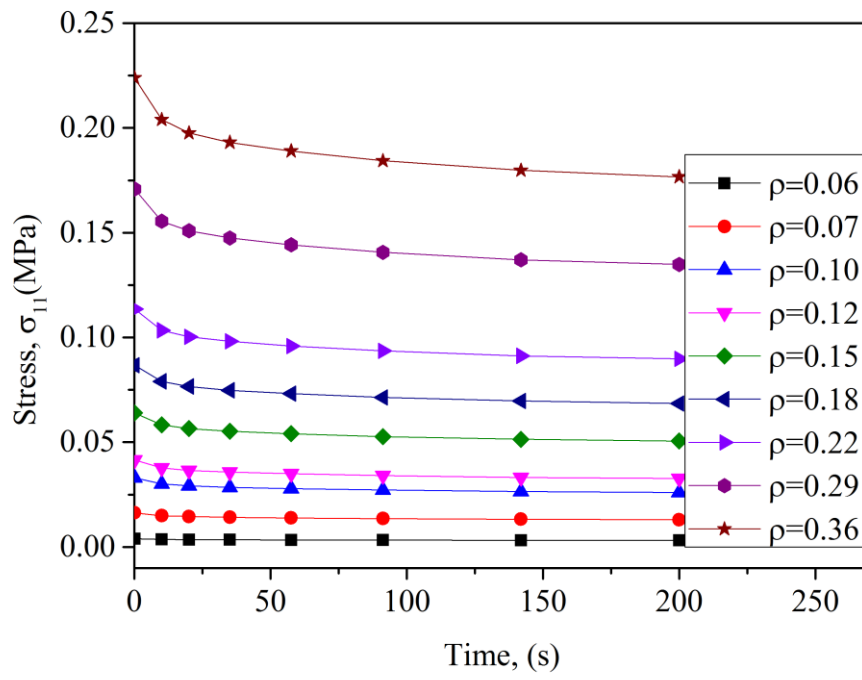
(d)

Figure 6.4. Normalised relaxation stress ((a) σ_{11} , (b) σ_{33} , (c) σ_{12} and (d) σ_{31}) of the collagen fibre network with the relative density of 0.15.

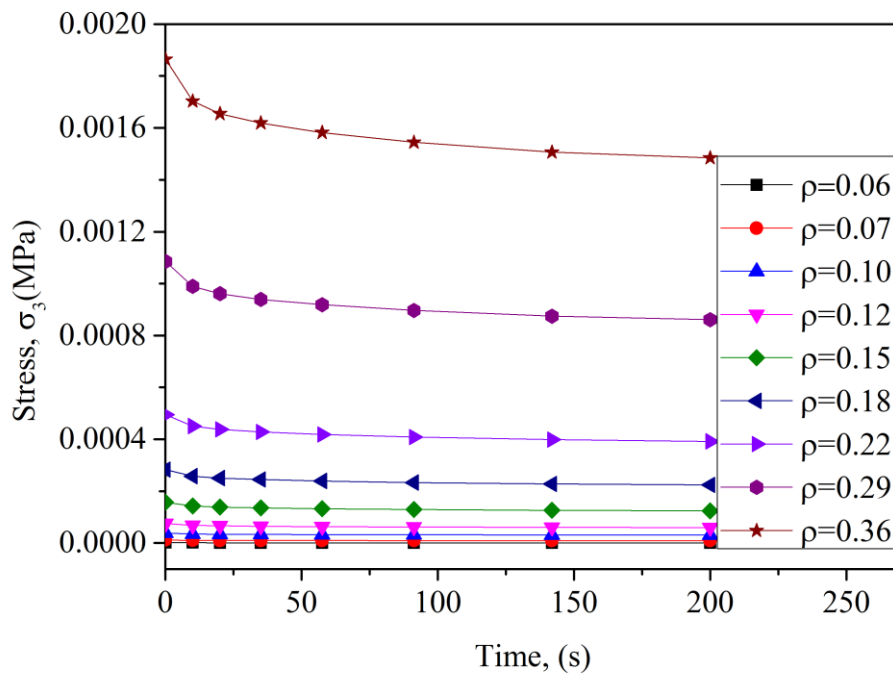
6.2.4 Dependence of Relaxation Modulus on Relative Density

6.2.4.1 Numerical Results

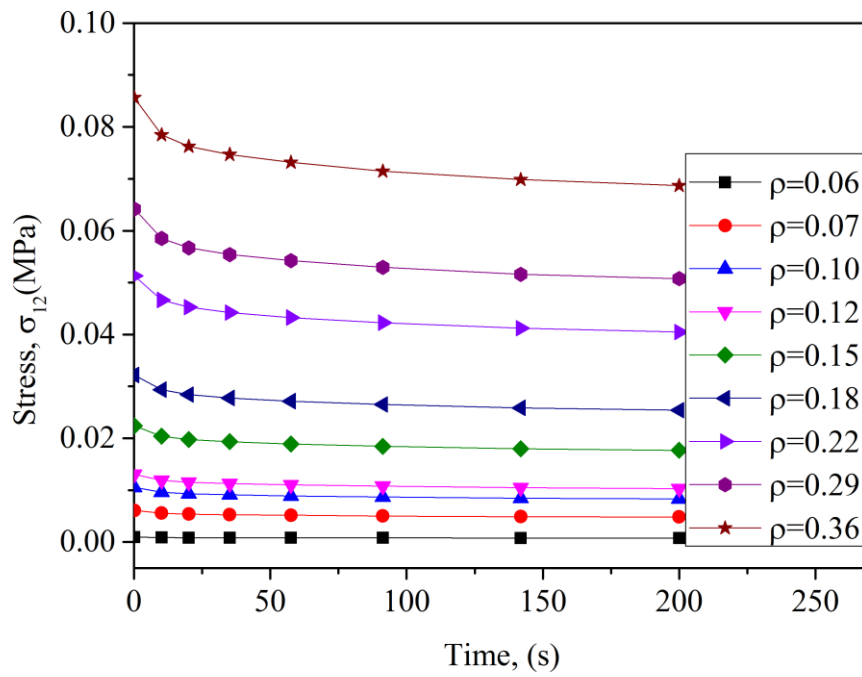
Since relative density in fibre network is the dominated parameter in influencing the elastic properties of the network, it is also very necessary to investigate the effect of relative density on the viscoelastic properties of the network, specifically, relaxation stress/modulus in this study. As shown in Figure 6.5, relaxation tensile and shear stress (i.e. σ_{11} , σ_{33} , σ_{12} and σ_{31}) of the fibre networks with various relative densities ranging from 0.06 to 0.36 have been explored as time progressing while the imposed strain ($\varepsilon = 2\%$) was kept constant for 200s. Generally speaking, σ_{11} , σ_{33} , σ_{12} and σ_{31} all arise as the increase of relative density. Moreover, the in-plane stresses, both tensile stress (σ_{11}) and shear stress (σ_{12}), indicate much larger values than the out-of-plane stresses (σ_{33} and σ_{31}) under the same relaxation time and relative density. This is consistent with the relative in-plane and out-of-plane elastic behaviours of this transversely isotropic structure [260], which also indicates that the relative in-plane and out-of-plane elastic behaviours are not fundamentally altered although there exists stress relaxation of the collagen fibre network.



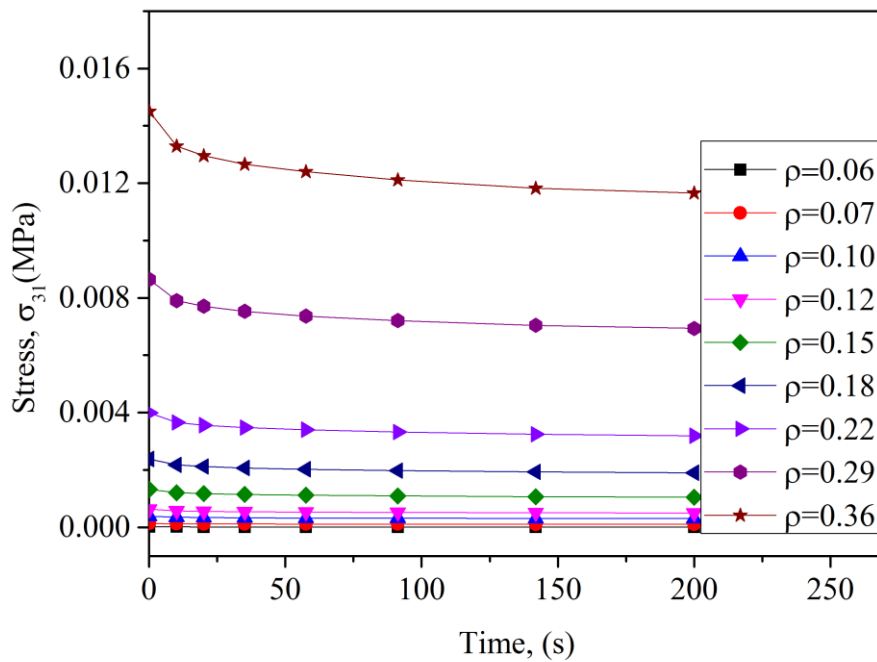
(a)



(b)



(c)

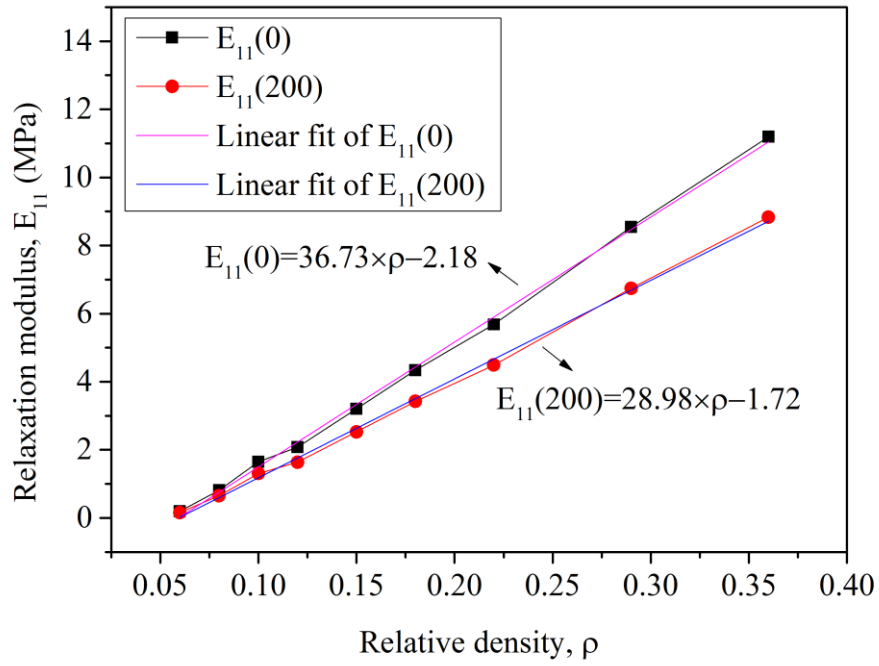


(d)

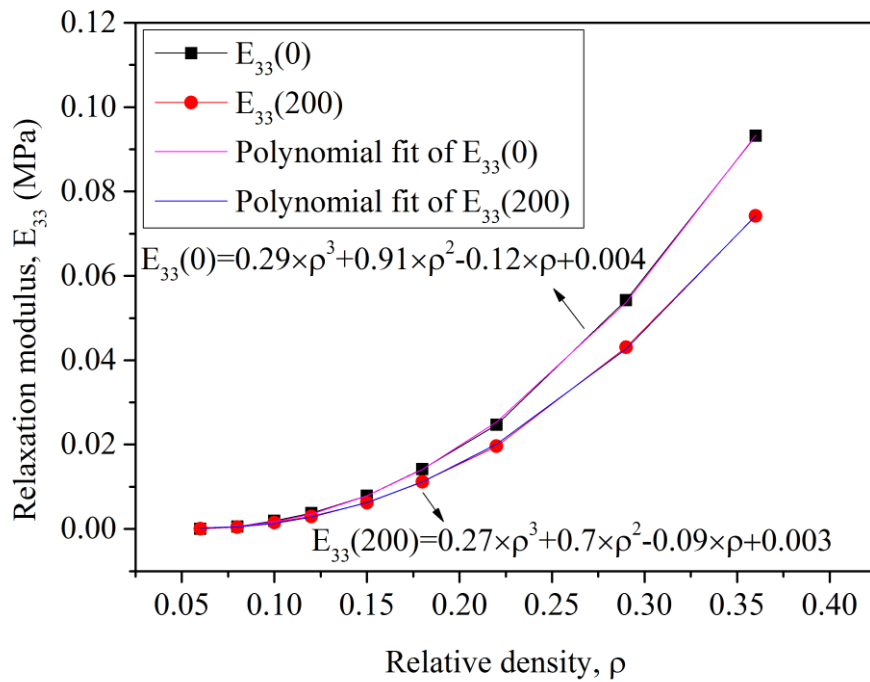
Figure 6.5. Relaxation stress ((a) σ_{11} , (b) σ_{33} , (c) σ_{12} and (d) σ_{31}) of fibre networks with different relative densities (0.06-0.36) under constant strain $\varepsilon = 2\%$.

In order to understand better the influence of relative density on the stress, the relationships between relaxation modulus ($E_{11}(t)$, $E_{33}(t)$, $G_{12}(t)$ and $G_{31}(t)$) and relative density were investigated and the specific results of $E_{11}(t)$, $E_{33}(t)$, $G_{12}(t)$ and $G_{31}(t)$ against relative density when $t = 0\text{s}$ (i.e. Instantaneous relaxation modulus) and $t = 200\text{s}$ (regarded as a long-term stage) have been shown in Figure 6.6. Figure 6.6 (a), the relationships between $E_{11}(0)$ and $E_{11}(200)$ and relative density, demonstrates that both $E_{11}(0)$ and $E_{11}(200)$ possess linear increases with relative density and it can be estimated that $E_{11}(t)$ is proportional to the relative density at any given time t . This indicates the stretching dominated deformation mechanism of the in-plane deformation of the collagen aerogel. By curve fitting, both linear expressions can be approximately obtained as shown in the figure. Since $G_{12} = E/2(1 + \nu)$ for transversely isotropic structures, there is no doubt that $G_{12}(0)$ and $G_{12}(200)$ show similar linear relationships with relative density (see Figure 6.6 (c)).

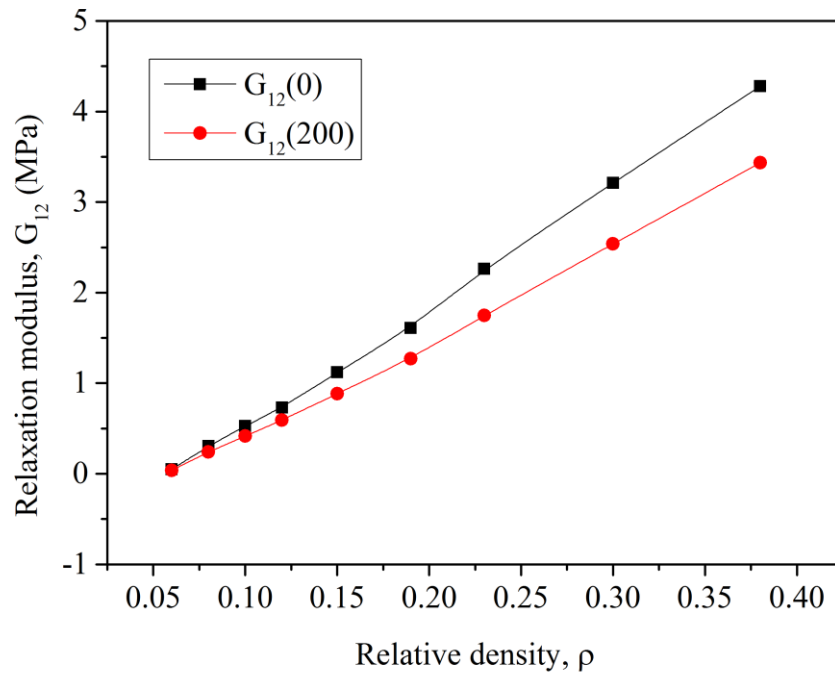
As for the out-of-plane relaxation moduli, $E_{33}(t)$ and $G_{31}(t)$, they exhibit an entirely different trend as the relative density increases as shown in Figure 6.6 (b), $E_{33}(0)$ and $E_{33}(200)$ against relative density, and Figure 6.6 (d), $G_{31}(0)$ and $G_{31}(200)$ against relative density. From Figure 6.6 (b) we can see that $E_{33}(0)$ and $E_{33}(200)$ indicate polynomial relationships with relative density and can be roughly fitted with the cubic polynomials as shown in the figure. Different from the in-plane deformation, the out-of-plane deformation mechanism is bending mechanism. As the the volume fraction increases, which means that the cross-linker density N_c is increasing and there are more intersections among fibres, the fibre segment length l_c is reduced. Thus, the fibre network demonstrates a polynomial rise with respect to volume fraction.



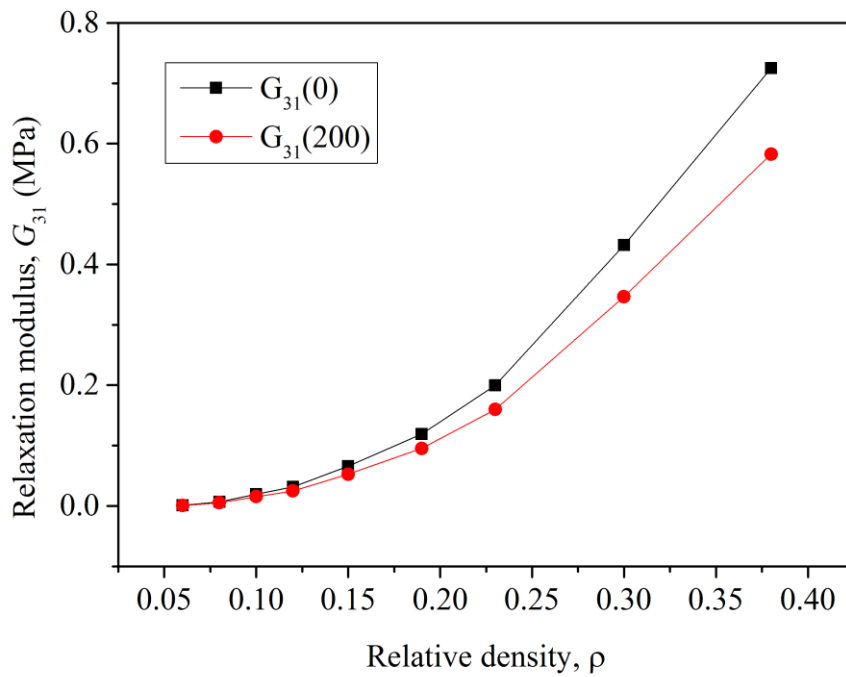
(a)



(b)



(c)



(d)

Figure 6.6. Instantaneous relaxation modulus (i.e. $E(0)$ or $G(0)$) and relaxation modulus at $t = 200$ s (i.e. $E(200)$ or $G(200)$) of fibre networks with different relative densities (0.06-0.36): (a) E_{11} , (b) E_{33} , (c) G_{12} and (d) G_{31} .

6.2.4.2 Analytical Model

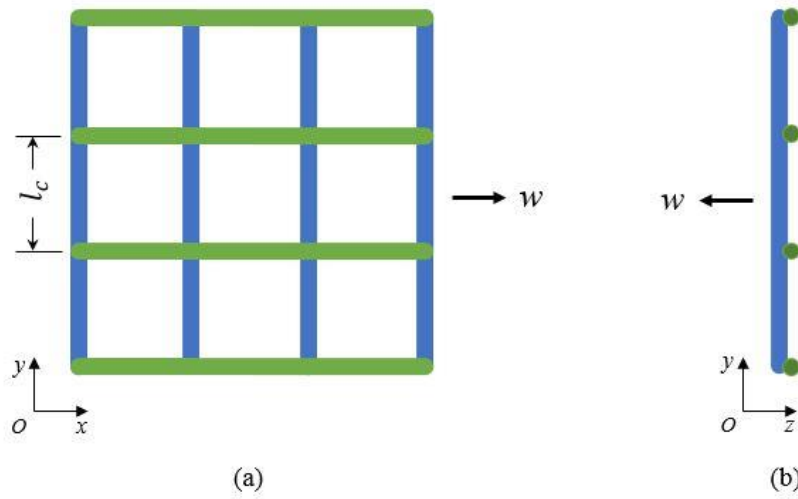


Figure 6.7. A simplified model of cross-linked fibre network with aligned fibres along x and y directions, respectively. (a) In-plane view; (b) Out-of-plane view.

Now that the numerical results of the dependence of relaxation modulus on relative density have been achieved, we also aim to explore the solution to the relationships of both in-plane and out-of-plane relaxation moduli with relative density from the theoretical point of view. To this end, a simplified schematic structure was proposed in Figure 6.7 where all fibres along the x -direction and y -direction, respectively, are well aligned (see Figure 6.7 (a)) and intersected with the overlap coefficient $c = 0.025(N_c + 1)$ (see Figure 6.7 (b)). The whole length of a fibre is L and each segment of it is l_c in length and d in diameter. Then the cross-linker density will be $N_c = L/l_c$. In addition, the value of L/d is fixed.

Firstly, the instantaneous relaxation modulus in the x -direction (i.e. $E_{11}(0)$) will be studied. Taking one fibre segment into consideration, it can be treated as a simply-supported beam [260] and a concentrated transverse load w along the x -direction is applied in the middle. Then the deflection can be given as,

$$\Delta x = \frac{wl_c^3}{48E(0)I} \quad (6.8)$$

where $E(0)$ is the instantaneous relaxation modulus and $I = \pi d^4/64$ is the second moment of the circular cross-section of the fibre.

The stress and strain in the x -direction are given as,

$$\sigma_{11}(0) = \frac{w}{l_c d} \quad (6.9)$$

$$\varepsilon_{11} = \frac{\Delta x}{l_c} = \frac{wl_c^2}{48E(0)I} \quad (6.10)$$

Therefore, the instantaneous relaxation modulus in the x -direction can be obtained as follows:

$$E_{11}(0) = \frac{\sigma_{11}(0)}{\varepsilon_{11}} = \frac{3\pi E(0)}{4} \left(\frac{d}{l_c}\right)^3 \quad (6.11)$$

Since the value of L/d is constant, it indicates that d/l_c is identical to L/l_c , the instantaneous relaxation modulus in the x -direction of the simplified model takes the form,

$$\frac{E_{11}(0)}{E(0)} = \alpha \left(\frac{L}{l_c}\right)^3 = \alpha N_c^3 \quad (6.12)$$

where α is a coefficient.

Eq. (6.12) has indicated an approximate cubic polynomial relation between $E_{11}(0)$ and N_c since $E(0)$ is a constant. As already obtained in Figure 6.6 (a) of the numerical results of $E_{11}(0)$ in terms of ρ , $E_{11}(0)$ can be fitted as a linear relationship with ρ . Since the relative density of the fibre network possesses a similar cubic polynomial relation with N_c as shown in Eq. (4.1), the numerical results also demonstrate an approximate cubic polynomial relation between $E_{11}(0)$ and N_c . Thus the numerical results in Figure 6.6 (a) is consistent with the form in Eq. (6.12).

Similarly, the relaxation modulus in the x -direction in terms of cross-linker density can be expressed as

$$\frac{E_{11}(t)}{E(t)} = \alpha \left(\frac{L}{l_c} \right)^3 = \alpha N_c^3 \quad (6.13)$$

where α is the same coefficient as that in Eq. (6.12). $E(t)$ has been expressed in Eq. (6.1). Therefore, $E_{11}(t)$ always indicates a linear relation with relative density. For instance, $E_{11}(200)$ in terms of relative density has also been plotted in Figure 6.6 (a) and it also demonstrates a linear growth as relative density increases. However, the growth rate tends to slow down as t progressing. This is because, the larger t is, the smaller $E(t)$ is, compared to $E(0)$. Comparing Eq. (6.12) with Eq.(6.13), it can be seen that $E_{11}(t)$ with a certain relative density is getting smaller and smaller as t progressing. Furthermore, it can also be concluded that the modulus change (i.e. $E_{11}(0) - E_{11}(t)$) is becoming larger as the relative density increases under the same relaxation time, in other words, the fibre network loses more modulus when relative density increases.

In terms of the instantaneous relaxation modulus in the z -direction (i.e. $E_{33}(0)$), each fibre segment which is regarded as a simply-supported beam, is subjected to a concentrated transverse load w along the z -direction in the middle. Then the central deflection of the beam is also expressed as

$$\Delta z = \frac{wl_c^3}{48E(0)I} \quad (6.14)$$

where $E(0)$ is the instantaneous relaxation modulus and $I = \pi d^4/64$ is the second moment of the circular cross-section of the fibre.

As there is an overlap with the coefficient of c between the intersected fibres in the x and y directions, respectively, the thickness of the simplified model is $(2d - cd)$

instead of $2d$. Then the strain in the z direction can be given as

$$\varepsilon_{33} = \frac{\Delta z}{d(2 - c)} \quad (6.15)$$

With regards to the stress in the z -direction, the applied concentrated force w is undertaken by $N_c \times N_c$ units in considering an area of $L \times L$ in the x - y plane for analysis.

Thus, the stress in the z -direction is given by

$$\sigma_{33}(0) = \frac{w}{L^2 / N_c^2} = \frac{w}{l_c^2} \quad (6.16)$$

Combining Eq. (6.15) and Eq. (6.16) the instantaneous relaxation modulus in the z -direction can be obtained as

$$E_{33}(0) = \frac{\sigma_{33}(0)}{\varepsilon_{33}} = \frac{3\pi(2 - c)E(0)}{4} \left(\frac{d}{l_c}\right)^5 \quad (6.17)$$

As the value of L/d is constant, it indicates that d/l_c is identical to L/l_c . Moreover, the overlap coefficient c takes the form $c = 0.025(N_c + 1)$. Therefore, the instantaneous relaxation modulus in the z -direction of the simplified model takes the form,

$$\frac{E_{33}(0)}{E(0)} = \frac{3\pi(2 - c)}{4} \left(\frac{d}{l_c}\right)^5 = pN_c^6 + qN_c^5 \quad (6.18)$$

where p and q are coefficients, which could be determined by data fitting.

Eq. (6.18) has indicated an approximate polynomial of degree six for the relationship between $E_{33}(0)$ and N_c . The numerical results of the fibre network in Figure 6.6 (c) have revealed that $E_{33}(0)$ can be fitted as a cubic polynomial relationship with the relative density ρ whereas the relative density ρ of the fibre network possesses a cubic polynomial relation with N_c as shown in Eq. (4.1). Therefore $E_{33}(0)$ also demonstrates a polynomial relationship of degree six with N_c from the numerical

analysis, which corresponds to Eq. (6.18) that is derived from theoretical analysis.

Not surprisingly, $E_{33}(t)$ also illustrates a similar polynomial trend with relative density as $E_{33}(0)$ and the difference between $E_{33}(0)$ and $E_{33}(t)$ is getting larger with relaxation time t increasing.

6.3 Viscoelastic Properties of Collagen Fibre

Network Hydrogel

In section 6.2, the stress relaxation of the collagen fibre network alone has been investigated. However, in most tissues, collagen fibrils are generally immersed in a ground substance composed of proteoglycans, water, cells and other nonfibrillar proteins [285] which also react to the collagen's support and the hybrid structure can be similar to hydrogels. Therefore, the viscoelastic properties, i.e. stress relaxation and creep, of the fibre network collagen hydrogel is to be studied in this section.

6.3.1 Geometry and Material Properties

The fibre network composite structure constructed according to the procedure in Chapter 3 can be directly adopted for the viscoelasticity analysis of collagen hydrogels. The beam fibre network serves as the collagen fibril network, such as the cytoskeleton, and the matrix is regarded as cytosol. Since the matrix is characterised by solid elements in the geometrical model while the ground substance in tissues is fluid which exhibits fluidity, there is an assumption that analysis is focused on quasi-static state and the fluidity is small enough to be neglected due to the intramolecular interactions among fibres [286]. Therefore, the matrix in collagen hydrogels is

simplified as an incompressible fluid and the collagen hydrogel is assumed to possess no volume loss when subjected to load [285]. Thus, the isotropic and incompressible ground substance can be represented by the Neo-Hookean hyperelastic model as [212]

$$W_m = \frac{\mu}{2}(I_1 - 3) - \frac{\mu}{2\gamma}(I_3^{-\gamma} - 1) \quad (6.19)$$

where W_m is the Neo-Hookean strain energy potential and, $I_1 = \text{tr}\mathbf{C}$ and $I_3 = \det\mathbf{C}$ are the first and third invariants of the right Cauchy-Green deformation tensor \mathbf{C} . $\mu = 26\text{KPa}$ for the shear modulus of the ground substance [287]. $\gamma = 0.49$ [212].

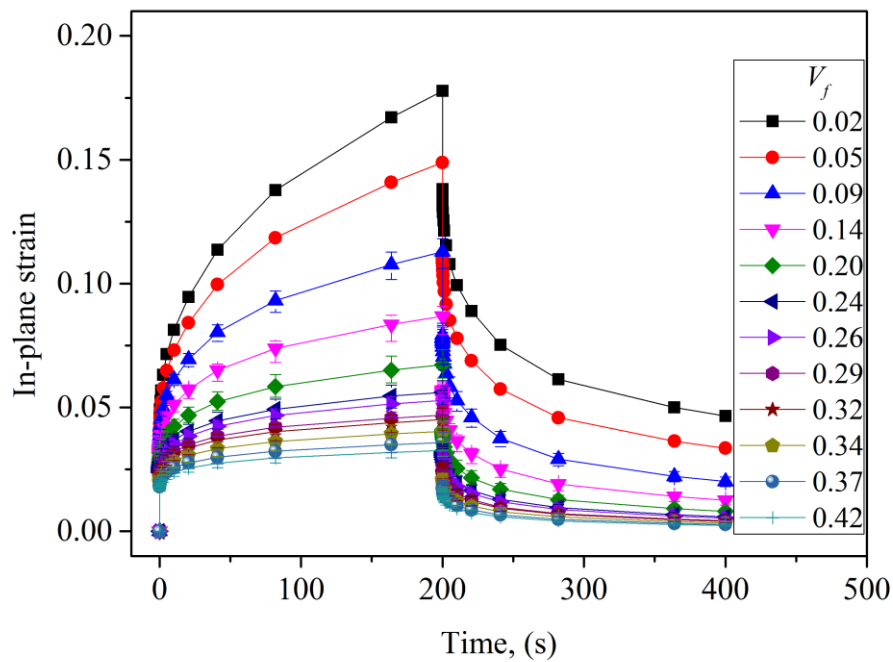
Furthermore, the same Maxwell-Weichert model as given in Section 6.2.1.2 is applied to the type I collagen fibril. Then the total strain energy density of the collagen hydrogel is assumed to be the sum of the strain energy density of the collagen network and that of the ground substance. In this way, the viscoelastic behaviours of the collagen fibril hydrogel are evaluated through the FEA method.

6.3.2 Creep

6.3.2.1 Creep under Constant Stress

Collagen gels exhibit the creep characteristic, more specifically, strain rises with time gradually, when undergoing a constant stress. Therefore, in order to study the creep of the collagen gel with the novel transversely isotropic fibre network, a constant normal tensile stress of 1MPa has been applied to the fibre network collagen gels with different volume fractions from $t = 0\text{s}$ until $t = 200\text{s}$, followed by a strain release process, which means that the applied stress has been dismissed, for another 200s from $t = 200\text{s}$ to $t = 400\text{s}$.

The constant stress has been applied to the x -direction and z -direction, respectively, and both the in-plane and out-of-plane strain changes with time have been obtained and shown in Figure 6.8 (a) and (b). It can be seen from the figures that it indicates a continuous increase of the strain over time but with reducing strain rates when the collagen gels are imposed the constant stress for $t = 0-200$ s. It can be seen that the strain tends to reach the limit at the infinite time and is determined by the applied constant stress and, the combination of the time-independent elastic modulus of the fibre network and elastic modulus of the matrix. We can see from Figure 6.8 (b) that the maximum strain when $t = 200$ s approaches nearly 0.2 and this can be much larger when the constant stress is applied for longer time according to the strain rate at $t = 200$ s.



(a)

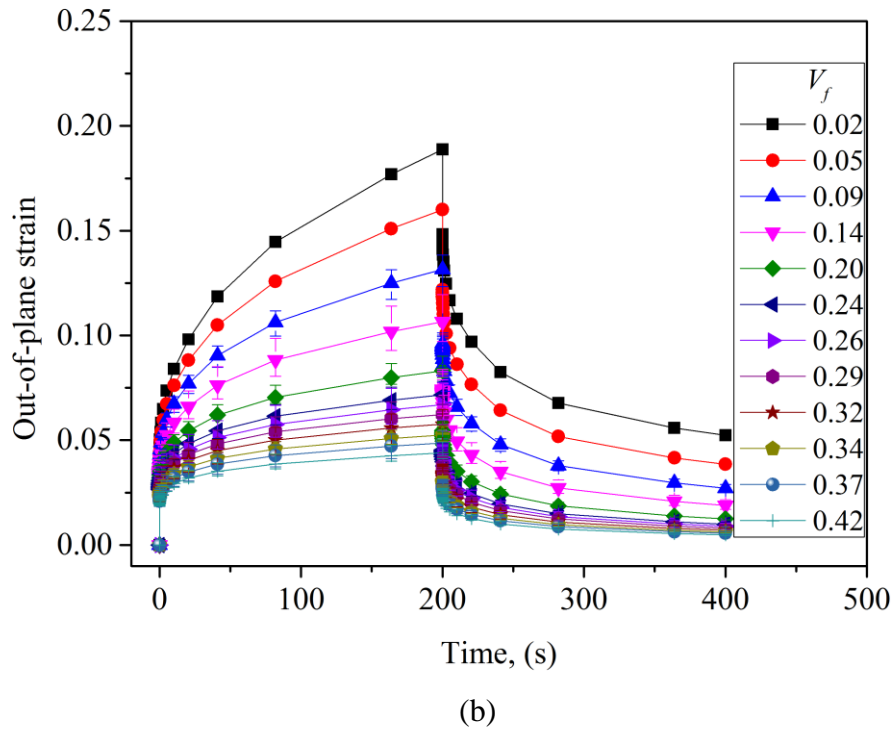


Figure 6.8. Time-dependent in-plane (a) and out-of-plane (b) strain changes of collagen gels with different volume fractions (0.02-0.42) under the constant stress $\sigma = 1\text{MPa}$. The constant stress is imposed on the collagen gels from $t = 0\text{s}$ to $t = 200\text{s}$ and then released from $t = 200\text{s}$.

When the constant stress is removed from $t = 200\text{s}$, the strain drops off gradually and there still exists a residual strain after 200s relaxation, which implies that the fibre network collagen gel takes a longer time to release the strain compared to the loading procedure. Furthermore, fibre network collagen gels with smaller volume fractions indicate larger strains, both after the loading and the releasing. This will be discussed in detail in the next section 6.3.2.2.

6.3.2.2 Dependence of strain on the volume fraction

As volume fraction is a crucial parameter in determining the mechanical properties,

including viscoelasticity, of the fibre network collagen gels, the dependences of the strains after loading for 200s ($t = 200\text{s}$) and the strains after load removed for 200s ($t = 400\text{s}$) have been shown in Figure 6.9. Both the in-plane and out-of-plane strains (i.e. ε_{11} and ε_{33}) have also been displayed in Figure 6.9 for comparison.

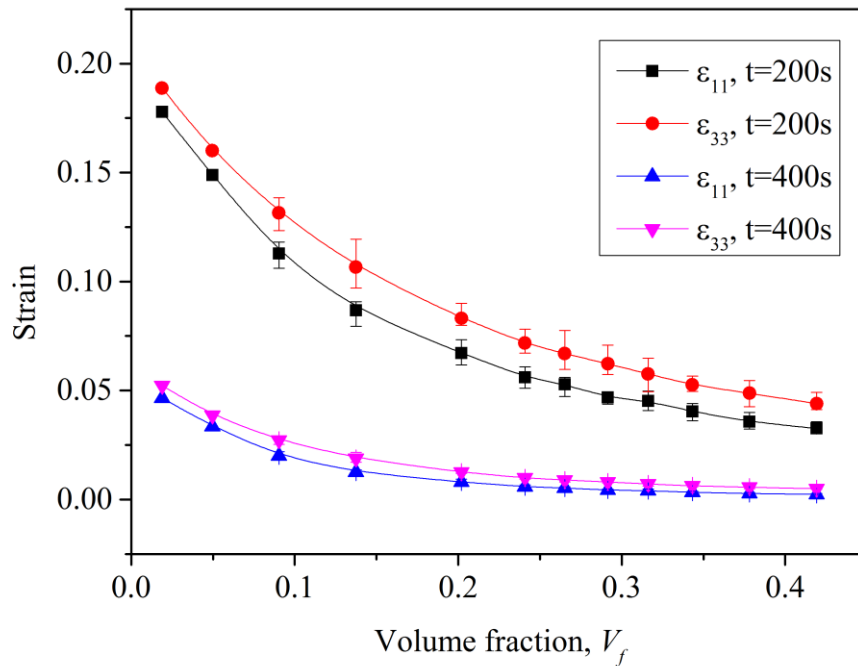


Figure 6.9. Dependence of in-plane strain (ε_{11}) and out-of-plane strain (ε_{33}) of collagen gels on volume fractions. Both the strains when a constant stress has been applied for 200s ($t = 200\text{s}$) and the strains after the constant stress has been removed for 200s ($t = 400\text{s}$) have been shown in this figure.

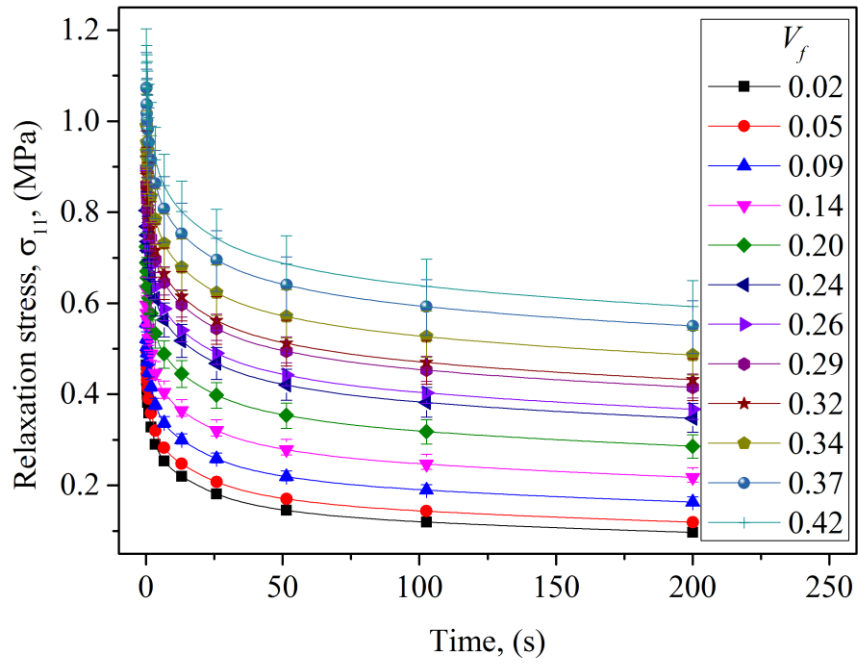
When $t = 200\text{s}$ after the constant stress has been applied for 200s, both in-plane strain (square dotted curve) and out-of-plane strain (circle dotted curve) decrease as the volume fraction increases. The same trend has also happened to the in-plane strain (upwards triangle dotted curve) and out-of-plane strain (downwards triangle dotted curve) when $t = 400\text{s}$ after the constant stress has been removed for 200s. This is mainly due to the increased stiffness of the fibre network as volume fraction increases

which leads to more effort to deform under load and less time to restore after the load is released. Moreover, the in-plane strains are smaller than the out-of-plane strains for all the different volume fractions when $t = 200\text{s}$ and $t = 400\text{s}$, on account of the larger stiffness in the in-plane direction than that in the out-of-plane direction.

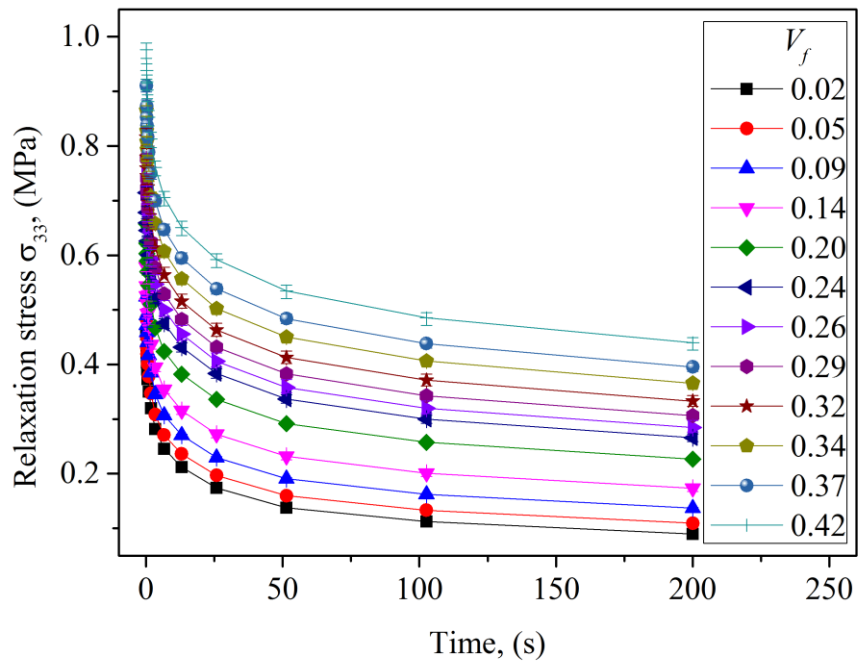
6.3.3 Stress Relaxation

6.3.3.1 Stress Relaxation over Time

A tensile/shear strain of 2% is applied to the fibre network collagen gels and has been held constantly over time to study the stress relaxation. Figure 6.10 (a)-(d) are the in-plane and out-of-plane tensile and shear stresses relaxation over time separately. All the relaxation stresses, either in tensile or in shear states, have indicated dramatic drops at the very early stage and then tend to reach a balance after a long period of relaxation. In addition, the relaxation stresses of fibre network collagen gels with different volume fractions have also been illustrated in the same figures in Figure 6.10. Generally speaking, the larger the volume fraction of fibre network collagen gel is, the larger the relaxation stress is under the same relaxation time. In other words, relaxation stress increases as volume fraction increases and the relationship between relaxation stress/modulus and volume fraction will be discussed in details in the following sections (see 6.3.3.2).



(a)



(b)

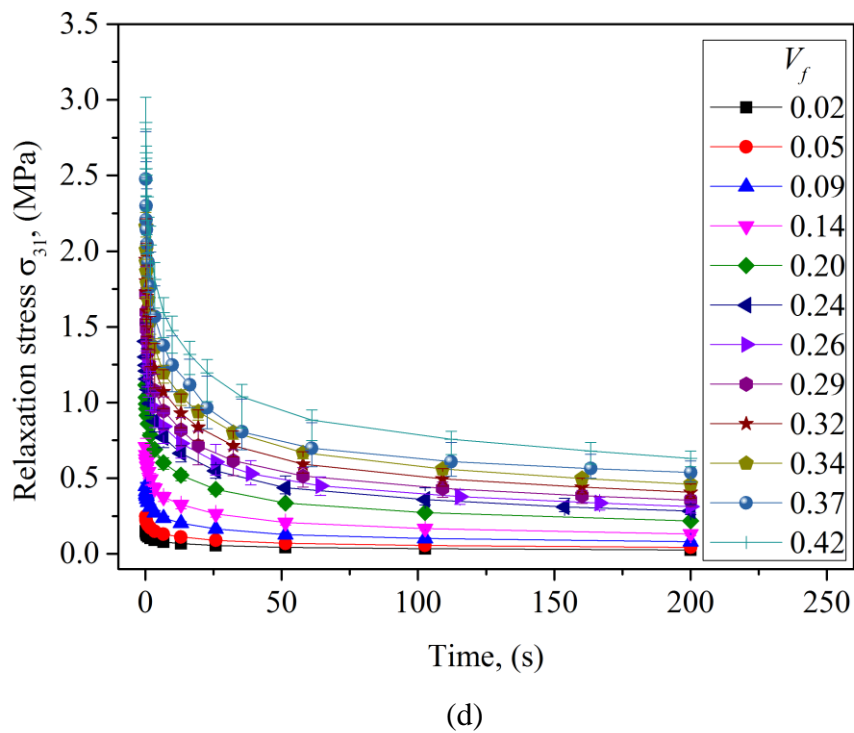
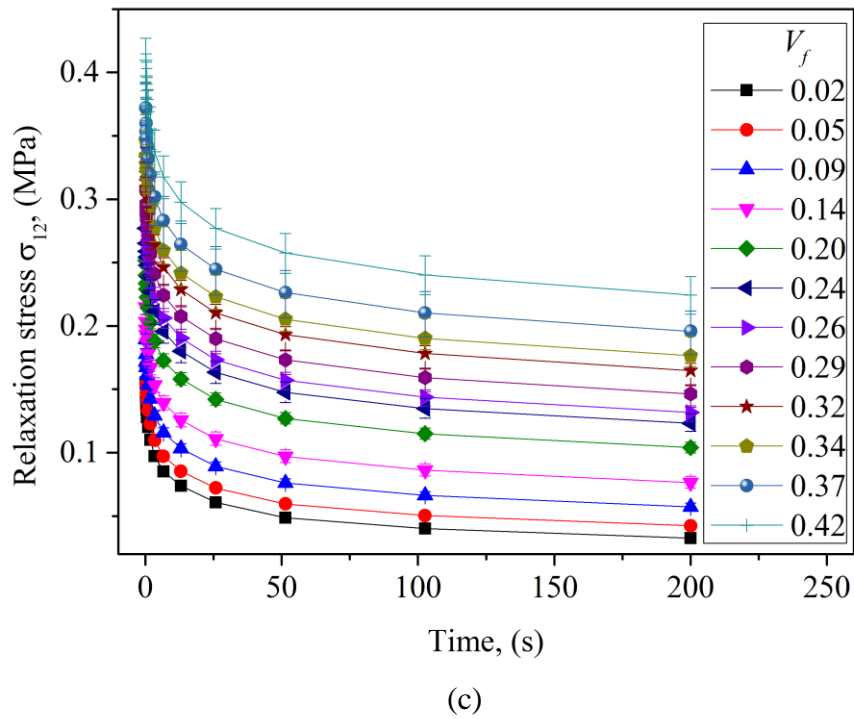
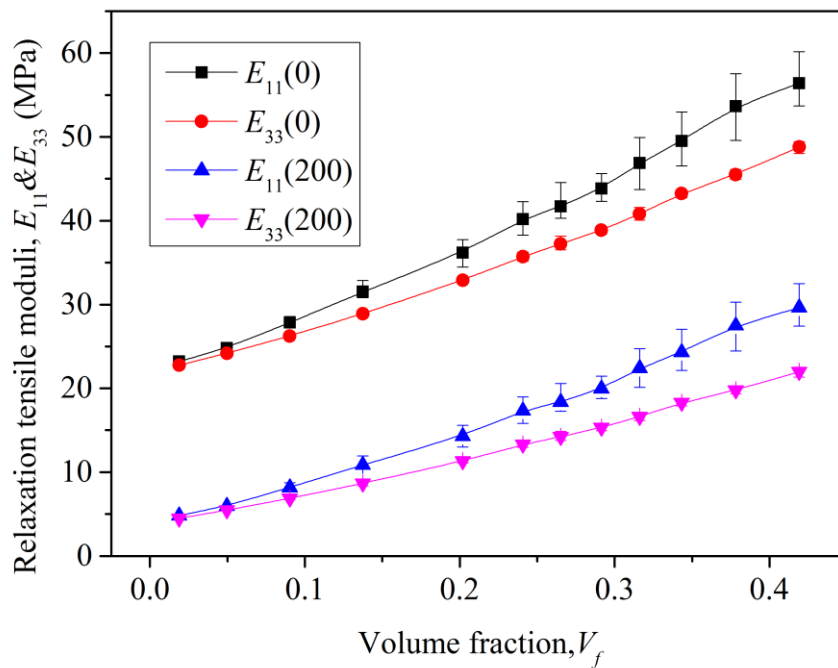


Figure 6.10. Relaxation stress ((a) σ_{11} , (b) σ_{33} , (c) σ_{12} and (d) σ_{31}) of collagen gels with different volume fractions (0.02-0.42) under constant strain $\varepsilon = 2\%$.

6.3.3.2 Dependence of Relaxation Modulus on the Volume Fraction

In this section, following the results of stress relaxation over time in 6.3.3.1, we aim to investigate the relationship between relaxation modulus and volume fraction regarding the designed fibre network collagen gel. As shown in Figure 6.11 (a) and (b), the in-plane and out-of-plane relaxation moduli under tension and shearing strain constant of 2%, respectively, have been illustrated for comparison. Furthermore, both the instantaneous relaxation moduli $E(0)$ and $G(0)$ (i.e. relaxation moduli when $t = 0$ s) and $E(200)$ and $G(200)$ (i.e. the relaxation moduli at $t = 200$ s) in terms of volume fraction have been demonstrated in Figure 6.11. We can see that both the in-plane and out-of-plane relaxation moduli under tension exhibit a nearly proportional relation with volume fraction and this trend is not affected by time. Furthermore, it is not surprising that the in-plane relaxation modulus is much larger than the out-of-plane relaxation modulus.



(a)

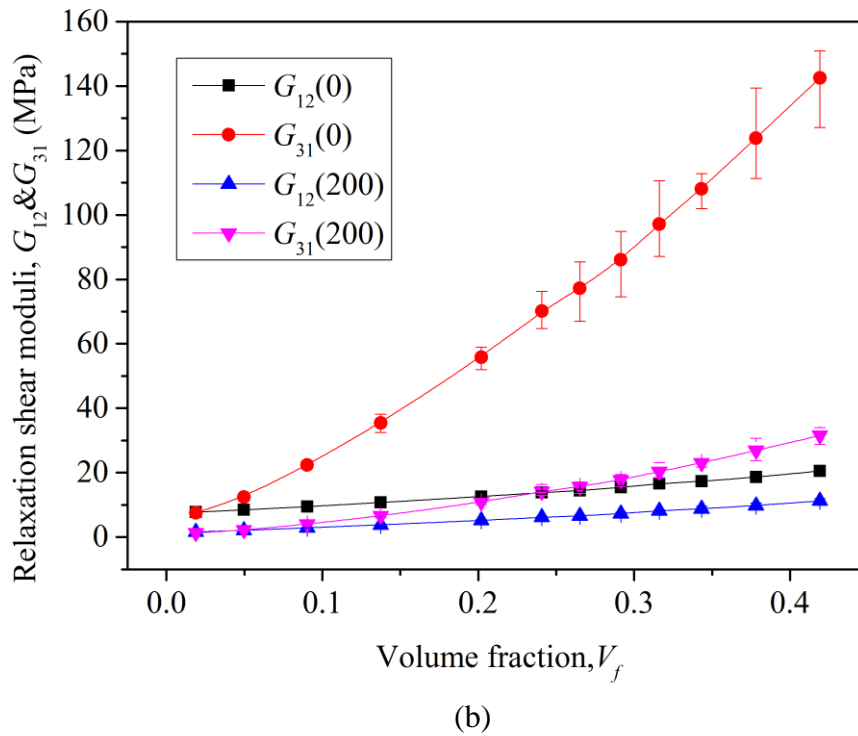


Figure 6.11. Comparison of in-plane and out-of-plane relaxation moduli of collagen gels with different volume fractions (0.02-0.42) under constant tension (a) or hearing (b) strain $\varepsilon = 2\%$. $E(0)$ and $G(0)$ are the instantaneous relaxation moduli, i.e. the relaxation moduli when $t = 0$ s. $E(200)$ and $G(200)$ are the relaxation moduli at $t = 200$ s under constant strain $\varepsilon = 2\%$.

6.4 Discussions

As both the fibre network alone and the fibre network surrounded by ground substances are investigated regarding the viscoelastic behaviours, the difference of the corresponding results can only be owing to the effect that the ground substance brings about to the collagen gel. In tissues, the role of the ground substance cannot be neglected in terms of the overall mechanical properties of the tissues [258]. By comparing the relaxation moduli of the fibre network alone (see Figure 6.6) and the fibre network surrounded by ground substances (see Figure 6.11), we can see that the

corresponding moduli have been dramatically enhanced for the fibre network model with ground substances. Thus, the ground substance exhibits a non-negligible effect in supporting the fibre network and restraining the deformation of the fibre network. In addition, if we compare the out-of-plane relaxation moduli of the aerogel and the hydrogel, we can see that there is a polynomial increase in E_{33} for the aerogel (see Figure 6.6(a)) while there is a linear increase in E_{33} for the hydrogel (see Figure 6.11(a)). This is expected to be attributed to the constraint of ground substance to the fibre deformation. Due to the introduction of the ground substance, the bending deformation is largely constrained and, instead, stretching becomes the dominated deformation mode. Therefore, the out-of-plane deformation becomes linear in terms of volume fraction. Moreover, the ground substance is modelled as incompressible and there is no volume loss in this research. However, the fluid flow and exudation are the key features in the real situations of tissues, which may weaken the modulus. Thus, the simplified model in this research may have overestimated the modulus. Some analytical models have been studied towards the fluid flow in tissues [250, 254, 258, 259, 288], which, however, is not the focus of this research. The research only considers the small-scale motion case of the ground substance.

In order to evaluate the improvement of the viscoelastic behaviours introduced by the fibre network to the composites, we also compare relaxation modulus of the proposed fibre network composite with that of the randomly dispersed short-fibre composites with glass fibres and polymer matrix [289]. Obaid et al. [289, 290] have proposed an analytical model of stress relaxation corresponding to the randomly distributed short-fibre composites and conducted the FE simulations for comparison. With the fibres defined as linear elastic and the matrix defined as a viscoelastic material, both the analytical (see the red curve in Figure 6.12) and FEA (see the

square dots in Figure 6.12) results of the instantaneous modulus of the random short-fibre composites during the stress relaxation are presented in Figure 6.12. Meanwhile, the instantaneous modulus results of our proposed geometry model are also shown as up-triangle dots in Figure 6.12 for various volume fractions.

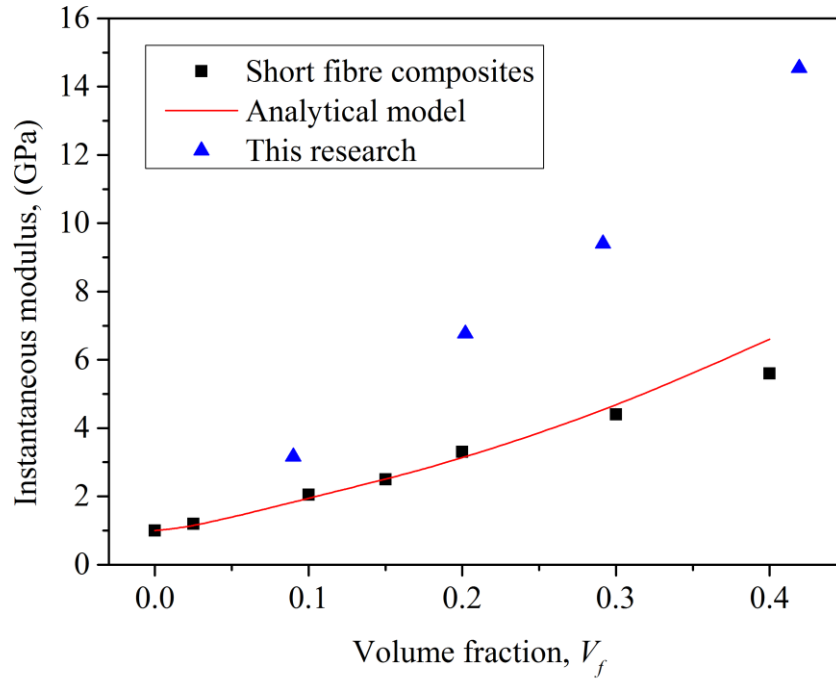


Figure 6.12. Comparison of the instantaneous moduli of the fibre network composites and random short fibre composites.

We can see from the figure that the proposed fibre network composites outweigh the dispersed short-fibre composites in the instantaneous modulus and the difference is expanded as the volume fraction increases. This has indicated the advantage of the fibre network over the dispersed fibres in enhancing the viscoelastic behaviours and the effect is getting more remarkable as the volume fraction increases due to the reason that more cross-linkers are introduced according to the relation of volume fraction with cross-linker density as shown in Eq. (4.1) and the enhancement by the cross-linkers is dramatically highlighted for larger volume fraction. Furthermore, it

can also be boldly estimated that the long-term modulus also exerts the similar relationship between the two types of composite structures since the stress will be relaxed at the same pace accordingly.

6.5 Conclusions

Fibre-network structure has been widely observed in biomaterials. Thus the viscoelastic properties of collagen aerogel and hydrogel have been investigated with respect to the transversely isotropic fibre network geometry.

For the collagen aerogel, the in-plane relaxation modulus indicates a linear relationship with relative density while the out-of-plane relaxation modulus demonstrates a cubic polynomial relation with relative density. These relations have been verified by a simplified analytical model. These results also indicate that the out-of-plane modulus grows faster than the in-plane modulus as the relative density rises.

For the collagen hydrogel, it illustrates a larger in-plane strain than the out-of-plane strain under constant stress. Moreover, the in-plane and out-of-plane strains decrease as volume fraction increases. When applied a constant tensile strain, both the in-plane and out-of-plane relaxation moduli exhibit a nearly proportional relation with volume fraction and the in-plane relaxation modulus is larger than the out-of-plane relaxation modulus.

Chapter 7 Conclusions and Further

Research

7.1 Conclusions

This research has proposed a novel fibre network composite model in which fibres are divided into continuous segments and intersected to generate a network. It is worth noting that the fibre network composite structure is transversely isotropic instead of commonly isotropic. This structure exists in various areas, for instance, biology and industry, and is expected to exhibit a wide range of promising applications when there is load-orientation preference.

In order to fully study the elasticity of the proposed fibre network composite, all the five independent constants required in characterising a transversely isotropic structure have been investigated through the geometrical model. Due to the orientation priority of fibre segments in the in-plane directions, the in-plane stiffness is superior to the out-of-plane stiffness. Moreover, the normalised in-plane stiffness has revealed a linear relation with volume fraction whereas the normalised out-of-plane stiffness has demonstrated a polynomial relation with volume fraction when the volume fraction remains not too large, which indicates that the out-of-plane stiffness grows faster than the in-plane stiffness as the volume fraction increases. This is due to the increasing quantity of cross-linkers in the out-of-plane direction as we raise the volume fraction, thus enhancing the out-of-plane stiffness dramatically. The fibre network composite is found to have improved elastic properties compared to other types of fibre composites. Another advantage of this fibre network composite

lies in that the fibre network, as a whole single ply, can dramatically improve the problem of delamination among fibres and prevent crack generation and progressing. As a plate structure, the thickness of the fibre network composite plate is adjustable and can be tailored as demand in the industry according to the combined requirements of plate thickness and mechanical behaviours. This can simplify the manufacturing process while maintaining improved mechanical behaviours, especially in the through-thickness direction. These results have met the intention of designing this transversely isotropic fibre network composite geometry with vertical cross-linkers.

In terms of the elastoplastic properties of the fibre network composite, the steel fibre composite with brittle and ductile matrices, respectively, have been investigated. The axial yield strengths and strains are determined by Johnson's apparent elastic limit method due to the lack of exact yield points through the axial stress-strain responses. There is an interesting finding that the fibre network composite structure exhibits a larger out-of-plane yield strength than the in-plane yield strength although the out-of-plane stiffness is smaller than the in-plane stiffness. This is related to the matrix properties. The introduction of the matrix into the fibre network has increased the out-of-plane yield strength more drastically compared to the in-plane yield strength. Further exploration of the in-plane and out-of-plane yield surfaces under biaxial stress states indicate that the yield strengths meet the Hill yield criterion. As a key parameter of the fibre network composite, volume fraction also affects the yield behaviours. It is found that the rise of volume fraction can enhance both in-plane and out-of-plane tensile and shearing yield strengths. As volume fraction increases, both in-plane and out-of-plane yield surfaces are expanded. However, the out-of-plane angle of tilt of the steel/PA-6 composite shows no major difference, except when the volume fraction is as large as 0.42. As a comparison, the out-of-plane angle of tilt of

the steel/828LVEL composite decreases as volume fraction increases. Furthermore, the addition of shear loading reduces the yield strength or yield surface, both in-plane and out-of-plane. An analytical model based on the incremental method has been proposed and has successfully predicted the yield point of the simplified RVE.

The application of fibre network structure in biomaterials has been investigated by studying the stress relaxation and creep behaviours of both collagen aerogel and hydrogel. For the collagen aerogel, the in-plane relaxation modulus exhibits a linear relationship with relative density while the out-of-plane relaxation modulus demonstrates a cubic polynomial relation with relative density, which indicates that the out-of-plane modulus grows faster than the in-plane modulus as relative density rises. These relations have been verified by a simplified analytical model. The collagen hydrogel illustrates a larger in-plane strain than the out-of-plane strain under constant stress. Furthermore, the in-plane and out-of-plane strains decrease as volume fraction increases. When applied a constant tensile strain, both the in-plane and out-of-plane relaxation moduli exhibit a nearly proportional relation with volume fraction and the in-plane relaxation modulus is much larger than the out-of-plane relaxation modulus. The comparison of stress relaxation results between the aerogel and hydrogel indicates that the ground substance exhibits a non-negligible effect in supporting the fibre network and restraining the deformation of the fibre network. Due to the introduction of the ground substance, the bending deformation is largely constrained and, instead, stretching becomes the dominated deformation mode.

7.2 Further Research

Explorations of the elasticity, elastoplasticity and viscoelasticity have been

conducted on the designed transversely isotropic fibre network composite in this research. Yet there is more to be done mainly in terms of the fibre-network structure.

Firstly, only overlap (with overlap coefficient $c=0-0.7$) is considered for the connection among the fibres in the current work. However, there also exists situations that fibres are connected by extra cross-linkers which are comprised of a certain collagen in biomaterials. In this situation, there is no overlap among fibres but still connected, or in other words, the overlap coefficient will be negative and the length of the added beam should be larger than the sum of the radii of the connected fibres. In this way, the model can be extended to also include structures in which individual fibres are connected with extra cross-linkers.

Secondly, the individual generated fibres are initially straight in this geometry. However, the generated fibres, such as the ones from the electrospinning technique [291], are usually curved along the in-plane direction. Thus, this improvement can be considered in the further study.

Thirdly, in the investigation of viscoelasticity of collagen hydrogel, the fluid matrix is assumed to introduce very limited motion around the fibre-network. Further exploration might be conducted to consider the situation with the large-scale motion of fluid matrix inside the fibre network.

Moreover, more mechanical properties based on this designed fibre-network composite can be investigated to better understand the properties of this structure and find more promising applications of it. Lastly, since this structure can also be promising in thermal or electric conduction application, these areas can also be further explored.

References

- [1] Pernice, M. F. and De Carvalho, N. V. and Ratcliffe, J. G. et al. 2015. Experimental study on delamination migration in composite laminates. *Composites Part A: Applied Science and Manufacturing*. 73, pp. 20-34.
- [2] Lu, Z. and Yuan, Z. and Liu, Q. 2014. 3D numerical simulation for the elastic properties of random fiber composites with a wide range of fiber aspect ratios. *Computational Materials Science*. 90, pp. 123-129.
- [3] Pan, Y. and Lorga, L. and Pelegri, A. A. 2008. Analysis of 3D random chopped fiber reinforced composites using FEM and random sequential adsorption. *Computational Materials Science*. 43(3), pp. 450-461.
- [4] Lau, K.-t. and Hung, P.-y. and Zhu, M.-H. et al. 2018. Properties of natural fibre composites for structural engineering applications. *Composites Part B: Engineering*. 136, pp. 222-233.
- [5] Zhu, H. X. and Hobdell, J. R. and Windle, A. H. 2000. Effects of cell irregularity on the elastic properties of open-cell foams. *Acta Materialia*. 48(20), pp. 4893-4900.
- [6] Zhu, H. X. and Mills, N. 2000. The in-plane non-linear compression of regular honeycombs. *International Journal of Solids and Structures*. 37(13), pp. 1931-1949.
- [7] Hirokawa, N. and Glicksman, M. A. and Willard, M. B. 1984. Organization of mammalian neurofilament polypeptides within the neuronal cytoskeleton. *The Journal of Cell Biology*. 98(4), p. 1523.
- [8] Nam, S. and Hu, K. H. and Butte, M. J. et al. 2016. Strain-enhanced stress relaxation impacts nonlinear elasticity in collagen gels. *Proceedings of the National Academy of Sciences*. 113(20), pp. 5492-5497.
- [9] Jin, T. and Stanciulescu, I. 2016. Numerical simulation of fibrous biomaterials with randomly distributed fiber network structure. *Biomechanics and Modeling in Mechanobiology*. 15(4), pp. 817-830.
- [10] Zhao, T. F. and Chen, C. Q. and Deng, Z. C. 2016. Elastoplastic properties of transversely isotropic sintered metal fiber sheets. *Materials Science and Engineering: A*. 662, pp. 308-319.
- [11] Zhou, W. and Wang, Q. H. and Ling, W. S. et al. 2014. Characterization of three- and four-point bending properties of porous metal fiber sintered sheet. *Materials & Design*. 56, pp. 522-527.
- [12] Zhao, T. F. and Jin, M. Z. and Chen, C. Q. 2013. A phenomenological elastoplastic model for porous metal fiber sintered sheets. *Materials Science and Engineering: A*. 582, pp. 188-193.
- [13] Liu, Q. and Lu, Z. and Zhu, M. et al. 2014. Experimental and FEM analysis of the compressive behavior of 3D random fibrous materials with bonded networks. *Journal of materials science*. 49(3), pp. 1386–1398.

- [14] Zhou, W. and Tang, Y. and Pan, M. Q. et al. 2009. Experimental investigation on uniaxial tensile properties of high-porosity metal fiber sintered sheet. *Materials Science and Engineering: A*. 525(1-2), pp. 133-137.
- [15] Zhou, W. and Tang, Y. and Liu, B. et al. 2012. Compressive properties of porous metal fiber sintered sheet produced by solid-state sintering process. *Materials & Design*. 35, pp. 414-418.
- [16] Jayanty, S. and Crowe, J. and Berhan, L. 2011. Auxetic fibre networks and their composites. *physica status solidi (b)*. 248(1), pp. 73-81.
- [17] Zhang, Y. and Lu, Z. and Yang, Z. et al. 2017. Compression behaviors of carbon-bonded carbon fiber composites: Experimental and numerical investigations. *Carbon*. 116, pp. 398-408.
- [18] Tatlier, M. and Berhan, L. 2009. Modelling the negative Poisson's ratio of compressed fused fibre networks. *physica status solidi (b)*. 246(9), pp. 2018-2024.
- [19] Zhu, H. and Fan, T. and Zhang, D. 2016. Composite Materials with Enhanced Conductivities. *Advanced Engineering Materials*. 18(7), pp. 1174-1180.
- [20] Yu, H. and Heider, D. and Advani, S. 2015. A 3D microstructure based resistor network model for the electrical resistivity of unidirectional carbon composites. *Composite Structures*. 134, pp. 740-749.
- [21] Ray, D. and Sarkar, B. K. and Rana, A. K. et al. 2001. The mechanical properties of vinylester resin matrix composites reinforced with alkali-treated jute fibres. *Composites Part A: Applied Science and Manufacturing*. 32(1), pp. 119-127.
- [22] Akil, H. M. and Omar, M. F. and Mazuki, A. A. M. et al. 2011. Kenaf fiber reinforced composites: A review. *Materials & Design*. 32(8-9), pp. 4107-4121.
- [23] Babu, K. M. 2015. Chapter 3 - Natural Textile Fibres: Animal and Silk Fibres A2 - Sinclair, Rose. *Textiles and Fashion*. Woodhead Publishing, pp. 57-78.
- [24] Fratzl, P. 2008. Collagen: Structure and Mechanics, an Introduction. In: Fratzl, P. ed. *Collagen: Structure and Mechanics*. Boston, MA: Springer US, pp. 1-13.
- [25] Perevozchikova, B. V. and Pisciotta, A. and Osovetsky, B. M. et al. 2014. Quality Evaluation of the Kuluevskaya Basalt Outcrop for the Production of Mineral Fiber, Southern Urals, Russia. *Energy Procedia*. 59, pp. 309-314.
- [26] Dunne, R. and Desai, D. and Sadiku, R. et al. 2016. A review of natural fibres, their sustainability and automotive applications. *Journal of Reinforced Plastics and Composites*. 35(13), pp. 1041-1050.
- [27] Meola, C. and Boccardi, S. and Carlomagno, G. M. 2016. *Infrared Thermography in the Evaluation of Aerospace Composite Materials: Infrared Thermography to Composites*. Woodhead Publishing.
- [28] Lin, J.-S. 2002. Effect of surface modification by bromination and metalation on Kevlar fibre-epoxy adhesion. *European Polymer Journal*.

- 38(1), pp. 79-86.
- [29] Lee-Sullivan, P. and Chian, K. S. and Yue, C. Y. et al. 1994. Effects of bromination and hydrolysis treatments on the morphology and tensile properties of Kevlar-29 fibres. *Journal of Materials Science Letters*. 13(5), pp. 305-309.
- [30] Wang, Y. and Xia, Y. M. 1999. Experimental and theoretical study on the strain rate and temperature dependence of mechanical behaviour of Kevlar fibre. *Composites Part A: Applied Science and Manufacturing*. 30(11), pp. 1251-1257.
- [31] Yue, C. Y. and Sui, G. X. and Looi, H. C. 2000. Effects of heat treatment on the mechanical properties of Kevlar-29 fibre. *Composites Science and Technology*. 60(3), pp. 421-427.
- [32] Monteiro, P. and Mehta, P. 2006. *Concrete: Microstructure, Properties and Materials*. McGraw-Hill Education.
- [33] Hassanpour, M. and Shafigh, P. and Mahmud, H. B. 2012. Lightweight aggregate concrete fiber reinforcement – A review. *Construction and Building Materials*. 37, pp. 452-461.
- [34] Imperatore, S. and Rinaldi, Z. and Drago, C. 2017. Degradation relationships for the mechanical properties of corroded steel rebars. *Construction and Building Materials*. 148, pp. 219-230.
- [35] Inman, M. and Thorhallsson, E. R. and Azrague, K. 2017. A Mechanical and Environmental Assessment and Comparison of Basalt Fibre Reinforced Polymer (BFRP) Rebar and Steel Rebar in Concrete Beams. *Energy Procedia*. 111, pp. 31-40.
- [36] Shield, C. K. and Costello, G. A. 1994. The Effect of Wire Rope Mechanics on the Material Properties of Cord Composites: An Elasticity Approach. *Journal of Applied Mechanics*. 61(1), pp. 1-8.
- [37] Vanooij, W. J. and Harakuni, P. B. and Buytaert, G. 2009. Adhesion of Steel Tire Cord to Rubber. *Rubber Chemistry and Technology*. 82(3), pp. 315-339.
- [38] Shah, S. P. and Weiss, W. J. and Yang, W. 1998. Shrinkage cracking - can it be prevented? *Concrete International*. 20(4), pp. 51-55.
- [39] Callens, M. 2014. *Development of ductile stainless steel fibre composites*. PhD thesis, KU Leuven university.
- [40] Callens, M. and Gorbatiikh, L. and Verpoest, I. 2014. Ductile steel fibre composites with brittle and ductile matrices. *Composites Part A: Applied Science and Manufacturing*. 61, pp. 235-244.
- [41] Rouison, D. and Sain, M. and Couturier, M. 2004. Resin transfer molding of natural fiber reinforced composites: cure simulation. *Composites Science and Technology*. 64(5), pp. 629-644.
- [42] Gutowski, W. 1990. Effect of fibre-matrix adhesion on mechanical properties of composites. *Controlled Interphases in Composite Materials*. Springer, pp. 505-520.
- [43] Zweben, C. 2014. *Composite Materials. Mechanical Engineers' Handbook*. John Wiley & Sons, Inc.

- [44] *Vinyl Ester Resin*. [Online]. Available at: <https://www.seahawkpaints.com/wp-content/uploads/2015/08/Vinyl-Ester-Resin-TDS-August-2015.pdf>. [Accessed: 2018.02.07].
- [45] *DUPONT™ KAPTON® SUMMARY OF PROPERTIES*. [Online]. Available at: <http://www.dupont.com/content/dam/dupont/products-and-services/membranes-and-films/polyimide-films/documents/DEC-Kapton-summary-of-properties.pdf>. [Accessed: 2018.02.07].
- [46] Callister, W. D. and Rethwisch, D. G. 2007. *Materials Science and Engineering-- An Introduction*. New York: Wiley, pp. 577-611.
- [47] Silberberg, M. S. 2007. *Principles of general chemistry*. McGraw-Hill Higher Education.
- [48] Voigt, W. 1928. *Lehrbuch der kristallphysik (mit ausschluss der kristalloptik)*, edited by bg teubner and jw edwards, leipzig berlin. *Ann Arbor, Mich.*
- [49] Reuss, A. 1929. Berechnung der fließgrenze von mischkristallen auf grund der plastizitätsbedingung für einkristalle. *ZAMM - Journal of Applied Mathematics and Mechanics/Zeitschrift für Angewandte Mathematik und Mechanik*. 9(1), pp. 49-58.
- [50] Cai, D. a. and Zhou, G. and Wang, X. et al. 2017. Experimental investigation on mechanical properties of unidirectional and woven fabric glass/epoxy composites under off-axis tensile loading. *Polymer Testing*. 58, pp. 142-152.
- [51] Kueh, A. B. H. 2013. Buckling of sandwich columns reinforced by triaxial weave fabric composite skin-sheets. *International Journal of Mechanical Sciences*. 66, pp. 45-54.
- [52] Santiago, R. C. and Cantwell, W. J. and Jones, N. et al. 2018. The modelling of impact loading on thermoplastic fibre-metal laminates. *Composite Structures*. 189, pp. 228-238.
- [53] Reyes V, G. and Cantwell, W. J. 2000. The mechanical properties of fibre-metal laminates based on glass fibre reinforced polypropylene. *Composites Science and Technology*. 60(7), pp. 1085-1094.
- [54] Sinmazçelik, T. and Avcu, E. and Bora, M. Ö. et al. 2011. A review: Fibre metal laminates, background, bonding types and applied test methods. *Materials & Design*. 32(7), pp. 3671-3685.
- [55] Al-Khudairi, O. and Hadavinia, H. and Waggott, A. et al. 2015. Characterising mode I/mode II fatigue delamination growth in unidirectional fibre reinforced polymer laminates. *Materials & Design (1980-2015)*. 66, pp. 93-102.
- [56] Chakraborty, D. 2007. Delamination of laminated fiber reinforced plastic composites under multiple cylindrical impact. *Materials & Design*. 28(4), pp. 1142-1153.
- [57] Carvalho, A. and Silva, T. and Loja, M. 2018. Assessing Static and Dynamic Response Variability due to Parametric Uncertainty on Fibre-Reinforced Composites. *Journal of Composites Science*. 2(1), p. 6.
- [58] Shahsavari, A. S. and Picu, R. C. 2013. Size effect on mechanical behavior

- of random fiber networks. *International Journal of Solids and Structures*. 50(20), pp. 3332-3338.
- [59] Leclerc, W. and Karamian-Surville, P. and Vivet, A. 2015. An efficient and automated 3D FE approach to evaluate effective elastic properties of overlapping random fibre composites. *Computational Materials Science*. 99, pp. 1-15.
- [60] El-Rahman, A. I. A. and Tucker, C. L. 2013. Mechanics of Random Discontinuous Long-Fiber Thermoplastics—Part I: Generation and Characterization of Initial Geometry. *Journal of Applied Mechanics*. 80(5), p. 051007.
- [61] Abd El-Rahman, A. and Tucker III, C. 2013. Mechanics of random discontinuous long-fiber thermoplastics. Part II: Direct simulation of uniaxial compression. *Journal of Rheology*. 57(5), pp. 1463-1489.
- [62] Sukiman, M. S. and Kanit, T. and N'Guyen, F. et al. 2017. Effective thermal and mechanical properties of randomly oriented short and long fiber composites. *Mechanics of Materials*. 107, pp. 56-70.
- [63] Williams, S. R. and Philipse, A. P. 2003. Random packings of spheres and spherocylinders simulated by mechanical contraction. *Physical Review E*. 67(5), p. 051301.
- [64] Song, W. and Liu, G. and Wang, J. et al. 2017. The effects of high temperature and fiber diameter on the quasi static compressive behavior of metal fiber sintered sheets. *Materials Science and Engineering: A*. 690, pp. 71-79.
- [65] van Wyk, C. M. 1946. Note on the compressibility of wool. *Journal of the Textile Institute Transactions*. 37(12), pp. T285-T292.
- [66] Kallmes, O. and Corte, H. 1960. The structure of paper, I. The statistical geometry of an ideal two dimensional fiber network. *Tappi J*. 43(9), pp. 737-752.
- [67] Kallmes, O. and Corte, H. and Bernier, G. 1961. The structure of paper II: the statistical geometry of a multiplanar fiber network. *Tappi Journal*. 44(7), pp. 519-528.
- [68] Dent, R. W. 2001. Inter-fiber Distances in Paper and Nonwovens. *The Journal of The Textile Institute*. 92(1), pp. 63-74.
- [69] Komori, T. and Makishima, K. 1977. Numbers of Fiber-to-Fiber Contacts in General Fiber Assemblies. *Textile Research Journal*. 47(1), pp. 13-17.
- [70] Komori, T. and Itoh, M. 1994. A modified theory of fiber contact in general fiber assemblies. *Textile research journal*. 64(9), pp. 519-528.
- [71] Toll, S. and Manson, J. A. E. 1995. Elastic Compression of a Fiber Network. *Journal of Applied Mechanics*. 62(1), pp. 223-226.
- [72] Toll, S. 2004. Packing mechanics of fiber reinforcements. *Polymer Engineering & Science*. 38(8), pp. 1337-1350.
- [73] Heyden, S. 2000. *Network Modelling for Evaluation of Mechanical Properties of Cellulose Fibre Fluff*. PhD thesis, Lund University.

- [74] Sampson, W. W. 2008. *Modelling Stochastic Fibrous Materials with Mathematica®*. Springer Science & Business Media.
- [75] Liu, W. and Canfield, N. 2012. Development of thin porous metal sheet as micro-filtration membrane and inorganic membrane support. *Journal of Membrane Science*. 409-410, pp. 113-126.
- [76] Bo, Z. and Tianning, C. 2009. Calculation of sound absorption characteristics of porous sintered fiber metal. *Applied Acoustics*. 70(2), pp. 337-346.
- [77] Yuranov, I. and Kiwi-Minsker, L. and Renken, A. 2003. Structured combustion catalysts based on sintered metal fibre filters. *Applied Catalysis B: Environmental*. 43(3), pp. 217-227.
- [78] Lu, W. and Zhao, C. Y. and Tassou, S. A. 2006. Thermal analysis on metal-foam filled heat exchangers. Part I: Metal-foam filled pipes. *International Journal of Heat and Mass Transfer*. 49(15), pp. 2751-2761.
- [79] Tang, Y. and Zhou, W. and Xiang, J. et al. 2010. An Innovative Fabrication Process of Porous Metal Fiber Sintered Felts with Three-Dimensional Reticulated Structure. *Materials and Manufacturing Processes*. 25(7), pp. 565-571.
- [80] Ducheyne, P. and Aernoudt, E. and De Meester, P. 1978. The mechanical behaviour of porous austenitic stainless steel fibre structures. *Journal of Materials Science*. 13(12), pp. 2650-2658.
- [81] Zhou, B. and Yuan, W. and Hu, J. Y. et al. 2015. Uniaxial tensile behavior of porous metal fiber sintered sheet. *Transactions of Nonferrous Metals Society of China*. 25(6), pp. 2003-2008.
- [82] Zhao, T. F. and Chen, C. Q. 2014. The shear properties and deformation mechanisms of porous metal fiber sintered sheets. *Mechanics of Materials*. 70, pp. 33-40.
- [83] Fletcher, D. A. and Mullins, R. D. 2010. Cell mechanics and the cytoskeleton. *Nature*. 463(7280), pp. 485-492.
- [84] Wickstead, B. and Gull, K. 2011. The evolution of the cytoskeleton. *The Journal of Cell Biology*. 194(4), pp. 513-525.
- [85] Imaoka, S. 2008. Analyzing viscoelastic materials. *ANSYS Advantage*. 2(4).
- [86] Leterrier, J. F. and Kas, J. and Hartwig, J. et al. 1996. Mechanical effects of neurofilament cross-bridges modulation by phosphorylation, lipids, and interactions with f-actin. *Journal of Biological Chemistry*. 271(26), pp. 15687-15694.
- [87] Stein, A. M. and Vader, D. A. and Weitz, D. A. et al. 2011. The micromechanics of three - dimensional collagen - I gels. *Complexity*. 16(4), pp. 22-28.
- [88] Münster, S. and Jawerth, L. M. and Leslie, B. A. et al. 2013. Strain history dependence of the nonlinear stress response of fibrin and collagen networks. *Proceedings of the National Academy of Sciences*. 110(30), pp. 12197-12202.

- [89] Weiss, J. A. and Gardiner, J. C. 2001. Computational modeling of ligament mechanics. *Crit Rev Biomed Eng.* 29(3), pp. 303-371.
- [90] Zhao, C. Y. 2012. Review on thermal transport in high porosity cellular metal foams with open cells. *International Journal of Heat and Mass Transfer.* 55(13), pp. 3618-3632.
- [91] Vijay, D. and Goetze, P. and Wulf, R. et al. 2018. Homogenized and pore-scale analyses of forced convection through open cell foams. *International Journal of Heat and Mass Transfer.* 123, pp. 787-804.
- [92] Fanelli, P. and Evangelisti, A. and Salvini, P. et al. 2017. Modelling and characterization of structural behaviour of Al open-cell foams. *Materials & Design.* 114, pp. 167-175.
- [93] Shafiq, M. and Ayyagari, R. S. and Ehaab, M. et al. 2015. Multiaxial yield surface of transversely isotropic foams: Part II—Experimental. *Journal of the Mechanics and Physics of Solids.* 76(Supplement C), pp. 224-236.
- [94] Ayyagari, R. S. and Vural, M. 2015. Multiaxial yield surface of transversely isotropic foams: Part I—Modeling. *Journal of the Mechanics and Physics of Solids.* 74, pp. 49-67.
- [95] Zhu, H. X. and Knott, J. F. and Mills, N. J. 1997. Analysis of the elastic properties of open-cell foams with tetrakaidecahedral cells. *Journal of the Mechanics and Physics of Solids.* 45(3), pp. 319-343.
- [96] Shunmugasamy, V. C. and Mansoor, B. 2018. Compressive behavior of a rolled open-cell aluminum foam. *Materials Science and Engineering: A.* 715, pp. 281-294.
- [97] Zhu, W. and Blal, N. and Cunsolo, S. et al. 2018. Effective elastic properties of periodic irregular open-cell foams. *International Journal of Solids and Structures.* 143, pp. 155-166.
- [98] Shunmugasamy, V. C. and Mansoor, B. 2018. Aluminum foam sandwich with density-graded open-cell core: Compressive and flexural response. *Materials Science and Engineering: A.* 731, pp. 220-230.
- [99] Kaya, A. C. and Fleck, C. 2014. Deformation behavior of open-cell stainless steel foams. *Materials Science and Engineering: A.* 615, pp. 447-456.
- [100] Zhu, H. X. and Hobdell, J. R. and Windle, A. H. 2001. Effects of cell irregularity on the elastic properties of 2D Voronoi honeycombs. *Journal of the Mechanics and Physics of Solids.* 49(4), pp. 857-870.
- [101] Zhu, H. and Thorpe, S. and Windle, A. 2006. The effect of cell irregularity on the high strain compression of 2D Voronoi honeycombs. *International journal of solids and structures.* 43(5), pp. 1061-1078.
- [102] Zhu, H. and Yan, L. and Zhang, R. et al. 2012. Size-dependent and tunable elastic properties of hierarchical honeycombs with regular square and equilateral triangular cells. *Acta Materialia.* 60(12), pp. 4927-4939.
- [103] Zhu, H. X. 2010. Size-dependent elastic properties of micro- and nano-honeycombs. *Journal of the Mechanics and Physics of Solids.* 58, pp. 696-709.
- [104] Bower, A. F. 2011. *Applied Mechanics of Solids.* CRC press.

- [105] Hashin, Z. and Shtrikman, S. 1962. On some variational principles in anisotropic and nonhomogeneous elasticity. *Journal of the Mechanics and Physics of Solids*. 10(4), pp. 335-342.
- [106] Hashin, Z. and Shtrikman, S. 1963. A variational approach to the theory of the elastic behaviour of multiphase materials. *Journal of the Mechanics and Physics of Solids*. 11(2), pp. 127-140.
- [107] Kalaprasad, G. and Joseph, K. and Thomas, S. et al. 1997. Theoretical modelling of tensile properties of short sisal fibre-reinforced low-density polyethylene composites. *Journal of Materials Science*. 32(16), pp. 4261-4267.
- [108] Bowyer, W. H. and Bader, M. G. 1972. On the re-inforcement of thermoplastics by imperfectly aligned discontinuous fibres. *Journal of Materials Science*. 7(11), pp. 1315-1321.
- [109] Munde, Y. S. and Ingle, R. B. 2015. Theoretical Modeling and Experimental Verification of Mechanical Properties of Natural Fiber Reinforced Thermoplastics. *Procedia Technology*. 19, pp. 320-326.
- [110] Curtis, P. T. and Bader, M. G. and Bailey, J. E. 1978. The stiffness and strength of a polyamide thermoplastic reinforced with glass and carbon fibres. *Journal of Materials Science*. 13(2), pp. 377-390.
- [111] Cox, H. L. 1952. The elasticity and strength of paper and other fibrous materials. *British Journal of Applied Physics*. 3(3), p. 72.
- [112] Nielsen, L. and Chen, P. 1968. Young's modulus of composites filled with randomly oriented fibers. *Journal of Materials*. 3(2), pp. 352-358.
- [113] Vannan, E. and Vizhian, P. 2014. Prediction of the Elastic Properties of Short Basalt Fiber Reinforced Al Alloy Metal Matrix Composites. *Journal of Minerals and Materials Characterization and Engineering*. 2(01), p. 61.
- [114] Okabe, T. and Takeda, N. 2002. Elastoplastic shear-lag analysis of single-fiber composites and strength prediction of unidirectional multi-fiber composites. *Composites Part A: Applied Science and Manufacturing*. 33(10), pp. 1327-1335.
- [115] Krstic, V. D. and Vlajic, M. D. 1983. Conditions for spontaneous cracking of a brittle matrix due to the presence of thermoelastic stresses. *Acta Metallurgica*. 31(1), pp. 139-144.
- [116] Kelly, A. and Tyson, W. R. 1965. Tensile properties of fibre-reinforced metals: Copper/tungsten and copper/molybdenum. *Journal of the Mechanics and Physics of Solids*. 13(6), pp. 329-350.
- [117] Tucker Iii, C. L. and Liang, E. 1999. Stiffness predictions for unidirectional short-fiber composites: Review and evaluation. *Composites Science and Technology*. 59(5), pp. 655-671.
- [118] Fukuda, H. and Kawata, K. 1974. On Young's modulus of short fibre composites. *Fibre Science and Technology*. 7(3), pp. 207-222.
- [119] Eshelby, J. D. 1957. The Determination of the Elastic Field of an Ellipsoidal Inclusion, and Related Problems. *Proceedings of the Royal Society of London. Series A, Mathematical and Physical Sciences*. 241(1226), pp. 376-

- 396.
- [120] Eshelby, J. D. 1961. Elastic inclusions and inhomogeneities. *Progress in Solid Mechanics*. 2, pp. 89-140.
- [121] Eshelby, J. 1959. *The elastic field outside an ellipsoidal inclusion*. Proc. R. Soc. Lond. A. The Royal Society. 252(1271), pp. 561-569.
- [122] Taya, M. and Mura, T. 1981. On Stiffness and Strength of an Aligned Short-Fiber Reinforced Composite Containing Fiber-End Cracks Under Uniaxial Applied Stress. *Journal of Applied Mechanics*. 48(2), pp. 361-367.
- [123] Ni, L. and Markenscoff, X. 2016. The self-similarly expanding Eshelby ellipsoidal inclusion: II. The Dynamic Eshelby Tensor for the expanding sphere. *Journal of the Mechanics and Physics of Solids*. 96, pp. 696-714.
- [124] Russel, W. B. 1973. On the effective moduli of composite materials: Effect of fiber length and geometry at dilute concentrations. *Zeitschrift für angewandte Mathematik und Physik ZAMP*. 24(4), pp. 581-600.
- [125] Kerner, E. 1956. The elastic and thermo-elastic properties of composite media. *Proceedings of the physical society. Section B*. 69(8), p. 808.
- [126] Hill, R. 1965. A self-consistent mechanics of composite materials. *Journal of the Mechanics and Physics of Solids*. 13(4), pp. 213-222.
- [127] Mori, T. and Tanaka, K. 1973. Average stress in matrix and average elastic energy of materials with misfitting inclusions. *Acta Metallurgica*. 21(5), pp. 571-574.
- [128] Wakashima, K. and Otsuka, M. and Umekawa, S. 1974. Thermal expansions of heterogeneous solids containing aligned ellipsoidal inclusions. *Journal of Composite Materials*. 8(4), pp. 391-404.
- [129] Abaimov, S. G. and Khudyakova, A. A. and Lomov, S. V. 2016. On the closed form expression of the Mori–Tanaka theory prediction for the engineering constants of a unidirectional fiber-reinforced ply. *Composite Structures*. 142, pp. 1-6.
- [130] Tandon, G. P. and Weng, G. J. 1984. The effect of aspect ratio of inclusions on the elastic properties of unidirectionally aligned composites. *Polymer Composites*. 5(4), pp. 327-333.
- [131] Benveniste, Y. 1987. A new approach to the application of Mori-Tanaka's theory in composite materials. *Mechanics of Materials*. 6(2), pp. 147-157.
- [132] Hashin, Z. 1983. Analysis of Composite Materials—A Survey. *Journal of Applied Mechanics*. 50(3), pp. 481-505.
- [133] Halpin, J. C. 1969. Stiffness and Expansion Estimates for Oriented Short Fiber Composites. *Journal of Composite Materials*. 3(4), pp. 732-734.
- [134] Hewitt, R. L. and De Malherbe, M. C. 1970. An Approximation for the Longitudinal Shear Modulus of Continuous Fibre Composites. *Journal of Composite Materials*. 4(2), pp. 280-282.
- [135] Lewis, T. and Nielsen, L. 1970. Dynamic mechanical properties of particulate - filled composites. *Journal of Applied Polymer Science*. 14(6), pp. 1449-1471.

- [136] Hill, R. 1964. Theory of mechanical properties of fibre-strengthened materials: I. Elastic behaviour. *Journal of the Mechanics and Physics of Solids*. 12(4), pp. 199-212.
- [137] Chu, T. and Hashin, Z. 1971. Plastic behavior of composites and porous media under isotropic stress. *International Journal of Engineering Science*. 9(10), pp. 971-994.
- [138] Hill, R. 1964. Theory of mechanical properties of fibre-strengthened materials: II. Inelastic behaviour. *Journal of the Mechanics and Physics of Solids*. 12(4), pp. 213-218.
- [139] Hill, R. 1967. The essential structure of constitutive laws for metal composites and polycrystals. *Journal of the Mechanics and Physics of Solids*. 15(2), pp. 79-95.
- [140] Miwa, M. and Nakayama, A. and Ohsawa, T. et al. 1979. Temperature dependence of the tensile strength of glass fiber–epoxy and glass fiber–unsaturated polyester composites. 23(10), pp. 2957-2966.
- [141] Hershey, A. 1954. The elasticity of an isotropic aggregate of anisotropic cubic crystals. *Journal of Applied mechanics-transactions of the ASME*. 21(3), pp. 236-240.
- [142] Kröner, E. 1958. Berechnung der elastischen Konstanten des Vielkristalls aus den Konstanten des Einkristalls. *Z. Phys.*
- [143] Hill, R. 1965. Continuum micro-mechanics of elastoplastic polycrystals. *Journal of the Mechanics and Physics of Solids*. 13(2), pp. 89-101.
- [144] Hutchinson, J. 1970. *Elastic-plastic behaviour of polycrystalline metals and composites*. Proc. R. Soc. Lond. A. The Royal Society. 319(1537), pp. 247-272.
- [145] Dvorak, G. J. and Bahei-El-Din, Y. A. 1979. Elastic-plastic behavior of fibrous composites. *Journal of the Mechanics and Physics of Solids*. 27(1), pp. 51-72.
- [146] Budiansky, B. and Wu, T. T. 1961. *Theoretical prediction of plastic strains of polycrystals*. Cambridge, Mass.: Division of Engineering and Applied Physics, Harvard University.
- [147] Kroner, E. 1961. On the plastic deformation of polycrystals. *Acta Metallurgica*. 9(2), pp. 155-161.
- [148] Berveiller, M. and Zaoui, A. 1978. An extension of the self-consistent scheme to plastically-flowing polycrystals. *Journal of the Mechanics and Physics of Solids*. 26(5-6), pp. 325-344.
- [149] Hutchinson, J. 1976. *Bounds and self-consistent estimates for creep of polycrystalline materials*. Proc. R. Soc. Lond. A. The Royal Society. 348(1652), pp. 101-127.
- [150] Castañeda, P. P. 1991. The effective mechanical properties of nonlinear isotropic composites. *Journal of the Mechanics and Physics of Solids*. 39(1), pp. 45-71.
- [151] Rekik, A. and Allaoui, S. and Gasser, A. et al. 2015. Experiments and nonlinear homogenization sustaining mean-field theories for refractory

- mortarless masonry: The classical secant procedure and its improved variants. *European Journal of Mechanics - A/Solids*. 49, pp. 67-81.
- [152] Bardella, L. 2003. An extension of the Secant Method for the homogenization of the nonlinear behavior of composite materials. *International Journal of Engineering Science*. 41(7), pp. 741-768.
- [153] Hu, G. 1996. A method of plasticity for general aligned spheroidal void or fiber-reinforced composites. *International Journal of Plasticity*. 12(4), pp. 439-449.
- [154] Suquet, P. 2001. Nonlinear composites: Secant methods and variational bounds. *Lemaitre Handbook of Materials Behaviour Models, Section 10.3*. Academic Press, pp. 968-983.
- [155] Suquet, P. 1995. Overall properties of nonlinear composites: a modified secant moduli theory and its link with Ponte Castañeda's nonlinear variational procedure. *Comptes rendus de l'Académie des sciences. Série II, Mécanique, physique, chimie, astronomie*. 320(11), pp. 563-571.
- [156] Suquet, P. 1997. Effective Properties of Nonlinear Composites. In: Suquet, P. ed. *Continuum Micromechanics*. Vienna: Springer Vienna, pp. 197-264.
- [157] Qiu, Y. and Weng, G. 1992. A theory of plasticity for porous materials and particle-reinforced composites. *Journal of Applied Mechanics*. 59(2), pp. 261-268.
- [158] Ortiz, M. and Stainier, L. 1999. The variational formulation of viscoplastic constitutive updates. *Computer Methods in Applied Mechanics and Engineering*. 171(3), pp. 419-444.
- [159] Hashin, Z. and Shtrikman, S. 1962. A variational approach to the theory of the elastic behaviour of polycrystals. *Journal of the Mechanics and Physics of Solids*. 10(4), pp. 343-352.
- [160] Hashin, Z. and Shtrikman, S. 1961. Note on a variational approach to the theory of composite elastic materials. *Journal of the Franklin Institute*. 271(4), pp. 336-341.
- [161] Hashin, Z. and Shtrikman, S. 1961. Note on the effective constants of composite materials. *Journal of the Franklin Institute*. 271(5), pp. 423-426.
- [162] Lahellec, N. and Suquet, P. 2007. On the effective behavior of nonlinear inelastic composites: I. Incremental variational principles. *Journal of the Mechanics and Physics of Solids*. 55(9), pp. 1932-1963.
- [163] Petit, P. and Waddoups, M. E. 1969. A method of predicting the nonlinear behavior of laminated composites. *Journal of Composite Materials*. 3(1), pp. 2-19.
- [164] Hahn, H. T. and Tsai, S. W. 1973. Nonlinear elastic behavior of unidirectional composite laminae. *Journal of Composite Materials*. 7(1), pp. 102-118.
- [165] Chow, C. and Yang, F. 1992. A simple model for brittle composite lamina with damage. *Journal of reinforced Plastics and Composites*. 11(3), pp. 222-242.
- [166] Lin, W.-P. and Hu, H.-T. 2002. Nonlinear analysis of fiber-reinforced

- composite laminates subjected to uniaxial tensile load. *Journal of Composite Materials*. 36(12), pp. 1429-1450.
- [167] Kenaga, D. and Doyle, J. F. and Sun, C. 1987. The characterization of boron/aluminum composite in the nonlinear range as an orthotropic elastic-plastic material. *Journal of Composite Materials*. 21(6), pp. 516-531.
- [168] Xie, M. and Adams, D. F. 1995. A plasticity model for unidirectional composite materials and its applications in modeling composites testing. *Composites science and technology*. 54(1), pp. 11-21.
- [169] Jansson, S. 1995. Non-linear constitutive equations for strongly bonded fibre-reinforced metal matrix composites. *Composites*. 26(6), pp. 415-424.
- [170] Sun, C. and Chen, J. 1989. A simple flow rule for characterizing nonlinear behavior of fiber composites. *Journal of Composite Materials*. 23(10), pp. 1009-1020.
- [171] Selezneva, M. and Swolfs, Y. and Katalagarianakis, A. et al. 2018. The brittle-to-ductile transition in tensile and impact behavior of hybrid carbon fibre/self-reinforced polypropylene composites. *Composites Part A: Applied Science and Manufacturing*. 109, pp. 20-30.
- [172] Cahoon, J. and Broughton, W. and Kutzak, A. 1971. The determination of yield strength from hardness measurements. *Metallurgical transactions*. 2(7), pp. 1979-1983.
- [173] Huang, M. and Liu, Y. and Sheng, D. 2011. Simulation of yielding and stress–strain behavior of shanghai soft clay. 38(3), pp. 341-353.
- [174] Witt, F. J. 1972. *The equivalent energy method for calculating elastic-plastic fracture*. Report, Oak Ridge, Tennessee
- [175] Witt, F. J. 1981. The equivalent energy method: An engineering approach to fracture. *Engineering Fracture Mechanics*. 14(1), pp. 171-187.
- [176] Ju, Y. K. and Kim, Y. C. and Ryu, J. 2013. Finite element analysis of concrete filled tube column to flat plate slab joint. *Journal of Constructional Steel Research*. 90, pp. 297-307.
- [177] Feng, P. and Cheng, S. and Bai, Y. et al. 2015. Mechanical behavior of concrete-filled square steel tube with FRP-confined concrete core subjected to axial compression. *Composite Structures*. 123, pp. 312-324.
- [178] Woo, S. L. and Johnson, G. A. and Smith, B. A. 1993. Mathematical modeling of ligaments and tendons. *J Biomech Eng*. 115(4B), pp. 468-473.
- [179] Fung, Y. C. 1972. Stress-strain-history relations of soft tissues in simple elongation. *Biomechanics: Its Foundations and Objectives*. pp. 181-208.
- [180] Lanir, Y. 1979. The rheological behavior of the skin: experimental results and a structural model. *Biorheology*. 16(3), pp. 191-202.
- [181] Lanir, Y. 1983. Constitutive equations for fibrous connective tissues. *Journal of Biomechanics*. 16(1), pp. 1-12.
- [182] Egan, J. M. 1987. A constitutive model for the mechanical behaviour of soft connective tissues. *Journal of biomechanics*. 20(7), pp. 681-692.
- [183] Woo, S. and Rajagopal, K. 1996. A single integral finite strain viscoelastic

- model of ligaments and tendons. *Journal of biomechanical engineering*. 118, p. 221.
- [184] Decraemer, W. F. and Maes, M. A. and Vanhuyse, V. J. et al. 1980. A non-linear viscoelastic constitutive equation for soft biological tissues, based upon a structural model. *Journal of Biomechanics*. 13(7), pp. 559-564.
- [185] Pond, D. and McBride, A. T. and Davids, L. M. et al. 2018. Microstructurally-based constitutive modelling of the skin – Linking intrinsic ageing to microstructural parameters. *Journal of Theoretical Biology*. 444, pp. 108-123.
- [186] Garikipati, K. and Arruda, E. M. and Grosh, K. et al. 2004. A continuum treatment of growth in biological tissue: the coupling of mass transport and mechanics. *Journal of the Mechanics and Physics of Solids*. 52(7), pp. 1595-1625.
- [187] Viidik, A. 1968. A rheological model for uncalcified parallel-fibred collagenous tissue. *Journal of Biomechanics*. 1(1), pp. 3-11.
- [188] Frisé, M. and Mägi, M. and Sonnerup, L. et al. 1969. Rheological analysis of soft collagenous tissue: Part I: Theoretical considerations. *Journal of Biomechanics*. 2(1), pp. 13-20.
- [189] Sanjeevi, R. and Somanathan, N. and Ramaswamy, D. 1982. A viscoelastic model for collagen fibres. *Journal of biomechanics*. 15(3), pp. 181-183.
- [190] Jamison, C. and Marangoni, R. and Glaser, A. 1968. Viscoelastic properties of soft tissue by discrete model characterization. *Journal of Engineering for Industry*. 90(2), pp. 239-247.
- [191] Fung, Y. 1967. Elasticity of soft tissues in simple elongation. *American Journal of Physiology--Legacy Content*. 213(6), pp. 1532-1544.
- [192] Fung, Y. C. 1968. Biomechanics: Its scope history and some problems of continuum mechanics in physiology. *Appl Mech Rev*. 21, pp. 1-20.
- [193] Abramowitz, M. 1974. *Handbook of Mathematical Functions, With Formulas, Graphs, and Mathematical Tables*. Dover Publications, Incorporated.
- [194] Huyghe, J. M. and van Campen, D. H. and Arts, T. et al. 1991. The constitutive behaviour of passive heart muscle tissue: a quasi-linear viscoelastic formulation. *J Biomech*. 24(9), pp. 841-849.
- [195] Myers, B. S. and McElhaney, J. H. and Doherty, B. J. 1991. The viscoelastic responses of the human cervical spine in torsion: Experimental limitations of quasi-linear theory, and a method for reducing these effects. *Journal of Biomechanics*. 24(9), pp. 811-817.
- [196] Pinto, J. G. and Patitucci, P. J. 1980. Visco-elasticity of passive cardiac muscle. *J Biomech Eng*. 102(1), pp. 57-61.
- [197] Simon, B. and Coats, R. and Woo, S.-Y. 1984. Relaxation and creep quasilinear viscoelastic models for normal articular cartilage. *Journal of Biomechanical Engineering*. 106(2), pp. 159-164.
- [198] Haut, R. C. and Little, R. W. 1972. A constitutive equation for collagen fibers. *Journal of biomechanics*. 5(5), pp. 423-430.

- [199] Woo, S. 1982. Mechanical properties of tendons and ligaments. I. Quasi-static and nonlinear viscoelastic properties. *Biorheology*. 19(3), p. 385.
- [200] Pioletti, D. P. and Rakotomanana, L. R. 2000. On the independence of time and strain effects in the stress relaxation of ligaments and tendons. *Journal of biomechanics*. 33(12), pp. 1729-1732.
- [201] Woo, S. L. Y. and Gomez, M. A. and Akeson, W. H. 1981. The Time and History-Dependent Viscoelastic Properties of the Canine Medial Collateral Ligament. *Journal of Biomechanical Engineering*. 103(4), pp. 293-298.
- [202] Dortmans, L. and Sauren, A. and Rousseau, E. 1984. Parameter estimation using the quasi-linear viscoelastic model proposed by Fung. *Journal of biomechanical engineering*. 106(3), pp. 198-203.
- [203] Nekouzadeh, A. and Pryse, K. M. and Elson, E. L. et al. 2007. A simplified approach to quasi-linear viscoelastic modeling. *Journal of biomechanics*. 40(14), pp. 3070-3078.
- [204] Sarver, J. J. and Robinson, P. S. and Elliott, D. M. 2003. Methods for quasi-linear viscoelastic modeling of soft tissue: application to incremental stress-relaxation experiments. *Journal of biomechanical engineering*. 125(5), pp. 754-758.
- [205] Shen, Z. L. and Kahn, H. and Ballarini, R. et al. 2011. Viscoelastic properties of isolated collagen fibrils. *Biophysical journal*. 100(12), pp. 3008-3015.
- [206] Lianis, G. 1963. *Constitutive equations of viscoelastic solids under finite deformation*. LOCKHEED PROPULSION CO REDLANDS CALIF.
- [207] Bingham, D. and DeHoff, P. 1979. A constitutive equation for the canine anterior cruciate ligament. *Journal of Biomechanical Engineering*. 101(1), pp. 15-22.
- [208] Bernstein, B. and Kearsley, E. and Zapas, L. 1963. A study of stress relaxation with finite strain. *Transactions of the Society of Rheology*. 7(1), pp. 391-410.
- [209] Dehoff, P. 1978. On the nonlinear viscoelastic behavior of soft biological tissues. *Journal of Biomechanics*. 11(1), pp. 35-40.
- [210] Coleman, B. D. and Noll, W. 1961. Foundations of linear viscoelasticity. *Reviews of modern physics*. 33(2), p. 239.
- [211] Kastelic, J. and Galeski, A. and Baer, E. 1978. The Multicomposite Structure of Tendon. *Connective Tissue Research*. 6(1), pp. 11-23.
- [212] Boyce, B. and Jones, R. and Nguyen, T. et al. 2007. Stress-controlled viscoelastic tensile response of bovine cornea. *Journal of biomechanics*. 40(11), pp. 2367-2376.
- [213] Jue, B. and Maurice, D. M. 1986. The mechanical properties of the rabbit and human cornea. *Journal of Biomechanics*. 19(10), pp. 847-853.
- [214] Marchi, B. C. and Luetkemeyer, C. M. and Arruda, E. M. 2018. Evaluating continuum level descriptions of the medial collateral ligament. *International Journal of Solids and Structures*. 138, pp. 245-263.
- [215] Sasaki, N. and Shukunami, N. and Matsushima, N. et al. 1999. Time-

- resolved X-ray diffraction from tendon collagen during creep using synchrotron radiation. *Journal of Biomechanics*. 32(3), pp. 285-292.
- [216] Johnson, G. A. and Tramaglini, D. M. and Levine, R. E. et al. 1994. Tensile and viscoelastic properties of human patellar tendon. *Journal of Orthopaedic Research*. 12(6), pp. 796-803.
- [217] Abramowitch, S. D. and Woo, S. L.-Y. 2004. An improved method to analyze the stress relaxation of ligaments following a finite ramp time based on the quasi-linear viscoelastic theory. *Journal of biomechanical engineering*. 126(1), pp. 92-97.
- [218] Castile, R. M. and Skelley, N. W. and Babaei, B. et al. 2016. Microstructural properties and mechanics vary between bundles of the human anterior cruciate ligament during stress-relaxation. *Journal of Biomechanics*. 49(1), pp. 87-93.
- [219] Komatsu, K. and Sanctuary, C. and Shibata, T. et al. 2007. Stress–relaxation and microscopic dynamics of rabbit periodontal ligament. *Journal of Biomechanics*. 40(3), pp. 634-644.
- [220] Liao, J. and Yang, L. and Grashow, J. et al. 2007. The relation between collagen fibril kinematics and mechanical properties in the mitral valve anterior leaflet. *Journal of biomechanical engineering*. 129(1), pp. 78-87.
- [221] Remache, D. and Caliez, M. and Gratton, M. et al. 2018. The effects of cyclic tensile and stress-relaxation tests on porcine skin. *Journal of the Mechanical Behavior of Biomedical Materials*. 77, pp. 242-249.
- [222] Quaglini, V. and Russa, V. L. and Corneo, S. 2009. Nonlinear stress relaxation of trabecular bone. *Mechanics Research Communications*. 36(3), pp. 275-283.
- [223] Tonsomboon, K. and Koh, C. T. and Oyen, M. L. 2014. Time-dependent fracture toughness of cornea. *Journal of the Mechanical Behavior of Biomedical Materials*. 34, pp. 116-123.
- [224] Marchi, G. and Baier, V. and Alberton, P. et al. 2017. Microindentation sensor system based on an optical fiber Bragg grating for the mechanical characterization of articular cartilage by stress-relaxation. *Sensors and Actuators B: Chemical*. 252, pp. 440-449.
- [225] Liu, X. and Dean, M. N. and Youssefpoor, H. et al. 2014. Stress relaxation behavior of tessellated cartilage from the jaws of blue sharks. *Journal of the Mechanical Behavior of Biomedical Materials*. 29, pp. 68-80.
- [226] Zeng, X. and Ye, L. and Sun, R. et al. 2015. Observation of viscoelasticity in boron nitride nanosheet aerogel. *Physical Chemistry Chemical Physics*. 17(26), pp. 16709-16714.
- [227] Chaudhuri, O. and Gu, L. and Klumpers, D. et al. 2015. Hydrogels with tunable stress relaxation regulate stem cell fate and activity. *Nature materials*. 15(3), pp. 326-334.
- [228] Janmey, P. A. and Euteneuer, U. and Traub, P. et al. 1991. Viscoelastic properties of vimentin compared with other filamentous biopolymer networks. *The Journal of Cell Biology*. 113(1), pp. 155-160.

- [229] Janmey, P. A. 1991. A torsion pendulum for measurement of the viscoelasticity of biopolymers and its application to actin networks. *Journal of biochemical and biophysical methods*. 22(1), pp. 41-53.
- [230] Wren, T. A. and Lindsey, D. P. and Beaupré, G. S. et al. 2003. Effects of creep and cyclic loading on the mechanical properties and failure of human Achilles tendons. *Annals of biomedical engineering*. 31(6), pp. 710-717.
- [231] Hasan, A. and Ragaert, K. and Swieszkowski, W. et al. 2014. Biomechanical properties of native and tissue engineered heart valve constructs. *Journal of Biomechanics*. 47(9), pp. 1949-1963.
- [232] Chen, G. and Cui, S. and You, L. et al. 2015. Experimental study on multi-step creep properties of rat skins. *Journal of the Mechanical Behavior of Biomedical Materials*. 46, pp. 49-58.
- [233] Rok, K. and Michael, G. and Ana, G. et al. 2017. Viscoelastic behaviour of hydrogel-based composites for tissue engineering under mechanical load. *Biomedical Materials*. 12(2), p. 025004.
- [234] Morris, V. J. and Kirby, A. R. and Gunning, A. P. 2010. *Atomic force microscopy for biologists*. Imperial College Press.
- [235] Wang, J. and Nie, S. 2018. Application of atomic force microscopy in microscopic analysis of polysaccharide. *Trends in Food Science & Technology*.
- [236] Xing, Y. and Xu, M. and Gui, X. et al. 2018. The application of atomic force microscopy in mineral flotation. *Advances in Colloid and Interface Science*.
- [237] Beckwitt, E. C. and Kong, M. and Van Houten, B. 2018. Studying protein-DNA interactions using atomic force microscopy. *Seminars in Cell & Developmental Biology*. 73, pp. 220-230.
- [238] Binnig, G. and Quate, C. F. and Gerber, C. 1986. Atomic force microscope. *Physical review letters*. 56(9), p. 930.
- [239] Ridgley, D. M. and Ebanks, K. C. and Barone, J. R. 2011. Peptide Mixtures Can Self-Assemble into Large Amyloid Fibers of Varying Size and Morphology. *Biomacromolecules*. 12(10), pp. 3770-3779.
- [240] Sweers, K. and van der Werf, K. and Bennink, M. et al. 2011. Nanomechanical properties of α -synuclein amyloid fibrils: a comparative study by nanoindentation, harmonic force microscopy, and Peakforce QNM. *Nanoscale Research Letters*. 6(1), p. 270.
- [241] Andriotis, O. G. and Manuyakorn, W. and Zekonyte, J. et al. 2014. Nanomechanical assessment of human and murine collagen fibrils via atomic force microscopy cantilever-based nanoindentation. *Journal of the Mechanical Behavior of Biomedical Materials*. 39, pp. 9-26.
- [242] Yang, P.-F. and Nie, X.-T. and Zhao, D.-D. et al. 2018. Deformation regimes of collagen fibrils in cortical bone revealed by in situ morphology and elastic modulus observations under mechanical loading. *Journal of the Mechanical Behavior of Biomedical Materials*. 79, pp. 115-121.
- [243] Cohen, S. R. and Bitler, A. 2008. Use of AFM in bio-related systems. *Current Opinion in Colloid & Interface Science*. 13(5), pp. 316-325.

- [244] Butt, H.-J. and Cappella, B. and Kappl, M. 2005. Force measurements with the atomic force microscope: Technique, interpretation and applications. *Surface Science Reports*. 59(1), pp. 1-152.
- [245] Cheng, Q. and Wang, S. and Harper, D. P. 2009. Effects of process and source on elastic modulus of single cellulose fibrils evaluated by atomic force microscopy. *Composites Part A: Applied Science and Manufacturing*. 40(5), pp. 583-588.
- [246] Svensson, R. B. and Hassenkam, T. and Hansen, P. et al. 2010. Viscoelastic behavior of discrete human collagen fibrils. *Journal of the Mechanical Behavior of Biomedical Materials*. 3(1), pp. 112-115.
- [247] Shen, Z. L. and Dodge, M. R. and Kahn, H. et al. 2008. Stress-strain experiments on individual collagen fibrils. *Biophysical Journal*. 95(8), pp. 3956-3963.
- [248] Shen, Z. L. and Dodge, M. R. and Kahn, H. et al. 2010. In vitro fracture testing of submicron diameter collagen fibril specimens. *Biophysical journal*. 99(6), pp. 1986-1995.
- [249] Eppell, S. and Smith, B. and Kahn, H. et al. 2006. Nano measurements with micro-devices: mechanical properties of hydrated collagen fibrils. *Journal of the Royal Society Interface*. 3(6), pp. 117-121.
- [250] Hong, W. and Zhao, X. and Zhou, J. et al. 2008. A theory of coupled diffusion and large deformation in polymeric gels. *Journal of the Mechanics and Physics of Solids*. 56(5), pp. 1779-1793.
- [251] Hvidberg, E. 1960. Investigations into the Effect of Mechanical Pressure on the Water Content of Isolated Skin. *Acta Pharmacologica et Toxicologica*. 16(3), pp. 245-249.
- [252] Wilson, W. and Van Donkelaar, C. and Van Rietbergen, B. et al. 2005. A fibril-reinforced poroviscoelastic swelling model for articular cartilage. *Journal of biomechanics*. 38(6), pp. 1195-1204.
- [253] Wilson, W. and van Donkelaar, C. and Huyghe, J. 2005. A comparison between mechano-electrochemical and biphasic swelling theories for soft hydrated tissues. *Journal of biomechanical engineering*. 127(1), pp. 158-165.
- [254] Lanir, Y. 1987. Biorheology and fluid flux in swelling tissues. I. Bicomponent theory for small deformations, including concentration effects. *Biorheology*. 24(2), pp. 173-187.
- [255] Hannafin, J. A. and Arnoczky, S. P. 1994. Effect of cyclic and static tensile loading on water content and solute diffusion in canine flexor tendons: an in vitro study. *Journal of Orthopaedic Research*. 12(3), pp. 350-356.
- [256] J. Thielke, R. and Phd, R. and Grood, E. 1995. Volumetric changes in ligaments under tension. In: *American Society of Mechanical Engineers, Bioengineering Division (Publication) BED*. Beaver Creek.
- [257] Weiss, J. and Lai, A. and Loui, S. et al. 2000. Behavior of human medial collateral ligament in unconfined compression. In: *46th Annual Meeting, Orthopaedic Research Society*. Orlando, Florida.

- [258] Butler, S. L. and Kohles, S. S. and Thielke, R. J. et al. 1997. Interstitial fluid flow in tendons or ligaments: A porous medium finite element simulation. *Medical and Biological Engineering and Computing*. 35(6), pp. 742-746.
- [259] Chen, C. T. and Malkus, D. S. and Vanderby, R., Jr. 1998. A fiber matrix model for interstitial fluid flow and permeability in ligaments and tendons. *Biorheology*. 35(2), pp. 103-118.
- [260] Ma, Y. 2016. *The mechanical properties of a three-dimensional stochastic fibrous network with cross-linking*. PhD thesis, Cardiff University.
- [261] Zhang, C. and Xu, X. and Yan, X. 2013. General periodic boundary conditions and their application to micromechanical finite element analysis of textile composites. *Acta Aeronautica et Astronautica Sinica*. 34(7), pp. 1636-1645.
- [262] Deogekar, S. and Picu, R. C. 2018. On the strength of random fiber networks. *Journal of the Mechanics and Physics of Solids*. 116, pp. 1-16.
- [263] Chen, N. and Silberstein, M. N. 2018. Determination of Bond Strengths in Non-woven Fabrics: a Combined Experimental and Computational Approach. *Experimental Mechanics*. 58(2), pp. 343-355.
- [264] Popov, V. L. 2010. *Contact mechanics and friction*. Berlin, Germany: Springer.
- [265] Yuan, Z. and Lu, Z. 2014. Numerical analysis of elastic–plastic properties of polymer composite reinforced by wavy and random CNTs. *Computational Materials Science*. 95, pp. 610-619.
- [266] Qian, C. and Harper, L. and Turner, T. et al. 2011. *Determination of the size of representative volume elements for discontinuous fibre composites*. 18th International conference on composite materials.
- [267] Chen, N. and Koker, M. K. A. and Uzun, S. et al. 2016. In-situ X-ray study of the deformation mechanisms of non-woven polypropylene. *International Journal of Solids and Structures*. 97-98, pp. 200-208.
- [268] Markaki, A. E. and Clyne, T. W. 2005. Magneto-mechanical actuation of bonded ferromagnetic fibre arrays. *Acta Materialia*. 53(3), pp. 877-889.
- [269] Clyne, T. W. and Markaki, A. E. and Tan, J. C. 2005. Mechanical and magnetic properties of metal fibre networks, with and without a polymeric matrix. *Composites Science and Technology*. 65(15), pp. 2492-2499.
- [270] Zhu, H. and Fan, T. and Zhang, D. 2015. Composite materials with enhanced dimensionless Young's modulus and desired Poisson's ratio. *Scientific reports*. 5, p. 14103.
- [271] Zhu, H. and Fan, T. and Xu, C. et al. 2016. Nano-structured interpenetrating composites with enhanced Young's modulus and desired Poisson's ratio. *Composites Part A: Applied Science and Manufacturing*. 91, pp. 195-202.
- [272] Thomason, J. L. and Vlug, M. A. 1996. Influence of fibre length and concentration on the properties of glass fibre-reinforced polypropylene: 1. Tensile and flexural modulus. *Composites Part A: Applied Science and Manufacturing*. 27(6), pp. 477-484.
- [273] Rousseau, C. E. and Tippur, H. V. 2000. Compositionally graded materials

- with cracks normal to the elastic gradient. *Acta Materialia*. 48(16), pp. 4021-4033.
- [274] Mi, C. and Jiang, Y. and Shi, D. et al. 2014. Mechanical property test of ceramic fiber reinforced silica aerogel composites. *Fuhe Cailiao Xuebao/Acta Materiae Compositae Sinica*. 31(3), pp. 635-643.
- [275] Pan, Y. and Iorga, L. and Pelegri, A. A. 2008. Numerical generation of a random chopped fiber composite RVE and its elastic properties. *Composites Science and Technology*. 68(13), pp. 2792-2798.
- [276] Kari, S. and Berger, H. and Rodriguez-Ramos, R. et al. 2007. Computational evaluation of effective material properties of composites reinforced by randomly distributed spherical particles. *Composite Structures*. 77(2), pp. 223-231.
- [277] Lu, Z. and Yuan, Z. and Liu, Q. et al. 2015. Multi-scale simulation of the tensile properties of fiber-reinforced silica aerogel composites. *Materials Science and Engineering: A*. 625, pp. 278-287.
- [278] Hill, R. 1948. *A theory of the yielding and plastic flow of anisotropic metals*. Proc. R. Soc. Lond. A. The Royal Society. 193(1033), pp. 281-297.
- [279] Ma, Y. H. and Zhu, H. X. and Su, B. et al. 2018. The elasto-plastic behaviour of three-dimensional stochastic fibre networks with cross-linkers. *Journal of the Mechanics and Physics of Solids*. 110, pp. 155-172.
- [280] Johnson, J. B. 1918. *Johnson's Materials of construction*. John Wiley & sons, Incorporated.
- [281] Feng, X.-Q. and Tian, Z. and Liu, Y.-H. et al. 2004. Effective Elastic and Plastic Properties of Interpenetrating Multiphase Composites. *Applied Composite Materials*. 11(1), pp. 33-55.
- [282] Salmon, C. and Boland, F. and Colin, C. et al. 1998. Mechanical properties of aluminium/Inconel 601 composite wires formed by swaging. *Journal of Materials Science*. 33(23), pp. 5509-5516.
- [283] Wegner, L. and Gibson, L. 2000. The mechanical behaviour of interpenetrating phase composites—II: a case study of a three-dimensionally printed material. *International journal of mechanical sciences*. 42(5), pp. 943-964.
- [284] Cheng, F. and Kim, S.-M. and Reddy, J. N. et al. 2014. Modeling of elastoplastic behavior of stainless-steel/bronze interpenetrating phase composites with damage evolution. *International Journal of Plasticity*. 61, pp. 94-111.
- [285] Tonge, Theresa K. and Ruberti, Jeffrey W. and Nguyen, Thao D. 2015. Micromechanical Modeling Study of Mechanical Inhibition of Enzymatic Degradation of Collagen Tissues. *Biophysical Journal*. 109(12), pp. 2689-2700.
- [286] Voorhaar, L. and Hoogenboom, R. 2016. Supramolecular polymer networks: hydrogels and bulk materials. *Chemical Society Reviews*. 45(14), pp. 4013-4031.
- [287] Nguyen, T. D. and Boyce, B. L. 2011. An inverse finite element method for

- determining the anisotropic properties of the cornea. *Biomechanics and Modeling in Mechanobiology*. 10(3), pp. 323-337.
- [288] Urayama, K. and Takigawa, T. 2012. Volume of polymer gels coupled to deformation. *Soft Matter*. 8(31), pp. 8017-8029.
- [289] Obaid, N. and Kortschot, T. M. and Sain, M. 2017. Modeling and Predicting the Stress Relaxation of Composites with Short and Randomly Oriented Fibers. *Materials*. 10(10).
- [290] Obaid, N. and Kortschot, M. and Sain, M. 2017. Understanding the Stress Relaxation Behavior of Polymers Reinforced with Short Elastic Fibers. *Materials*. 10(5), p. 472.
- [291] Lannutti, J. and Reneker, D. and Ma, T. et al. 2007. Electrospinning for tissue engineering scaffolds. *Materials Science and Engineering: C*. 27(3), pp. 504-509.

Publications

Journal papers

Lin, X. and Zhu, H. and Yuan, X. et al. 2019. The elastic properties of composites reinforced by a transversely isotropic random fibre-network. *Composite Structures*. 208, pp. 33-44.

Xiude Lin, Hanxing Zhu. Enhanced elastic properties of honeycomb reinforced composites. In preparation.

Xiude Lin, Hanxing Zhu. The Elastoplastic Behaviours of Composites Reinforced by a Transversely Isotropic Random Fibre-Network. In preparation.

Conference papers/proceedings

Lin, Xiude, Ma, YanHui and Zhu, Hanxing. Viscoelastic properties of fibre-network materials. Presented at: *6TH European Conferences on Computational Mechanics*, Glasgow, UK, 10-15 June 2018.

Lin, Xiude and Zhu, Hanxing. Numerical simulation for the yield behaviour of stochastic fibre reinforced composites with overlap. Presented at: *The 3rd International Conference on Mechanics of Composites*, Bologna, Italy, 4-7, July 2017.